

**A Numerical Study of Quantum Forces:
Casimir Effect, Vortices
and Coulomb Gauge Yang-Mills Theory**

DISSERTATION

zur Erlangung des Grades eines
Doktors der Naturwissenschaften

der Fakultät für Mathematik und Physik
der Eberhard-Karls-Universität zu Tübingen

vorgelegt von
Laurent Moyaerts
aus Verviers, Belgien

2004

Tag der mündlichen Prüfung: 19. November 2004
Dekan: Prof. Dr. Peter Schmid
1. Berichterstatter: PD Dr. Kurt Langfeld
2. Berichterstatter: Prof. Dr. Frithjof Karsch

Abstract

The present thesis is devoted to the numerical investigation of Quantum Field Theories (QFT) by means of non-perturbative methods. It is composed of two parts. In the first part, we present a new numerical approach to the study of physical systems under the influence of external classical fields. In the second part, we investigate by means of lattice simulations the gluon sector of two-colour Quantum Chromo Dynamics (QCD) formulated in Coulomb gauge.

Quantum field theory with external conditions (QFEXT) is the investigation framework of quantum phenomena related to the presence of a given classical background. This technique is used in the context of solid state physics, e.g. in the study of (super-)conducting matter under the influence of external electromagnetic fields, in the context of high energy physics, where special chromo-magnetic configurations in the QCD vacuum are investigated, and has recently found an application in nanotechnology, with the study of the Casimir effect. We propose to treat these applications of QFEXT in the light of the worldline formulation of quantum field theories. Expressed in terms of Schwinger proper-time integrals and first quantized Feynman path integrals, the worldline technique provides a formulation of QFEXT which is conveniently implemented on the computer by means of Monte-Carlo techniques. In this framework, the effective action at one-loop level can be computed for arbitrary background configurations.

Our first investigation concerns the study of magnetic vortex systems, in particular the quantum energy induced by fluctuating fermionic fields. This investigation is relevant for the physics of Type-II superconductors, as well as for the vortex picture of quark confinement in QCD. In the case of a single vortex, the numerical estimates are compared with the analytical results provided by the derivative expansion technique, based on an expansion of the effective action in the gradient of the external field. Exploiting the universality of the numerical method regarding the background potential, we test the limits of validity of the analytical approach at a quantitative level. We find that renormalization induces a serious breakdown of the derivative expansion. The binary vortex system, beyond the range of applicability of analytical techniques, is also investigated and an effective vortex-vortex interaction is obtained as a function of the distance between the vortex cores.

In a second step, we focus on the study of the Casimir effect. The interaction of the fluctuating field with the physical boundary is described in a complete field theoretic way in terms of an external potential accounting for the interface. The Casimir energy of a fluctuating scalar field is investigated for several geometric configurations in the case of rigid bodies. The analytical result for the plate-plate configuration serves as a benchmark test of the method. A study of the sphere-plate and cylinder-plate configurations permits to investigate the effects induced by a curved geometry. The numerical method allows a study beyond the limits of validity of the standard analytical procedure, the Proximity Force Approximation (PFA), which is based on an integration of the parallel plate result along the boundaries. In contrast to PFA, we obtain the Casimir energy for any distance-to-curvature ratio.

The second part is devoted to the lattice study of the $SU(2)$ Yang-Mills theory in the Coulomb gauge formulation. Despite practical disadvantages which render the approach inconvenient for perturbative calculations, Coulomb gauge gained in recent years increasing interest in relation to the problem of confinement in QCD. This formulation indeed allows a

direct access to the Coulomb interaction potential between static colour sources. We review the properties of the Coulomb gauge approach, in particular the quantization of the theory and the scenario of colour confinement, originally formulated by Gribov. In order to avoid any confusion, we distinguish carefully the Coulomb potential from the Wilson potential extracted from the Wilson loop expectation value. The mathematical expression of the Coulomb potential contains the so-called Faddeev-Popov operator. Its central role in the confining property of the potential is discussed in the context of Gribov's scenario.

After a short section devoted to the basic aspects of the lattice approach to gauge theories, we report the results of our simulations for the ghost propagator, i.e. the expectation value of the inverse Faddeev-Popov operator, as well as for the Coulomb potential. We address also equal-time gluonic correlations via the study of the gluon propagator. Our estimates are compared to the results obtained analytically in the Hamiltonian formulation of Yang-Mills theory. We compute therefore the expectation value of the propagators in a fixed time slice. The numerical results in three and four dimensions indicate an enhancement of the ghost propagator in the small momentum regime and a Coulomb potential compatible with a linear confinement of static quarks. The investigation of equal-time gluonic correlations in three and four dimensions reveals a striking behaviour of the gluon propagator in the perturbative regime in the form of an anomalous scaling, whose origin is still under ongoing debate. In four dimensions, the numerical gluon propagator attains a non-vanishing finite value at zero momentum transfer.

Zusammenfassung

Diese Dissertation ist der Untersuchung von Quantenfeldtheorien (QFT) mithilfe nichtstörungstheoretischer Methoden gewidmet. Sie besteht aus zwei Teilen. Im ersten Teil stellen wir eine neuere numerische Methode vor, die die Studie der Quanteneigenschaften physikalischer Systeme in Anwesenheit äußerer klassischer Felder ermöglicht. Im zweiten Teil werden die Eigenschaften des Gluon-Sektors der Quantenchromodynamik (QCD) mit zwei Farben mit Hilfe von Gittersimulationen in Coulomb-Eichung untersucht.

Die Untersuchung von Quantenphänomenen eines physikalischen Systems in Anwesenheit klassischer Hintergrundfelder erfolgt im Rahmen der sogenannten "Quantenfeldtheorie unter äußeren Bedingungen" (QFEXT). Diese Technik wird eingesetzt sowohl in der Festkörperphysik, beispielsweise bei der Untersuchung der (supra-)leitenden Materie in äußeren elektromagnetischen Feldern, als auch in der Hochenergiephysik, z.B. in der Studie spezieller chromomagnetischer Felder im QCD Vakuum. Die Studie des Casimireffekts kann ebenso anhand dieser Methode durchgeführt werden. In dieser Arbeit werden diese Anwendungen der QFEXT im Rahmen des Weltlinien-Formalismus der QFT untersucht. Dieser auf Schwinger und Feynman zurückgehende Formalismus ermöglicht die Berechnung der effektiven Wirkung auf 1-Schleifen-Niveau für beliebige Hintergrundfelder mithilfe des Monte-Carlo Verfahrens.

Wir wenden unsere numerische Methode zuerst auf die Bestimmung der Quantenenergie eines Systems magnetischer Wirbel (Vortex) an, die durch fluktuierende fermionische Felder induziert wird. Diese Untersuchung ist sowohl für die Physik des Typ-II-Supraleiters relevant, als auch für das Confinement-Szenario der QCD, das auf chromomagnetischen Flusswirbeln basiert. Im einfachsten Fall eines einzelnen Vortex werden die numerischen Daten mit den analytischen Ergebnissen verglichen, die mit der Gradiententwicklung erhalten wurden. Diese Näherung basiert auf der Entwicklung der effektiven Wirkung nach Potenzen des Gradienten des Hintergrundfeldes. Die Universalität unserer Methode ermöglicht die Bestimmung der Gültigkeitsgrenze des analytischen Zuganges auf einem quantitativen Niveau. Unsere numerischen Ergebnisse zeigen, dass die Renormierung der effektiven Wirkung eine signifikante Verschlechterung des Konvergenzverhaltens der Ableitungsentwicklung verursacht. Das 2-Vortex-System, welches für die analytischen Methoden unzugänglich ist, wird untersucht, und wir erhalten eine effektive Vortex-Vortex-Wechselwirkung als Funktion vom Abstand der Vortexkerne.

Desweiteren wenden wir unsere Methode auf die Studie des Casimireffekts an. Die Wechselwirkung zwischen dem fluktuierenden Feld und den Grenzflächen wird durch ein äußeres Potential beschrieben. Die Casimirenergie wird im einfachsten Fall eines fluktuierenden Skalarfeldes und starrer Grenzflächen für mehrere geometrische Konfigurationen bestimmt. Das analytische Ergebnis für die Konfiguration mit zwei parallelen Platten dient als Test unserer Methode. Eine Studie der Konfiguration mit Platte und Kugel bzw. Platte und Zylinder, ermöglicht die Analyse der Effekte, die durch die gekrümmte Geometrie induziert werden. Unser numerischer Zugang erlaubt die Bestimmung des Gültigkeitsbereiches der sogenannten "Proximity Force Approximation" (PFA). Diese basiert auf der Integration des analytischen Ergebnisses für parallele Platten entlang der Randflächen. Im Gegensatz zur PFA bestimmen wir die Casimirenergie für beliebige Verhältnisse zwischen Abstand und Krümmung.

Der zweite Teil ist der Formulierung der $SU(2)$ Yang-Mills-Theorie in Coulomb-Eichung

gewidmet. Diese Eichung hat im Bezug auf das Quark-Confinement während der letzten Jahre wachsendes Interesse erfahren: Sie erlaubt einen direkten Zugang zum Coulomb-Potential, das die Wechselwirkung zweier statischer Quarks beschreibt. Wir geben einen Überblick über die Eigenschaften der Formulierung der Yang-Mills Theorie in Coulomb-Eichung, insbesondere die Quantisierung der Theorie und das von Gribov formulierte Szenario für das Quark-Confinement. Das Coulomb-Potential wird vom eichinvarianten Wilson-Potential unterschieden, das durch die Berechnung des Erwartungswertes des Wilson-Loops im Yang-Mills-Vakuum bestimmt werden kann. Der mathematische Ausdruck des Coulomb-Potentials enthält den sogenannten Faddeev-Popov-Operator, dessen Rolle in Bezug auf das Gribov-Szenario diskutiert wird.

Nach einem kurzen Abschnitt über die Grundlagen der Gittertheorie werden die numerischen Ergebnisse unserer Simulationen für den Geist-Propagator, das Coulomb-Potential und den Gluon-Propagator vorgestellt. Wir vergleichen unsere Daten mit den aus der Hamiltonschen Formulierung der Yang-Mills-Theorie erhaltenen Ergebnissen. Der Erwartungswert der Propagatoren wird deshalb innerhalb einer fixierten Zeitschicht bestimmt. Unsere numerischen Abschätzungen in drei und vier Dimensionen zeigen eine Verstärkung des Geist-Propagators im Bereich kleiner Impulse und sind kompatibel mit einem linearen Confinement von statischen Quarks. Die Untersuchung des Gluon-Propagators bei fixierter Zeit zeigt ein auffallendes Verhalten im Bereich großer Impulse in Form einer anomalen Skalierung, für die keine definitive Erklärung bis zur Veröffentlichung dieser Arbeit gefunden werden konnte. In vier Dimensionen erreicht der Gluon-Propagator einen endlichen Wert im Bereich kleiner Impulse.

A mes grands-parents

Contents

I	Worldline Numerics	13
1	Introduction	15
2	Worldline Techniques	19
2.1	The quantum effective action on the worldline	19
2.1.1	Scalar effective action	19
2.1.2	Scalar QED effective action	23
2.1.3	Spinor QED effective action	24
2.2	Renormalization	25
2.3	Worldline Numerics: the 'loop cloud' method	26
2.3.1	Loop rescaling, unit loops and discretization	26
2.3.2	Generation of the unit loop ensemble	27
2.3.3	Calculating the effective action: the method	35
2.4	Summary	37
3	Magnetic Backgrounds	39
3.1	Constant magnetic field	40
3.1.1	One-loop Euler-Heisenberg-Schwinger Lagrangians	41
3.1.2	Renormalization	42
3.1.3	A benchmark test: Wilson loop average over scalar loops	44
3.1.4	A numerical problem: average over fermionic loops	44
3.2	Fermion-induced action of vortex systems	47
3.2.1	General framework	47
3.2.2	The derivative expansion	49
3.2.3	Single-vortex configuration in $D = 2 + 1$	50
3.2.4	Single-vortex configuration in $D = 3 + 1$	52
3.2.5	Binary-vortex interactions	54
3.3	Summary and outlook	55
4	Casimir effect on the worldline	57
4.1	Imposing boundary conditions on quantum fields	58
4.2	Worldline approach to the Casimir effect	59
4.2.1	General framework	59
4.2.2	Casimir interaction energy between rigid bodies	61
4.2.3	Worldline numerics in the sharp limit	62
4.3	Numerical results	64

4.3.1	Parallel plates	64
4.3.2	Sphere above plate	66
4.3.3	Cylinder above plate	70
4.4	Summary and outlook	71
II Lattice $SU(2)$ Yang-Mills Theory in Coulomb Gauge		79
5	Introduction	81
6	Yang-Mills theory in Coulomb gauge	87
6.1	Quantization of constrained systems	88
6.1.1	Canonical quantization	88
6.1.2	Path integral quantization	91
6.2	Quantization of Maxwell theory	92
6.2.1	Canonical quantization	92
6.2.2	Path integral quantization	96
6.3	Quantization of Yang-Mills theory	97
6.4	Gribov's scenario of confinement	99
6.4.1	Gribov copies	100
6.4.2	Minimal Coulomb gauge and fundamental modular region	101
6.4.3	Coulomb potential vs. Wilson potential	102
6.4.4	Coulomb potential and renormalization	108
6.4.5	Confinement scenario	108
6.5	Summary	109
7	Coulomb gauge on the lattice	111
7.1	Basic facts about lattice gauge theories	111
7.1.1	Basic definitions	111
7.1.2	Wilson's action - Partition function - Observable	113
7.1.3	Continuum limit	113
7.2	Fixing the Coulomb gauge	116
7.2.1	General framework	116
7.2.2	Gauge fixing as a minimization problem	117
7.2.3	Complete gauge fixing	118
7.2.4	Numerical implementation	120
7.3	Lattice measurements	121
7.3.1	Numerical procedure	121
7.3.2	Renormalization	122
7.3.3	Simulation parameters	122
7.4	Lattice observables	123
7.4.1	Ghost propagator	123
7.4.2	Coulomb potential and form factor $f(p)$	124
7.4.3	Equal-time transverse gluon propagator	125
7.5	Numerical results	126
7.5.1	D=2+1	126
7.5.2	D=3+1	130

7.6	Summary and outlook	135
A	Conventions and notations	137
A.1	Units, metric and notations	137
A.2	SU(N) algebra	137
B	Non-Abelian gauge theory in the continuum	139
B.1	Covariant derivative - Gauge potential	139
B.2	Field strength - E and B fields	140
B.3	Lagrangian - classical field equations	141
C	Lattice technicalities	143
C.1	Conventions	143
C.2	Basic concepts	143
C.3	Links and lattice gauge potential	145
C.4	Gauge transformation	146
C.5	Covariant derivative	146
C.6	Faddeev-Popov operator	147
C.7	Lattice gauge fixing	148
C.8	Inverse Faddeev-Popov operator	149
D	Lattice algorithms	151
D.1	Heatbath algorithm	151
D.2	Conjugate gradient	153
E	Elementary calculations	155
E.1	Plane center vortices	155
E.2	Numerical computation of the Wilson loop	156
E.2.1	Constant magnetic field	156
E.2.2	Vortex field	157
E.3	Linear potential in Fourier space	157

Part I

Worldline Numerics

Chapter 1

Introduction

The first stages of the development of Quantum Electro Dynamics (QED), the quantum field theory of interacting electrons and photons, are bound to the interest for new effects, of pure quantum nature, induced in the presence of strong electromagnetic fields. In 1936, Heisenberg and Euler [HE36] predicted theoretically quantum effects in the vacuum when intense electromagnetic fields are turned on. For example, they were able to calculate the probability of a creation of an electron-positron pair from the vacuum in the presence of a strong electric field. This quantum polarization of the vacuum results from the interaction of the *external field*, treated in a full classical way, with a *fluctuating quantum field*, in the present case the electron-positron field. *Quantum field theories* with *classical background potential*, or QFEXT¹, build nowadays a general framework which permits to treat a large spectrum of physical problems classified according to the nature of the fluctuating field and the background potential. In the context of solid state physics, this framework is used to study the quantum theory of charge carriers, electrons or holes, in the presence of various magnetic field configurations: constant magnetic field applied to a conventional conductor, giving rise to the Hall effect [PG90], or *magnetic vortices*, captured inside superconducting matter responsible for the induction of an undesirable resistance [CN97]. Both phenomena are still under numerous experimental and theoretical investigations. In the context of QCD, the formalism is used to study fluctuating quarks in the presence of center magnetic vortices, which are believed to play a crucial role in the phenomenon of colour confinement, as suggested by lattice investigations [Gre03]. The Casimir effect came recently enlarge the family of theories described in the QFEXT framework. A formulation of the problem in terms of a renormalizable quantum field theory was recently proposed [GJK⁺02]. In this approach, the interaction of the fluctuating field with the Casimir boundary is taken into account via a field theoretic interaction with a classical background potential. The Casimir effect, considered for a long time only as a beautiful illustration of quantum effects, has become in recent years a high relevant topic in nanotechnology, e.g. engineering of microscopical devices at nanoscale.

Mathematically, the quantum correction *induced* by the fluctuating electron-positron field in the Heisenberg-Euler problem is represented under the form of an additional term to the classical Maxwell action. This is an *effective action*, in the sense that the quantum effects induced by the electron field are contained in a function of the electromagnetic field only, which describes the new physical properties of the vacuum without explicit reference to the electronic degrees of freedom. In the field theoretic language, the effective action is

¹Quantum Field theory under the influence of EXTERNAL conditions.

obtained by *integrating out* the electron-positron field. This integration over the fluctuating field gives rise to a *functional determinant*, whose analytical calculation is a non-trivial task for arbitrarily shaped background potentials. If the coupling constant characterizing the interaction between the fluctuating field and the background potential is small, a perturbative expansion can be performed. This gives rise to a diagrammatic representation in terms of *Feynman diagrams* containing one loop of the fluctuating field with insertions of the external potential. A non-perturbative treatment can be achieved in the *Worldline Formalism*, which, by means of the Schwinger proper-time technique and the Feynman path integral formulation, provides a representation of the functional determinant under the form of a path integral in quantum mechanics [Sch01]. More precisely, the determinant is expressed as a sum over *loops*, i.e. closed paths in space-time also called *worldlines*, which experience the background potential around their perimeter, i.e. in a *non-local* way. The effective action on the worldline can be exactly computed only in ideal cases, like configurations with homogeneous background fields. The standard approximation consists in studying deviations from this ideal case by means of *derivative expansion* techniques, i.e. expanding the action in terms of the gradients of the background potential. This has been until now achieved up to first order derivatives of the electromagnetic field in the case of QED [GS99].

The worldline formulation of the one-loop effective action as a first-quantized path integral allows an exact numerical treatment: the integral over the loops can be understood as a weighted average over the loop ensemble, which suggests a numerical implementation by means of the Monte-Carlo method. This technique, which we call *loop cloud method*, generates stochastically an ensemble of loops and achieves the calculation of the effective action by performing statistical *loop averages* [GL02]. Since the loop weight factor is independent of the background potential, a loop ensemble can be used for several physical problems, i.e. the numerical method is *independent of the background potential*. The loop cloud method was initially tested in the case of a constant magnetic background and applied to the study of the quantum properties of a magnetic step configuration [GL01], which can by no means be handled by the derivative expansion method.

In view of the fact that the loop cloud method is a recent technique, we propose to review it in details in chapter 2. We start with the definition of the effective action, derive the worldline formulation in an explicit way and discuss the renormalization in this formalism. Though the formulation is an alternative approach to QFT without Feynman diagrams, it is not free of divergences and does not bypass the regularization of infinite expressions. Finally, we give in a technical section a detailed description of the numerical procedure. The reader who is more interested in the applications is invited to skip this part and consult directly chapter 3 and chapter 4.

In the present work, we apply the loop cloud method to the study of two physical problems: quantum effects induced by fermions in the presence of magnetic vortex systems are treated in chapter 3, while chapter 4 is devoted to the study of the Casimir effect. In each case, the loop cloud method is tested by confronting the numerical estimates with the results provided by the standard analytical approaches in their respective range of applicability. After this test phase, we perform simulations of physical configurations for which no analytical result is yet available. In the context of magnetic backgrounds, we repeat for pedagogical purposes the simulations at constant magnetic field performed in a previous reference [GL01] and point out a technical limitation of the loop cloud method in the case of fermionic fluctuations

(fermion problem). In a second step, we calculate the effective action induced by fermions in the presence of magnetic vortex systems, a configuration for which the fermion problem has a harmless impact. The simple configuration of one single vortex permits to compare our estimates to the results obtained using the derivative expansion and therefore allows for a discussion on the range of validity of the latter on a quantitative level. The calculations are performed in $D = 2 + 1$ and $D = 3 + 1$, illustrating the effects induced by renormalization. We turn to the case of a binary vortex configuration and study the quantum corrections to the interaction energy as a function of the distance between the vortex cores.

We begin chapter 4 with a discussion of the field theoretic formulation of the Casimir effect developed recently [GJK⁺02]. In contrast to the standard approach which consists in implementing *ad hoc* boundary conditions on the fluctuating field, a clear advantage of this formulation is its ability to distinguish between divergences of pure field theoretic nature and divergences arising from idealizations of the Casimir boundaries. We test the applicability of the loop cloud method to the study of the Casimir effect by performing simulations of the parallel plate configuration, which is analytically well known. All simulations are done with respect to a fluctuating scalar field and *rigid*, i.e. non deformable, Casimir boundaries. In this case, the infinities due to the idealization of perfectly conducting and infinitely thin boundaries do not prevent the calculation of the Casimir *interaction energy* giving rise to the Casimir force. Turning to the sphere-plate configuration, which is the standard experimental setup used for the measurements of the Casimir force, we compare our numerical estimates to the analytical results furnished by the *proximity force approximation*. This technique approximates the full calculation of the Casimir energy by an integration of the parallel plate result over the surfaces of the Casimir boundaries. The approach considers only local interactions of infinitesimal bits on each boundary and neglects *de facto* effects due to the curvature. The loop cloud method is on the contrary by construction non-local, since a loop experiences the background potential along its perimeter. The comparison of our results with proximity force calculations provides therefore a way to investigate curvature effects at a quantitative level in any range of the distance-to-curvature ratio. We close the chapter with a study of the cylinder-plate configuration.

Chapter 2

Worldline Techniques

In this chapter, we present the worldline approach to the computation of one-loop effective actions in quantum field theories. The effective action is defined in the context of a scalar field theory in the presence of a scalar background and a representation in terms of a worldline integral is derived. After a straightforward generalization to the cases of scalar and spinor QED and some general remarks on the renormalization procedure in the worldline formalism, we present a new numerical approach to the calculation of the one-loop effective action, which regards the worldline integrals as weighted averages over ensembles of loops in space-time. The generation of the statistical loop ensembles is described in detail in a separate section, which can be skipped by the reader mainly interested in an overview of the method. A recipe and a summary of the main features of the method conclude the chapter.

2.1 The quantum effective action on the worldline

This work concerns the study of physical systems in the framework of a quantum field theory under the influence of external conditions. This concretely means that we investigate the effects induced by the fluctuations of a *quantum field* in the presence of a background modelled by a *classical potential*. We will in a first step consider the simplest case of a fluctuating real scalar field in the presence of a scalar background potential.

2.1.1 Scalar effective action

Let us start with the field theoretic Lagrangian. In Euclidean space-time, it is given by

$$\mathcal{L}[\phi, V] = \frac{1}{2} \partial_\mu \phi \partial_\mu \phi + \frac{1}{2} m^2 \phi^2 + \frac{1}{2} V(x) \phi^2, \quad (2.1)$$

where m is the mass of the fluctuating field ϕ and $V(x)$ denotes the space-time dependent scalar background potential. This field theory is quantized in the path integral formalism. In this framework, the fundamental quantity is the *generating functional* defined by

$$Z[V] = \int \mathcal{D}\phi e^{-S[\phi, V]}, \quad (2.2)$$

where $S[\phi, V] = \int d^D x \mathcal{L}[\phi, V]$ denotes the classical action. The analogy with statistical physics is clear if we think of quantum fluctuations in terms of thermal fluctuations, of field

configurations in terms of microstates of the system and of the factor e^{-S} in terms of a Boltzmann factor. The generating functional then is the analogue of the partition function and we define the *quantum effective action* $\Gamma[V]$ by $Z[V] = e^{-\Gamma[V]}$ in complete analogy with the free energy in statistical physics.

Since the argument of the exponential function is quadratic in the field ϕ , the Gaussian integral can be performed, yielding

$$Z[V] = \text{Det}^{-1/2} \left[\frac{-\partial^2 + m^2 + V(x)}{-\partial^2 + m^2} \right], \quad \Gamma[V] = \frac{1}{2} \text{Tr} \ln \left[\frac{-\partial^2 + m^2 + V(x)}{-\partial^2 + m^2} \right], \quad (2.3)$$

where we used the identity $\ln \text{Det}[\hat{\mathcal{O}}] = \text{Tr} \ln[\hat{\mathcal{O}}]$. In standard QFT textbooks, the effective action is generally given in terms of a *loop expansion*¹

$$\Gamma = \Gamma^{(1)} + \Gamma^{(2)} + \dots + \Gamma^{(n)} + \dots,$$

where $\Gamma^{(n)}$ resums the contributions of n -loops Feynman diagrams. For the field theory (2.1), we show that the contribution (2.3) resums precisely one-loop Feynman diagrams, i.e. corresponds to the first term $\Gamma^{(1)}$ in the expansion above. We rewrite (2.3) under the form

$$\Gamma[V] = \frac{1}{2} \text{Tr} \ln [1 + (-\partial^2 + m^2)^{-1} V].$$

Expanding the logarithm and noting that $(-\partial^2 + m^2)^{-1} := G_F$ is the bare scalar propagator, we find

$$\begin{aligned} \Gamma[V] &= \sum_{n=1}^{\infty} \frac{(-1)^{n-1}}{2n} \text{Tr} \{ [G_F V]^n \} \\ &= \sum_{n=1}^{\infty} \frac{(-1)^{n-1}}{2n} \int d^D z_1 \dots d^D z_n G_F(z_1 - z_2) V(z_2) G_F(z_2 - z_3) \dots \\ &\dots V(z_n) G_F(z_n - z_1) V(z_1). \end{aligned}$$

A representation in terms of Feynman diagrams is given in Fig. 2.1, left panel. The fact that the effective action contains the sum over all one-loop diagrams only, i.e. $\Gamma[V] = \Gamma^{(1)}[V]$, is particular to Lagrangians of the type (2.1) for which

- the potential V is purely classical, i.e. does not fluctuate,
- the interaction term is quadratic in the fluctuating field.

Higher orders in ϕ or a fluctuating potential would induce diagrams depicted in Fig. 2.1, right panel.

Let us now restart from (2.3) and derive the worldline representation of the effective action. First, we use the Schwinger proper-time representation of the logarithm [Sch51]:

$$\ln \left[\frac{A}{B} \right] = \int_0^{\infty} \frac{dT}{T} [e^{-BT} - e^{-AT}].$$

¹This corresponds to an expansion in powers of \hbar .

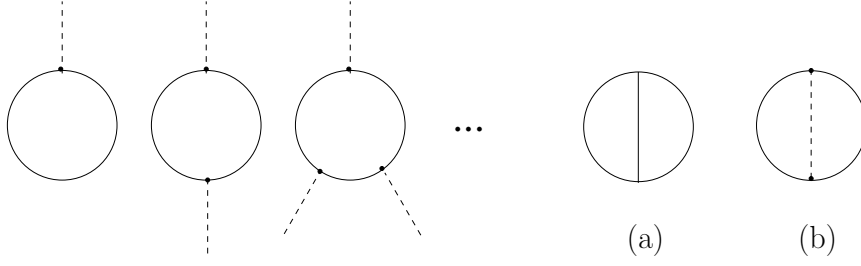


Figure 2.1: The one-loop effective action $\Gamma^{(1)}[V]$ resums all Feynman diagrams containing one loop in the fluctuating field with insertions of the external potential V (dashed line). The two-loop diagrams on the right cannot contribute to the effective action. Diagram (a) is excluded by the structure of the Lagrangian, which contains no ϕ^3 interaction, while diagram (b) contains an internal dashed line, which is excluded since the external V field is non fluctuating.

The effective action becomes

$$\Gamma^{(1)}[V] = -\frac{1}{2} \text{Tr} \left\{ \int_0^\infty \frac{dT}{T} e^{-m^2 T} \left[e^{-(-\partial^2 + V)T} - e^{-(-\partial^2)T} \right] \right\}. \quad (2.4)$$

Second, the functional trace is expressed in terms of quantum mechanical matrix elements

$$\text{Tr}[\hat{\mathcal{O}}] = \int d^D x \langle x | \hat{\mathcal{O}} | x \rangle, \quad (2.5)$$

leading us to the evaluation of $\langle x | e^{\partial^2 T} | x \rangle$ and $\langle x | e^{-(-\partial^2 + V)T} | x \rangle$. The former is trivially obtained by inserting a complete set of momentum states $\int \frac{d^D p}{(2\pi)^D} |p\rangle \langle p| = 1$:

$$\langle x | e^{\partial^2 T} | x \rangle = \int \frac{d^D p}{(2\pi)^D} e^{-p^2 T} = \frac{1}{(4\pi T)^{D/2}}.$$

For the second matrix element, we perform a discretization of the proper-time interval into N small slices of length $\epsilon = \frac{T}{N}$. We split the operator into N factors

$$e^{-(-\partial^2 + V)T} = \underbrace{e^{-(-\partial^2 + V)\epsilon} \dots e^{-(-\partial^2 + V)\epsilon}}_{N \text{ factors}}$$

and insert $N - 1$ complete sets of states in position space and N complete sets of states in momentum space:

$$\begin{aligned} \langle x | e^{-(-\partial^2 + V)T} | x \rangle &\simeq \int d^D p_1 \dots d^D p_N d^D x_1 \dots d^D x_{N-1} \langle x | e^{-(-\partial^2 + V)\epsilon} | p_1 \rangle \langle p_1 | x_1 \rangle \\ &\quad \langle x_1 | e^{-(-\partial^2 + V)\epsilon} | p_2 \rangle \langle p_2 | x_2 \rangle \dots \langle x_{N-1} | e^{-(-\partial^2 + V)\epsilon} | p_N \rangle \langle p_N | x \rangle, \\ &\simeq \int d^D p_1 \dots d^D p_N d^D x_1 \dots d^D x_{N-1} e^{-V(x)\epsilon} e^{-p_1^2 \epsilon} e^{-ip_1 \cdot (x - x_1)} \dots \\ &\quad \dots e^{-V(x_{N-1})\epsilon} e^{-p_N^2 \epsilon} e^{-ip_N \cdot (x_{N-1} - x)} \end{aligned} \quad (2.6)$$

where the relation ' \simeq ' is exact up to some constant prefactors. The last expression is nothing else than the Feynman path integral formula for the amplitude:

$$\langle x, T | x, 0 \rangle \simeq \prod_{n=1}^{N-1} \left[\int d^D x_n \right] \prod_{n=1}^N \left[\int d^D p_n \right] e^{-iS_N}, \quad (2.7)$$

where

$$\mathcal{S}_N = \sum_{n=1}^N [p_n(x_n - x_{n-1}) - i\epsilon H(p_n, x_n, t_n)]$$

with the ‘‘Hamilton’’ function² $H(p_n, x_n, t_n) = p_n^2 + V(x_n)$. The representation of the scalar effective action is mapped onto the quantum mechanical problem of a particle of mass $M = 1/2$ in the potential $V(x)$. Performing all momentum integrations, we obtain

$$\begin{aligned} \langle x | e^{-(\partial^2 + V)T} | x \rangle &= \mathcal{N} \int d^D x_1 \dots d^D x_{N-1} e^{-V(x)\epsilon} e^{-\frac{(x-x_1)^2}{4\epsilon}} e^{-V(x_1)\epsilon} e^{-\frac{(x_1-x_2)^2}{4\epsilon}} \dots \\ &\dots e^{-V(x_{N-1})\epsilon} e^{-\frac{(x_{N-1}-x)^2}{4\epsilon}}, \end{aligned}$$

where the constant prefactors have been absorbed in the normalization \mathcal{N} . The ‘‘continuum limit’’ $N \rightarrow \infty$ is denoted by a functional integral over paths $x(\tau)$ parameterized by the proper-time $\tau \in [0, T]$:

$$\Gamma^{(1)}[V] = -\frac{1}{2} \int_0^\infty \frac{dT}{T} e^{-m^2 T} \int d^D x \left[\mathcal{N} \int_{x(0)=x}^{x(T)=x} \mathcal{D}x e^{-\int_0^T d\tau \left[\frac{\dot{x}^2}{4} + V(x(\tau)) \right]} - \frac{1}{(4\pi T)^{D/2}} \right].$$

The normalization \mathcal{N} is determined from the limit of zero potential

$$\mathcal{N} \int_{x(0)=x(T)} \mathcal{D}x e^{-\int_0^T d\tau \frac{\dot{x}^2}{4}} = \frac{1}{(4\pi T)^{D/2}}$$

such that the path integral can be interpreted as an expectation value with respect to an ensemble of closed loops with Gaussian velocity distribution:

$$\begin{aligned} \mathcal{N} \int \mathcal{D}x e^{-\int_0^T d\tau \left[\frac{\dot{x}^2}{4} + V(x(\tau)) \right]} &= \frac{1}{(4\pi T)^{D/2}} \frac{\int \mathcal{D}x e^{-\int_0^T d\tau V(x(\tau))} e^{-\int_0^T d\tau \frac{\dot{x}^2}{4}}}{\int \mathcal{D}x e^{-\int_0^T d\tau \frac{\dot{x}^2}{4}}} \\ &:= \frac{1}{(4\pi T)^{D/2}} \left\langle e^{-\int_0^T d\tau V(x(\tau))} \right\rangle_x. \end{aligned}$$

In a last step, we shift all loops $x(\tau)$ to have a common center of mass x_{CM} , implying $\int_0^T d\tau x_\mu(\tau) = 0$. The effective action reads finally

$$\Gamma^{(1)}[V] = -\frac{1}{2(4\pi)^{D/2}} \int_0^\infty \frac{dT}{T^{D/2+1}} e^{-m^2 T} \int d^D x_{\text{CM}} \left[\left\langle e^{-\int_0^T d\tau V(x_{\text{CM}} + x(\tau))} \right\rangle_x - 1 \right]. \quad (2.8)$$

This result shows that the quantum field theory defined by (2.1) and (2.2) is mapped onto a one-dimensional field theory, if we regard the particle position $x_\mu(\tau)$ as a set of D fields living in the one-dimensional space of proper-time. This set, describing a loop for which the proper-time $\tau \in [0, T]$ plays the role of the parameter, is called *worldline*.

²Since the proper-time element ϵ has energy dimension -2, the function H possesses the dimension of a squared energy .

The calculation of the effective action to one-loop level (2.8) is then reduced in the so called *worldline* - or *string-inspired*³ - *formalism* to the computation of the expectation value of the “*holonomy factor*⁴”

$$\left\langle e^{-\int_0^T V(x_{\text{CM}}+x(\tau))} \right\rangle_x \quad (2.9)$$

over the ensemble of all closed worldlines $x(\tau)$ centered upon x_{CM} , with respect to the *loop distribution* given by $\exp\left\{-\int_0^T d\tau \dot{x}^2/4\right\}$. In the following, we will refer to this expectation value $\langle \dots \rangle_x$ as *worldline* or *loop average*. We will also use the notation

$$W_V[T, x(\tau), x_{\text{CM}}] := e^{-\int_0^T V(x_{\text{CM}}+x(\tau))}.$$

2.1.2 Scalar QED effective action

Let us consider the theory of a fluctuating complex scalar field in the presence of a classical background Abelian gauge field given by the vector potential $A_\mu(x)$. We are now dealing with a gauge theory whose Lagrangian is given by

$$\mathcal{L}[\phi, \phi^*, A] = -\phi^* D^2 \phi + m^2 \phi^* \phi,$$

with the covariant derivative $D_\mu = \partial_\mu + iA_\mu$. The effective action reads in this case

$$\Gamma^{(1)}[A] = \frac{1}{2} \text{Tr} \ln \left[\frac{-(\partial + iA)^2 + m^2}{-\partial^2 + m^2} \right].$$

We cut short the complete derivation of the matrix element $\langle x | e^{D^2 T} | x \rangle$ and start directly with the expression (2.7), which is now the propagation amplitude of a charged particle of mass $M = 1/2$ and unitary charge in the magnetic field derived from the potential A_μ . The corresponding Hamiltonian is given by $H(p_n, x_n, t_n) = [p_n + A(x_n)]^2$ and the matrix element reads

$$\langle x | e^{D^2 T} | x \rangle \simeq \int \mathcal{D}x \mathcal{D}p e^{-i \int_0^T d\tau p \cdot \dot{x}} e^{-\int_0^T d\tau [p(\tau) + A(x(\tau))]^2}.$$

If we perform a re-parametrization of the momentum path integral $p + A \rightarrow p'$ and integrate over p' , we obtain the equivalent expression to (2.8) in scalar QED:

$$\Gamma^{(1)}[A] = -\frac{1}{(4\pi)^{D/2}} \int_0^\infty \frac{dT}{T^{D/2+1}} e^{-m^2 T} \int d^D x_{\text{CM}} \left[\left\langle e^{i \int_0^T d\tau A(x_{\text{CM}}+x(\tau)) \cdot \dot{x}} \right\rangle_x - 1 \right]. \quad (2.10)$$

For field theories with internal degrees of symmetry, note that the trace operation in (2.3) is not only given by the functional operation (2.5) but also includes a trace over these internal

³Let us note that the worldline formulation of QFT emerged originally from string theory [BK92], which corresponds to QFT in a certain limiting case. The string-inspired rules of calculation, called Bern-Kosower rules, were rederived later in the framework of QFT by Strassler [Str92] using proper-time representation and first-quantized path integral similarly to the above derivation.

⁴The term ‘holonomy’, used here by extension to refer to the potential part of the worldline representation, is, strictly speaking, only valid for a theory with vector background field, in which case it indeed corresponds to the Wilson loop (see below).

degrees. This explains the different prefactors in (2.8) and (2.10). From this result, we see that the computation of the one-loop effective action for a gauge theory is reduced to the evaluation of the loop average of the *Wilson loop*

$$\left\langle W_A[T, x(\tau), x_{\text{CM}}] \right\rangle_x := \left\langle e^{i \int_0^T d\tau A(x_{\text{CM}} + x(\tau)) \cdot \dot{x}} \right\rangle_x, \quad (2.11)$$

which is gauge invariant with respect to the background gauge field.

2.1.3 Spinor QED effective action

We finally derive the worldline one-loop effective action for the theory of a fluctuating Dirac field minimally coupled to a classical background Abelian gauge field $A_\mu(x)$. The Lagrangian reads

$$\mathcal{L}[\psi, \bar{\psi}, A] = \bar{\psi}[i\mathcal{D} - m]\psi$$

where m is now the mass of the fluctuating fermion field, $\mathcal{D} = \gamma_\mu D_\mu$, with the covariant derivative $D_\mu = \partial_\mu + iA_\mu$. The matrices γ_μ are the anti-hermitian Euclidean γ -matrices, $\gamma_\mu^\dagger = -\gamma_\mu$ satisfying $\{\gamma^\mu, \gamma^\nu\} = -2\delta^{\mu\nu}$. As a consequence, the operator \mathcal{D} is hermitian. The quantum field theory is defined as usual by the generating functional

$$Z[A] = \int \mathcal{D}\psi \mathcal{D}\bar{\psi} e^{-\int d^D x \bar{\psi}(x)[-i\mathcal{D} + m]\psi(x)}$$

where ψ and $\bar{\psi}$ are Grassmann fields. The integration over Grassmann variables yields

$$\Gamma^{(1)}[A] = -\text{Tr} \ln \left[\frac{-i\mathcal{D} + m}{-i\partial + m} \right] = -\frac{1}{2} \text{Tr} \ln \left[\frac{\mathcal{D}^2 + m^2}{-\partial^2 + m^2} \right].$$

The operator \mathcal{D}^2 reads explicitly

$$\mathcal{D}^2 = -(\partial + iA)^2 + \frac{1}{2} \sigma_{\mu\nu} F_{\mu\nu}$$

where $F_{\mu\nu} = \partial_\mu A_\nu - \partial_\nu A_\mu$ is the field strength tensor and $\sigma_{\mu\nu} := \frac{i}{2}[\gamma_\mu, \gamma_\nu]$. The spinor QED effective action is identical to the scalar QED expression, up to the global sign due to the integration over Grassman fields, the presence of the potential term $\frac{1}{2} \sigma_{\mu\nu} F_{\mu\nu}$ and the prefactors. It reads explicitly

$$\begin{aligned} \Gamma^{(1)}[A] &= \frac{1}{2(4\pi)^{D/2}} \int_0^\infty \frac{dT}{T^{D/2+1}} e^{-m^2 T} \int d^D x_{\text{CM}} \\ &\times 4 \left[\left\langle e^{i \int_0^T d\tau A(x_{\text{CM}} + x(\tau)) \cdot \dot{x}} \frac{1}{4} \text{tr} P_T e^{\frac{1}{2} \int_0^T d\tau \sigma_{\mu\nu} F_{\mu\nu}(x_{\text{CM}} + x(\tau))} \right\rangle_x - 1 \right]. \end{aligned} \quad (2.12)$$

The mathematical symbol P_T denotes path ordering with respect to the proper-time T . Comparing this result with (2.10), we see that the transition from scalar to Dirac fields in a background gauge field has introduced an additional factor in the loop average. The quantity

$\frac{1}{4}\text{tr}P_T \exp\left\{\frac{1}{2}\int_0^T d\tau\sigma_{\mu\nu}F_{\mu\nu}\right\}$ is the *Pauli* or *spin factor* and takes the spinor structure of the fluctuating field into account. The tracing operation is performed relatively to the Dirac structure of the exponential function, due to the presence of $\sigma_{\mu\nu}$ in its argument. Let us note that the Pauli factor, as well as the Wilson loop, is a gauge invariant quantity. The loop average will in the following be abbreviated by

$$\left\langle W_A^{\text{ferm}}[T, x(\tau), x_{\text{CM}}] \right\rangle_x := \left\langle e^{i\int_0^T d\tau A(x_{\text{CM}}+x(\tau))\cdot\dot{x}} \frac{1}{4}\text{tr} e^{\frac{1}{2}\int_0^T d\tau\sigma_{\mu\nu}F_{\mu\nu}(x_{\text{CM}}+x(\tau))} \right\rangle_x.$$

2.2 Renormalization

In this section, we limit our discussion to general aspects of renormalization in the worldline formalism. We will discuss the renormalization procedures specific to each physical problem in the next chapters.

When studying a physical problem formulated in the QFEXT framework, we are possibly confronted with two types of divergences:

- (i) field theoretic ultraviolet divergences,
- (ii) divergences related to the modeling of the physical background, i.e. to the external potential.

The occurrence of divergences of the first type is clear since we are dealing with quantum field theories. The divergences of the second type are far more subtle and are not to be mistaken for the field theoretic ones. The external potential *models* the background, such as magnetic field configurations or physical boundaries. Mathematically, this is expressed by the dependence of the potential on some parameters $\{\lambda_i\}$ of phenomenological nature (field strength amplitude, shape of the magnetic configuration, penetration depth of a material, etc.). For the sake of simplicity, some parameters may be tuned to take some critical values λ_{cr} corresponding to convenient assumptions (ideal cases). This can lead to a divergence of the effective action:

$$\Gamma[V(\lambda_i \rightarrow \lambda_{\text{cr}})] \rightarrow \infty.$$

Contrary to the divergences of the first type (i), these divergences may not be removed in a physically meaningful way. The problem can possibly be bypassed if the physical observable of interest (e.g. a force, a pressure), which is derived from $\Gamma[V]$, remains finite in this critical limit even if $\Gamma[V]$ does not. If it is not the case, the assumption $\lambda_i \rightarrow \lambda_{\text{cr}}$ is unphysical and has to be dropped.

Let us now discuss how the renormalization procedure concerning the occurrence of divergences of the first type is performed in the worldline formalism. The proper-time integral

$$\Gamma^{(1)}[V] \simeq \int_0^\infty \frac{dT}{T^{D/2+1}} e^{-m^2 T} \int d^D x_{\text{CM}} [\langle W_V[T, x(\tau), x_{\text{CM}}] \rangle_x - 1]$$

is possibly ill-defined for small values of T . Introducing an UV regularization (e.g. by means of a cutoff at the lower integral bound) and expanding the proper-time integrand for small T (this can be done analytically), we obtain

$$\Gamma^{(1)}[V] \simeq \int_{1/\Lambda^2}^\infty \frac{dT}{T^{D/2+1}} e^{-m^2 T} \int d^D x (f_1[V]T + f_2[V]T^2 + \mathcal{O}(T^3)). \quad (2.13)$$

[The subscript CM has been dropped to simplify the notation.] From this expression, it is clear that the number of divergent contributions depends on the space-time dimension D . For each divergent term, we introduce a counter-term in such a way as to render the proper-time integral finite:

$$\begin{aligned} \Gamma^{(1)}[V] &= \underbrace{\mathcal{N} \int_0^\infty \frac{dT}{T^{D/2+1}} e^{-m^2 T} \int d^D x \left[\langle W_V[T, x] \rangle_x - 1 - f_1[V]T - f_2[V]T^2 - \dots \right]}_{\Gamma_R^{(1)}} \\ &+ \underbrace{\mathcal{N} \int_{1/\Lambda^2}^\infty \frac{dT}{T^{D/2+1}} e^{-m^2 T} \int d^D x \left[f_1[V]T + f_2[V]T^2 + \dots \right]}_{\Gamma_{\text{c.t.}}^{(1)}(\Lambda)}. \end{aligned}$$

The first part of this expression is now finite, i.e. we can remove the cutoff safely ($\Lambda \rightarrow \infty$). When the counter-terms are fixed, it represents the renormalized part of the effective action $\Gamma_R^{(1)}$. The counter-terms present in the second term $\Gamma_{\text{c.t.}}^{(1)}(\Lambda)$, still depending on the cutoff, need to be fixed by imposing renormalization conditions. This last procedure, which consists in reabsorbing the counter-terms in the redefinition of the parameters in the bare action (such as the charge of the fluctuating field, for instance), is specific to each physical problem and will be discussed later on in the corresponding chapters.

2.3 Worldline Numerics: the 'loop cloud' method

The computation of the effective action in the worldline formalism reduces to the calculation of loop averages (see (2.8), (2.10) and (2.12)) of the type $\langle \dots \rangle_x$ over the ensemble of all closed worldlines $x(\tau)$ centered upon a given point x_{CM} . On the analytical level, this can be achieved in an exact way only in a few simple cases or otherwise requires strong assumptions. The idea of the *worldline numerics* is to calculate this expectation value on a computer by generating the worldline or loop ensemble in a numerical way, either in a continuous space-time [GL01, GL02] or in a latticized space-time [SS]. It is evident that we can generate neither the whole loop ensemble, which is infinite, nor an arbitrary big amount of loops, for clear reasons of computational time. We will adopt a strategy which is widely used in statistical physics, called *importance sampling*, which selects the relevant configurations contributing to the loop average among the ensemble of all loops. These ones are generated by a standard Monte-Carlo procedure according to the Gaussian loop distribution $p_{\text{loop}}[T, x(\tau)] \simeq e^{-\int_0^T d\tau \frac{\dot{x}^2}{4}}$. Generating an ensemble of N_{lp} loops $\{x(\tau)|_l, l = 1, \dots, N_{\text{lp}}\}$, the expectation value is approximated by

$$\boxed{\langle \mathcal{O}[x(\tau)] \rangle_x \simeq \frac{1}{N_{\text{lp}}} \sum_{l=1}^{N_{\text{lp}}} \mathcal{O}[x(\tau)|_l]} \quad (2.14)$$

for any observable \mathcal{O} depending on the path $x(\tau)$.

2.3.1 Loop rescaling, unit loops and discretization

Let us point out that this approach is, at this stage, not practicable. The loop probability distribution p_{loop} indeed depends on the proper-time T , which means that a loop ensemble

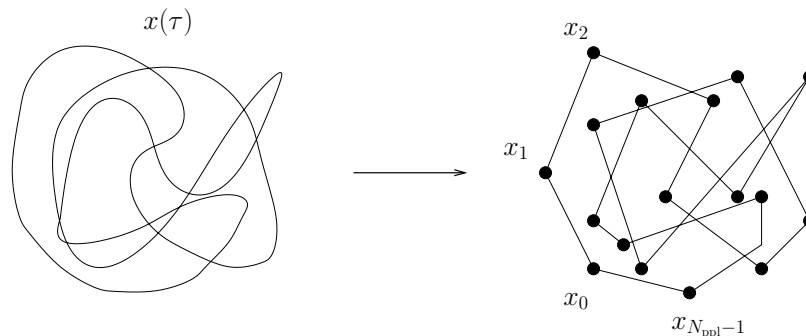


Figure 2.2: Discretization of the continuous loop $x(\tau)$. This corresponds to a discretization of the proper-time interval $[0, T]$, not of the space-time. Every point $x_i = x(\tau_i)$ can move freely.

has to be generated for each value of T . This fact renders the numerical approach very expensive in computing time. In this context, the observation that the worldlines $x_\mu(\tau)$ can be rescaled in such a way that the distribution p_{loop} becomes T -independent is a crucial point in favour of the applicability of Monte-Carlo techniques to the computation of worldline averages. Let us consider the following rescaling transformations:

$$\tau \in [0, T] \rightarrow t := \frac{\tau}{T} \in [0, 1], \quad x(\tau) \rightarrow y(t) := \frac{x(tT)}{\sqrt{T}}.$$

Under this transformation, the following proper-time integral becomes

$$\int_0^T d\tau \dot{x}^2(\tau) \rightarrow \int_0^1 dt \dot{y}^2(t),$$

which renders the loop distribution p_{loop} independent of T . The numerical burden is then reduced to the all-at-once generation of an ensemble of y -loops, which we call *unit loops* in the following, and the evaluation of the expectation value (2.14) for a given value of T simply consists in the rescaling of all members of the unit loop ensemble

$$x(\tau) = \sqrt{T}y(\tau/T) \quad (2.15)$$

before the sum (2.14) is performed. It is also obvious that the concept of continuous loops has to be abandoned. In simulations a loop is defined by a collection of N_{ppl} points, denoted by $\{x_i\}$ and corresponding to the discretization of the proper-time interval $[0, T]$:

$$\begin{aligned} \tau \in [0, T] &\rightarrow \tau_0 = 0, \tau_1, \dots, \tau_{N_{\text{ppl}}} = T, \\ x(\tau) &\rightarrow x_0 = x(\tau_0), x_1 = x(\tau_1), \dots, x_{N_{\text{ppl}}-1} = x(\tau_{N_{\text{ppl}}-1}), x_{N_{\text{ppl}}} = x_0 \end{aligned} \quad (2.16)$$

Let us point out that this discretization is not to be mistaken for a space-time discretization. Every point x_i can move freely in continuous space-time. This is illustrated in Fig. 2.2.

2.3.2 Generation of the unit loop ensemble

After rescaling and discretization, the unit loop distribution reads

$$p_{\text{loop}}[\{y_i\}] = \frac{1}{\mathcal{N}} \delta(y_0 + \dots + y_{N_{\text{ppl}}-1}) \exp \left[-\frac{N_{\text{ppl}}}{4} \sum_{i=1}^{N_{\text{ppl}}} (y_i - y_{i-1})^2 \right], \quad (2.17)$$

where

$$\mathcal{N} = \int d^D y_0 \dots d^D y_{N_{\text{ppl}}-1} \delta(y_0 + \dots + y_{N_{\text{ppl}}-1}) \exp \left[-\frac{N_{\text{ppl}}}{4} \sum_{i=1}^{N_{\text{ppl}}} (y_i - y_{i-1})^2 \right],$$

$y_{N_{\text{ppl}}} = y_0$ and the delta function accounts for the fact that the loop center of mass is located at the origin, i.e. $y_{\text{CM}} = 0$. The generation of the unit loop ensemble with respect to this distribution can be achieved in several ways:

1. thermalization of the loop ensemble by means of a heat-bath procedure,
2. 'random walker' techniques,
3. Fourier decomposition, i.e. diagonalization in momentum space,
4. diagonalization in space-time.

The first method is the most straightforward one to be implemented and has been employed in the first simulations concerning scalar and fermionic fluctuations in the presence of magnetic backgrounds [GL01, LMG02]. The principal disadvantage of thermalization is that the number of thermalization sweeps required increases dramatically with the number of points per loop N_{ppl} . Method 2 is based on the relation existing between random walk processes and path integrals [Sam79, SS] and generates a loop by letting a walker randomly propagate in space-time. This method avoids thermalization but introduces the walker step as a second loop parameter besides N_{ppl} and does not produce exactly closed loops. Method 3 and 4 circumvent the thermalization problem by diagonalizing the loop distribution, i.e. each point of the loop can be randomly determined with its nearest-neighbours interaction taken automatically into account by the algorithm.

Heat-bath algorithm. The idea of the heat-bath procedure is to consider that each point on a loop is regarded as exposed to a 'heat bath' of all neighbouring points. Let us isolate in the unit loop distribution $p_{\text{loop}}[\{y_i\}]$ the contributions containing the particular point y_i (we forget for the moment the delta function, i.e. we generate in a first step loops without center of mass constraint):

$$p_{\text{loop}}[\{y_i\}] \simeq \dots e^{-\frac{N_{\text{ppl}}}{4} [(y_i - y_{i-1})^2 + (y_{i+1} - y_i)^2]} \dots$$

After some algebraic operations, the probability distribution for the point y_i reads, dropping all y_i -independent factors,

$$p[y_i] \simeq e^{-\frac{N_{\text{ppl}}}{2} \left[y_i - \frac{y_{i-1} + y_{i+1}}{2} \right]^2}.$$

The heat-bath procedure now consists in the following steps: (i) choose a site $i \in [0, N_{\text{ppl}} - 1]$, consider all variables y_k , $k \neq i$ as constant, and generate the y_i according to its probability; (ii) visit all variables of the loop. The closeness is exactly realized with $y_{N_{\text{ppl}}-1}$ being in the heat bath of $y_{N_{\text{ppl}}-2}$ and y_0 . In order to generate a 'thermalized' loop, one starts with a random ensemble $\{y_i\}$ and performs n_t heat-bath sweeps. Finally, a stopping criterion has to be implemented. This is done by considering the extension e of the loop ensemble expressed by the loop mean square

$$e^2 = \int dy_0 \dots dy_{N_{\text{ppl}}-1} y_i^2 p_{\text{loop}}[y(t)].$$

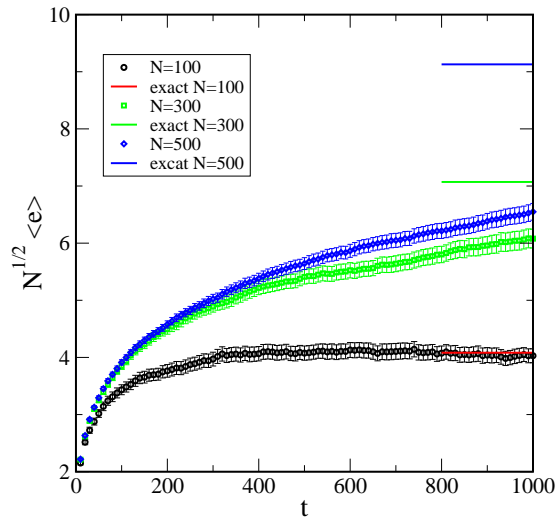


Figure 2.3: The average extension e (multiplied by $\sqrt{N_{\text{ppl}}}$ for better visualization) of the loops as a function of the number of thermalizations n_t .

This quantity can be calculated analytically. It reads

$$e = \sqrt{\frac{1}{6} \left(1 - \frac{1}{N_{\text{ppl}}^2} \right)}$$

and is shown in Fig. 2.3. One clearly observes that the thermalization of loop ensembles is expensive for $N > 500$. In fact, roughly $n_t = 45000$ is needed for an acceptable loop ensemble consisting of $N = 1000$ points. We then see that the heat bath method can become relatively expensive in computing time for problems requiring a big amount of points per loop, i.e. problems which are sensitive to the systematic error introduced by discretization, as for instance the study of the Casimir effect. This method has however produced good results in the case of magnetic backgrounds [GL01, LMG02]. The last step of the loop generation is performed by shifting each loop after thermalization in such a way that $y_{\text{CM}} = 0$.

Random walk. In order to circumvent the thermalization problem, one may exploit the connection between loops with Gaussian velocity distribution and random walks [Sam79, ID89]. Let us mention that this has already been adapted to worldline numerics with latticized space-time in [SS]; here, as already pointed out, we keep the space-time continuous.

Let us give up the concept of unit loops for a moment, and reinstate the naturally emerging coordinate space loops $x(\tau)$,

$$x(\tau) = \frac{1}{\sqrt{T}} y(\tau/T), \quad x(0) = x(T). \quad (2.18)$$

Probability theory tells us that random walks automatically implement the Gaussian velocity

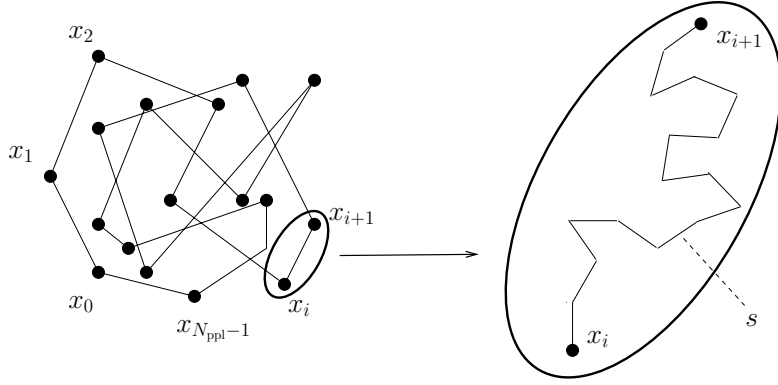


Figure 2.4: Each Gaussian factor in (2.19) is obtained by coarse graining a random walk process between the points x_i and x_{i+1} . The walker step is denoted by s .

distribution

$$\prod_{i=0}^{N_{\text{pp1}}-1} \exp\left\{-\frac{1}{4\epsilon}(x_{i+1} - x_i)^2\right\}, \quad (2.19)$$

where ϵ is the measure of the small proper-time slices. The crucial point is to establish the relation between a loop that a random walker with step length s would generate for us and a thermalized loop at a given proper-time T . This relation results from a coarse-graining procedure, which we present here briefly. Given that the random walker starts at the point x_i , the probability density for reaching the point x_{i+1} after n steps is given by

$$p(x_{i+1} | x_i, n, s) = \int d^D z_2 \dots d^D z_{n-1} \prod_{k=1}^{n-1} \frac{1}{\Omega(D)s^{D-1}} \delta(|z_{k+1} - z_k| - s),$$

with $\Omega(D)$ being the solid angle in D dimensions, $z_1 = x_i$ and $z_n = x_{i+1}$. This is depicted in Fig. 2.4. For $n \gg 1$, but ns^2 fixed, the central-limit theorem can be applied [Sam79]:

$$\lim_{n \rightarrow \infty} p(x_{i+1} | x_i, n, s) = \left(\frac{D}{2\pi ns^2}\right)^{\frac{D}{2}} \exp\left\{-\frac{D}{2ns^2}(x_{i+1} - x_i)^2\right\}, \quad ns^2 = \text{fixed}. \quad (2.20)$$

Comparing (2.20) with (2.19), one identifies

$$\epsilon = \frac{ns^2}{2D}. \quad (2.21)$$

The dimension of the proper-time as well as its relation to the loop length L appears here in an obvious way,

$$T = \frac{N_w s^2}{2D} = \frac{Ls}{2D}, \quad (2.22)$$

where N_w now is the total number of walker steps. It is important to point out that the proper-time can be tuned in two ways: we can adjust either the walker step s or the number of points N_w . The corresponding two methods to generate a loop ensemble at given proper-time T work as follows.

Method 1 : s is fixed.

- (1) choose the walker step s ;
- (2) read off from Eq. (2.22) the number of points N_w corresponding to T ;
- (3a) generate N_w points by letting a random walker go N_w steps, and accept the configuration if the last step leads him into a small sphere (radius ε_R) centered upon the starting point;
- (3b) close the loop 'by hand' by shifting the last point to the starting point;
- (4) shift the center of mass to zero;
- (5) repeat steps (3) and (4) N_{lp} times for an ensemble of N_{lp} loops.

We point out that the value of s must be much smaller than the characteristic length scale provided by the background potential. A second constraint on s arises from the applicability of the central limit theorem, i.e. $n \gg 1$ in (2.20). A third systematic numerical uncertainty follows from the shift in step (3b). Unfortunately, small values for ε_R result in low acceptance rate for loops, and, therefore, increase the numerical effort to generate the loop ensemble. A good compromise is to set the radius ε_R to some percentage of the step length: $\varepsilon_R = \varepsilon s$.

For illustration, we consider the following example. We compute the average Wilson Loop (2.11) in scalar QED for the case of a constant magnetic background field $\mathbf{B} = B\mathbf{e}_z$ at $T = 1$ and $D = 2$,

$$\mathbf{A} = B/2(y, -x)$$

using a loop ensemble constructed by means of this random walk method. For $T = 1$ the walker step length is given by $s = \frac{2}{\sqrt{N_w}}$. Fig. 2.5 shows our numerical result as a function of N_w in comparison with the exact value. Circles with error bars correspond to loop ensembles generated with $\varepsilon_R = 0.05s$. The limit (2.20) seems to be attained for $50 < N_w < 100$. For a further improvement of the numerical accuracy, large values of N_w and a decrease of ε_R at the same time are required: a further calculation for $\varepsilon_R = 0.03s$ is in agreement with the analytical result at $N_w = 150$ (black square with error bar). Finally, we point out that the deviation from the exact result in the case of the heat-bath-generated loop ensemble (grey square) is probably due to thermalization effects. Note that we have to generate a loop ensemble for each value of T ($\sim N_w s^2$), which makes this procedure far more memory consuming than the heat-bath approach. If we decide to generate the loop ensembles once and for all and save them to disk, we have to handle huge amounts of data. On the other hand, if we create our loops 'on demand' (while performing the T or x integrations), we are confronted with a serious waste of computing time.

Method 2: N_w is fixed.

- (1) choose the number of points N_w ;
- (2) set the walker step to $s = 1$;
- (3) proceed with steps (3), (4) and (5) of the first method.

The loop ensemble is here generated only once and then rescaled to adjust the step length to the value s corresponding to T in (2.22). This method therefore works as in the case of the re-scalable thermalized unit loops, with the difference that the proper-time rescaling is realized via the rescaling of the step length. This tuning at the level of s provides for a

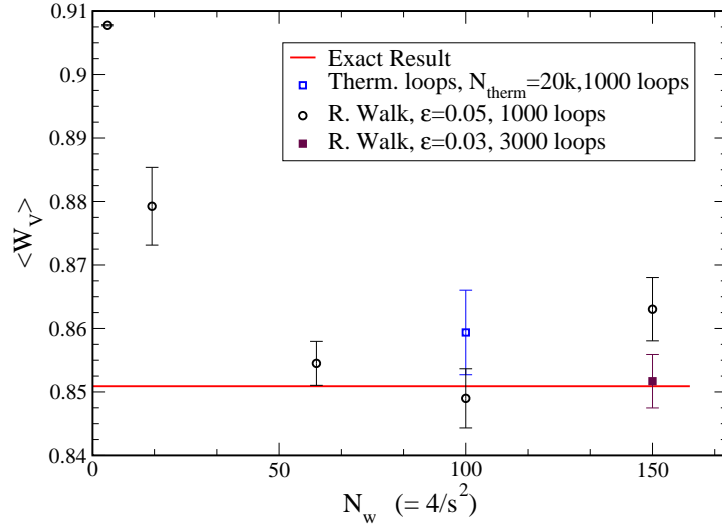


Figure 2.5: Average Wilson Loop (2.11) for the case of a constant magnetic background field B for $B = 1$, $T = 1$ and $D = 2$ as a function of the number of points per loop.

better control of the microscopic features of the loops. The second procedure is thus a good candidate to replace the thermalized loops since it combines the absence of thermalization and the rescaling of an all-at-once generated ensemble. It should however be emphasized that most of the computer time is spent on generating redundant open loops. This is due to the fact that, for a given ϵ_R , the fraction of loops which close after N_w steps decreases like $N_w^{-D/2}$.

Fourier decomposition: “f loops”. We are now looking for alternative methods that could combine some advantages of the two previous approaches and bypass the problems rendering them impractical. A highly efficient procedure arises from a Fourier representation of our unit loops

$$y(t) = \sum_{\nu=1}^{N_{\text{pp1}}} \left[a_\nu \cos(2\pi \nu t) + b_\nu \sin(2\pi \nu t) \right], \quad a_0 = 0, \quad (2.23)$$

where N_{pp1} is the number of Fourier modes included (which agrees with the number of points specifying each loop, see below). The choice $a_0 = 0$ guarantees that the loop center of mass is located at the origin. Inserting Eq. (2.23) into the loop distribution (2.17), the probability distribution for the Fourier coefficients is given by

$$P[a, b] = \exp \left\{ -\frac{\pi^2}{2} \sum_{\nu=1}^{N_{\text{pp1}}} \nu^2 (a_\nu^2 + b_\nu^2) \right\}. \quad (2.24)$$

We can take advantage of the fact that the Fourier components $\{a, b\}$ are not correlated, in order to generate our loops in momentum space. The reconstruction of the unit loop $y(t)$ in Eq. (2.23) is most efficiently performed by using the fast Fourier transformation (FFT). For

these purposes, we define complex coefficients $c_\nu := a_\nu + i b_\nu$, and obtain

$$y(t) = \operatorname{Re} \sum_{\nu=1}^{N_{\text{pp1}}} c_\nu \exp\{-i 2\pi t \nu\}. \quad (2.25)$$

The FFT procedure generates a series of points y_i , $i = 0 \dots N_{\text{pp1}} - 1$ which discretize the continuous curve $y(t)$ and thereby constitute the unit loops.

Explicit diagonalization: “v loops” We propose an algorithm that is based on a linear variable transformation $\{y_k\} \rightarrow \{\bar{v}_k\}$, such that the discretized distribution (2.17) becomes purely Gaussian. These new variables are velocity-like and diagonalize the quadratic form in the exponent.

Because of the δ function in (2.17), only $N_{\text{pp1}} - 1$ coordinates per loop are independent. Defining $\int \mathcal{D}y = \int_{-\infty}^{\infty} \prod_{i=0}^{N_{\text{pp1}}-1} dy_i$, we may perform, e.g., the $y_{N_{\text{pp1}}-1}$ integration using the δ function,

$$\begin{aligned} & \int \mathcal{D}y P[\{y_k\}] \dots \\ &= \int \prod_{i=0}^{N_{\text{pp1}}-2} dy_i e^{\left[-\frac{N_{\text{pp1}}}{4} \left(\sum_{i=1}^{N_{\text{pp1}}-2} (y_i - y_{i-1})^2 + (2y_0 + y_1 + \dots + y_{N_{\text{pp1}}-2})^2 + (y_0 + y_1 + \dots + 2y_{N_{\text{pp1}}-2})^2 \right)\right]} \dots \\ &=: \int \prod_{i=0}^{N_{\text{pp1}}-2} dy_i e^{\left[-\frac{N_{\text{pp1}}}{4} Y\right]} \dots, \end{aligned} \quad (2.26)$$

where the dots represent an arbitrary y -dependent operator, and we introduced the abbreviation Y for the quadratic form. In order to turn the exponential into a product of simple Gaussians, we define $N_{\text{pp1}} - 1$ new velocity-like variables,

$$\begin{aligned} \bar{v}_0 &:= \frac{3}{2}y_0 + y_1 + y_2 + \dots + y_{N_{\text{pp1}}-3} + \frac{3}{2}y_{N_{\text{pp1}}-2}, \\ v_i &:= y_i - y_{i-1}, \quad i = 1, 2, \dots, N_{\text{pp1}} - 2. \end{aligned} \quad (2.27)$$

For notational simplicity, it is useful to also introduce the auxiliary variable,

$$v_{i,j} = v_i + v_{i-1} + \dots + v_{j+1} \equiv y_i - y_j, \quad \text{for } i \geq j = 0, 1, \dots, N_{\text{pp1}} - 2, \quad (2.28)$$

such that the exponent Y can be written as

$$\begin{aligned} Y &= \sum_{i=1}^{N_{\text{pp1}}-2} v_i^2 + \left(\bar{v}_0 - \frac{1}{2}v_{N_{\text{pp1}}-2,0} \right)^2 + \left(\bar{v}_0 + \frac{1}{2}v_{N_{\text{pp1}}-2,0} \right)^2 \\ &= 2\bar{v}_0^2 + \frac{1}{2}v_{N_{\text{pp1}}-2,0}^2 + \sum_{i=1}^{N_{\text{pp1}}-2} v_i^2. \end{aligned} \quad (2.29)$$

We observe that the variable \bar{v}_0 now appears quadratically in the exponent as desired. The same has still to be achieved for $v_1 \dots v_{N_{\text{pp1}}-2}$. For this, we note that $v_{N_{\text{pp1}}-2,0} = v_{N_{\text{pp1}}-2} + v_{N_{\text{pp1}}-3,0}$ by definition (2.28). Defining

$$\bar{v}_{N_{\text{ppl}}-2} := v_{N_{\text{ppl}}-2} + \frac{1}{3}v_{N_{\text{ppl}}-3,0}, \quad (2.30)$$

we indeed obtain for the exponent Y

$$\begin{aligned} Y &= 2\bar{v}_0^2 + v_{N_{\text{ppl}}-2}^2 + \frac{1}{2}(v_{N_{\text{ppl}}-2} + v_{N_{\text{ppl}}-3,0})^2 + \sum_{i=1}^{N_{\text{ppl}}-3} v_i^2 \\ &= 2\bar{v}_0^2 + \frac{3}{2}\bar{v}_{N_{\text{ppl}}-2}^2 + \frac{1}{3}v_{N_{\text{ppl}}-3,2} + \sum_{i=1}^{N_{\text{ppl}}-3} v_i^2, \end{aligned} \quad (2.31)$$

where $\bar{v}_{N_{\text{ppl}}-2}^2$ also appears quadratically. We can continue this construction by defining

$$\bar{v}_{N_{\text{ppl}}-i} := v_{N_{\text{ppl}}-i} + \frac{1}{i+1}v_{N_{\text{ppl}}-i-1,0}, \quad i = 2, \dots, N_{\text{ppl}} - 1, \quad (2.32)$$

which turns the exponent Y into a purely Gaussian form:

$$Y = 2\bar{v}_0^2 + \frac{3}{2}\bar{v}_{N_{\text{ppl}}-2}^2 + \frac{4}{3}\bar{v}_{N_{\text{ppl}}-3}^2 + \dots + \frac{i+1}{i}\bar{v}_{N_{\text{ppl}}-i}^2 + \dots + \frac{N_{\text{ppl}}}{N_{\text{ppl}}-1}\bar{v}_1^2. \quad (2.33)$$

The last step of this construction consists in noting that we can substitute the integration variables according to

$$\prod_{i=0}^{N_{\text{ppl}}-2} dy_i = J \prod_{i=1}^{N_{\text{ppl}}-2} dv_i d\bar{v}_0 = \bar{J} \prod_{i=0}^{N_{\text{ppl}}-2} d\bar{v}_i \equiv \mathcal{D}\bar{v} \quad (2.34)$$

with nonzero but constant Jacobians J, \bar{J} , the value of which is unimportant for the calculation of expectation values. This allows us to write the path integral (2.26) as

$$\begin{aligned} \int \mathcal{D}y P[\{y_k\}] \dots &= \bar{J} \int \mathcal{D}\bar{v} \exp \left[-\frac{N_{\text{ppl}}}{4} \left(2\bar{v}_0^2 + \sum_{i=2}^{N_{\text{ppl}}-1} \frac{i+1}{i} \bar{v}_{N_{\text{ppl}}-i}^2 \right) \right] \dots \\ &\equiv \bar{J} \int \mathcal{D}\bar{v} P[\{\bar{v}_k\}] \dots, \end{aligned} \quad (2.35)$$

where $P[\{\bar{v}_k\}]$ can now be generated straightforwardly with the Box-Müller method [BM58].

For the construction of unit loops (“v loops”), the above steps have to be performed backwards. The recipe is the following:

- (1) generate $N_{\text{ppl}} - 1$ numbers $w_i, i = 0, \dots, N_{\text{ppl}} - 2$ via the Box-Müller method such that they are distributed according to $\exp(-w_i^2)$;
- (2) compute the $\bar{v}_i, i = 0, \dots, N_{\text{ppl}} - 2$, by normalizing the w_i :

$$\begin{aligned} \bar{v}_0 &= \sqrt{\frac{2}{N_{\text{ppl}}}} w_0, \\ \bar{v}_i &= \frac{2}{\sqrt{N_{\text{ppl}}}} \sqrt{\frac{N_{\text{ppl}} - i}{N_{\text{ppl}} + 1 - i}} w_i, \quad i = 1, \dots, N_{\text{ppl}} - 2; \end{aligned} \quad (2.36)$$

(3) compute the v_i , $i = 1, \dots, N_{\text{ppl}} - 2$, using

$$v_i = \bar{v}_i - \frac{1}{N_{\text{ppl}} + 1 - i} v_{i-1,0}, \quad \text{where } v_{i-1,0} = \sum_{j=1}^{i-1} v_j ; \quad (2.37)$$

(4) construct the unit loops according to

$$\begin{aligned} y_0 &= \frac{1}{N_{\text{ppl}}} \left(\bar{v}_0 - \sum_{i=1}^{N_{\text{ppl}}-2} \left(N_{\text{ppl}} - i - \frac{1}{2} \right) v_i \right), \\ y_i &= y_{i-1} + v_i, \quad i = 1, \dots, N_{\text{ppl}} - 2, \\ y_{N_{\text{ppl}}-1} &= - \sum_{i=0}^{N_{\text{ppl}}-2} y_i ; \end{aligned} \quad (2.38)$$

(5) repeat this procedure N_{lp} times for N_{lp} unit loops.

The formulas in step (4) can be checked straightforwardly by inserting the definitions of the v_i 's and \bar{v}_0 .

This v-loop algorithm allows us to generate unit loops efficiently without thermalization, i.e., no redundant thermalization sweeps have to be performed, and works for an arbitrary number of points per loop N_{ppl} .

2.3.3 Calculating the effective action: the method

We present in this section the whole machinery under the form of a recipe. The numerical computation of the effective action at the one-loop level (expressions (2.8),(2.10) and (2.12)) by means of the loop cloud method works according to the following scheme.

1. Generating a unit loop ensemble

Choose one of the techniques described in the previous section to generate an ensemble of N_{lp} loops, each of them being defined by N_{ppl} points.

This ensemble has the following properties:

- the loops are distributed with respect to the distribution (2.17),
- the loops are centered upon the origin, i.e. $\sum_{i=0}^{N_{\text{ppl}}-1} y_i = 0$ for each loop $\{y_0, \dots, y_{N_{\text{ppl}}-1}\}$.

The influence of thermalization effects on the quality of the numerical estimate should be kept in mind. We recommend the use of f- or v-loops, which implement the first condition automatically. The second condition is realized by shifting by hand all members of the loop ensemble to zero center-of-mass.

2. Computing the action density - proper-time integral

The calculation of the effective Lagrangian $\mathcal{L}_{\text{eff}}(x_{\text{CM}})$ at the point x_{CM} results from the evaluation of a proper-time integral which is performed by means of a standard integration algorithm [PFTV]. For each value of T required by the integration algorithm, an ensemble average over loops centered upon x_{CM} , described under points (a) and (b) has to be performed.

For a fixed space-time point x_{CM} and a fixed proper-time T ,

- (a) perform the average (2.14) of the holonomy factor as follows: for each term of the sum, i.e. for each member of the loop ensemble,
 - rescale the unit loop according to $y_i \rightarrow x_i = \sqrt{T}y_i$, for each loop point y_i , $i = 0, \dots, N_{\text{ppl}} - 1$,
 - shift the loop to the center of mass x_{CM} , by translating each loop point according to $x_i \rightarrow x_i + x_{\text{CM}}$,
 - evaluate $W_V[x(\tau), x_{\text{CM}}, T]$ for the loop $x(\tau)$.

Repeat this procedure and compute the arithmetic mean value of the N_{lp} contributions.

- (b) subtract one, the counter-terms if needed and multiply by the remaining T -dependent factors.

Repeat the whole procedure for each value of the proper-time T required by the integration algorithm implementing the T -integration until convergence is achieved.

Let us at this stage recall that, while the interval $[0, T]$ is discretized for the purposes of the numerical treatment, the value of T can vary continuously in the interval $[0, +\infty[$. The discretization has no influence on the computation of the proper-time integral, i.e. the integration algorithm can consider the loop average as a usual continuous function of T . The choice of this algorithm should be done after examination of a plot of the proper-time integrand, which permits to determine its fall-off rate at large T 's and the possible presence of an integrable singularity at $T = 0$.

3. Computing the effective action - space-time integral

The numerical estimate of the effective action is obtained as followed:

- fix the value of the parameters: fluctuating field mass, geometrical and phenomenological quantities which parametrize the external potential,
- perform the space-time integration using a standard integration algorithm: for each space-time point x_{CM} required by the integration routine, perform the proper-time integration described under point 2.

The loop center of mass can move continuously in space-time: the loop discretization does not affect the space-time integral.

Remark: gauge invariance and loop discretization. In order to avoid a violation of gauge invariance in the numerical computation, we have to deal with a subtlety concerning the discretization of the integrals along the worldlines: a particular loop in our ensemble is considered to be a polygon with straight lines \mathcal{C}_i connecting the points x_i and x_{i+1} . In order to evaluate the holonomy factor (2.11), we consider the ‘‘infinitesimal’’ part

$$\exp\left\{i \int_{\mathcal{C}_i} A(x) \cdot \dot{x} d\tau\right\} \quad (2.39)$$

for each \mathcal{C}_i separately and evaluate the integral analytically using the gauge potential describing the background under consideration. This procedure guarantees that our numerical

result is invariant under gauge transformations of the background gauge field $A_\mu(x)$ for any number N_{ppl} of points defining the polygons. Moreover, the flux enclosed by the polygon is exactly taken into account as desired (and not only within discretization errors). Of course, this procedure can be generalized to arbitrary potentials for which the “infinitesimal” integrations along the C_i ’s can be performed numerically; thereby, the properties mentioned above can be preserved to any numerically desired precision. However, we should stress that the use of a smooth gauge (e.g. covariant gauges) for the background field is recommended in this case; this facilitates a fast convergence of the numerical integration. The evaluation of the line integral in (2.39) for the gauge potentials describing the magnetic field configurations of Chapter 3 is performed in Sec. E.2.

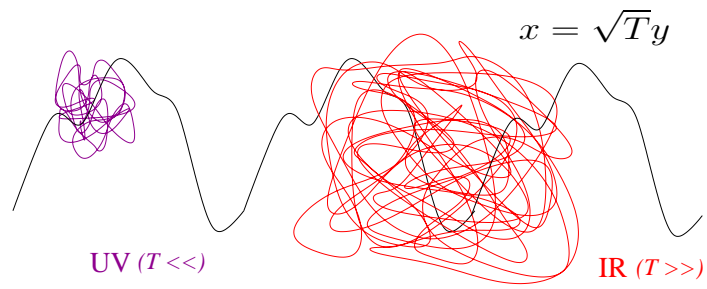
2.4 Summary

To conclude this chapter, we enumerate the principal features of the loop cloud method.

1. The method is exact to one-loop order. From the starting point (2.2) to the expression (2.8) (and correspondingly for scalar and spinor QED), no approximation has been made. The possible sources of numerical error are
 - the loop discretization (2.16),
 - the statistical average (2.14).

They are controlled by the number of points per loop N_{ppl} and the number of loops in the loop ensemble N_{lp} , respectively.

2. As a consequence of the first point, the method manifests exact gauge invariance: the worldline formulation of a gauge theory involves only gauge invariant quantities, like Wilson loop and Pauli factor. The numerical implementation respects moreover the gauge invariance of these quantities (see the concluding remark of the previous section).
3. The method inherits the advantages of the worldline formulation of QFT:
 - it contains all diagrams in one expression (see Fig. 2.1),
 - the formalism does not involve any momentum integral or discrete sum over the energy spectrum.
4. The method has been developed independently of the background potential. It is based on the average over an ensemble of *free loops*, which can in principle be used for any physical problem, i.e. for different types of potential.
5. The method is intuitive. Some non trivial information, like the sign of an interaction or its qualitative dependence on some external parameters, can be obtained only by thinking in terms of rescaled loops. The crucial point in this context is the geometric interpretation of the proper-time. This is illustrated in the figure below. The UV regime, i.e. small values of T , is controlled by small loops which, as depicted in the following figure, can probe the high frequency regime of a given background. On the contrary, the big loops, which control the IR regime, are highly non localized and can *de facto* collect information over the background on a larger scale.



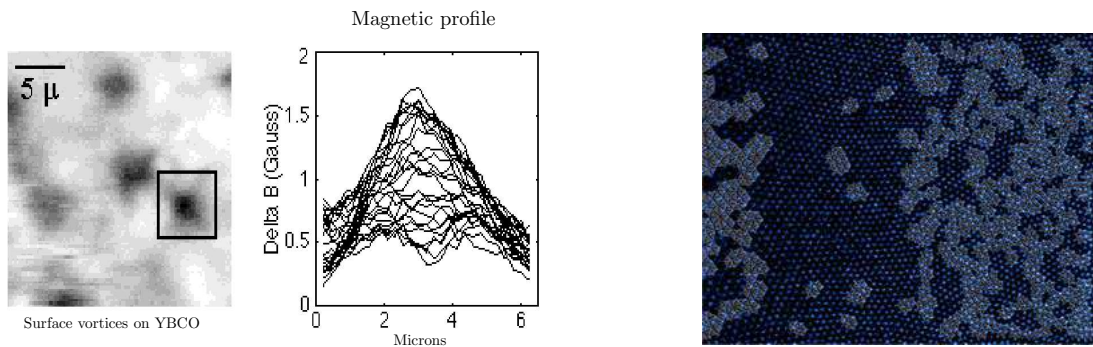
In the following chapters, point number 4 will be widely exploited. The wide range of applicability of the method offers the opportunity to go beyond the domains of applicability of standard analytical procedures, which are limited due to unavoidable approximations.

Chapter 3

Magnetic Backgrounds

In this chapter, we apply the loop cloud method to the study of fermionic quantum fluctuations in the presence of a classical magnetic background. We investigate in particular the fermion-induced quantum energy of magnetic vortex systems. The magnetic vortex configuration is nowadays at the center of experimental and theoretical investigations performed in solid state physics, especially in relation to the conducting properties of superconductors, and in QCD, where special gluonic configurations, called center vortices and comparable to the magnetic vortices in the superconductor, provide a scenario of quark confinement.

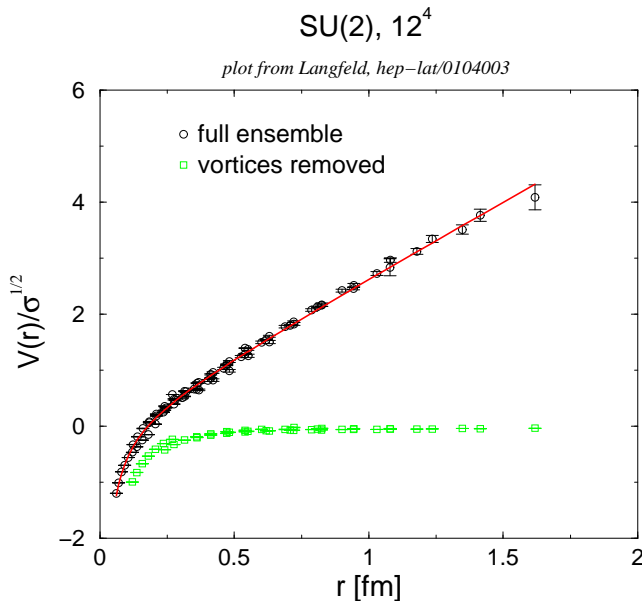
Superconductors of Type-I are characterized by their ability to repel a magnetic field completely (Meißner effect). Type-II superconductors in the so-called mixed state allow on the contrary some penetration by an external magnetic field into its surface, leading to the appearance of magnetic vortices inside the superconductor, which carry some fraction of magnetic flux. Moreover, the superconductors of this type possess higher critical temperatures T_c than those of Type-I. A magnetic vortex has a typical extension of some microns and can be visualized as illustrated in the following figure.



The application of a current to a superconductor of Type-II in the mixed state induces movements among the vortices which can in turn produce an undesirable resistance [CN97]. For this reason, it appears valuable to study the influence of the electrons on such vortex systems, in particular evaluate the effective vortex-vortex interaction induced by the quantum fluctuations of the electrons. The right panel of the figure above illustrates the influence of a current on the patterns built by the vortices (grey star-shaped regions): a current flows through the left-hand side of the figure while the other side is current free.

In the context of Yang-Mills theory, lattice simulations have shown that a Yang-Mills

vacuum populated by color-magnetic vortices, the so-called center vortices, manifests in the continuum limit [LRT98] the property of confining static colour sources. This property is lost for a vacuum where they are detected and removed by hand, using some projection technique [DDFGO97, DDFG⁺98]. The next figure represents the potential of two static quarks in the Yang-Mills vacuum. When calculated with respect to the full gluonic configurations, the potential is linearly confining, whereas the removal of the vortices induces a Coulomb like potential.



A random gas of vortices can grasp the essence of quark confinement at zero temperature, and the deconfinement phase transition at finite temperatures can be understood as a vortex de-percolation transition. In this context, a deep knowledge of the interplay of quarks with vortex-like solitons would help to describe hadron properties in the vortex picture.

We begin our investigations by the simplest case of a background given by a constant¹ magnetic field, in the framework of which we will discuss the renormalization procedure specific to QED on the worldline, test our numerical approach and point out a numerical problem specific to worldline fermions. We investigate the single-vortex configuration in $D = 2 + 1$ and $D = 3 + 1$ and propose an interesting comparison with derivative expansion calculations before turning to the study of binary-vortex interactions.

3.1 Constant magnetic field

Beside its historical interest, the constant magnetic field configuration will permit us to get familiar with the proper-time representation of effective Lagrangians and serves as a test of our numerical method, since analytic results are available for this special case.

¹We limit ourselves to time-independent field configurations. The adjective “constant” will have throughout this chapter the meaning of “homogeneous” or “space-independent”.

3.1.1 One-loop Euler-Heisenberg-Schwinger Lagrangians

Our starting point is the worldline formulation of the effective action for scalar and spinor QED. For convenience, we recall here the (unrenormalized) one-loop spinor effective action

$$\Gamma_{\text{ferm}}^{(1)}[A] = \frac{2}{(4\pi)^{D/2}} \int_0^\infty \frac{dT}{T^{D/2+1}} e^{-m^2 T} \int d^D x_{\text{CM}} \left[\left\langle W_A^{\text{ferm}}[T, x(\tau), x_{\text{CM}}] \right\rangle_x - 1 \right], \quad (3.1)$$

which differs from the scalar one (2.8) by the presence of the Pauli factor

$$P[T, F(x_{\text{CM}}), x(\tau)] := \frac{1}{4} \text{tr} P_T e^{\frac{1}{2} \int_0^T d\tau \sigma_{\mu\nu} F_{\mu\nu}(x_{\text{CM}}+x(\tau))}$$

in the loop average: $W_A^{\text{ferm}} = W_A \times P$.

In the constant field case, the Pauli factor can be computed very easily. Let us choose the magnetic field to be parallel to the z -axis, $\mathbf{B} = B \mathbf{e}_3$. On the one hand, the only non-vanishing elements of the electromagnetic tensor are $F_{12} = -B$ and $F_{21} = B$. On the other hand, the *hermitian* Dirac algebra element σ_{12} is given by $\sigma_{12} = \gamma_3$ ($\gamma_3 = \gamma_3^\dagger$). Since the magnetic field is independent of the loop $x(\tau)$, the integral over τ in the Pauli factor can be trivially performed. Note that we can also drop the path ordering operator. Using fundamental properties of the Dirac matrices, we have

$$P(T) = \frac{1}{4} \text{tr} e^{-BT} \gamma_3 = \cosh(BT).$$

We can factorize $P(T)$ out of the loop average in (3.1) and obtain

$$\Gamma_{\text{ferm}}^{(1)}[A] = \frac{2}{(4\pi)^{D/2}} \int_0^\infty \frac{dT}{T^{D/2+1}} e^{-m^2 T} \int d^D x_{\text{CM}} \left[\left\langle e^{i \int_0^T d\tau A(x_{\text{CM}}+x(\tau)) \cdot \dot{x}} \right\rangle_x \cosh(BT) - 1 \right]. \quad (3.2)$$

The problem then reduces to the loop average of the Wilson loop with respect to the vector potential

$$A(x) = \frac{B}{2} (-x_2, x_1, 0, \dots, 0)$$

describing the magnetic configuration at hand. This task can be performed analytically. It is indeed well known from elementary quantum mechanics that the quantum problem of a charged particle in a constant magnetic field can be mapped onto the problem of a harmonic oscillator with the Cyclotron frequency (Landau problem). In this case, the solution of the Schrödinger equation is known analytically and the corresponding Feynman path integral can be performed in an exact way [Kle95]. In our unit conventions, the cyclotron frequency is simply $\omega = B$ and the loop average reads

$$\left\langle e^{i \int_0^T d\tau A(x_{\text{CM}}+x(\tau)) \cdot \dot{x}} \right\rangle_x = \frac{BT}{\sinh(BT)} \quad (3.3)$$

yielding the following expression for the effective action

$$\Gamma_{\text{ferm}}^{(1)}[A] = \int d^D x_{\text{CM}} \underbrace{\frac{2}{(4\pi)^{D/2}} \int_0^\infty \frac{dT}{T^{D/2+1}} e^{-m^2 T} [BT \coth(BT) - 1]}_{\mathcal{L}_{\text{ferm}}^{(1)}(x_{\text{CM}})}. \quad (3.4)$$

The effective Lagrangian defined above is a so-called *Heisenberg-Euler-Schwinger*-type Lagrangian particularized to the case of a purely magnetic field. Generally speaking, these Lagrangians resum to one-loop order the fluctuations of a spinor field in the presence of a constant electromagnetic (i.e. electric and/or magnetic) background. It is quite remarkable that the non-linear effects of the Maxwell theory (like for instance the e^+e^- pair production in a constant uniform electric field) arising from quantum corrections of the type (3.4) have been studied in the very early stages of the development of quantum field theory, when renormalization was still far from being discovered [HE36]. This early work of Heisenberg and Euler was worked out 15 years later in the light of renormalizable quantum field theory by Schwinger [Sch51]. The interested reader may find a discussion of the problem of a quantized spinor field interacting with a classical potential expressed in terms of QFT basic tools (i.e. no worldline representation) in classic textbooks on QFT (see for example [IZ80]). For a more involved discussion concerning Euler-Heisenberg-Schwinger Lagrangians, see for instance [DR85].

3.1.2 Renormalization

The unrenormalized effective action (3.1) is, depending on the dimension, possibly divergent. We isolate the potentially divergent parts by performing the Taylor expansion (2.13) of the loop average (3.3)

$$\left\langle e^{i \int_0^T d\tau A(x_{\text{CM}} + x(\tau)) \cdot \dot{x}} \right\rangle_x - 1 = -\frac{1}{6} B^2 T^2 + \mathcal{O}(T^4)$$

as well as of the Pauli factor $\cosh(BT) \simeq 1 + \frac{1}{2} B^2 T^2 + \mathcal{O}(T^4)$. For didactical purposes which will become clear in the next section, we reinstate the space-time dependence of the proper-time integrand by writing $B^2 = \frac{1}{2} F_{\mu\nu}[A](x) F_{\mu\nu}[A](x)$. The expansion (2.13) reads in the present case

$$\Gamma_{\text{ferm}}^{(1)}[A, \Lambda] = \frac{2}{(4\pi)^{D/2}} \int_{1/\Lambda^2}^{\infty} \frac{dT}{T^{D/2+1}} e^{-m^2 T} \int d^D x \left[\frac{1}{6} T^2 F_{\mu\nu}[A](x) F_{\mu\nu}[A](x) + \mathcal{O}(T^4) \right],$$

which has been regularized by means of an UV cut-off Λ at the lower bound of the proper-time integral. [The subscript CM has been dropped in order to simplify the notation.]

In the case $D = 2 + 1$, the term of order T^2 in the previous expression corresponds to a singularity $1/\sqrt{T}$, which is integrable, and the cut-off Λ can be safely removed.

For $D = 3 + 1$, the proper-time integral is rendered finite by introducing a counter-term in the proper-time integrand:

$$\begin{aligned} \Gamma_{\text{ferm}}^{(1)}[A, \Lambda] &= \frac{2}{(4\pi)^{D/2}} \int d^D x \int_0^{\infty} \frac{dT}{T^{D/2+1}} e^{-m^2 T} \left[\left\langle W_A^{\text{ferm}}[T, x(\tau), x_{\text{CM}}] \right\rangle_x - 1 \right. \\ &\quad \left. - \frac{1}{6} T^2 F_{\mu\nu}[A](x) F_{\mu\nu}[A](x) \right] \\ &\quad + c(\Lambda) \underbrace{\int d^D x F_{\mu\nu}[A](x) F_{\mu\nu}[A](x)}_{\Gamma_{\text{ferm}}^{\text{c.t.}}[A, \Lambda]}, \end{aligned} \quad (3.5)$$

where

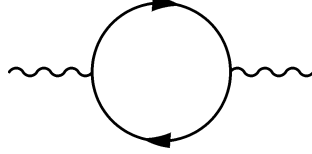
$$c(\Lambda) = -\frac{1}{48\pi^2} \left(\ln \frac{m^2}{\Lambda^2} + \gamma_E \right) + \mathcal{O}(m^2/\Lambda^2). \quad (3.6)$$

Here γ_E denotes the Euler constant. The first term is now finite (note that the cutoff has been safely sent to infinity) and represents the renormalized part of the fermion-induced effective action:

$$\Gamma_{\text{ferm}}^{(1),R}[A] := \Gamma_{\text{ferm}}^{(1)}[A, \Lambda] - \Gamma_{\text{ferm}}^{\text{c.t.}}[A, \Lambda].$$

By contrast, the counter-term $\Gamma_{\text{ferm}}^{\text{c.t.}}$ still depends on the cutoff, which is eliminated according to the standard renormalization procedure by fixing a renormalization condition.

Before proceeding with the renormalization program, we pause for a moment and comment briefly the result (3.5)-(3.6). Let us recall that the effective action in the representation (3.1) is an alternative formulation of one-loop QED in the presence of a magnetic background. For this reason, the divergence structure of the unrenormalized effective action on the worldline can be expressed in the language of conventional Feynman diagrams. In view of the structure of the divergent term $\sim \int F_{\mu\nu} F_{\mu\nu}$ and the fact that the effective action (3.1) resums one-fermionic-loop diagrams only, it is clear that the divergence in (3.5) corresponds to the divergence occurring in the following diagram:



which possesses the same structure as the kinetic term in the classical Maxwell action and leads to the redefinition of the fermion charge (see standard QFT textbooks, e.g. [PS, IZ80]). Keeping this statement in mind, we can perform the remaining part of the renormalization program in a straightforward way.

We add the bare “classical” Maxwell action

$$\Gamma_{F^2}^B[A, \Lambda] = \frac{1}{g_B^2(\Lambda)} \int d^4x F_{\mu\nu}[A](x) F_{\mu\nu}[A](x)$$

to the expression (3.5) and obtain the total effective action $\Gamma_{\text{eff}}^{(1)}[A]$ resumming the (classical) photonic and fermion-induced contributions:

$$\Gamma_{\text{eff}}^{(1)}[A] = \Gamma_{\text{ferm}}^{(1),R}[A] + \underbrace{\Gamma_{F^2}^B[A, \Lambda] + \Gamma_{\text{ferm}}^{\text{c.t.}}[A, \Lambda]}_{\Gamma_{F^2}^R[A]}.$$

The cutoff dependence in the second and third terms can finally be eliminated by enforcing the renormalization condition

$$\frac{1}{g_B^2(\Lambda)} + \frac{1}{12\pi^2} \left[\ln \left(\frac{\Lambda^2}{\mu^2} \right) - \gamma_E \right] = \frac{1}{g_R^2(\mu)}.$$

Here $g_R(\mu)$ denotes the renormalized coupling at a given renormalization point μ , and we rediscover the QED β function $\beta(g_R^2) = \mu \partial_\mu g_R^2(\mu) = g_R^4/(6\pi^2)$. The renormalized Maxwell action then reads

$$\Gamma_{F^2}^R[A] = \frac{1}{4} \left[\frac{1}{g_R^2(\mu)} - \frac{1}{12\pi^2} \ln \left(\frac{m^2}{\mu^2} \right) \right] \int d^4x F_{\mu\nu}[A](x) F_{\mu\nu}[A](x).$$

We can impose fermion-mass-shell renormalization by choosing $\mu = m$, so that the log term in the previous expression drops out.

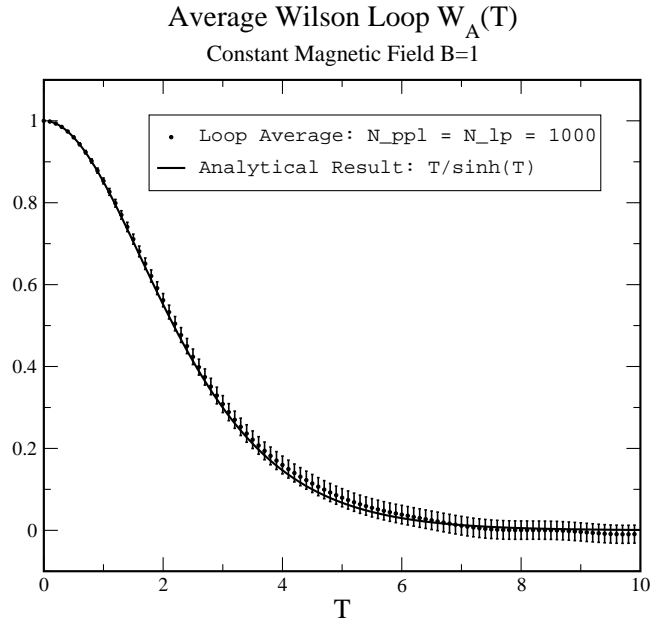


Figure 3.1: Loop average (3.3) in the constant background magnetic field configuration. The numerical results obtained via the loop cloud method are compared to the analytical result.

3.1.3 A benchmark test: Wilson loop average over scalar loops

We test in a first step the loop cloud method by performing the loop average (3.3) numerically. We used an ensemble of 1000 two-dimensional loops of 1000 points using our algorithm based on the Fast Fourier Transform (see Sec. 2.3.2). The results are presented in Fig. 3.1 and are in very good agreement with the analytical curve. The error bars have two origins. First, let us recall that the exact loop average (3.3) is approximated by the mean value (2.14), which induces a numerical error of statistical nature. In this case, the error bars are correlated to the number of loops per ensemble N_{lp} . The second possible source of error is of systematic nature and is related to the fact that the continuous loops entering the exact average (3.3) are on a computer implemented by discretized paths with N_{ppl} points per loop. The effect of the discretization can be seen in the enhancement of the error bars at big values of proper-time. This can be understood if we recall the geometric interpretation of the proper-time². Since the unit loops are simply rescaled with respect to T , the big loops contain the same number of points per loop as the small ones, which means that the systematic error tends to increase with increasing proper-time. This point is developed further in the next paragraph.

3.1.4 A numerical problem: average over fermionic loops

We turn to the case of fermionic loops in the same constant magnetic background configuration. Our numerical estimates are presented in Fig. 3.2 and compared with the analytical result $f(T) = BT \coth(BT)$. The agreement is good in the small T regime but our numerics fails in a rather spectacular way to reproduce the asymptotic behaviour $f(T) \simeq BT$ at large T . An intuitive explanation of this problem can be found if we return for a moment to the average (3.3) and discuss this result at the level of the loop ensemble.

²cf. remark 5 in Sec. 2.4

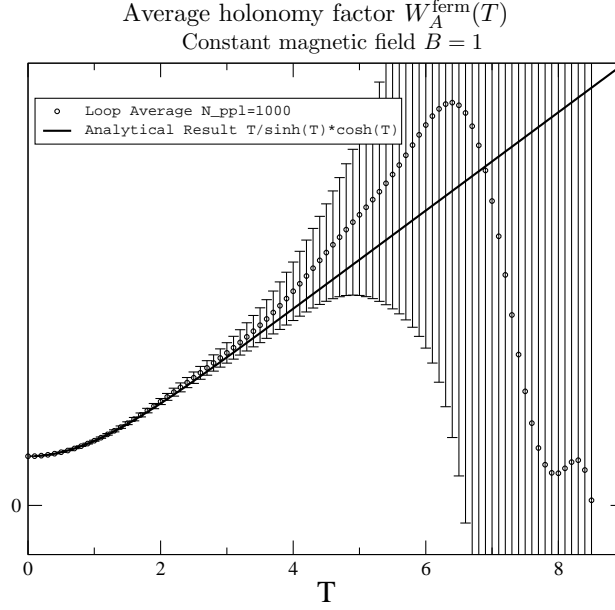


Figure 3.2: Loop average over fermionic loops in the constant background magnetic field configuration. The numerics fails to reproduce the asymptotic behaviour $f(T) \rightarrow BT$.

Since the background field is constant, we have for a given loop C

$$e^{i \oint_C A(x(\tau)) \cdot dx} = e^{i\phi_C},$$

where ϕ_C denotes the magnetic flux through C . We can therefore rewrite the loop average in (3.3) as a conventional integral over the flux ϕ :

$$\left\langle e^{i \int_0^T d\tau A(x_{\text{CM}} + x(\tau)) \cdot \dot{x}} \right\rangle_x = \int_{-\infty}^{+\infty} d\phi \cos(\phi) f(\phi), \quad (3.7)$$

where $f(\phi)$ represents the distribution of the flux over the whole loop ensemble, at fixed proper-time T . Note that we have dropped the loop average of the imaginary part of the Wilson loop. We indeed expect the distribution $f(\phi)$ to be symmetric in the flux ϕ , since there is no preferred orientation for the loops in the ensemble. The flux is explicitly given by $\phi_C = B\mathcal{A}_C$, where \mathcal{A}_C is the *algebraic area*³ of the loop C . The loop average can therefore be rewritten as

$$\int_{-\infty}^{\infty} d\mathcal{A} \cos(B\mathcal{A}) \tilde{f}(\mathcal{A}) = \frac{BT}{\sinh(BT)}.$$

This relation shows that the distribution of the algebraic area over the loop ensemble is given by the inverse Fourier cosinus transformation of its right-hand side. This yields⁴

$$\tilde{f}(\mathcal{A}) = \frac{\pi}{4T \cosh^2\left(\frac{\pi\mathcal{A}}{2T}\right)} \quad \text{and} \quad f(\phi) = \frac{\pi}{4BT \cosh^2\left(\frac{\pi\phi}{2BT}\right)}.$$

³The algebraic area enclosed by a trajectory $(x_1(t), x_2(t))$ in 2 dim. is given by

$$\mathcal{A}_C = \frac{1}{2} \int_0^T dt [x_1(t)\dot{x}_2(t) - x_2(t)\dot{x}_1(t)].$$

⁴ $\int_0^\infty dx \cos(ax) \frac{1}{\cosh^2(bx)} = \frac{a\pi}{2b^2 \sinh\left(\frac{a\pi}{2b}\right)}$

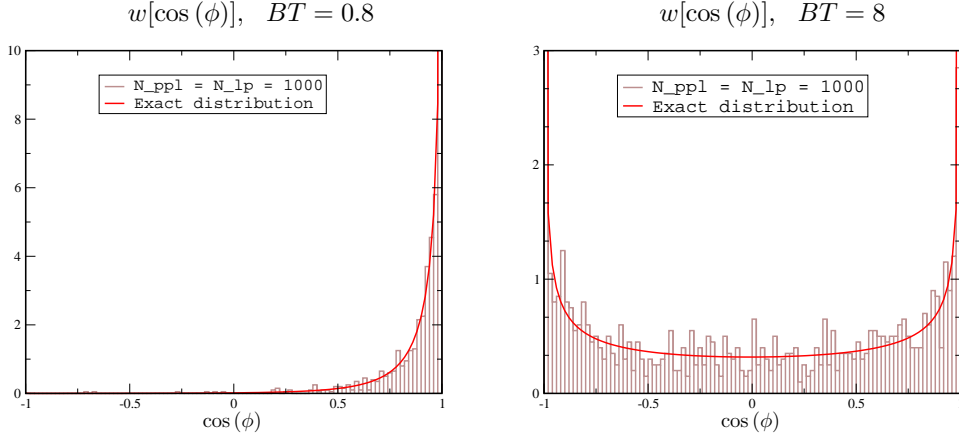


Figure 3.3: Probability distribution $w(y)$ as defined in (3.8) of the Wilson loop $\cos\left(i \int_0^T d\tau A(x(\tau)) \cdot \dot{x}(\tau)\right)$ over a loop ensemble of 1000 loops with 1000 points (histograms) compared with the exact distribution (3.8) for $BT = 0.8$ (left panel) and $BT = 8$ (right panel).

As expected, the distribution $f(\phi)$ is symmetric with respect to the magnetic flux. Let us finally derive the probability distribution of the Wilson loop $\cos(\phi)$. For this, we transform the flux integral (3.7) in the following way:

$$\begin{aligned}
 \int_{-\infty}^{+\infty} d\phi \cos(\phi) f(\phi) &= \sum_{n=-\infty}^{+\infty} \int_{n\pi}^{(n+1)\pi} d\phi \cos(\phi) f(\phi) \\
 &= \sum_{n=-\infty}^{+\infty} (-1)^n \int_0^\pi d\phi \cos(\phi) f(\phi + n\pi) \\
 &= \int_{-1}^1 dy y w(y)
 \end{aligned}$$

with⁵

$$w(y) = \frac{1}{\sqrt{1-y^2}} \sum_{n=-\infty}^{+\infty} [f(\arccos(y) + 2n\pi) + f(-\arccos(y) + 2n\pi)]. \quad (3.8)$$

The distribution $w(y)$ and its numerical estimate is given in Fig. 3.3 in the case $B = 1$ and for two values of the proper-time.

The results are easily interpreted if we recall the geometric interpretation of the proper-time. At small T , the loop ensemble contains small loops having a flux in a small interval centered upon 0 and giving rise to a Wilson loop distribution enhanced in the neighbourhood of 1. Notice also that the histogram follows the analytical curve in a satisfactory way. As T increases, so does the loop extension and the Wilson loop distribution is spread over the whole interval $[-1, 1]$. The decrease of the average Wilson loop $BT/\sinh(BT)$ as a function of the proper-time now clearly appears as a consequence of the increasing symmetry of the Wilson loop distribution. In the limit $T \rightarrow \infty$, the exact distribution $w(y)$ is perfectly symmetric and the integral (3.7) is exactly 0. At the numerical level, such a symmetry can only be

⁵We take into account the fact that the numerical implementation of the $\arccos()$ function returns a number in the interval $[0, \pi]$.

achieved by increasing drastically the number of points per loop N_{ppl} in order to minimize the discretization error. For large T however, this would dramatically increase the numerical burden. The effects of the loop discretization are clearly seen in the quite irregular pattern of the histogram at large T and in the enhancement of the error bars in Fig. 3.1.

Returning to the fermionic case, it is now clear that the asymptotic behaviour $f(T) \simeq BT$ at large T results from the subtle cancellation of huge numbers produced by the $\cosh(BT)$ factor. This can by no means be achieved in a numerical way, unless another implementation permits to bypass the cancellation problem.

Even if the success of the loop cloud method is shadowed by this *fermion problem*, the hope to study fluctuating fermionic fields in the light of worldline numerics should not be definitively abandoned. As we will see in the next section, physical parameters characterizing the configuration may help to minimize the effects of the fermion problem in such a way that relevant physical information can be extracted from loop cloud simulation even in the case of fermionic fluctuations. Among them, the fermion mass plays certainly a crucial role through the factor $e^{-m^2 T}$ in (3.1). In the following, we will study configurations for which the magnetic flux has a finite support. For a localized flux, the fermion problem can possibly be avoided, since the field strength is collected by a loop ($\propto \cosh\left(\int_0^T d\tau B(x(\tau))\right)$) only on some part of its perimeter. In this context the homogeneous magnetic field configuration studied in the massless case appears as the most unfavourable situation from which no information can be gained without modifying the numerical approach.

3.2 Fermion-induced action of vortex systems

3.2.1 General framework

The program is identical to the constant field case: we simply replace the generic vector potential $A(x)$ by the adequate vortex potential in (3.1) and proceed according to the rules of Chapter 2 to compute loop average, proper-time and space-time integrals.

Renormalization. Special attention has to be paid to the renormalization procedure, which we have until now discussed in the case of a constant background only. In this case, an analytical expression for the Pauli factor and the average Wilson loop could be obtained, from which the counter-term in (3.5) was derived. The fact that this counter-term results from a small T expansion and the geometric interpretation of the proper-time⁶ indicate that the expressions (3.5)-(3.6) are in fact also valid for inhomogeneous electromagnetic backgrounds. In the $T \rightarrow 0$ limit, the rescaled loops⁷ are shrunk in such a way that their extension is limited to the neighbourhood of their center of mass x_{CM} and experience therefore the *local* value of the background $F_{\mu\nu}(x_{\text{CM}})$ at this point. As a consequence, the Taylor expansion of the loop average at a given point x_0 is computed considering that the loops of the statistical ensemble, all centered upon x_0 , experience the constant magnetic field $F_{\mu\nu}(x_0)$ in the neighbourhood of x_0 .

⁶cf. Remark 5 at the end of Sec. 2.4.

⁷See Eq. (2.15)

Vortex interfaces. The independence of the background field which characterizes our algorithm allows us in principle to study fermionic fluctuations in the presence of any magnetic background. In particular, a high degree of symmetry of the background is not required, even if it can reduce the numerical burden. We will use this advantage in the study of binary-vortex interactions. In the first investigation, devoted to the study of the quantum energy of one single vortex, we will concentrate on the simplest vortex configurations of interest in solid state or particle physics. In the context of Yang-Mills vortices, we will moreover limit ourselves to the gauge group $SU(2)$.

We study in this work the quantum energy induced by fermionic fluctuations in the presence of magnetic vortices described by the following $U(1)$ potential:

$$A_\mu^{\text{CV}}(x) = \frac{1}{2} \frac{1}{x_1^2 + x_2^2} (x_2, -x_1, 0, \dots, 0)_\mu.$$

If the choice of an Abelian vortex is clear in the context of solid state physics, one could wonder whether the last expression is really suited to describe center vortices of the non-Abelian $SU(2)$ Yang-Mills gauge theory. Such a vortex is in fact described by the following potential:

$$\mathcal{A}_\mu^{\text{CV}}(x) = A_\mu^{\text{CV}}(x) \tau^3. \quad (3.9)$$

[The interested reader may find a detailed derivation of this expression from the general definition of a center vortex of arbitrary geometry in Sec. E.1.]

We show that the remaining color structure under the form of the Pauli matrix τ^3 in the previous expression does not enter the numerical simulation, producing only a constant prefactor. We have

$$\begin{aligned} \text{tr}_{\text{color}} \left\{ \left\langle W_{\mathcal{A}^{\text{CV}}}^{\text{ferm}} \right\rangle_x - 1 \right\} &= \text{tr}_{\text{color}} \left\{ \left\langle e^{i \oint A^{\text{CV}} \cdot dx} \tau^3 \frac{1}{4} \text{tr}_{\text{spin}} P_T e^{\frac{1}{2} \int_0^T d\tau \sigma_{\mu\nu} F_{\mu\nu}^{\text{CV}}(x_{\text{CM}} + x(\tau))} \tau^3 \right\rangle - 1 \right\} \\ &= 2 \times \left\{ \left\langle W_{\mathcal{A}^{\text{CV}}}^{\text{ferm}} \right\rangle_x - 1 \right\} \end{aligned}$$

using elementary properties of the Pauli matrices.

A center vortex is in its very definition (E.1) singular on the vortex sheet, which, in the present case, is the plane $x_1 = x_2 = 0$. This is of course an idealization: a magnetic vortex in a superconductor has a finite extension. In the context of center vortices in Yang-Mills theory, lattice simulations show that the vortex surface possesses a finite thickness d with respect to the directions perpendicular to the flux, implying that the gauge potential singularity in the surface is smeared. We therefore take the finite thickness of the vortex surface into account by introducing the vortex *core size* d in the gauge potential:

$$A_\mu^{\text{V}}(x) = \frac{\varphi}{2} \frac{1}{d^2 + x_1^2 + x_2^2} (x_2, -x_1, 0, \dots, 0)_\mu. \quad (3.10)$$

Here, we have generalized the expression to a vortex with flux $\phi = \varphi\pi$, the center vortex corresponding to the case $\varphi = 1$. The corresponding field strength is given by

$$F_{12}(x) = \frac{\varphi d^2}{[d^2 + x_1^2 + x_2^2]^2}. \quad (3.11)$$

	$D=2+1$	$D=3+1$
C_{d0}	$\frac{1}{4\pi^{3/2}}$	$\frac{1}{8\pi^2}$
C_{d1}	$\frac{1}{4(4\pi)^{3/2}}$	$\frac{1}{(8\pi)^2}$
α	1.5	1
ν	2.5	3
ρ	0.5	1

Table 3.1: Prefactors and exponents of the derivative expansion.

Quantum energy. The vortex configuration (3.10) is independent of the time coordinate x_D . As a consequence, the time integration can be carried out trivially and gives

$$\Gamma_{\text{ferm}}^{(1)}[A^V] = E[A^V]L_t$$

where L_t is the extent in the time direction and $E[A^V]$ is the *quantum energy* of the vortex interface A^V . In $D = 2 + 1$, the energy is given by

$$E = \int dx_1 dx_2 \mathcal{L}_{\text{ferm}}^{(2+1)}(x, y) = 2\pi \int_0^\infty d\rho \rho \mathcal{L}_{\text{ferm}}^{(2+1)}(\rho), \quad (3.12)$$

where the effective Lagrangian $\mathcal{L}_{\text{ferm}}^{(2+1)}(x, y)$ plays the role of the energy density. In the case $D = 3 + 1$, the vortex core is at a given time-slice a straight line of length L_{x_3} . The quantum energy is proportional to the extent L_{x_3} :

$$E[A^V] = \chi[A^V]L_{x_3} \quad (3.13)$$

where $\chi = \int dx_1 dx_2 \mathcal{L}_{\text{ferm}}^{(3+1)}(x_1, x_2)$ is the *string tension* of the vortex line in the 3D hypercube.

3.2.2 The derivative expansion

The single vortex configuration has a sufficiently simple geometry to allow an analytical study of the problem. The standard analytical approach to quantum energies for such inhomogeneous backgrounds is the *derivative expansion*. The idea of this approach is to investigate deviations from the Euler-Heisenberg result, only valid for a constant field configuration, by performing an expansion in terms of a small parameter constructed from derivatives of the background field. In the present case, there are two options for the choice of the expansion parameter:

- $\partial^2/m^2 \ll 1$, the field gradient is small compared to the scale set by the fermion mass,
- $\partial^2/B(x) \ll 1$, the derivatives of the background field should be smaller than the local field strength.

Let us point out that only one of the conditions mentioned above has to be satisfied. It is remarkable that closed-form expressions at the next-to-leading order (NLO) level in $D = 2 + 1$ and $D = 3 + 1$ have been found in recent years [GS99] which are applicable in both cases.

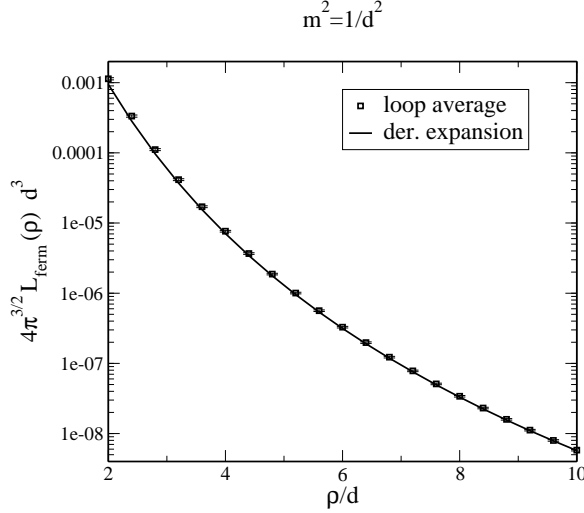


Figure 3.4: Effective Lagrangian as a function of the radial distance ρ to the vortex core for the case $m=1$, $\varphi=1$, $D=2+1$. The NLO derivative expansion (solid line) is compared with the numerical computation (squares with error bars).

The leading order of the derivative expansion corresponds to the Euler-Heisenberg-Schwinger result (3.4):

$$\mathcal{L}_{\text{ferm}}^{d0}(x) = C_{d0} \int_0^\infty \frac{dT}{T^\nu} e^{-m^2 T} [B(x)T \coth(B(x)T) - 1 + \{\text{c.t.}\}]. \quad (3.14)$$

Note that the counter-term $\{\text{c.t.}\} = -\frac{1}{3}(B(x)T)^2$ must be added to the integrand for $D = 3+1$ for the same reasons as discussed in Sec. 3.1.2. The next-to-leading (NLO) correction can be written as [CDD95, GS99]⁸

$$\mathcal{L}_{\text{ferm}}^{d1}(x) = C_{d1} \frac{(\partial_i B(x))^2}{B^\alpha(x)} \int_0^\infty \frac{d\omega}{\omega^\rho} e^{-\frac{m^2}{B(x)}\omega} \frac{d^3}{d\omega^3} [\omega \coth(\omega)]. \quad (3.15)$$

The prefactors $C_{d0,1}$ and exponents α , ν and ρ depend on the number D of space-time dimensions and are summarized in Table 3.1.

Particularizing the conditions of validity to the smeared vortex configuration (3.10), we expect the NLO Lagrangian to give reasonable answer if

$$\begin{aligned} md &\gg 1, \\ \rho/d &\gg 1. \end{aligned}$$

3.2.3 Single-vortex configuration in $D = 2 + 1$

Benchmark test. In a first step, we test our method in the presence of the vortex background. We calculate the effective Lagrangian $\mathcal{L}_{\text{ferm}}(\rho)$ for large values of ρ , $\rho \gg d$, where the derivative expansion is expected to give reliable results. The result of the numerical worldline approach is compared with the derivative expansion in Fig. 3.4 for $D = 2 + 1$. The agreement between the two curves is satisfactory.

⁸A representation of the integral in terms of the Hurwitz Zeta function as well as asymptotic expansions have been found; see, for example, [GS99].

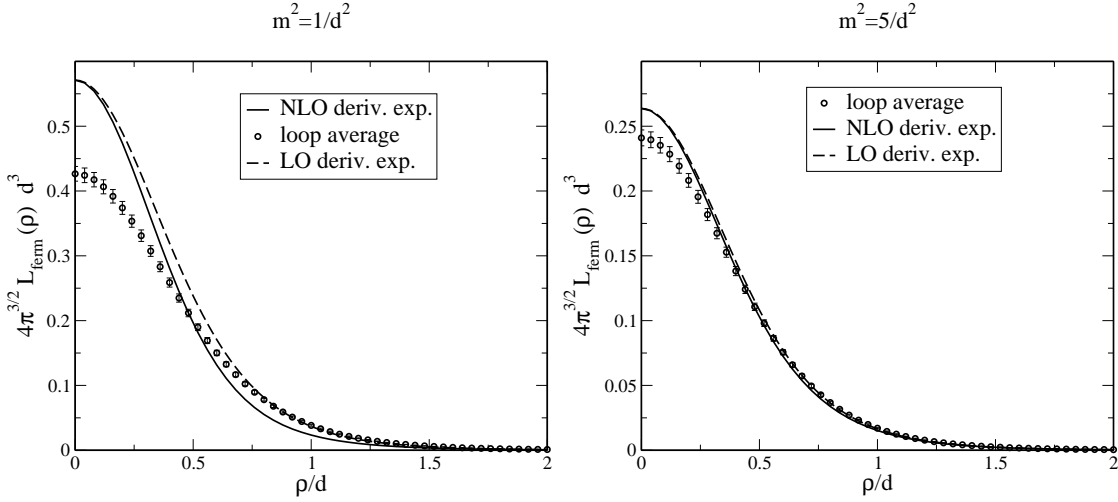


Figure 3.5: Effective Lagrangian in the small ρ region for the cases $m=1$ (left panel) and $m^2=5$ (right panel), $\varphi=1$, $D=2+1$.

Derivative expansion vs. worldline numerics. In the region close to the core of the vortex, i.e., $\rho \approx d$, the gradients of the background field are as large as the field itself, so that the reliability of the derivative expansion now depends on the value of the mass. Our numerical findings for this regime are shown in Fig. 3.5 for $m^2 = 1$ (left panel) and $m^2 = 5$ (right panel). For larger masses, we observe a good qualitative and a reasonable quantitative agreement. But even for the small mass value $m^2 = 1$, there is at least qualitative agreement between the numerical result and the derivative expansion, indicating that the applicability of the derivative expansion can be pushed to its formal validity limit in $D = 2 + 1$. This observation is also supported by the fact that the NLO term (3.15) is only a small correction to the zeroth-order result (3.14). Moreover, we expect that the (up to now unknown) NNLO correction, which is sensitive to the curvature of the field strength, improves the result near the vortex core. In this sense, it is reassuring to observe that the numerical result agrees with the NLO derivative expansion precisely at the turning point of the curve at $\rho \simeq 0.5$, because the NNLO correction must vanish here. We should finally stress that for even smaller masses $m < 1$, the discrepancy between our numerical result and the derivative expansion increases, so that the derivative expansion should be abandoned here.

Quantum energy. Let us now examine the fermion-induced quantum energy E of the vortex soliton as defined in (3.12), which we obtain by numerically integrating the effective Lagrangian. Our result for this energy is shown in Fig. 3.6 as function of the fermion mass m in units of the vortex thickness d . Since fermion fluctuations are suppressed with increasing mass, the quantum energy decreases with increasing m , and vanishes in the large mass limit. For phenomenological purposes, it is important to notice that the quantum energy is positive. This implies that potential effective models for vortex dynamics have to account for the fact that vortex nucleation is suppressed by the fermion-induced effective action in $D = 2 + 1$ dimensions.

Furthermore, let us consider the variation of the quantum energy with respect to the flux ϕ , which is carried by the vortex. Our numerical result is shown in Fig. 3.6 (right panel).

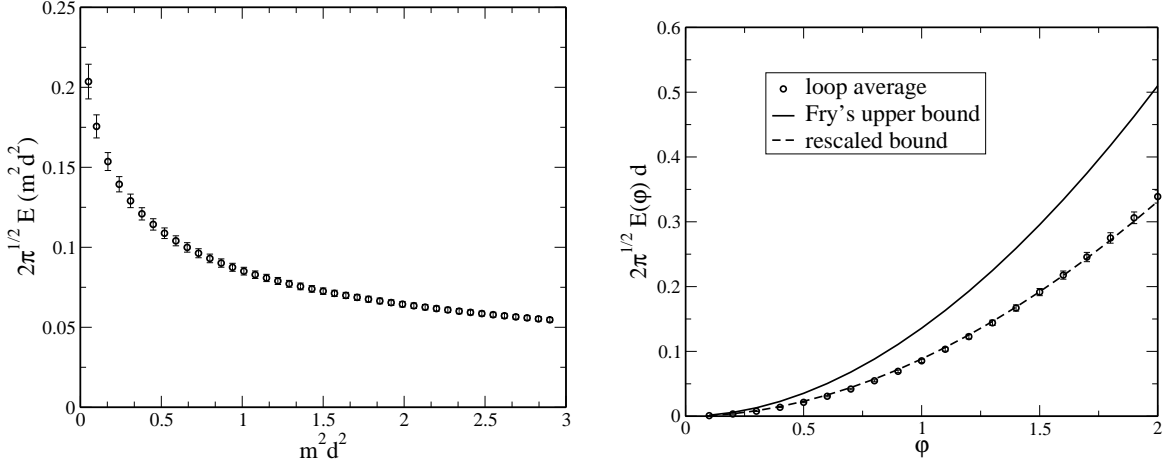


Figure 3.6: Quantum energy as a function of the mass m^2 for $\varphi=1$ (left panel) and as a function of the flux φ carried by the vortex for $m = 1$ (right panel) in comparison with Fry's upper bound given in (3.16).

We find that the energy is monotonically increasing with the flux ϕ . It is interesting to compare our result for $E(\varphi)$ with a general result for fermionic determinants described by M. Fry in [Fry96]; therein a lower bound has been derived for unidirectional magnetic fields in $D = 2 + 1$, which translates into an upper bound E_b for the quantum energy of our vortex configuration given by

$$\begin{aligned}
 E(\varphi) &\leq E_b(\varphi), \\
 E_b(\varphi) &= \left(\frac{1}{d}\right) \frac{1}{6} \left[2 - 3\varphi - 2\sqrt{1+\varphi} + \varphi\sqrt{1+\varphi} + 3\sqrt{\varphi} \operatorname{arsinh}(\sqrt{\varphi}) \right]
 \end{aligned}
 \tag{3.16}$$

for the case $md = 1$ and Dirac 4-component spinors. For other values of md , this formula receives a total factor of $(md)^3$ and the flux has to be replaced by $\varphi \rightarrow \varphi/(md)^2$. As shown in Fig. 3.6, our numerical result lies well within this bound. More remarkable is the fact that the functional dependence of our result agrees with the bound within the error bars, if the bound is scaled by a factor of roughly 0.65.

As a further check, we have compared all our above-mentioned results with those of [Pas01], where the single-vortex case with profile functions different from ours was considered within the phase-shift approach. We find good agreement within the error bars except for a global factor of 2 by which the result of [Pas01] for $E(\varphi)$ is larger.

3.2.4 Single-vortex configuration in $D = 3 + 1$

Similarly to the previous studies of the $D = 2 + 1$ case, we investigate the effective Lagrangian $\mathcal{L}_{\text{ferm}}$ as a function of ρ and compare the result with the one obtained from the derivative expansion (see Fig. 3.7). Contrary to $D = 2 + 1$, we observe that unless $\rho \gg d$, the leading order (LO) of the derivative expansion falls far too short of reproducing the numerical result for $(md)^2 = \mathcal{O}(1)$. For instance, for $(md)^2 = 1$, we find an order-of-magnitude difference at $\rho = 0$ (Fig. 3.7 (left panel)). Moreover, the NLO contribution of the derivative expansion

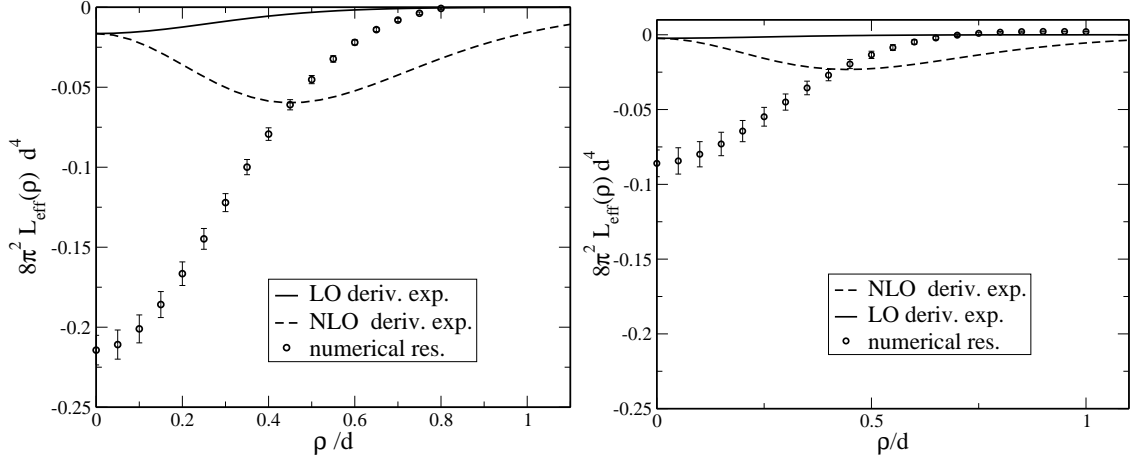


Figure 3.7: Effective Lagrangian for $m^2 = 1$ (left panel) and $m^2 = 3$ (right panel), $\varphi=1$, $D = 3 + 1$.

also exceeds the leading order result by almost an order of magnitude for $\rho \approx d$. This signals the break-down of the derivative expansion for the case of the field, its gradient and the mass being all of the same order. Contrary to the case of $D = 2 + 1$, the applicability of the NLO derivative expansion cannot be pushed to its formal validity limits $md \approx 1$. Even for larger values of the mass, $m^2 = 3$ (right panel), there is only a minor improvement of the quality of the NLO derivative expansion. Of course, the NNLO contribution could, in principle, improve the results of the derivative expansion, but this would only emphasize the fact that there is no clear hierarchy from term to term in the derivative expansion.

We believe that the striking difference to the $D = 2 + 1$ dimensional case is indeed remarkable and points to a deeper reason in terms of a renormalization effect. To illustrate this, we note that the quantity $\langle W_{\text{spin}} - 1 \rangle$ occurring in the proper-time integrand is positive for the vortex background, whereas the counter-term $-\frac{1}{3}B^2(x)T^2$ is negative. Since the effective Lagrangian is largely negative as seen in Fig. 3.7, it is mainly driven by the counter-term. Now the leading-order derivative expansion obviously overestimates the value of $\langle W_{\text{spin}} - 1 \rangle$ near the vortex core, since it is a local expansion. The true value as seen in the numerical computation is much smaller because it is a nonlocal average over the extended *loop cloud* that also “feels” the much weaker field at a radial distance from the core. The final value of the total effective Lagrangian at a point x therefore results from a nontrivial interplay between nonlocal (and nonlinear) vacuum polarization ($\sim \langle W_{\text{spin}} - 1 \rangle$) and a local definition of the coupling giving rise to a local counter-term. In regions where the background field varies rapidly, such as the near vortex core in our case, this interplay can lead to an order-of-magnitude enhancement of the effective Lagrangian as compared with the constant-field approximation (leading-order derivative expansion). In our opinion, this phenomenon clearly deserves further investigation.

Though the comparison of the results in $D = 2 + 1$ and $D = 3 + 1$ is *per se* very interesting, let us emphasize that the numerical estimates should not be considered at the same level. In $D = 3 + 1$, we renormalize the theory, i.e. we fix the values of the parameters at a given renormalization point. This is rendered necessary by the occurrence of a divergent proper-time integral. The theory in $D = 2 + 1$ is on the contrary free of divergences. In the present

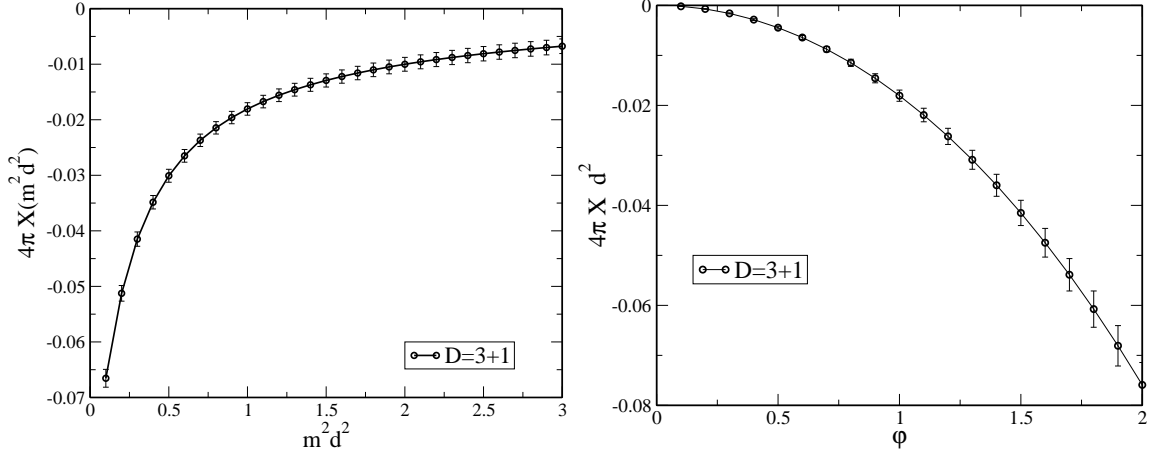


Figure 3.8: Effective action as a function of the dimensionless quantity $m^2 d^2$, $\varphi=1$, $D=3+1$ (left panel), and as function of the flux, $m^2 d^2 = 1$ (right panel).

study, we chose to work with the bare, i.e. unrenormalized parameter. It is however possible to perform a renormalization by introducing a *finite counter-term* to the bare action. In this case, this counter-term can possibly also lead to a discrepancy between worldline and derivative expansion results.

Returning to our numerical study of the one-vortex background, we calculate the string tension χ as defined in (3.13) as a function of the fermion mass m and plot it in Fig. 3.8 for $\varphi = 1$. The negative values of χ show that the fermion-induced effective action Γ_{ferm} favors the nucleation of vortices. Since the modulus of this effective action increases if the vortex thickness d is decreased, the fermionic part of the vortex action supports the existence of thin vortices.

3.2.5 Binary-vortex interactions

The binary-vortex configuration is given by the superposition of two single vortex gauge fields $A_\mu(x)$ (3.10),

$$A_\mu^{(2)}(x) = A_\mu\left(x - \frac{l}{2}\right) \pm A_\mu\left(x + \frac{l}{2}\right), \quad (3.17)$$

where l denotes the vortex distance. Below, we will study the case of the so-called center vortices the flux of which is given by $\varphi = 1$. The relative sign between the gauge fields on the right-hand side of (3.17) corresponds to the relative orientation of the fluxes: the plus sign corresponds to an equal orientation of the flux in each vortex, while the minus sign signals an opposite orientation.

Figure 3.9 shows the lines of equal effective Lagrangian $L_{\text{eff}}^{(3)}(x, y)$ in the xy -plane which is perpendicular to the vortex fluxes. The vortices are located at the x axis at a distance $l = 3d$. It is straightforward (but computer time consuming) to integrate the effective action over the xy -plane in order to derive the quantum energy E of the binary-vortex configuration. The result is shown in Fig. 3.10 for the case $D = 2 + 1$. For large distances $l \gg d$, the quantum energy approaches twice the value of a single vortex. For $l = 0$, the vortices fall on top

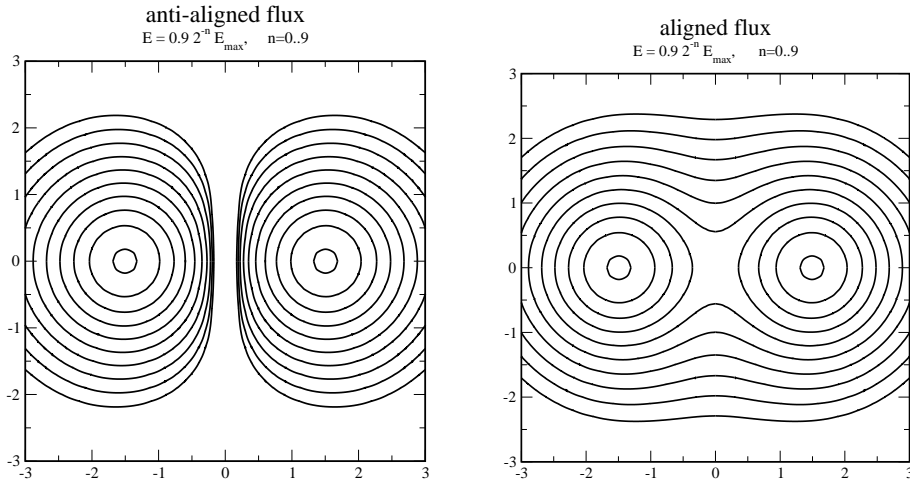


Figure 3.9: Effective Lagrangian $L_{\text{ferm}}^{(3)}(x, y)$ as function of the xy -plane for the two vortex configuration: parallel (right panel) and anti-parallel (left panel) orientation of the flux, $m^2 d^2 = 0.5$, $\varphi=1$, $D=2+1$.

of each other. If the fluxes of the vortices are oppositely oriented, the vortices annihilate each other, and the quantum energy of the configuration vanishes. If the vortex fluxes are equally oriented, the configuration is equivalent to the single vortex configuration with flux $\varphi = 2$. Since the quantum energy is roughly proportional to φ^2 (see Fig. 3.6), the vortex configuration with flux $\varphi = 2$ possesses a higher energy than twice the energy of a single vortex, carrying flux $\varphi = 1$. Hence, vortices with an equal flux orientation repel each other in $D = 2 + 1$, while vortices with oppositely oriented flux attract each other. The same line of argument applies to the case $D = 3 + 1$. Since the fermionic contribution to the effective action is negative in this case, the fermion-induced force is attractive (repulsive) for equally (oppositely) oriented vortices, contrary to the $D = 2 + 1$ case.

3.3 Summary and outlook

Our numerical implementation of the worldline picture of QFT was applied to the study of the quantum energy induced by fermionic fluctuations in the presence of a magnetic background. In a first step, the method was tested for a constant magnetic background and vanishing mass. Our simulation in the scalar case produced results in very good agreement with the analytical estimates, whereas it failed to address the fermionic case due to severe cancellations in the large T regime. This fermion problem can however be bypassed at finite mass and for magnetic fields whose support has a finite extension in space. In particular, we applied our method to the calculation of the quantum energy induced by fermions in the presence of a vortex system.

We first investigated the single-vortex configuration. Our numerical approach has been successfully tested in the parameter regime where the derivative expansion is expected to provide reliable results: in the large-mass regime $md \gg 1$ or for strong-field suppression of the inhomogeneities $\partial^2/B \ll 1$. The comparison of our numerical results to the derivative expansion in $D = 2 + 1$ has shown that this analytical technique provides a reasonable

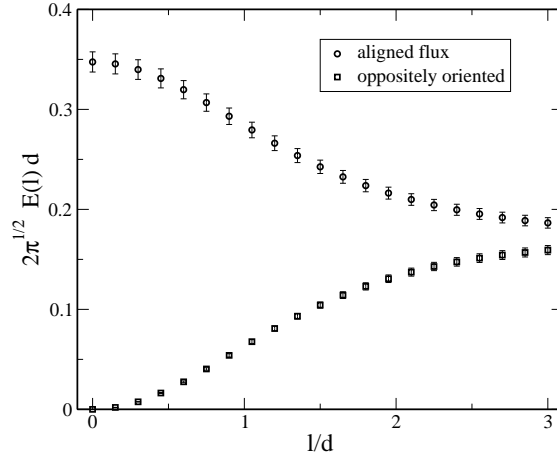


Figure 3.10: The interaction of two parallel vortex lines in $D = 2 + 1$, $\varphi = 1$, $m^2 d^2 = 1$.

approximation to the quantum energy of a single vortex configuration even for small masses, $md \lesssim 1$. Our simulations in $D = 3 + 1$ have signalled the breakdown of the derivative expansion due to renormalization effects, which can occur near regions where the background varies rapidly. From a physical point of view, we find that the quantum action is positive in $D = 2 + 1$, implying that the presence of vortices is suppressed, and large vortex core sizes d are preferred. In $D = 3 + 1$, the properly renormalized quantum action turns out to be negative: the nucleation of thin ($d \rightarrow 0$) vortices in $D = 3 + 1$ is supported by the fermion induced quantum action.

Finally, we studied the binary-vortex interaction, for which no analytical investigation has until now been performed. We found that the fermion-induced interaction favors vortices with an opposite orientation of the fluxes in $D = 2 + 1$ without finite renormalization, while in $D = 3 + 1$, an equal orientation of the fluxes is preferred, due to the change of the global sign induced by the counter-term.

Further investigations are at the moment performed in the context of Yang-Mills vortex systems. Since our numerics imposes no restriction on the degree of complexity of the background potential, our numerical method can be used to investigate the vortex gas mentioned in the introduction of this chapter. In particular, it provides a numerical access to the fermion condensate, related to the effective action Γ_{ferm} by differentiation with respect to the fermion mass m ,

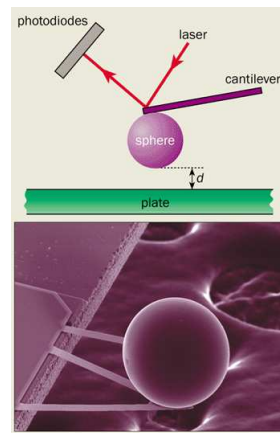
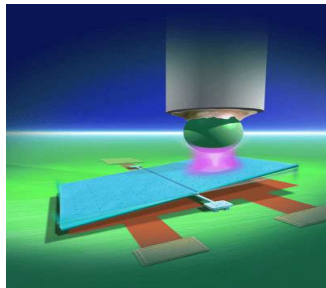
$$\int d^D x_0 \langle \bar{\psi} \psi \rangle = - \lim_{m \rightarrow 0} \frac{\partial \Gamma_{\text{ferm}}}{\partial m}.$$

The study of the quark condensate in the presence of the vortex gas permits to get some hints over the role played by center vortices in the breaking of chiral symmetry. This could be a step towards a unified description of confinement and chiral symmetry breaking in terms of center vortices, as suggested by lattice simulations. In the chiral limit $m \rightarrow 0$, the method can unfortunately not be used in the implementation described in the previous chapter, due to the fermion problem. A modified representation of the loop average, where the Pauli factor responsible for the huge cancellations taking place in the large T regime is replaced by the spin factor [KK91], is currently under investigation.

Chapter 4

Casimir effect on the worldline

The Casimir effect was for a long time since its theoretical prediction [Cas48] considered as a beautiful illustration of the effects induced by vacuum fluctuations of quantum fields but no more than an interesting problem in its own right. In its evolution from microtechnology towards nanotechnology, the engineering of electronic devices [CAK⁺01] came inevitably across this effect, which can no more be neglected at these scales. The Casimir effect is nowadays the subject of precise measurements [MR98] as well as of theoretical investigations including thermal effects, finite conductivity and surface roughness (see [Mil, BMM01] for a review of the latest experimental and theoretical developments in the study of the Casimir effect).



The most recent measurements are based on the geometry illustrated in the figure above, right panel: the Casimir force is most accurately measured for the sphere-plate configuration. Analytical tools for the study of the Casimir effect for arbitrary geometries are unfortunately still lacking. Beyond the ideal plate-plate configuration studied by Casimir, the analytical studies of more involved geometries like the relevant sphere-plate configuration require assumptions concerning the geometry and the physical properties of the Casimir interfaces.

In this work, we apply the loop cloud method to the study of the Casimir effect for arbitrary configurations. The fact that our method is well suited for this problem results from

- the embedding of the Casimir effect in the framework of Quantum Field Theory with

the Casimir interfaces modelled by an external potential,

- the applicability of the numerical method to arbitrary potentials.

In this chapter, we focus on the study of the Casimir effect induced by the fluctuations of a real scalar field. This is done for various configurations including the classic plate-plate configuration which serves as a test for the numerical method, the experimentally relevant plate-sphere configuration as well as the plate-cylinder, for which we compare our numerical estimates with the results furnished by the proximity force approximation. We begin with a discussion regarding the problem of implementing boundary conditions on a quantum field, which is still an ongoing debate in the literature. The computational framework is then introduced, firstly in a general way and secondly particularising to the case of rigid bodies, on which we will focus here. The last sections are devoted to the numerical results, which will underline the intuitive aspects of the loop cloud method, and finally concluding remarks regarding further applications of the method to the Casimir physics will be made.

4.1 Imposing boundary conditions on quantum fields

At the microscopic level, the Casimir effect arises from the interaction of the fluctuating field with the material of the Casimir boundary. In the standard approach, this interaction is modelled by boundary conditions imposed on the fluctuating field [MT97, Mil01, BMM01]. It must however be kept in mind that an *ab initio* implementation of, let us say, a Dirichlet type boundary condition is an idealization of the real physical problem. If we take the simplest example of a one-dimensional scalar field constrained to vanish at the Casimir interfaces $x = 0$ and $x = a$, we have

$$\phi(0) = 0 = \phi(a). \quad (4.1)$$

In this idealized case, the properties of the material are such that all modes of the fluctuating field are suppressed on the interfaces. The theoretical approach on which our work is based, i.e. the embedding of the Casimir problem in the framework of a renormalizable quantum field theory, permits in this context a careful and critical discussion of the implementation of such *ab initio* boundary conditions as a substitute of the real interactions between field and matter [Jaf].

The starting point is typically given by a field theoretic Lagrangian of the form

$$\mathcal{L} = \frac{1}{2} \partial_\mu \phi \partial^\mu \phi - \frac{1}{2} m^2 \phi^2 - \lambda \sigma(x) \phi^2,$$

where the interaction field-boundary matter is modelled by the coupling of the fluctuating field ϕ with a static background $V(x) = -\lambda \sigma(x)$, the function $\sigma(x)$ accounting for the shape of the physical boundary and λ being the strength of the interaction. In this framework, the Casimir energy, as a function of the parameters σ and λ , $E_{\text{Cas}}[\lambda, \sigma]$, is accessed via the effective action $\Gamma^{(1)}[V]$ either numerically using the loop cloud method or, depending on the degree of symmetry of the modeling background, analytically resumming over the energy spectrum using a recent method based on quantum mechanical considerations [GJK⁺02, GJK⁺03]. In the field theoretic language, the boundary condition (4.1) can be approached by taking the limits $\sigma(x) \rightarrow \delta(x) + \delta(x - a)$ (*sharp limit*) and $\lambda \rightarrow \infty$ (*strong limit*):

$$E_{\text{Cas}}^{\text{b.c.}} = \lim_{\substack{\lambda \rightarrow \infty \\ \sigma \rightarrow \delta}} E_{\text{Cas}}[\lambda, \sigma]. \quad (4.2)$$

The crucial point is then to compare $E_{\text{Cas}}^{\text{b.c.}}$ to the result furnished by the standard approach. In the limiting case (4.2), the result [Jaf] shows that

- the Casimir energy diverges in the sharp limit for $D > 1 + 1$,
- the Casimir energy diverges in the strong limit, in any case.

Let us emphasize that the energy $E_{\text{Cas}}[\lambda, \sigma]$ is the *renormalized* Casimir energy, for which the field theoretic divergences have already been eliminated by means of standard QFT renormalization procedures. The fact that the divergences appearing in the sharp and/or strong limit implementing the boundary condition have nothing to do with standard infinities of quantum field theory underlines the physical origin of these divergences: the energy needed by the material to enforce the suppression of arbitrary high frequency modes at the interface is infinite.

These findings, obtained in the light of quantum field theoretic techniques, seem to contradict the original prediction of Casimir: the force between two metallic plates is of course finite. Let us refine the above statement. A careful study shows that the *energy density* is finite at any point not sitting on the Casimir boundaries in the strong limit $\lambda \rightarrow \infty$. Moreover, the result *agrees* with the energy density obtained with *ab initio* boundary conditions. The divergences occur precisely at the boundaries, i.e. at $x = 0$, $x = a$, and render the total Casimir energy infinite. Likewise, the *Casimir force* between the two interfaces agrees with the boundary condition calculation, which is the original Casimir result:

$$F(a) = -\frac{\pi}{48a^2} \quad \text{for } D = 1 + 1 \text{ and } m = 0. \quad (4.3)$$

This agreement between the field theoretic approach and the standard approach is in fact valid when the change in vacuum energy is calculated respectively to a *rigid* displacement of the interfaces, i.e. the bodies are not deformed during the displacement. As far as the *interaction energy* (or the force, which is derived from it by differentiation) for such a displacement is concerned, the divergences which are localized on the boundaries are harmless. On the contrary, the Casimir force, or Casimir pressure of a *closed* geometric configuration, which is obtained by studying small deformations of the body, is even infinite in the sharp limit. In this case, the force or the pressure cannot be obtained simply by imposing boundary conditions. For such a problem, like for instance the determination of the Casimir pressure exerted on a thin sphere, the material properties of the body have to be imperatively taken into account and the description of the problem in the framework of quantum field theory [G⁺04, GLM] appears to be the most adequate.

4.2 Worldline approach to the Casimir effect

4.2.1 General framework

We focus in this work on the calculation of Casimir forces induced by quantum fluctuations of a real scalar field. The field theoretic Lagrangian is

$$\mathcal{L} = \frac{1}{2} \partial_\mu \phi \partial_\mu \phi + \frac{1}{2} m^2 \phi^2 + \frac{1}{2} V(x) \phi^2. \quad (4.4)$$

As discussed in the previous section, we take into account the interaction between the fluctuating field and the matter of the Casimir boundary by means of the interaction term $\frac{1}{2}V(x)\phi^2$, where the potential $V(x)$ will model in shape and strength the physical properties of the interface. The worldline representation of the one-loop effective action for the field theory defined by (4.4) is given by the expression (2.8) which we recall here for convenience:

$$\Gamma^{(1)}[V] = -\frac{1}{2(4\pi)^{D/2}} \int_0^\infty \frac{dT}{T^{D/2+1}} e^{-m^2 T} \int d^D x_{\text{CM}} \left[\left\langle e^{-\int_0^T d\tau V(x_{\text{CM}}+x(\tau))} \right\rangle_x - 1 \right]. \quad (4.5)$$

In this work, we concentrate exclusively on static Casimir configurations, i.e. the modeling potential

$$V(x) = V(\mathbf{x})$$

is time independent. In this case, the proper-time integrand does not itself depend on time and the time integration can be carried out trivially, $\int dx_{\text{CM}}^4 = L_{x_4}$, where L_{x_4} denotes the ‘‘volume’’ in time direction. We define the (unrenormalized) Casimir energy as

$$\mathcal{E}_V = \Gamma[V]/L_{x_4}. \quad (4.6)$$

Range of applicability. Let us recall that the loop cloud method has been developed independently of the background potential. In the context of Casimir configurations, it means that the Casimir effect can be studied numerically for arbitrary geometries. In particular, the applicability of the numerical method is independent of the degree of symmetry of the physical boundaries. In the present study, this will permit us to go beyond the geometry assumptions required by the ‘proximity force approximation’ (PFA) [DAL56, BRST77], which is the standard analytical approach to the Casimir effect for non-trivial geometric configurations. The assumption of perfect surfaces can also be dropped: in a future work, we could for instance study corrugated surfaces, and compare our results to the new approach developed recently in [Emi03].

Renormalization. As discussed in Sec. 2.2, the renormalization procedure in the worldline formalism is based on an analytic expansion of the proper-time integrand for small proper-times (high momentum scales). The quantity to be expanded is the loop average of the holonomy factor W_V , which, expressed in terms of the rescalable unit loops $y(t)$, reads

$$\left\langle \exp \left[-T \int_0^1 dt V(x_{\text{CM}} + \sqrt{T}y(t)) \right] \right\rangle_y. \quad (4.7)$$

Using $\int_0^1 dt y_\mu(t) = 0$ and $\int_0^1 dt \langle y_\mu(t) y_\nu(t) \rangle_y = (1/6)\delta_{\mu\nu}$, we find up to order T^2 ,

$$\begin{aligned} \int d^D x \langle W_V - 1 \rangle_y &= -T \int d^D x V(x) - \frac{T^2}{6} \int d^D x \partial^2 V(x) \\ &\quad + \frac{T^2}{2} \int d^D x V(x)^2 + \mathcal{O}(T^3), \end{aligned} \quad (4.8)$$

which should be read together with the proper-time factor $1/T^{D/2+1}$ in the expression of the effective action (4.5). [We dropped the subscript CM in order to simplify the notation.] Each term $\sim V^n$, which, depending on the space-time dimension D , can possibly lead to

a divergent proper-time integral, corresponds to a one-loop Feynman diagram containing n insertions of the potential V . The term $\sim V(x)$, which gives a divergence of the T integral for $D > 1$, corresponds to the tadpole graph. In the conventional “no-tadpole” renormalization scheme, the renormalization counter term $\sim V(x)$ is chosen such that it cancels the tadpole contribution completely. Of course, other renormalization schemes can be used as well. Let us note that the term containing the second derivative of V vanishes anyway. This is due to the fact that a typical potential describing a Casimir configuration is localized on the physical boundaries¹. For $D = 2 + 1$, the term $\sim V^2$ is finite, which means that we don’t need any further counter term. In $D = 3 + 1$ this term diverges and we need a further subtraction. Renormalization provides us with a further counter term $\sim \int_x V^2$ subject to a physically chosen renormalization condition such that the divergence arising from the last T^2 term is canceled. With this renormalization condition, the physical value of the renormalized operator $\sim V^2$ is fixed. For even higher dimensions, similar subtractions are required that involve higher-order terms not displayed in (4.8).

4.2.2 Casimir interaction energy between rigid bodies

In this work, we model the physical boundaries by a potential of the form

$$V(\mathbf{x}) = \lambda\sigma(\mathbf{x}),$$

where the parameter λ is the strength of the field-matter interaction and $\sigma(\mathbf{x})$ describes the geometry of the Casimir configuration. The coupling λ has mass dimension 1 and is assumed to be positive. It can roughly be viewed as a plasma frequency of the boundary matter: for fluctuations with frequency $\omega \gg \lambda$, the Casimir boundaries become transparent. As discussed in Sec. 4.1, two types of limits can be taken regarding the shape function and the coupling:

$$\sigma(\mathbf{x}) \rightarrow \int_{\Sigma} d\sigma \delta^d(\mathbf{x} - \mathbf{x}_{\sigma}) \text{ (“sharp limit”)}, \quad (4.9)$$

$$\lambda \rightarrow \infty \text{ (“strong limit”)}. \quad (4.10)$$

Here Σ represents the geometry of the Casimir configuration and denotes a $d - 1$ dimensional surface, generally disconnected (e.g. two disconnected plates, $\Sigma = S_1 + S_2$). The first limit can safely be taken, as far as the Casimir energy of *rigid bodies* (i.e. which are not deformed during the displacement) is concerned. The second limit imposes the *Dirichlet boundary condition*, implying that all modes have to vanish on Σ . As pointed out in Sec. 4.1, this limit is unfortunately spoiled by the occurrence of a divergence in the Casimir energy, which corresponds precisely to the second type (*ii*) of divergences described in section 2.2, since it is due to the particular assumption $\lambda \rightarrow \lambda_{\text{cr}} = \infty$. As stated before, it cannot be removed by standard field theoretic renormalization. However, this problem can be bypassed if we consider instead the Casimir force acting on the rigid bodies. The force is defined by

$$F_{\text{Cas}}(a) = -\frac{\partial}{\partial a} E_{\text{Cas}}(a)$$

¹Strictly speaking, infinitely extended surfaces such as idealized infinitely large plates do not belong to this class, but we can always think of large but finite surfaces and then take the infinite-surface limit *after* the infinite-volume limit.

where a denotes the distance between the boundaries. This definition gives us a certain freedom in the choice of what shall be called the *Casimir interaction energy* $E_{\text{Cas}}(a)$. We define this energy as follows. For a Casimir configuration of two rigid bodies whose surfaces are denoted by S_1 and S_2 , we have

$$E_{\text{Cas}}(a) = \mathcal{E}_{V_{1+2}}(a) - \mathcal{E}_{V_1} - \mathcal{E}_{V_2}, \quad (4.11)$$

where $\mathcal{E}_{V_{1+2}}$, \mathcal{E}_{V_1} and \mathcal{E}_{V_2} are the energies (4.6) with the potentials V_{1+2} , V_1 and V_2 given in the limiting form (4.9) where $\Sigma = S_1 \cup S_2$, $\Sigma = S_1$ and $\Sigma = S_2$, respectively. As indicated in the last expression, the first term depends on the distance a and contributes to the Casimir force. Since the remaining terms do not depend on a , the way they are chosen has no influence on the Casimir force. In the present case, they are chosen in such a way that $E_{\text{Cas}}(a)$ is rendered finite, by subtracting the Casimir energy of the single bodies. This can be done for the following two reasons.

- The divergences arising in the Dirichlet limit cancel exactly in (4.11). This is due to the fact that the divergences are *localized* on the surfaces S_1 , S_2 of the physical interfaces and are *de facto* independent of a .
- The field theoretic divergences cancel exactly as well, since the bodies described by S_1 and S_2 are disconnected. This is obvious for $D = 3$, in the case $D = 4$ we have

$$\int d^4x V_{1+2}^2(x) = \int d^4x (V_1(x) + V_2(x))^2 = \int d^4x [V_1^2(x) + V_2^2(x)],$$

since the supports of the potentials V_1 and V_2 are disconnected.

We would like to stress that the definition of the interaction energy in (4.11) should not be confused with renormalization. It is a procedure for extracting exact information about the Casimir force between rigid bodies, circumventing the tedious question as to whether Casimir energy densities are locally well defined. This procedure also removes the field theoretic UV divergences. In this case, renormalization conditions which fix the counter terms do not have to be specified. These local counter terms cannot exert an influence on the Casimir force for disconnected rigid bodies anyway, because the latter is a nonlocal phenomenon. Expressed in physical terms of the QED Casimir effect: the renormalized strength of the coupling between the electromagnetic field and the electrons in the metal is, of course, important for a computation of the local energy density near a plate, but the Casimir force between two plates (see (4.3)) is independent of the electromagnetic coupling constant².

4.2.3 Worldline numerics in the sharp limit

As pointed out in the concluding remarks of the second chapter, one of the advantages of the loop cloud method is its demonstrative power, which will appear to be particularly useful when the method is applied to the study of rigid and sharp bodies. In this limit, the argument of

²This is, of course, only true in the Dirichlet limit, i.e. for idealized boundary conditions. Casimir's classic result can in fact be viewed as the limit of electromagnetic coupling $\alpha \rightarrow \infty$.


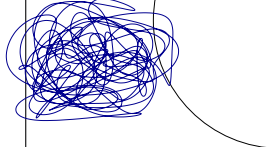

	$E_{\text{Cas}}(a)$	\mathcal{E}_{V_1}	\mathcal{E}_{V_2}
	No	Yes	Yes
	$\in]0, 1[$	Yes	Yes
	No	No	No

Figure 4.1: Three possible loop configurations and their contribution to the interaction energy $E_{\text{Cas}}(a)$ according to (4.12) (left column) and to the separate energies \mathcal{E}_{V_1} and \mathcal{E}_{V_2} of the surfaces alone (right column). The Dirichlet limit corresponds to the realization of the upper bound 1 of the interval $[0, 1]$ in which the loop contribution can vary. This renders the interaction energy in the Dirichlet limit proportional to the number of loops piercing both surfaces.

the exponential in the holonomy factor average (4.7) becomes

$$\begin{aligned}
 I_V[y(t); T, x_{\text{CM}}] &:= \int_0^1 dt V(x_{\text{CM}} + \sqrt{T}y(t)) = \lambda \int_0^1 dt \int_{\Sigma} d\sigma \delta(\sqrt{T}y(t) + (x - x_{\sigma})) \\
 &= \frac{\lambda}{\sqrt{T}} \int_{\Sigma} d\sigma \sum_{\{t_i | \sqrt{T}y(t_i) + x = x_{\sigma}\}} \frac{1}{|\dot{y}(t_i)|},
 \end{aligned}$$

where $\{t_i\}$ is the set of all points where a given scaled unit loop $\sqrt{T}y(t)$ centered upon x pierces the Casimir surface Σ at x_{σ} . If a loop does not pierce the surface (for given T and x), $I_V[y(t)] = 0$ for this loop. Of course, there are also loops that merely touch the Casimir surface but do not pierce it. For these loops, the inverse velocity $1/|\dot{y}(t_i)|$ diverges on the surface. But since this divergence occurs in the argument of an exponential function, these loops remove themselves from the ensemble average.

Let us apply this result to the calculation of the Casimir interaction energy (4.11). For a certain loop $x_0(\tau)$ corresponding to the rescaled unit loop $y_0(t)$ at the proper-time T and shifted to the center of mass x_{CM} , the contribution to the loop average of $x_0(\tau)$ is given by

$$\begin{aligned}
 \text{contrib. of } x_0(\tau) &= (W_{V_1+2}[T, x_{\text{CM}}] - 1) - (W_{V_1}[T, x_{\text{CM}}] - 1) - (W_{V_2}[T, x_{\text{CM}}] - 1) \\
 &= 1 - (e^{-TI_{V_1}} + e^{-TI_{V_2}} - e^{-TI_{V_1+2}})
 \end{aligned} \tag{4.12}$$

where the simplified notation I_{V_i} stands for $I_{V_i}[y_0(t), T, x_{\text{CM}}]$. From the previous expression, it is clear that

- loops which do not pierce any surface do not contribute to the loop average,
- loops which pierce only one of the interfaces do not contribute to the loop average, only those loops which pierce *both* surfaces contribute to the interaction energy.

The second point is clear if we note for that $I_{V_{1+2}} = I_{V_1}$ or $I_{V_{1+2}} = I_{V_2}$ for a loop which does not pierce the surface S_2 or S_1 , respectively. This was of course to be expected, since only loops which “see” both interfaces can contribute to an a -dependent Casimir energy. The situation is depicted in Fig. 4.1. We can see in (4.12) that the contribution of a loop to the interaction energy takes its value in the interval $[0, 1]$. From this and the global minus sign in (4.5), we learn that Casimir forces between rigid bodies in our scalar model are always attractive. This statement holds, independently of the shape of the bodies and the details of the potential (as long as $V(x)$ is non-negative).

Let us finally particularize to the Dirichlet limit $\lambda \rightarrow \infty$. For a contributing loop, all holonomy factors e^{-TI_V} in (4.12) vanish and the loop contributes a +1 to the loop average. As a consequence, the interaction energy for two rigid bodies in the sharp and Dirichlet limit is simply proportional to the number of loops which pierce both surfaces of the Casimir configuration. This fact contributes to an intuitive understanding of the numerical results.

4.3 Numerical results

4.3.1 Parallel plates

We consider the Casimir configuration of two rigid parallel plates separated by a distance a and located at $z = -a/2$ and $z = a/2$ orthogonal to the z axis. The potential reduces in this case to

$$V(\mathbf{x}) = \lambda[\delta(z + a/2) + \delta(z - a/2)].$$

We compare our numerical estimates with the analytically known result [BHR92] and test our numerical approach for arbitrary coupling λ and scalar mass m , which are expressed in units of the plate separation a .

Benchmark test. We will in a first step study the quality of our numerical estimates. Let us recall the two possible sources of error which we introduce when performing the worldline averages on a computer: loop discretization (2.16) and statistical average (2.14). The former is controlled by the number of points per loop N_{ppl} . This is illustrated in Fig. 4.2. In this figure, we plot the numerical estimates for the parallel plates Casimir energy per unit area in the Dirichlet limit ($\lambda \rightarrow \infty$) and for a massless scalar field as a function of the number of points per loop N_{ppl} and compare it with the analytical result, which reads³

$$E_{\text{Cas}}(a)/A = -\frac{1}{2(4\pi)^2} \frac{\pi^4}{45} \frac{1}{a^3} \simeq -\frac{1}{2(4\pi)^2} \times 2.16\dots \times \frac{1}{a^3}, \quad (4.13)$$

where A is the total surface of the plates. As is visible, the analytical result is reproduced with an error $\lesssim 0.5\%$ using $N_{\text{ppl}} \gtrsim 10^5$ for v-loops. It appears also that the only price to be paid to achieve high precision estimates is to increase the number of points per loop. Note that a systematic 1% error in the high-precision data is observed for f-loops. This is of unclear origin. On the other hand, the error bars, which witness the approximation of the exact result by the statistical average (2.14), can be controlled by tuning the number N_{lp} of loops per ensemble. It is evident from the plot that the magnitude of the error bars can

³Here and in the following, we have explicitly displayed the common proper-time prefactors $1/[2(4\pi)^{D/2}]$ for convenience (see prefactor in (4.5)).

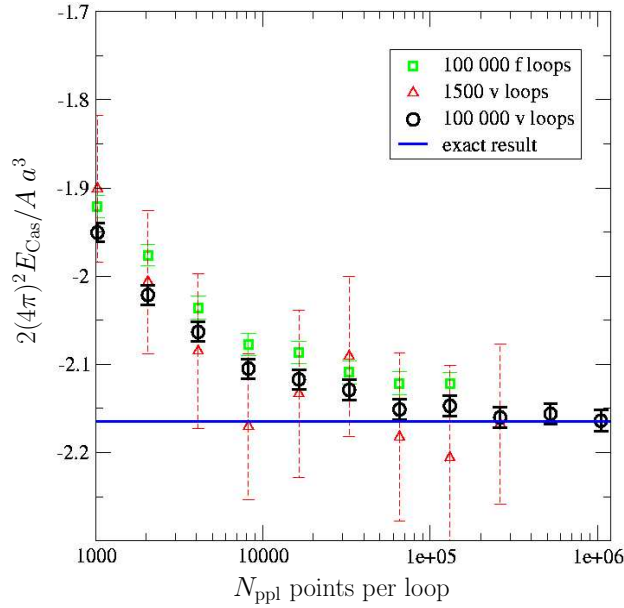


Figure 4.2: Numerical estimate of the interaction Casimir energy per unit area of the parallel-plate configuration for various loop ensembles as a function of the number of points per loop N_{pp1} . The error bars correspond to the Monte-Carlo statistical error; deviations from the exact result on top of the statistical error measure the systematic error due to loop discretization.

be reduced when increasing N_{lp} . Let us emphasize that a rather small number of several thousand points per loop and loops per ensemble ($N_{\text{pp1}}, N_{\text{lp}} \gtrsim \mathcal{O}(1000)$) are sufficient to get a numerical estimate with $\lesssim 5\%$ error (triangle curve), which means that reasonable good estimates can be obtained at a relatively low cost in CPU time. The important conclusion of this test is that worldline numerics has proved its ability to describe quantum fluctuations with Dirichlet boundary conditions quantitatively.

Beyond the Dirichlet limit. The next we can test is whether the quantitative agreement of our estimates with the analytical result holds in all coupling regimes. In Fig. 4.3, we study a wide range of couplings and the approach to the Dirichlet limit, $\lambda a \gg 1$, which is given by (4.13). The simulations are performed in the massless limit $m = 0$. As is visible in this figure, the agreement is satisfactory. Note the relative small amount of points per loop and loops per ensemble, which means that the quality of the “low cost” simulations is independent of the coupling.

Finite scalar mass. Finally, we test our numerical method in a wide range of scalar masses. In Fig. 4.4, we plot the Casimir energy per unit area as function of the dimensionless parameter ma . Let us discuss this result as function of m and a separately, when the other parameter is fixed (a and m resp.).

- a fixed. In the intermediate region, $m \simeq 1/a$, the value of the coupling $\lambda = 100m \gg 1/a$ is such that that the Dirichlet limit is approached and the curve follows the Dirichlet result (dashed line). For bigger values of the mass, i.e. $m \gg 1/a$, the interaction energy is dominated by the mass factor $e^{-m^2 T}$ in the proper-time integral. As a result, the

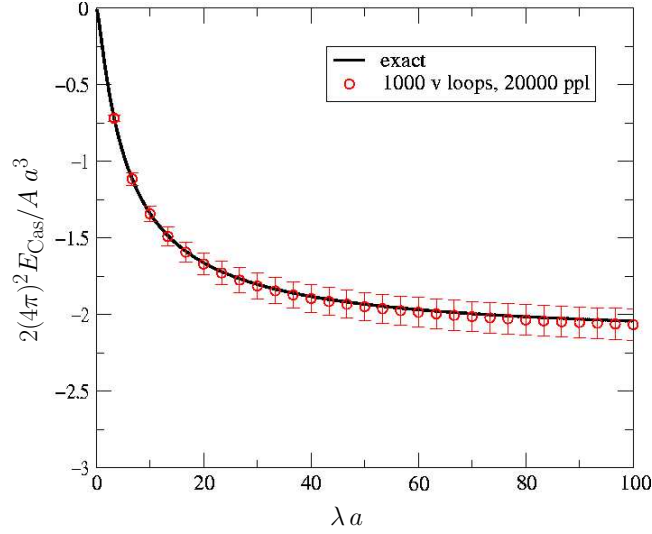


Figure 4.3: **Parallel plates:** interaction Casimir energy per unit area for the parallel-plate configuration as a function of the coupling λ (units are set by the plate separation a). The numerical estimate reproduces the exact result for a wide range of couplings including the Dirichlet limit (cf. Fig. 4.2).

energy falls exponentially for big scalar masses. On the contrary, in the small mass region, $m \ll 1/a$, the coupling is such that the interfaces become transparent to an increasing value of modes as the scalar mass is decreased. It can be also quantitatively understood by examining the contribution (4.12) for decreasing coupling.

- **m fixed.** The comment is of course identical in the intermediate region $a \simeq 1/m$, which corresponds to the Dirichlet power law $\sim 1/a^3$. For increasing a , the effect of the mass factor $e^{-m^2 T}$ is to suppress the large loops contributing precisely to the energy when the distance between the plates is large. This explains the exponential fall-off of the energy with the distance. In the small distance regime, the number of modes which fit between the plates and are beyond the plasma frequency $\omega > \omega_P \simeq \lambda$ increases as the distance decreases. This explains qualitatively why the energy turns from $\sim 1/a^3$ into a $\sim \lambda^2/a$ law [BHR92].

In any case, we see a very good agreement of the numerical estimate with the analytical result [BHR92] in a wide range of scalar masses.

4.3.2 Sphere above plate

In this section, we apply our method to the experimentally relevant Casimir configuration of a sphere above a plate. The standard analytical approach to the study of Casimir configurations with curved geometries is the proximity force approximation (PFA) [DAL56, BRST77], which we describe briefly below.

Proximity force approximation. As already mentioned, Casimir forces can be analytically computed for only a small number of rigid-body geometries among which there is the parallel-plate configuration. The classic result for the Casimir interaction energy per unit

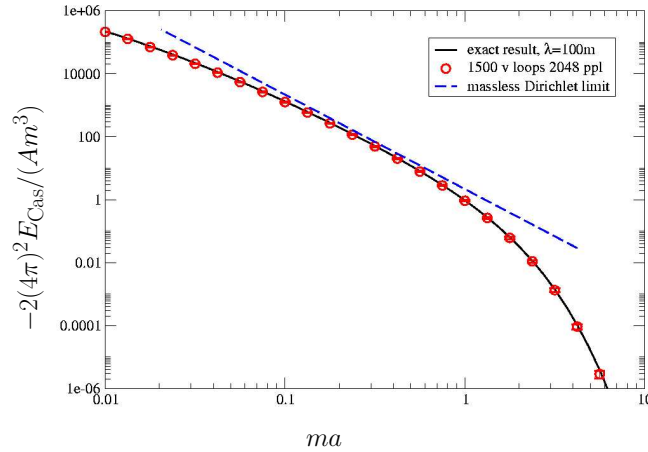


Figure 4.4: **Parallel plates:** interaction Casimir energy per unit area for the parallel-plate configuration as a function of the distance a in units of the mass m for $\lambda = 100m$. The exact result (solid line) is well reproduced by the numerical estimate over many orders of magnitude. For intermediate parameter values, the classic Casimir result (idealized Dirichlet limit (4.13), dashed line) represents a reasonable approximation.

area of perfectly conducting plates at a distance a is given by

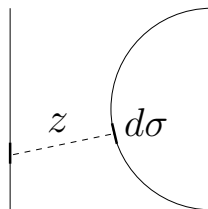
$$E_{PP}(a) = -\frac{1}{2} \frac{\pi^2}{720} \frac{1}{a^3}$$

for a fluctuating scalar field. For a complex scalar field as well as for electromagnetic fluctuations, the factor $1/2$ has to be dropped.

The basic idea of the PFA is to apply the parallel-plate result to infinitesimal bits of the generally curved surfaces and integrate them up,

$$E = \int_S E_{PP}(z) d\sigma. \quad (4.14)$$

The symbol S represents the integration domain and denotes either one of the surfaces of the interacting bodies or a suitably chosen mean surface [BRST77]. At this point, the proximity force approximation is ambiguous, and we will simply insert both surfaces in order to determine the variance. In (4.14) $d\sigma$ denotes the invariant surface measure, and z represents the separation between the two surfaces associated with the surface element $d\sigma$ on S . The distance z is here taken radial to the sphere. This is illustrated in the following figure in the case of a sphere-based integration.



To each infinitesimal bit on the sphere surface, one associates the nearest bit sitting on the plate at the distance z . The bit on the curved surface is considered to be parallel to the

plate bit and the contribution to the Casimir interaction energy is given by $E_{\text{PP}}(z)$. The contributions of each bit on the sphere are resummed by performing the surface integration (4.14). From this simple example, it appears clearly that the PFA method is based on the following two approximations:

- the PFA neglects any nonparallelity,
- the PFA neglects any non-local curvature effects.

The first point is clear from the figure, the second is due to the fact that each element on a surface is assumed to “speak” to only one surface element on the other boundary at separation z ; but curvature effects require information about a whole neighborhood of the element on the curved surface. As a consequence, the proximity force approximation is expected to give reasonable results only if

- the typical curvature radii of the surface elements is large compared to the element distance,
- the surface elements with strong nonparallelity are further separated than the more parallel ones.⁴

For configurations that do not meet the validity criteria of the proximity force approximation, a number of further approximations or improvements exist, such as an additive summation of interatomic pairwise interactions and the inclusion of screening effects of more distant layers by closer ones [MT97, Mil01, BMM01]. Though these methods have proved useful and are even quantitatively precise for a number of examples, to our knowledge, a general, unambiguous and systematically improvable recipe without *ad hoc* assumptions is still missing.

The loop cloud method at work. Beside its physical interest, the sphere-plate configuration with its relatively simple geometry provides us with a beautiful illustration of the loop cloud machinery. As we shall see, curvature effects can be understood qualitatively without any calculation simply by thinking in terms of loops and loop clouds.

In Fig. 4.5 we plot the interaction energy density along the C_∞ symmetry axis for the sphere-plate configuration in the Dirichlet limit and for a massless scalar field (data points with error bars). The radius of the sphere is equal to the distance sphere-plate, i.e. $R = a$. For comparison, the energy density in the case where the sphere is replaced by a plate is also shown (dashed line). We observe that the energy density close to the sphere is well approximated by the energy density provided by the parallel-plates scenario. Close to the plate, we see that the energy density is smaller for the sphere-plate configuration than for the plate-plate configuration. The effects due to the curved geometry become visible at a distance of $a/2$ from the sphere. This fact can easily be understood when formulated in the language of loops.

Let us recall that the energy density at a given point x_0 is obtained by averaging over loop clouds in which all loops have the common center of mass $x_{\text{CM}} = x_0$. In the figure we consider

⁴The second condition is not so well discussed in the literature; it is the reason why the proximity force approximation gives reasonable results for a convex spherical lens over a plate (convex as seen from the plate), but fails for a concave lens.

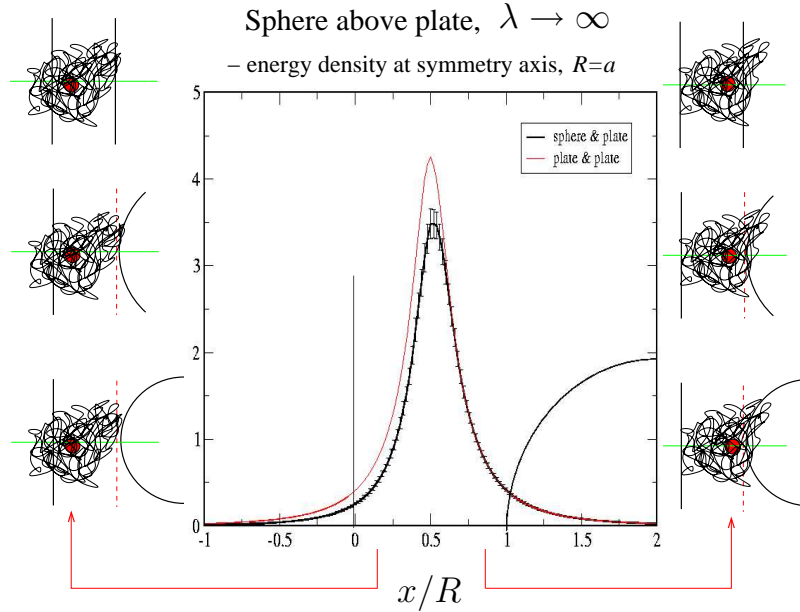


Figure 4.5: **Sphere above Plate:** interaction Casimir energy density along the symmetry axis (x axis) for the sphere-plate configuration in comparison to the parallel-plate case. Close to the sphere, the worldline loops do not “see” the curvature; but at larger distances, curvature effects enter the energy density. For illustration, the sphere-plate geometry is also sketched (thin black lines).

two points on the symmetry axis, each of them being close to one of the interfaces. In each case, we pick up a loop among the loop ensemble and represent it together with the Casimir configurations on both sides of the plot. For both points, we mimic the transition from the plate-plate configuration (top) to the sphere-plate configuration with $R = a$ (bottom) by increasing by hand the curvature of the right boundary. Remember also that the interaction energy in the Dirichlet limit is proportional to the number of loops which pierce both surfaces. At a point close to the “deformable” body⁵, we can easily see that the curvature does not play any role for a loop cloud centered at this point: the number of contributing loops is almost the same in each of the three configurations. As a consequence, the interaction energy density does not change with the curvature. On the other hand, for a loop cloud centered upon a point close to the plate, there may exist critical loops, such as depicted in the figure, which are very sensitive to a change in the curvature of the opposite boundary. For the particular loop depicted here, there exists a critical value of the curvature above which it does not contribute any more to the loop average. This explains nicely why the energy density is smaller further away from the sphere: the number of contributing loops decreases as the curvature of the distant boundary increases.

PFA vs. worldline numerics. Let us now consider the complete interaction Casimir energy for the sphere-plate configuration as a function of the sphere-plate distance a (we express all dimensionful quantities as a function of the sphere radius R). In Fig. 4.6, we plot our numerical results in the range $a/R \simeq \mathcal{O}(0.001 \dots 10)$. Since the energy varies over a wide

⁵It is deformable for this purpose only. In each of the three configurations depicted above this body is considered as rigid.

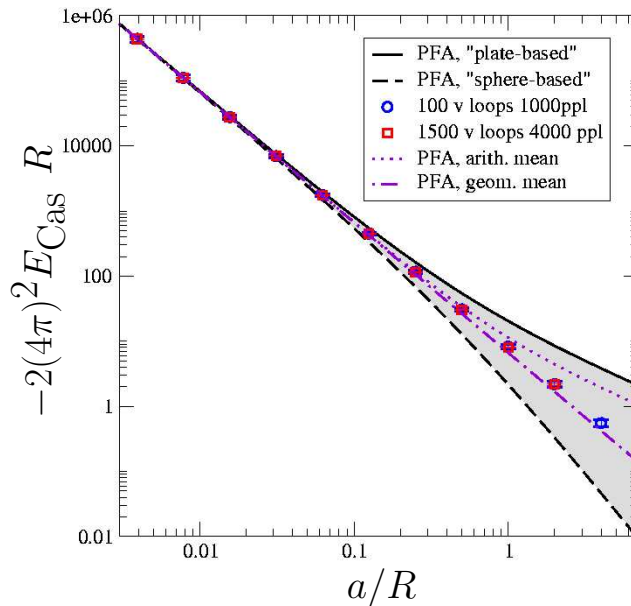


Figure 4.6: **Sphere above Plate**: logarithmic plot of the interaction Casimir energy for the sphere-plate configuration. For small separations/large spheres, $a/R \lesssim 0.02$, the proximity force approximation (PFA) approximates the numerical estimate well; but for larger a/R , curvature effects are not properly taken into account. The PFA becomes ambiguous for larger a/R , owing to possible different choices of the integration domain S in (4.14). A geometric mean (dotted-dashed line) of $S = S_{\text{plate}}$ and $S = S_{\text{sphere}}$ shows reasonable agreement with the numerical result.

range of scales, already small loop ensembles with rather large errors suffice for a satisfactory estimate (the size of the error bars of an ensemble of 1500 v loops with 4000 ppl are within the size of the plotting symbols in Fig. 4.6).

Let us compare our numerical estimate with the proximity force approximation: using the plate surface as the integration domain in (4.14), $S = S_{\text{plate}}$, we obtain the solid line in Fig. 4.6 (PFA, plate-based), corresponding to a “no-curvature” approximation. As expected, the PFA approximation agrees with our numerical result for small distances (large sphere radius). Sizable deviations from the PFA approximation of the order of a few percent occur for $a/R \simeq 0.02$ and larger. Here, the curvature-neglecting approximations are clearly no longer valid. This can be read off from Fig. 4.7, where the resulting interaction energies are normalized to the numerical result.

4.3.3 Cylinder above plate

In order to study the relation between PFA approximations and the full numerical estimate a bit further, let us consider a second example of a cylinder above a plate. Apart from the difference in the third dimension, all parameters and conventions are as before.

Again, we observe in Fig. 4.8 that the numerical estimate is well approximated by the PFA for $a/R \lesssim 0.02$, but curvature effects become important for larger distance-to-curvature-radius ratios. As in the sphere-plate case, the plate-based PFA neglects, but the cylinder-based PFA over-estimates, the curvature effects for a/R of order one.

Our results seem to suggest that the various possible choices for the integration domain in

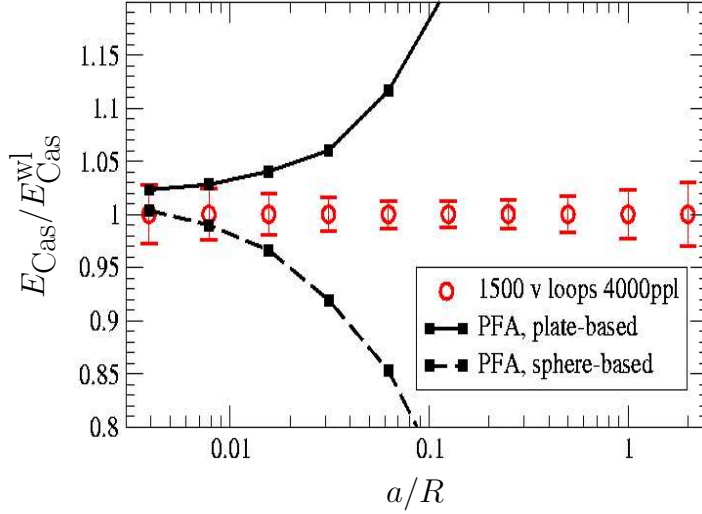


Figure 4.7: **Sphere above Plate**: interaction Casimir energies normalized to the numerical result (further conventions as in Fig. 4.6). For $a/R \gtrsim 0.02$, the fluctuation-induced curvature effects occur at the percent level.

the proximity force approximation may give upper and lower bounds for the correct answer. Indeed, the geometric mean between the two possible choices for the sphere-plate configuration is rather close to the numerical estimate (dotted-dashed line in Figs. 4.6 and 4.8). Similar positive results for the geometric mean have been found for the two-concentric-cylinder configuration [MSSvS] using semiclassical approximations [SS98, SS00] and for a “chaotic” geometry [BRST77]. However, we believe that this “agreement” beyond the strict validity limit of the PFA is accidental. First, detailed inspection reveals that the geometric mean and the numerical estimate are not fully compatible within error bars; this is particularly visible in the cylinder-plate case in Fig. 4.8. Secondly, there are no fundamental arguments favoring the geometric mean; by contrast, the arithmetic mean (as well as the quadratic mean) are not good approximations. Thirdly, for even larger separations, $a/R \rightarrow \infty$, it is known that the interaction Casimir energy in the sphere-plate case behaves as $\sim R^3/a^4$ [DF81], whereas even the sphere-based PFA decreases only with $\sim R^2/a^3$. From the viewpoint of the worldline, it is obvious anyway that true fluctuation-induced curvature effects cannot be taken into account by PFA-like arguments. Nevertheless, the geometric-mean prescription may yield a reasonable first guess for Casimir forces in a parameter range beyond the formal validity bounds of the PFA where the expansion parameter is maximally of order one.

4.4 Summary and outlook

In this chapter, we have applied the loop cloud method discussed in chapter 2 to the study of the Casimir effect. This approach is based on quantum field theoretic techniques where the Casimir energy is accessed via the effective action formulated in the worldline formalism and an external potential mimics the interaction between the fluctuating field and the boundary matter. This differs from the standard approach where the presence of the boundaries is taken into account by imposing *ab initio* boundary conditions on the fluctuating field. In the field theoretic language, this corresponds to the sharp limit, where the boundaries are

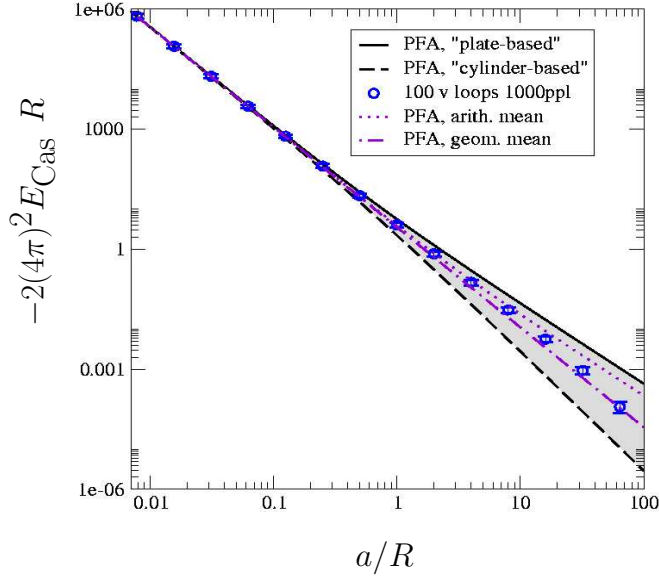


Figure 4.8: **Cylinder above Plate**: logarithmic plot of the interaction Casimir energy for the sphere-plate configuration (cf. Fig. 4.6).

modelled by δ -like potentials, and to the limit of infinite coupling. These conditions induce the occurrence of infinities in the Casimir energy which are not of field theoretic origin and may not be removed in a physically meaningful way. The problem can however be bypassed if the Casimir force between rigid bodies is considered, for which a computation of the interaction energy suffices and explicit renormalization is not needed.

In this work, we have focused on the computation of the Casimir interaction energy between rigid bodies induced by the fluctuations of a real scalar field. The study of the classic and analytically well known plate-plate configuration has been performed as a test of our numerical approach. It has been tested relatively to the loop parameters, N_{ppl} and N_{lp} , which have been found to be the only parameters to be adjusted for higher precision, as well as to the external parameters, i.e. coupling and scalar mass. In the sphere-plate configuration, we have compared our numerical estimates with the results provided by the proximity force approximation. Using the geometry independence which characterises the loop cloud method, we were able to study the usually neglected nonlocal curvature effects which become sizable for a distance-to-curvature-radius ratio of $a/R \gtrsim 0.02$. We found (accidental) agreement between our numerical estimate and the PFA with a “geometric-mean prescription”: the latter implies a geometric mean over the possible choices of surface integration in (4.14). This geometric mean PFA might provide for a first guess of the Casimir force for a/R of order one, but has to be treated with strong reservations.

There remains of course a lot of space for further investigations. Some generalizations to more realistic systems are straightforward.

- In this work, we have confined ourselves to the modeling of Casimir boundaries by δ potentials. This is not really a simplification. A Casimir configuration modelled by finite and smooth potential is more realistic and numerically less demanding, since it requires worldline ensembles with a much smaller number of points per loop.

- Finite temperature effects can be taken into account from first principles by combining the worldline formalism with the Matsubara formulation. In this case, the worldlines satisfy boundary conditions in Euclidean time direction and the time integral transforms into a sum over the loop winding number [GL01].
- The geometry independence of the method can be used to study more realistic surface profiles, like for instance corrugated plates [Emi03]. Surface roughness can be accounted for by adding a characteristic random “noise” to the local support of the potential.
- The Casimir force can also be computed by performing the differentiation with respect to the distance first analytically and afterwards performing the loop averages relatively to the new expression. This remark also applies to the energy-momentum tensor, which is obtained from the effective action by differentiating it with respect to the metric.
- Radiative corrections to the Casimir effect can also be included in our method, employing the higher-loop techniques of the worldline approach [Sch01]. We expect these computations to be numerically more demanding, since more integrations are necessary, but the general framework remains the same.

Let us finally emphasize that a further step towards the simulation of the real Casimir effect, i.e. the implementation of the worldline numerics for a fluctuating electromagnetic field, is still to be achieved. This is not due to some numerical obstacle, which renders the method non practicable, but to the lack of a field theoretic formulation of the interaction between the electromagnetic field and the Casimir boundaries. The starting point can be a field theoretic Lagrangian defining a model for this interaction as suggested, e.g., in [FS70]. Although these Lagrangians are generally not renormalizable, one may expect that the dispersive properties of the bodies provide for a physical ultraviolet cutoff (although this has to be studied with great care [Bar02, SF02]).

Bibliography

- [Bar02] G. Barton. *Int.J.Mod.Phys.A*, 17:767, 2002.
- [BHR92] M. Bordag, D. Hennig, and D. Robaschik. Vacuum energy in quantum field theory with external potentials concentrated on planes. *J. Phys.*, A25:4483–4498, 1992.
- [BK92] Zvi Bern and David A. Kosower. The Computation of loop amplitudes in gauge theories. *Nucl. Phys.*, B379:451–561, 1992.
- [BM58] G.E.P. Box and M.E. Mueller. *Ann. Math. Stat.*, 29:610, 1958.
- [BMM01] M. Bordag, U. Mohideen, and V. M. Mostepanenko. New developments in the Casimir effect. *Phys. Rept.*, 353:1–205, 2001.
- [BRST77] J. Blocki, J. Randrup, W.J. Swiatecki, and C.F. Tsang. Proximity Forces. *Ann.Phys.(N.Y.)*, 105:427, 1977.
- [CAK⁺01] H.B. Chan, V.A. Aksyuk, R.N. Kleiman, D.J. Bishop, and F. Capasso. *Science*, 291:1941, 2001.
- [Cas48] H. B. G. Casimir. On the attraction between two perfectly conducting plates. *Kon. Ned. Akad. Wetensch. Proc.*, 51:793–795, 1948.
- [CDD95] Daniel Cangemi, Eric D’Hoker, and Gerald V. Dunne. Derivative expansion of the effective action and vacuum instability for QED in (2+1)-dimensions. *Phys. Rev.*, D51:2513–2516, 1995.
- [CN97] G.W. Crabtree and D.R. Nelson. *Physics Today*, 50:38, 1997.
- [DAL56] B.V. Derjaguin, I.I. Abrikosova, and E.M. Lifshitz. *Q.Rev.*, 10:295, 1956.
- [DDFG⁺98] L. Del Debbio, M. Faber, J. Giedt, J. Greensite, and S. Olejnik. Detection of center vortices in the lattice Yang-Mills vacuum. *Phys. Rev.*, D58:094501, 1998.
- [DDFGO97] L. Del Debbio, M. Faber, J. Greensite, and S. Olejnik. Some cautionary remarks on Abelian projection and Abelian dominance. *Nucl. Phys. Proc. Suppl.*, 53:141–147, 1997.
- [DF81] T. Datta and L.H. Ford. *Phys.Lett.A*, 83:314, 1981.
- [DR85] W. Dittrich and M. Reuter. *Effective Lagrangians in quantum electrodynamics*. Springer-Verlag, Berlin, 1985.

- [Emi03] Thorsten Emig. Casimir Forces: An Exact Approach for Periodically Deformed Objects. *Europhys. Lett.*, 62:466–472, 2003.
- [Fry96] M. P. Fry. QED in inhomogeneous magnetic fields. *Phys. Rev.*, D54:6444–6452, 1996.
- [FS70] G. Feinberg and J. Sucher. *Phys.Rev.A*, 2:2395–2415, 1970.
- [G⁺04] N. Graham et al. The Dirichlet Casimir problem. *Nucl. Phys.*, B677:379–404, 2004.
- [GJK⁺02] N. Graham, R.L. Jaffe, V. Khemani, M. Quandt, M. Scandurra, and H. Weigel. Calculating vacuum energies in renormalizable quantum field theories: A new approach to the Casimir problem. *Nucl. Phys.*, B645:49–84, 2002.
- [GJK⁺03] N. Graham, R.L. Jaffe, V. Khemani, M. Quandt, M. Scandurra, and H. Weigel. Casimir energies in light of quantum field theory. *Phys. Lett.*, B572:196–201, 2003.
- [GL01] Holger Gies and Kurt Langfeld. Quantum diffusion of magnetic fields in a numerical worldline approach. *Nucl. Phys.*, B613:353–365, 2001.
- [GL02] Holger Gies and Kurt Langfeld. Loops and loop clouds: A numerical approach to the worldline formalism in QED. *Int. J. Mod. Phys.*, A17:966–978, 2002.
- [GLM] Holger Gies, Kurt Langfeld, and Laurent Moyaerts. in preparation.
- [Gre03] J. Greensite. The confinement problem in lattice gauge theory. *Prog. Part. Nucl. Phys.*, 51:1, 2003.
- [GS99] V. P. Gusynin and I. A. Shovkovy. Derivative expansion of the effective action for QED in 2+1 and 3+1 dimensions. *J. Math. Phys.*, 40:5406–5439, 1999.
- [HE36] W. Heisenberg and H. Euler. Konsequenzen der Dirac’schen Theorie des Positrons. *Z. Phys.*, 98:714–732, 1936.
- [ID89] C. Itzykson and J.M. Drouffe. *Statistical Field Theory*. Cambridge Univ. Pr., 1989.
- [IZ80] C. Itzykson and J.B. Zuber. *Quantum Field Theory*, chapter 4.3. McGraw-Hill, 1980.
- [Jaf] Robert L. Jaffe. Unnatural acts: Unphysical consequences of imposing boundary conditions on quantum fields. hep-th/0307014.
- [KK91] I. A. Korchemskaya and G. P. Korchemsky. Polyakov spin factor, Berry phase and random walk of spinning particles. *J. Phys.*, A24:4511–4526, 1991.
- [Kle95] H. Kleinert. *Path Integrals in Quantum Mechanics, Statistics and Polymer Physics*. World Scientific Pub Co, 2nd edition (1995).
- [LMG02] Kurt Langfeld, Laurent Moyaerts, and Holger Gies. Fermion-induced quantum action of vortex systems. *Nucl. Phys.*, B646:158–180, 2002.

- [LRT98] Kurt Langfeld, Hugo Reinhardt, and Oliver Tennert. Confinement and scaling of the vortex vacuum of SU(2) lattice gauge theory. *Phys. Lett.*, B419:317–321, 1998.
- [Mil] Kimball A. Milton. The Casimir effect: Recent controversies and progress. *hep-th/0406024*.
- [Mil01] K.A. Milton. *The Casimir Effect : Physical Manifestations Of Zero-Point Energy*. World Scientific, 2001.
- [MR98] U. Mohideen and A. Roy. Precision Measurement of the Casimir Force from 0.1 to 0.9 microns. *Phys.Rev.Lett.*, 81, 1998.
- [MSSvS] Francisco D. Mazzitelli, Maria J. Sanchez, Norberto N. Scoccola, and Javier von Stecher. Casimir interaction between two concentric cylinders: exact versus semiclassical results. *quant-ph/0209097*.
- [MT97] V.M. Mostepanenko and M.M. Trunov. *The Casimir Effect and its Application*. Clarendon Press, Oxford, 1997.
- [Pas01] Pavlos Pasipoularides. Fermion-induced effective action in the presence of a static inhomogeneous magnetic field. *Phys. Rev.*, D64:105011, 2001.
- [PFTV] W.H. Press, B.P. Flannery, S.A. Teukolsky, and W.T. Vetterlink. *Numerical Recipes in Fortran*. Cambridge university Press.
- [PG90] R.E. Prange and S.M. Girvin. *The Quantum Hall Effect*. Springer Verlag, 1990.
- [PS] Michael E. Peskin and D. V. Schroeder. An introduction to quantum field theory. Reading, USA: Addison-Wesley (1995) 842 p.
- [Sam79] Stuart Samuel. Topological Symmetry Breakdown and Quark Confinement. *Nucl. Phys.*, B154:62, 1979.
- [Sch51] Julian S. Schwinger. On gauge invariance and vacuum polarization. *Phys. Rev.*, 82:664–679, 1951.
- [Sch01] Christian Schubert. Perturbative quantum field theory in the string-inspired formalism. *Phys. Rept.*, 355:73–234, 2001.
- [SF02] V. Sopova and L. H. Ford. The Energy Density in the Casimir Effect. *Phys. Rev.*, D66:045026, 2002.
- [SS] Michael G. Schmidt and Ion-Olimpiu Stamatescu. Determinant calculations with random walk worldline loops. *hep-lat/0201002*.
- [SS98] M. Schaden and L. Spruch. *Phys.Rev.A*, 58:935, 1998.
- [SS00] M. Schaden and L. Spruch. *Phys.Rev.Lett.*, 84:459, 2000.
- [Str92] Matthew J. Strassler. Field theory without Feynman diagrams: One loop effective actions. *Nucl. Phys.*, B385:145–184, 1992.

Part II

Lattice $SU(2)$ Yang-Mills Theory in Coulomb Gauge

Chapter 5

Introduction

Quantum Field Theories (QFT) build nowadays a standard framework for the theoretical description of nature at atomic and subatomic scales. With the invention of quantum mechanics, the classical description of a particle as an object of defined extension at a defined location, whose dynamics is governed by Newton's law, was abandoned in favour of the concept of wave packets. In a second step, historically called "second quantization", the quantization of field theories provided a way to describe the fundamental interactions taking place between elementary particles. In the QFT language, a *field* acts as an operator on the vacuum to create a *quantum*, i.e. a wave packet, in space-time. At the dynamical level, interaction processes between elementary particles is seen in terms of creations and annihilations of wave packets operated by quantum fields. The two most prominent quantum field theories in modern particle physics are the Glashow-Salam-Weinberg Model of electroweak interactions, which succeeded in providing a unified description of the electromagnetic and weak interactions, and Quantum Chromo Dynamics (QCD), which describes the strong interaction. They build together the so-called Standard Model of elementary particle physics.

A milestone in the history of the field theoretic description of physical phenomena is certainly the formulation by Maxwell at the end of the 19th century of a unified theory of electricity and magnetism. A remarkable feature of Maxwell's formulation is its property of *gauge invariance*: a local redefinition of the electric and magnetic potentials does not affect the laws of electromagnetism. In the context of QFT, this property is crucial in the sense that it permits to embed the description of matter and the description of interaction into a single quantum field theory. Quantum Electro Dynamics (QED) results for instance from the unification of Maxwell theory on the one hand and Dirac's quantum theory of the electron on the other hand, rendered possible precisely due to the property of gauge invariance. This property is so crucial that gauge symmetry is considered as fundamental and postulated as principle from which a quantum field theory describing interacting matter is derived. The construction of an interacting quantum field theory from the gauge principle was initiated by Yang and Mills in the fifties and is also at the base of the field theories building the Standard Model.

QCD was invented in the late sixties, after it was established, theoretically and experimentally, that a quark field of a given flavour (u, d or s) possesses an additional internal degree of freedom, comparable to the electric charge and called *colour*, which can take *three* possible values (red, blue and green). Using the gauge principle, the QCD Lagrangian results from the theory of free quarks (Dirac Lagrangian) by postulating the invariance of the theory

under a local gauge transformation of the quark field in colour space. From a mathematical point of view, the gauge transformation is represented by a matrix belonging to the *gauge group* $SU(3)$. This process introduces, besides the quarks, additional degrees of freedom, the *gluons*, which are responsible in QCD for the transmission of the strong interaction between the quarks, like the photons transmit the electromagnetic interaction in QED. The gluon field, which emerges as a byproduct of the gauge principle, is also called *gauge field*. The mathematical properties of the gauge group do not only permit to distinguish QED, gauge theory of group $U(1)$, from QCD, gauge theory of group $SU(3)$, but also have crucial implications at the physical level. Among them, the *non-Abelian* character of the gauge group, i.e. non-commutativity of the group matrices, implies in QCD a *gluonic self-interaction*, whereas the photons in the Abelian QED do not interact among themselves. This fact implies in particular the property of *asymptotic freedom*: at high momentum transfers, i.e. small distances, the quark-gluon coupling becomes small. This property can be schematised by comparing the properties in the vacuum of colour and electric charges, which measure the strength of the quark-gluon and electron-photon interactions, respectively. Whereas the electric charge is at big distances screened due to vacuum polarization, i.e. the effective charge decreases as the distance from the charge increases, the inverse effect, *anti-screening*, is observed for the colour charge in QCD, due to the self-interacting property of the gluons. Asymptotic freedom renders perturbation theory applicable to the high energy regime, also called Ultra-violet (UV) regime, and allows for the comparison of QCD to experiments performed at high momentum transfer. The agreement of the predictions of perturbation theory with numerous high energy collision experiments (see e.g. [ESW96]) supports nowadays the belief that QCD is the correct theory of strong interaction. On the other hand, the study of QCD in the low energy regime, often called Infrared (IR) regime, requires the implementation of *non-perturbative methods* of calculation.

One of the most prominent phenomenon characterizing the IR regime of QCD is that of *colour confinement*, the fact that coloured objects (quarks and gluons) are not observed in nature as separate entities but rather in colour neutral compounds of quark and gluons, e.g. mesons, baryons or glueballs. If QCD is indeed the correct theory of strong interaction, this phenomenon has to be explained from first principles. This has since its invention not yet been solved and is still nowadays one of the most challenging problem for field theorists. The problem of colour confinement has been the object of numerous investigations in the recent years, especially in the framework of lattice gauge theory (LGT). This technique, based on the simulation of QCD on a latticized space-time, covers all non-perturbative effects and, in particular, bears witness of quark confinement. Moreover, this approach has been able to provide *confinement mechanisms* by identifying among the field fluctuations, using some projection techniques, the degrees of freedom responsible for the confining property of QCD. In particular, lattice simulations indicate that confinement is produced by condensation of chromomagnetic *monopoles* in the vacuum, suggesting that this vacuum behaves like a dual superconductor, i.e. for which the roles of electric and magnetic fields are inversed (see e.g. [DGLMP00]). Another mechanism is provided by center projection techniques, which suggest that confinement arises from the percolation of *center vortices* in the vacuum. These special gauge field configurations are singular magnetic potentials sitting on closed sheets in space-time (for a review, see [Gre03]), which can be identified and removed from the ensemble of configurations. It has been shown that a vacuum without its vortex content loses its confining property [DDFGO]. A serious limitation of the lattice approach to QCD

is, despite numerous attempts, the lack of a satisfying implementation of dynamical (light) quarks. At the present stage, systems at finite baryon densities are hardly accessible in the realistic case of a $SU(3)$ gauge group. The above confinement mechanisms are in fact obtained by simulating the pure gluonic part, also called *Yang-Mills* part, of the QCD action. In this so-called *quenched approximation*, the effects induced by dynamical quarks are *de facto* neglected. Quark confinement can in this approach nevertheless be investigated, since the (non-relativistic) potential of two static heavy quarks in the vacuum can be extracted from the *Wilson loop*, an operator depending on gluonic degrees of freedom only. Moreover, some simulations are performed with respect to the gauge group $SU(2)$, i.e. considering a two-colour QCD. This is justified by the fact that the non-Abelian character of the gauge group is much more relevant for the physical properties than the number of colours itself, and at the practical level by a reduction of the numerical burden.

Besides LGT, there exist non-perturbative techniques formulated in continuous space-time, like *Dyson-Schwinger equations* (DSE). The DSE approach addresses the exact field correlation functions, or *Green functions*, of a quantum field theory (for a review, see [RW94]). In particular, information in relation to the confinement problem is encoded in the basis correlation functions, the *propagators*, which describe the propagation in space-time of the elementary fields [AvS01, AFvS03]. In contrast to LGT, it can deal with dynamical quarks and can furthermore be used to study hadron phenomenology [MR03]. The disadvantage of the DSE approach is that it deals with an infinite system of coupled integral equations for the correlation functions, which has to be truncated in order to provide a practicable computational framework. This approximation is very difficult to control and to improve systematically and, in this respect, lattice investigations of elementary propagators can provide interesting information about the impact of truncation schemes [LRG02]. This example shows how the study of QCD benefits of complementary approaches of the same problem. Among other non-perturbative approaches in continuous space-time, the *Hamilton picture* investigates QCD from a quantum mechanical point of view. Quarks and gluons are represented by a *wave functional* of the gluon and quark fields, solution of a functional Schrödinger equation. By means of variational techniques, the elementary propagators can be calculated analytically via a system of coupled integral equations, whose closeness requires as in DSE a truncation scheme.

The present work concerns a further scenario of quark confinement, based on the study of the Yang-Mills part of the QCD action in the *Coulomb gauge* formulation. The quantization procedure of a gauge theory, like QCD, requires the implementation of an additional condition on the gluonic field, called *gauge fixing*. Physics does of course not depend on the choice made for the gauge condition, due to the gauge invariance of the theory. Among the possible gauge fixing procedures, *Landau gauge* is the most usual formulation of QCD. It imposes transversality of the gluon field in space-time and possesses many practical advantages: it preserves the Lorentz invariance of the theory, gives rise to simple Feynman rules and in the framework of DSE allows for simple ansätze in the truncation of the equation tower. On the contrary, Coulomb gauge enforces transversality of the gluon field in space only and breaks therefore Lorentz invariance explicitly, giving rise to cumbersome calculations in perturbation theory. For this reason, the Coulomb gauge formulation stayed “behind the scene” for many years. A crucial feature renders however Coulomb gauge very attractive in relation to the problem of quark confinement: it provides a direct access to the Coulomb potential of two static coloured charges, equivalent to the Coulomb electric potential between two charged

particles in Maxwell theory. The first suggestion of a confinement scenario in Coulomb gauge was originally made by Gribov in the late seventies [Gri78]. Gribov pointed out a weakness of the Landau and Coulomb gauge conditions: there exist gluon field configurations satisfying the transversality condition, which can be transformed into each other by means of gauge transformations. Trying to get rid of these “gauge copies”, nowadays called *Gribov copies*, Gribov proposed to restrict the space of the gluon field configurations to the *Gribov region*, a domain of the configuration space which he hoped to be free of copies. The geometrical and topological aspects of the configuration space have since then been the object of rigorous mathematical investigations [Zwa94, SvBZ03] and the original statement of Gribov refined, but his idea of a confinement mechanism remained actual: the confining property of the Coulomb potential can be explained by gluon field configurations sitting near the border of the Gribov region, called *Gribov horizon*, which produce an enhancement of the potential at large scales. It was shown recently [GOZ04] that the scenarios based on the dominance of center vortices or magnetic monopoles in the confining properties of the QCD vacuum are compatible with Gribov’s scenario. The interest for the Coulomb gauge formulation has grown in recent years and is the object of actual investigations in LGT [CZ02a, CZ03, GOZ04] as well as in the Hamilton picture [SS02, FRa]. In this work, we propose a study on the lattice of the pure Yang-Mills theory formulated in Coulomb gauge and a confrontation of the results with the most recent investigations performed in the Hamilton picture [FRa].

The first chapter is devoted to a theoretical overview of the Coulomb gauge formulation of Yang-Mills theory. In a first step, a detailed description of the quantization procedure, in the light of Dirac’s quantization procedure for constrained systems, will lead to the derivation of the colour Coulomb potential. We will see in particular how the restriction to “physical” gluons, i.e. transverse polarized gluons imposed by the transversality condition of the Coulomb gauge, induces in a natural way an explicit Coulomb interaction term in the Yang-Mills Hamiltonian. This term contains the *Faddeev-Popov operator*, which plays a crucial role in the confining property of the Coulomb potential. In a second step, the notions of Gribov region and Gribov horizon will be defined in terms of the Faddeev-Popov operator and their relation to quark confinement problem considered, providing Gribov’s scenario.

Our lattice study of Coulomb gauge is discussed in the second chapter. For those readers who are not familiar with the lattice formulation of gauge theories, we briefly review the basic concepts of LGT. We proceed with a detailed description of the gauge fixing procedure used in our simulations. In particular, we handle the problem of Gribov copies by means of a simulated annealing algorithm. The last part of the chapter is devoted to the presentation and discussion of the numerical results. In relation to the confinement scenario, we investigate the ghost propagator, i.e. the expectation value of the inverse Faddeev-Popov operator, and the Coulomb potential in three and four dimensions for different lattice volumes and compare our estimates with the results obtained in the Hamilton framework. The study in three dimensions will reveal a satisfactory agreement between the two approaches for the ghost propagator and the Coulomb potential, whereas significant discrepancies will be observed in the four dimensional case. Our numerical estimates of these quantities provide in three and four dimensions a picture compatible with a linear confining interaction. We study also gluonic correlations by measuring the equal-time transverse gluon propagator, whose inverse is generally interpreted as an energy dispersion relation for the gluonic fields. Our results for the gluon propagator at fixed time will reveal a striking but interesting feature of the numerical study of gluonic correlations at equal-time: the instantaneous gluon propagator shows in

three and four dimensions an anomalous behaviour in the perturbative regime, which seems to be incompatible with asymptotic freedom. The reasons for which this anomaly occurs are still under debate and will be the object of investigations in the next future.

Chapter 6

Yang-Mills theory in Coulomb gauge

This chapter is devoted to the formulation of Yang-Mills theory in the Coulomb gauge approach and its relation to the problem of colour confinement. In a first part, we show, through a precise description of the quantization procedure, how Coulomb gauge provides in an elegant way access to the Coulomb potential of colour charges. In order to disentangle the general aspects of a gauge theory, specific to the gauge symmetry itself, from features specific to the mathematical structure of the gauge group, we illustrate the quantization procedure of gauge theories in the light of simple systems: the quantization of a non-relativistic mechanical problem will give the opportunity to introduce briefly the Dirac quantization procedure of constrained systems, which we transpose afterwards in the field theoretic context of Maxwell theory. We then turn to Yang-Mills theory and derive the Coulomb gauge Yang-Mills Hamiltonian. The second part is devoted to the properties of the Coulomb gauge approach. We will in particular focus on the problem of gauge copies (Gribov problem) and its interesting relation to the confinement of colour charges, in terms of Gribov's confinement scenario. In order to avoid any confusion, we will also carefully distinguish the Coulomb potential from the more conventional gauge invariant Wilson potential.

Quantization of gauge theories cannot be achieved by means of standard procedures. Let us for instance consider the Maxwell theory of electromagnetism. The Lagrangian density defining this field theory is given by

$$\mathcal{L} = -\frac{1}{4}F_{\mu\nu}F^{\mu\nu} + g_0 A_\mu j^\mu, \quad (6.1)$$

where the four-current $j^\mu = (\rho, \mathbf{j})$ is a function of the matter fields. We compute the conjugated momentum fields:

$$\Pi_\mu = \frac{\partial \mathcal{L}}{\partial(\partial_0 A^\mu)}.$$

They read explicitly

$$\Pi^0 = 0, \quad (6.2)$$

$$\Pi^i = F^{i0}. \quad (6.3)$$

Following usual rules of quantization¹, we should set

$$[\hat{A}_\mu(\mathbf{x}, t), \hat{\Pi}^\nu(\mathbf{y}, t)] = i\delta_\mu^\nu \delta^{(3)}(\mathbf{x} - \mathbf{y}),$$

which is not compatible with the constraint (6.2). It appears necessary to introduce modified rules which take the presence of constraints into account. Such a procedure belongs to the more general quantization of constrained systems, developed by Dirac [Dir64].

Conventions. Throughout this chapter, we work in $D = 3 + 1$ dimensions and use the “continuum conventions” of Appendix B. The Yang-Mills theory is addressed with respect to the gauge group $SU(N)$.

6.1 Quantization of constrained systems

Let us leave field theory for a moment and illustrate the quantization of systems with constraints in the light of a simple mechanical example.

Our starting point is the following mechanical problem [CL80]:

$$L = \frac{1}{2}(\dot{x}^2 + \dot{y}^2) - (x\dot{y} - y\dot{x})q + \frac{1}{2}q^2r^2 - V(r).$$

As usual, the dot denotes the time derivative and $r = \sqrt{x^2 + y^2}$. Except for the term $\frac{1}{2}q^2r^2$, this Lagrangian describes a non-relativistic charged particle in the central potential $V(r)$ and under the influence of an external magnetic field $q(t)$, which we treat as a dynamical degree of freedom. In terms of the polar coordinates $x = r \cos \theta$ and $y = r \sin \theta$, the Lagrangian reads

$$L = \frac{1}{2}[\dot{r}^2 + r^2(\dot{\theta} - q)^2] - V(r).$$

Let us point out the invariance of L under the following transformations

$$\theta \rightarrow \theta + \varepsilon(t), \tag{6.4}$$

$$q \rightarrow q + \dot{\varepsilon}(t). \tag{6.5}$$

We consider separately the canonical and path integral quantization schemes.

6.1.1 Canonical quantization

Computing the conjugated momenta gives

$$p_r = \dot{r}, \quad p_\theta = r^2(\dot{\theta} - q), \quad p_q = 0 \tag{6.6}$$

and usual rules enforce the following commutation relations

$$[\hat{\theta}, \hat{p}_\theta] = [\hat{r}, \hat{p}_r] = [\hat{q}, \hat{p}_q] = i. \tag{6.7}$$

First, the last commutator is manifestly incompatible with the *primary constraint* $p_q = 0$ in (6.6). Second, the velocity \dot{q} cannot be eliminated because of this constraint and the

¹In the following, \hat{O} denotes the quantum operator associated to the quantity O .

Legendre transformation leading to the Hamiltonian cannot be performed. A way to bypass this problem is to let this velocity unfixed and perform the Legendre transformation with the unknown parameter $\lambda = \dot{q}$. The Hamiltonian reads in this case

$$H_\lambda = \frac{1}{2}p_r^2 + \frac{1}{2r^2}p_\theta^2 + p_\theta q + V(r) + \lambda p_q.$$

The task to be done before proceeding with the quantization of the theory is to remove the indetermination by eliminating λ .

In a first step, we derive a *secondary constraint* by demanding that the constraint $p_q = 0$ in (6.6) holds at all times:

$$\{p_q, H_\lambda\}_P = 0 \Rightarrow p_\theta = 0 \quad (6.8)$$

where $\{\dots\}_P$ denotes the Poisson bracket. Proceeding with the stability condition of the secondary constraint and so on, a chain of secondary constraints is obtained, which possibly leads to the elimination of λ . The constraint chain

$$p_q = 0 \Rightarrow p_\theta = 0 \Rightarrow 0 = 0 \quad (6.9)$$

obtained in our example furnishes no conditions on λ . This fact is typical for a *gauge theory* and its origin is to be found in the invariance of the Lagrangian under the *gauge transformations* (6.4) and (6.5). In such a case, we have to *fix the gauge*, i.e. eliminate the arbitrariness by hand, by imposing a further condition on θ or q or by directly fixing λ .

Fixing θ . Let us for instance choose $\theta = 0$. This condition must be satisfied at all times, i.e. the stability condition of the new constraint, i.e. $\{\theta, H_\lambda\}_P = 0$, must hold. We derive in this way a new chain of secondary constraints:

$$\theta = 0 \Rightarrow q = 0 \Rightarrow \lambda = 0. \quad (6.10)$$

The gauge fixing procedure provides a condition on λ and the theory can be quantized.

We leave our example for a moment and describe the quantization procedure at a more general level. Let us denote the ensemble of all constraints, i.e. primary and secondary constraints, gauge condition and its stability conditions by $\{\varphi_\alpha\}$. The maximal ensemble of constraints $\{\phi_\alpha\} \subseteq \{\varphi_\alpha\}$ for which the matrix of the Poisson brackets

$$C_{ij} = \{\phi_i, \phi_j\}_P$$

is non-singular is called *second-class* ensemble. To any dynamical variable (coordinate or momentum) A , let us associate the *first-class* quantity A' defined by

$$A' = A - \{A, \phi_m\}_P C_{mn}^{-1} \phi_n. \quad (6.11)$$

We justify the introduction of this quantity by pointing out that

$$\{A', \phi_i\}_P = 0,$$

i.e. A' is compatible with all constraints of the second-class ensemble. For any variables A and B , we define the *Dirac bracket* $\{\dots\}_D$ by

$$\{A, B\}_D := \{A', B'\}_P, \quad \{A', B'\}_P = \{A, B\}_P - \{A, \phi_m\}_P C_{mn}^{-1} \{\phi_n, B\}_P,$$

which is compatible with all constraints of the second-class ensemble. The quantization of the theory is performed by *replacing the Dirac bracket by the commutator*, i.e.

$$\{A, B\}_D \rightarrow -i[\hat{A}, \hat{B}], \quad (6.12)$$

and *setting to zero all constraints of the second-class ensemble* in the Hamiltonian.

We return to our example and illustrate the Dirac quantization procedure. If we choose $\phi_1 = p_q$, $\phi_2 = p_\theta$, $\phi_3 = \theta$ and $\phi_4 = q$ the matrix C reads

$$C = \begin{pmatrix} 0 & 0 & 0 & -1 \\ 0 & 0 & -1 & 0 \\ 0 & 1 & 0 & 0 \\ 1 & 0 & 0 & 0 \end{pmatrix}$$

and we see that all constraints build a second-class ensemble. In the classification of gauge conditions, a procedure leading to $\{\phi_\alpha\} \equiv \{\varphi_\alpha\}$ belongs to the *class I type* of gauge conditions. The computation of the Dirac brackets is straightforward and gives

$$\{\theta, p_\theta\}_D = \{q, p_q\}_D = 0, \quad \{r, p_r\}_D = \{r, p_r\}_P,$$

which are compatible with the constraints. The theory is quantized by replacing $\{r, p_r\}_D \rightarrow -i[\hat{r}, \hat{p}_r]$ and setting all constraints to zero in the Hamiltonian:

$$H = \frac{1}{2}p_x^2 + V(x).$$

[Note: in order to get the correct spectrum of H , it is important not to treat x as a Cartesian coordinate; \hat{p}_x^2 is the operator $-\frac{1}{x}\frac{d}{dx}(x\frac{d}{dx})$.]

Fixing q . Let us choose $q = 0$. This yields the constraint chain

$$q = 0 \Rightarrow \lambda = 0,$$

which fixes λ but does not furnish any condition on the variable θ . The maximal second-class ensemble is made up of the two constraints $\phi_1 = p_q$ and $\phi_2 = q$. The computation of the Dirac brackets gives

$$\{q, p_q\}_D = 0, \quad \{r, p_r\}_D = \{r, p_r\}_P. \quad (6.13)$$

Since $p_\theta = 0$ does not belong to the second-class ensemble, no bracket can be found which is compatible with this constraint. When the theory is quantized, p_θ is not set to 0 and the Poisson bracket $\{\theta, p_\theta\}_P$ is simply replaced by the commutator. This means that the constrained degree of freedom (θ, p_θ) is treated as free² and given a dynamical evolution governed by

$$H = \frac{1}{2}p_r^2 + \frac{1}{2r^2}p_\theta^2 + V(r).$$

The elimination of p_θ is done after the quantization, i.e. at the level of the Hilbert space: the restriction of the Hilbert space to the *physical sector* $\{|\Psi\rangle_{\text{phys}}\}$ is achieved by imposing the condition

$$\hat{p}_\theta|\Psi\rangle_{\text{phys}} = 0 \quad (6.14)$$

²in the sense of 'unconstrained'

on the physical states $|\Psi\rangle_{\text{phys}}$. Since the gauge condition fixes only the variable q , the quantum theory is still invariant under the transformation (6.4). This remaining gauge symmetry at the quantum level is signaled by the vanishing commutator

$$[\hat{H}, \hat{p}_\theta] = 0$$

and the condition (6.14) ensures the invariance of the physical quantum states under (6.4). A gauge fixing procedure for which only a part of the constraints can be eliminated at the level of the Hamiltonian belongs to the *class II type* of gauge conditions.

Fixing λ . Let us choose $\lambda = 0$. In this case, all constrained degrees of freedom are kept as dynamical variables and the Hamiltonian reads

$$H = \frac{1}{2}p_r^2 + \frac{1}{2r^2}p_\theta^2 + p_\theta q + V(r).$$

The physical sector is defined by the conditions

$$\hat{p}_\theta |\Psi\rangle_{\text{phys}} = \hat{p}_q |\Psi\rangle_{\text{phys}} = 0. \quad (6.15)$$

Gauge fixing procedures for which all degrees of freedom take part in the dynamical evolution belong to the *class III type* of gauge conditions.

6.1.2 Path integral quantization

We show how the Feynman path integral quantization procedure has to be modified in the case of a gauge theory. Let us consider a classical system with N degrees of freedom (q_i, p_i) and the set of constraints

$$\phi_\alpha(q, p) = 0, \quad \alpha = 1, \dots, M.$$

We assume that this set is second-class, which means that a class I gauge condition has been chosen. We give without proof (see [Kug97]) the modified expression of the partition function in phase space

$$Z = \int \mathcal{D}p \mathcal{D}q \prod_{\alpha=1}^M \delta(\phi_\alpha) \text{Det}^{\frac{1}{2}}[C](q, p) \exp \left\{ i \int dt [p\dot{q} - H(p, q)] \right\}, \quad (6.16)$$

where $C_{ij} = \{\phi_i, \phi_j\}_P$ denotes as before the matrix of the Poisson brackets and the constraints are expressed in terms of the delta functions.

Returning to our mechanical example, we write the partition function in the class I gauge $\theta = 0$:

$$\begin{aligned} Z &= \int \mathcal{D}r \mathcal{D}\theta \mathcal{D}q \mathcal{D}p_r \mathcal{D}p_\theta \mathcal{D}p_q \delta(p_q) \delta(p_\theta) \delta(\theta) \delta(q) \\ &\times \exp \left\{ i \int dt \left(p_r \dot{r} + p_\theta \dot{\theta} + p_q \dot{q} - \frac{1}{2}p_r^2 - \frac{1}{2r^2}p_\theta^2 - p_\theta q - V(r) \right) \right\} \end{aligned} \quad (6.17)$$

where we have dropped the determinant since C does not depend on the dynamical variables. The integrals over q , p_q and p_r are performed trivially and the elimination of p_θ is done after

having introduced the functional representation of the delta function $\delta(p_\theta)$ with auxiliary field α :

$$\begin{aligned} Z &= \int \mathcal{D}r \mathcal{D}\theta \mathcal{D}p_\theta \mathcal{D}\alpha \delta(\theta) e^{i \int dt [p_\theta(\dot{\theta}-\alpha) - \frac{1}{2r^2} p_\theta^2 + \frac{1}{2} \dot{r}^2 - V(r)]} \\ &= \int \mathcal{D}r \mathcal{D}\theta \mathcal{D}\alpha \text{Det}^{-1/2}[1/r^2] \delta(\theta) e^{i \int dt [\frac{1}{2} \dot{r}^2 + \frac{1}{2} r^2 (\dot{\theta}-\alpha)^2 - V(r)]}. \end{aligned} \quad (6.18)$$

[Note: in the context of path integrals, the “=” symbol always means an equality up to irrelevant prefactors, i.e. independent of the dynamical degrees of freedom, which drop out when expectation values are computed.] If the auxiliary field is reinterpreted as the variable q , we obtain the partition function under its Lagrangian form, with the restriction imposed by the gauge fixing condition $\theta = 0$.

The quantization of constrained systems, in particular its application to gauge field theory, is discussed in textbooks [Kug97, GT90] and reviews, see e.g. [Bur82].

6.2 Quantization of Maxwell theory

We illustrate the quantization procedure à la Dirac in the field theoretic case in the light of Maxwell theory.

6.2.1 Canonical quantization

We already pointed out the primary constraint (6.2). First, we write down the Hamiltonian density

$$\mathcal{H}_\Lambda = \frac{1}{2}(\mathbf{\Pi}^2 + \mathbf{B}^2) - (g_0 J_0 + \mathbf{\Pi} \cdot \nabla) A_0 + \Lambda \Pi_0 + g_0 \mathbf{A} \cdot \mathbf{J},$$

where Λ stands for the unknown velocity \dot{A}_0 . Since \mathcal{H} is an energy density, an integration by part does not affect the Hamiltonian $H = \int d^3x \mathcal{H}$, under the condition that the surface term vanishes. We can therefore write

$$\mathcal{H}_\Lambda = \frac{1}{2}(\mathbf{\Pi}^2 + \mathbf{B}^2) + (\nabla \cdot \mathbf{\Pi} - g_0 J_0) A_0 + \Lambda \Pi_0 + g_0 \mathbf{A} \cdot \mathbf{J}. \quad (6.19)$$

Second, we derive the chain of secondary constraints by temporal derivation of (6.2). It reads

$$\Pi_0 = 0 \Rightarrow \partial_i \Pi^i = g_0 J_0 \Rightarrow 0 = 0. \quad (6.20)$$

As it should be for a gauge theory, this chain does not provide any condition involving Λ . We then have to fix the gauge in order to eliminate the arbitrariness.

Coulomb gauge. We impose transversality of the spatial components of the photon field by the condition

$$\partial_i A^i = 0. \quad (6.21)$$

The stability chain of the gauge condition reads

$$\partial_i A^i = 0 \Rightarrow \Delta A_0 = -\partial_i \Pi^i \Rightarrow \Delta \Lambda = 0. \quad (6.22)$$

It is clear that the ensemble of constraints (6.20) and (6.22) is second-class, i.e. the dimension of the matrix C of the Poisson brackets is maximum. If we choose $\phi_1 = \Pi_0$, $\phi_2 = \partial_i \Pi^i - g_0 J_0$, $\phi_3 = \partial_i A^i$ and $\phi_4 = \Delta A_0 + \partial_i \Pi^i$, it reads

$$C = \begin{pmatrix} 0 & 0 & 0 & -\Delta \\ 0 & 0 & \Delta & 0 \\ 0 & -\Delta & 0 & -\Delta \\ \Delta & 0 & \Delta & 0 \end{pmatrix} \delta^{(3)}(\mathbf{x} - \mathbf{y}). \quad (6.23)$$

Coulomb gauge belongs therefore to the class I type of gauge conditions. We know from the previous section that all constraints can be set to 0 at the level of the Hamiltonian if we quantize the theory using the Dirac brackets. Inverting C , we find

$$C^{-1} = \begin{pmatrix} 0 & -\Delta^{-1} & 0 & \Delta^{-1} \\ \Delta^{-1} & 0 & -\Delta^{-1} & 0 \\ 0 & \Delta^{-1} & 0 & 0 \\ -\Delta^{-1} & 0 & 0 & 0 \end{pmatrix} \delta^{(3)}(\mathbf{x} - \mathbf{y}).$$

Using (6.11), the following first-class quantities are derived

$$\begin{aligned} A'_0 &= -g_0 \Delta^{-1} J_0, \\ \Pi'_0 &= 0, \\ A'_k &= A_k - \partial_k \partial_l \Delta^{-1} A_l, \\ \Pi^{k'} &= \Pi^k - \partial_k \partial_l \Delta^{-1} \Pi^l + g_0 \partial_k \Delta^{-1} J_0, \end{aligned} \quad (6.24)$$

while the non-vanishing Dirac brackets are

$$\{A_k(x), \Pi^l(y)\}_D^{x_0=y_0} = (\delta_k^l - \partial_k \partial_l \Delta^{-1}) \delta^{(3)}(\mathbf{x} - \mathbf{y}).$$

We can now write down the Hamiltonian density in which all constraints $\phi_1 \dots \phi_4$ are set to zero. The second and third term in (6.19) are easily eliminated. We have to express the remaining ones

$$\mathcal{H} = \frac{1}{2}(\mathbf{\Pi}^2 + \mathbf{B}^2) + g_0 \mathbf{A} \cdot \mathbf{J}$$

in terms of 2×2 independent variables, let us say A_1, A_2, Π_1, Π_2 , while A_3 and Π_3 are solution of $\phi_3 = 0$ and $\phi_2 = 0$ respectively. Moreover, the dependence on the matter field J_0 is now hidden in the first term, $\frac{1}{2} \mathbf{\Pi}^2$, and the constraint $\phi_2 = 0$. It is possible to derive an equivalent and more satisfactory expression. The idea is to replace the fields \mathbf{A} and $\mathbf{\Pi}$ by the corresponding first-class quantities in the last expression. It is allowed because these quantities differ from the original ones by some terms involving the constraints, which can be set to 0. If we denote the transversal part of any field φ by

$$\varphi_k^\perp := \varphi_k - \partial_k \partial_l \Delta^{-1} \varphi_l,$$

we make the substitutions

$$\begin{aligned} A_k &\rightarrow A_k^\perp, \\ \Pi^k &\rightarrow \Pi_\perp^k + g_0 \partial_k \Delta^{-1} J_0. \end{aligned}$$

This yields

$$\frac{1}{2}(\mathbf{\Pi}^2 + \mathbf{B}^2) \rightarrow \frac{1}{2} \left[\mathbf{\Pi}_\perp^2 + \mathbf{B}^2 + (g_0 \partial_t \Delta^{-1} J_0)^2 - 2g_0 \Pi_\perp^l \partial_t \Delta^{-1} J_0 \right]. \quad (6.25)$$

Performing an integration by part of the last two terms,

$$\begin{aligned} (g_0 \partial_t \Delta^{-1} J_0)^2 &= g_0^2 \partial_t \Delta^{-1} J_0 \partial_t \Delta^{-1} J_0 \rightarrow -J_0 \Delta^{-1} J_0, \\ \Pi_\perp^l \partial_t \Delta^{-1} J_0 &\rightarrow \partial_t \Pi_\perp^l \Delta^{-1} J_0 = 0, \end{aligned} \quad (6.26)$$

we find

$$\mathcal{H}_\perp = \frac{1}{2} [\mathbf{\Pi}_\perp^2 + \mathbf{B}^2] - \frac{1}{2} g_0^2 J_0 \Delta^{-1} J_0 + g_0 \mathbf{A}_\perp \cdot \mathbf{J}. \quad (6.27)$$

The integration over the spatial coordinates gives rise to the Coulomb gauge Hamiltonian, which we write in terms of the electric field $\mathbf{E}_\perp = \mathbf{\Pi}_\perp$ and the charge density $\rho(\mathbf{x}) = J_0(\mathbf{x})$:

$$H = \int d^3x \left[\frac{1}{2} (\mathbf{E}_\perp^2 + \mathbf{B}^2) + g_0 \mathbf{A}_\perp \cdot \mathbf{J} \right] + \underbrace{\frac{1}{2} g_0^2 \int d^3x d^3y \rho(\mathbf{x}) \mathcal{V}_{Coul}(\mathbf{x}, \mathbf{y}) \rho(\mathbf{y})}_{H_{Coul}}, \quad (6.28)$$

$$\text{with } \mathcal{V}_{Coul}(\mathbf{x}, \mathbf{y}) = -\Delta^{-1}|_{(\mathbf{x}, \mathbf{y})}. \quad (6.29)$$

Remarks.

1. Due to the transversality conditions

$$\partial_i A_\perp^i = 0, \quad \partial_i \Pi_\perp^i = 0,$$

the fields \mathbf{A}_\perp and $\mathbf{\Pi}_\perp$ possess two linearly independent components, which represent the two transversal photon polarizations. The Coulomb gauge fixing, as a class I gauge, eliminates the unphysical degrees of freedom at the level of the Hamiltonian. In other words, timelike and longitudinal photons are no more present in the quantized theory. Let us also point out the physical meaning of the secondary constraint ϕ_2 , which is nothing else than Gauss's law, one of the Maxwell equations. It is automatically satisfied and does not need to be imposed after the quantization as an operatorial constraint on the physical states.

2. The inverse Laplace operator in the coordinate representation in $D = 3 + 1$ is given by

$$\Delta^{-1}|_{(\mathbf{x}, \mathbf{y})} = -\frac{1}{4\pi} \frac{1}{|\mathbf{x} - \mathbf{y}|}.$$

Note that the operator Δ^{-1} in this representation has the dimension of an energy when expressed in physical units.

3. The introduction of the first-class fields into the Hamiltonian has let explicitly reappear the J_0 dependence in the expression

$$-\frac{1}{2} g_0^2 J_0 \Delta^{-1} J_0 = \frac{1}{2} g_0^2 \int d^3y \frac{J_0(\mathbf{x}) J_0(\mathbf{y})}{4\pi |\mathbf{x} - \mathbf{y}|},$$

which is nothing else than the familiar *Coulomb energy density*.

4. In view of remarks 1 and 3, it is often said that Coulomb gauge is a *physical gauge*. Unfortunately, the price to be paid is the sacrifice of the Lorentz invariance of Maxwell theory.

Let us consider for instance the photon propagator:

$$\begin{aligned} iD_{\mu\nu}^F(x-y) &:= \langle T(A_\mu(x)A_\nu(y)) \rangle \\ &= i \int \frac{d^4k}{(2\pi)^4} \frac{e^{-ik \cdot (x-y)}}{k^2 + i\epsilon} \sum_{\lambda=1}^2 \epsilon_\mu^\lambda(k) \epsilon_\nu^\lambda(k), \end{aligned}$$

where ϵ_μ^λ represents the polarisation vectors. This expression is manifestly non-covariant due to the transversality of the gauge fields. However, the terms violating Lorentz invariance should vanish when physical amplitudes (elements of the S -matrix) are computed, due to gauge invariance. Let us choose the orthogonal basis $\{\epsilon_\mu^1(k), \epsilon_\mu^2(k), k^\mu, n^\mu = (1, 0, 0, 0)\}$, in which the Feynman propagator reads

$$D_{\mu\nu}^F(k) = \frac{-i}{k^2 + i\epsilon} \left[g_{\mu\nu} + \frac{(k \cdot n)(n_\mu k_\nu + n_\nu k_\mu) - k_\mu k_\nu + k^2 n_\mu n_\nu}{|\mathbf{k}|^2} \right].$$

When physical amplitudes are calculated, this expression is sandwiched between conserved currents and the terms proportional to k_μ and k_ν vanish (Ward identity). The remaining n -dependent term is

$$- \int \frac{d^4k}{(2\pi)^4} \frac{e^{-ik \cdot (x-y)}}{|\mathbf{k}|^2} n_\mu n_\nu = \frac{-g_{\mu 0} g_{\nu 0} \delta(x_0 - y_0)}{4\pi |\mathbf{x} - \mathbf{y}|},$$

which is nothing else than the Coulomb potential. Between two conserved currents, it picks the charge densities and gives rise to a contribution which cancels exactly the Coulomb interaction term in the Hamiltonian. We see that the photon propagator in Coulomb gauge can be replaced by the covariant expression $D_{\mu\nu}^F(k) = \frac{-ig_{\mu\nu}}{k^2 + i\epsilon}$ arising in a natural way when the theory is quantized in a covariant gauge. By the way, we see that the Coulomb potential is given by the instantaneous part of the $\langle A_0 A_0 \rangle$ correlation function.

Temporal gauge. A class II gauge condition is given by

$$A_0 = 0,$$

which gives the constraint chain

$$A_0 = 0 \Rightarrow \Lambda = 0.$$

The set of second class constraints $\phi_1 = \Pi_0, \phi_2 = A_0$ is eliminated at the level of the Hamiltonian, which reads

$$\mathcal{H} = \frac{1}{2}(\mathbf{\Pi}^2 + \mathbf{B}^2) + g_0 \mathbf{A} \cdot \mathbf{J}.$$

The constrained, and therefore unphysical, degrees of freedom (A_i, Π^i) are eliminated by imposing that the physical states are annihilated by Gauss's law $\phi_3 = \partial_i \Pi^i - g_0 J_0$:

$$[\partial_i \hat{\Pi}^i - g_0 \hat{J}_0] |\Psi\rangle_{\text{phys}} = 0. \quad (6.30)$$

This condition, which is the pendant of (6.14), ensures the remaining invariance of the quantum theory under time-independent gauge transformations

$$A_i(x) \rightarrow A_i(x) + \partial_i \alpha(\mathbf{x}),$$

for which the operator $\partial_i \hat{\Pi}^i - g_0 \hat{J}_0$ is the generator.

Covariant gauges. We consider gauge conditions of the form

$$\partial_\mu A^\mu = \omega(x), \quad (6.31)$$

where $\omega(x)$ is some scalar function. If we rewrite the previous expression under the form

$$\dot{A}_0 = -\partial_i A^i + \omega(x),$$

we see that the unknown velocity \dot{A}_0 , which we denoted by the parameter Λ in (6.19) is directly fixed by the gauge condition. Any covariant gauge of the form (6.31) is thus a class III gauge, i.e. for which all degrees of freedom are given a dynamical evolution. The elimination of non-physical states of the Hilbert space in covariant gauges is no trivial task and is described in the Gupta-Bleuler formalism in QED and in the BRST formalism in quantized Yang-Mills theories. Both approaches are beyond the scope of this work and will not be discussed here.

6.2.2 Path integral quantization

We consider here only quantization in Coulomb gauge. The field theoretic pendant of (6.16) is given by

$$Z = \int \mathcal{D}A \mathcal{D}\Pi \exp \left\{ i \int \left[\Pi_\mu \dot{A}^\mu - \frac{1}{2}(\mathbf{\Pi}^2 + \mathbf{B}^2) - g_0 \mathbf{A} \cdot \mathbf{J} \right] dx \right\} \\ \times \delta(A_0 + \Delta^{-1} \partial_i \Pi^i) \delta(\Pi_0) \delta(\partial_i A^i) \delta(\partial_i \Pi^i - g_0 J_0),$$

where we omit the determinant of the matrix (6.23), since it does not depend on the fields. The transformation of this partition function works in two steps and parallel to the calculation leading from (6.17) to (6.18). First, we integrate over A_0 and Π_0 :

$$Z = \int \mathcal{D}A \mathcal{D}\Pi \exp \left\{ i \int \left[\Pi_i \dot{A}^i - \frac{1}{2}(\mathbf{\Pi}^2 + \mathbf{B}^2) - g_0 \mathbf{A} \cdot \mathbf{J} \right] dx \right\} \delta(\partial_i A^i) \delta(\partial_i \Pi^i - g_0 J_0). \quad (6.32)$$

Second, we introduce the integral representation of $\delta(\partial_i \Pi^i - g_0 J_0)$, for which the field A_0 is reintroduced as the integration variable:

$$\delta(\partial_i \Pi^i - g_0 J_0) = \int \mathcal{D}A_0 \exp \left\{ -i \int A_0 (\partial_i \Pi^i - g_0 J_0) dx \right\}.$$

Inserting this expression in the partition function, we find

$$Z = \int \mathcal{D}A \mathcal{D}\Pi \exp \left\{ i \int \left[\Pi_i (\dot{A}^i - \partial^i A_0) - \frac{1}{2}(\mathbf{\Pi}^2 + \mathbf{B}^2) + g_0 A_\mu J^\mu \right] dx \right\} \delta(\partial_i A^i).$$

The final result is obtained by performing the Gaussian integral over $\mathbf{\Pi}$ and reads

$$Z = \int \mathcal{D}A \exp \left\{ i \int \mathcal{L} dx \right\} \delta(\partial_i A^i), \quad \mathcal{L} = -\frac{1}{4} F_{\mu\nu} F^{\mu\nu} + g_0 A_\mu J^\mu. \quad (6.33)$$

The successive integrations have let appear the full Maxwell Lagrangian, while the gauge condition is the only constraint that remains under the form of a delta function. It is possible to re-express this result in terms of an integral involving the physical degrees of freedom \mathbf{A}_\perp and $\mathbf{\Pi}_\perp$. For this, we restart from the expression (6.32), where we separate the transverse and longitudinal parts of the $\mathbf{\Pi}$ field: $\mathbf{\Pi} = \mathbf{\Pi}_\perp - \nabla\phi$. The measure becomes $\mathcal{D}\mathbf{\Pi} \simeq \mathcal{D}\mathbf{\Pi}_\perp \mathcal{D}\phi$. If we reintroduce the irrelevant factor $\text{Det}[-\Delta]$, we can write

$$\text{Det}[-\Delta] \delta(\partial_i \Pi^i - g_0 J_0) = \text{Det}[-\Delta] \delta(-\Delta^{-1} \phi - g_0 J_0) = \delta(\phi + g_0 \Delta^{-1} J_0). \quad (6.34)$$

Performing finally the ϕ integration, we obtain

$$Z = \int \mathcal{D}\mathbf{A}_\perp \mathcal{D}\mathbf{\Pi}_\perp \exp \left\{ i \int (\Pi_{\perp,i} \dot{A}^i - \mathcal{H}_\perp) dx \right\} \quad (6.35)$$

where \mathcal{H}_\perp is the Hamiltonian density (6.27).

6.3 Quantization of Yang-Mills theory

We are now armed to attack the quantization problem in the framework of a non-Abelian gauge theory of gauge group $SU(N)$. We will from now limit ourselves to the quantization in Coulomb gauge.

Our starting point is the Lagrangian density (B.9)

$$\mathcal{L} = -\frac{1}{4} F_{\mu\nu}^a F_a^{\mu\nu} + g_0 A_\mu^a J_a^\mu.$$

The canonical conjugates are given by

$$\begin{aligned} \Pi_a^0 &= 0, \\ \Pi_a^i &= F_a^{i0}, \end{aligned}$$

and a primary constraint appears similarly to (6.2). The stability of this condition provides a first secondary constraint:

$$\Pi_a^0 = 0 \Rightarrow [D_i \Pi^i]_a = g_0 J_a^0 \Rightarrow 0 = 0.$$

The Hamiltonian density reads

$$\mathcal{H}_T = \frac{1}{2} (\mathbf{\Pi}^2 + \mathbf{B}^2) - (g_0 J_0^a + \mathbf{\Pi}^b \cdot \mathbf{D}^{ab}) A_0^a + \Lambda^a \Pi_0^a + g_0 \mathbf{A}^a \cdot \mathbf{J}^a, \quad (6.36)$$

where for all quantity X , \mathbf{X}^2 stands for the product $X_a^i X_a^i$. As the constraint chain shows, Yang-Mills theory is a gauge theory and a gauge has to be fixed. The Coulomb gauge condition reads

$$\partial_i A_a^i = 0. \quad (6.37)$$

Stability of the gauge condition provides a further secondary constraint and a condition on Λ .

$$\partial_i A_a^i = 0 \Rightarrow \nabla \cdot \mathbf{D}^{ab} A_0^b = -\partial_i \Pi_a^i \Rightarrow \nabla \cdot \mathbf{D}^{ab} \Lambda^b = 0.$$

The set of constraints is second-class, i.e. Coulomb gauge belongs to the class I type of gauge conditions. We could from now follow the usual program of quantization in the canonical formalism, i.e. compute the matrix of the Poisson brackets, invert it, calculate the first-class quantities, the Dirac brackets and finally obtain the Hamiltonian density. The constraint chains clearly show that the matrix of the Poisson brackets contains the differential operator $\nabla \cdot \mathbf{D}$. The calculation of the Dirac brackets requires its inversion, which is by no means trivial. The quantization procedure is generally addressed canonically in the temporal gauge $A_0^a = 0$, in the axial gauge $A_3^a = 0$ or is performed directly in the path integral formalism, which is our framework for the remaining part of this section. We give directly the Yang-Mills pendant of the path integral (6.33):

$$Z = \int \mathcal{D}A \exp \left\{ i \int \mathcal{L} dx \right\} \delta(\partial_i A_a^i) \text{Det}[-\nabla \cdot \mathbf{D}], \quad \mathcal{L} = -\frac{1}{4} F_{\mu\nu}^a F_a^{\mu\nu} + g_0 A_\mu^a J_a^\mu, \quad (6.38)$$

which differs from its Abelian analogue by the presence of the determinant $\text{Det}[-\nabla \cdot \mathbf{D}]$. This additional factor is due to the fact that the determinant of the C matrix in (6.16) cannot be neglected, since it depends on the dynamical variable \mathbf{A} through the covariant derivative in $\nabla \cdot \mathbf{D}$.

We re-express the generating functional under the form of a path integral involving the physical degrees of freedom \mathbf{A}_\perp and $\mathbf{\Pi}_\perp$, similarly to the transformation that lead from (6.33) to (6.35). First, the factor

$$\exp \left\{ i \int \left(-\frac{1}{2} F_{0i}^a F_a^{0i} \right) dx \right\} \simeq \int \mathcal{D}\mathbf{\Pi} \exp \left\{ i \int \left(\Pi_i^a F_a^{0i} - \frac{1}{2} \mathbf{\Pi}^2 \right) \right\}$$

is linearized in terms of new variables $\mathbf{\Pi}$, which are interpreted as the conjugated momenta. The partition function becomes

$$Z = \int \mathcal{D}A \mathcal{D}\mathbf{\Pi} \exp \left\{ i \int \left[\Pi_i^a (\dot{A}_a^i - [D^i A_0]_a) - \frac{1}{2} (\mathbf{\Pi}^2 + \mathbf{B}^2) + g_0 A_0^a J_0^a - g_0 \mathbf{A}^a \cdot \mathbf{J}^a \right] \right\} \\ \times \delta(\partial_i A_a^i) \text{Det}[-\nabla \cdot \mathbf{D}].$$

Performing the integration on A_0^a enforces Gauss's law, $[D_i \Pi^i]^a = g_0 J_0^a$, yielding

$$Z = \int \mathcal{D}A \mathcal{D}\mathbf{\Pi} \exp \left\{ i \int \left[\Pi_i^a \dot{A}^{i,a} - \frac{1}{2} (\mathbf{\Pi}^2 + \mathbf{B}^2) - g_0 \mathbf{A}^a \cdot \mathbf{J}^a \right] \right\} \\ \times \delta(\partial_i A_a^i) \delta([D_i \Pi^i]^a - g_0 J_0^a) \text{Det}[-\nabla \cdot \mathbf{D}].$$

This result is the Yang-Mills pendant of (6.32). We separate the transverse and longitudinal parts of the conjugated fields: $\mathbf{\Pi}^a = \mathbf{\Pi}_\perp^a - \nabla \phi^a$. The integration measure factorizes, i.e. $\mathcal{D}\mathbf{\Pi} \simeq \mathcal{D}\mathbf{\Pi}_\perp \mathcal{D}\phi$. As in (6.34), we absorb the determinant in the delta function imposing Gauss's law:

$$\text{Det}[-\nabla \cdot \mathbf{D}] \delta([D_i \Pi^i]^a - g_0 J_0^a) = \text{Det}[-\nabla \cdot \mathbf{D}] \delta(-[\mathbf{D} \cdot \nabla \phi]^a + g_0 f^{abc} A_i^b \cdot \Pi_c^i - g_0 J_0^a) \\ = \delta(\phi^a - [(-\nabla \cdot \mathbf{D})^{-1} (g_0 \rho_{\text{gl}} + g_0 J_0)]^a),$$

where we used the transversality of the gauge field to permute $\nabla \cdot \mathbf{D} = \mathbf{D} \cdot \nabla$ and we defined $\rho_{\text{gl}}^a = f^{abc} A_i^b E_c^i$, the colour-charge density of the dynamical degrees of freedom. Performing the integration over ϕ , we obtain finally

$$Z = \int \mathcal{D}\mathbf{A}_\perp \mathcal{D}\mathbf{\Pi}_\perp \exp \left\{ i \int (\mathbf{\Pi}_{\perp,i}^a \dot{A}^{i,a} - \mathcal{H}_\perp) \right\} \quad (6.39)$$

where the Hamiltonian density \mathcal{H}_\perp is derived from (6.36) by making the substitutions $\mathbf{A} \rightarrow \mathbf{A}_\perp$ and $\mathbf{\Pi} \rightarrow \mathbf{\Pi}_\perp - \nabla\phi$ and setting all constraints to zero. It reads

$$\mathcal{H}_\perp = \frac{1}{2}(\mathbf{\Pi}_\perp^2 + \mathbf{B}^2) - \frac{1}{2}g_0^2(\rho_{\text{gl}} + J_0)(-\nabla \cdot \mathbf{D})^{-1} \Delta (-\nabla \cdot \mathbf{D})^{-1}(\rho_{\text{gl}} + J_0) + g_0 \mathbf{A}_\perp \cdot \mathbf{J},$$

if we omit the colour indices for clarity. We can finally write the Yang-Mills pendant of the expressions (6.28)-(6.29):

$$H = \int d^3x \left[\frac{1}{2}(\mathbf{E}_\perp^2 + \mathbf{B}^2) + g_0 \mathbf{A}_\perp^a \cdot \mathbf{J}^a \right] + \underbrace{\frac{1}{2}g_0^2 \int d^3x d^3y \rho^a(\mathbf{x}) \mathcal{V}_{\text{Coul}}^{ab}(\mathbf{x}, \mathbf{y}) \rho^b(\mathbf{y})}_{H_{\text{Coul}}}, \quad (6.40)$$

$$\text{with } \left\{ \begin{array}{l} \mathcal{V}_{\text{Coul}}(\mathbf{x}, \mathbf{y})^{ab} = M^{-1}(-\Delta)M^{-1}|_{(\mathbf{x}, \mathbf{y})}^{ab} \\ \rho = \rho_{\text{gl}} + J_0, \\ M = -\nabla \cdot \mathbf{D}. \end{array} \right\}. \quad (6.41)$$

The operator $M := -\nabla \cdot \mathbf{D}$ is called *Faddeev-Popov operator* and plays a crucial role in the Coulomb quantization scheme of Yang-Mills theory, especially in Gribov's scenario of colour confinement. Note that the Faddeev-Popov operator reduces simply to the Laplacian in the Abelian case.

The operator $\mathcal{V}_{\text{Coul}}(\mathbf{x}, \mathbf{y})$ in (6.41) is the non-Abelian pendant of (6.29). In the Abelian case, we indeed have $M = -\Delta$ and $\mathcal{V}_{\text{Coul}}(\mathbf{x}, \mathbf{y})$ reduces to the Coulomb potential of electrodynamics. We discuss the properties of the colour Coulomb potential in Sec. 6.4.3.

6.4 Gribov's scenario of confinement

Let us have a look back at the gauge condition (6.37). Given a gauge potential \mathbf{A} satisfying the condition of transversality $\nabla \cdot \mathbf{A} = 0$, we consider the gauge-transformed potential $\mathbf{A}^g = g\mathbf{A}g^{-1} - \frac{i}{g_0}(\nabla g)g^{-1}$, with respect to the element g of the gauge group. If the condition of transversality fixes the gauge completely, we should not encounter along the gauge orbit associated to \mathbf{A} any other transverse gauge configurations. Stated in a mathematical way, the solution g of the following equation

$$\nabla \cdot \mathbf{A}^g = 0 \quad (6.42)$$

should reduce to the identity under suitable conditions at spatial infinity. In a famous paper [Gri78], Gribov pointed out that the equation does admit non-trivial solutions g in the case of non-Abelian theories. In other words, the quantization of Yang-Mills theory is spoiled by the presence of gauge copies, known today as *Gribov copies*.

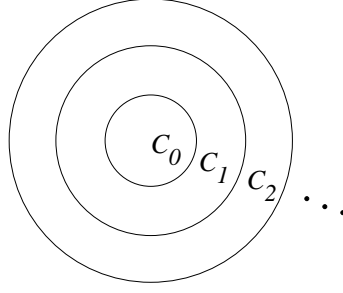


Figure 6.1: The functional space of gauge field configurations is divided in regions C_n according to the number n of negative eigenvalues of the Faddeev-Popov operator. On each of the boundaries, this operator possesses a non trivial zero-mode.

As we shall see, the problem of gauge copies, generally called *Gribov problem*, has in fact more fundamental implications than the technical difficulties occurring in the gauge fixing procedure, namely a direct relation to the problem of colour confinement.

6.4.1 Gribov copies

In the Abelian case, we have $g = e^{ig_0\Lambda}$ and the gauge-transformed potential is given by $\mathbf{A}^g = \mathbf{A} + \nabla\Lambda$. The equation (6.42) reduces to

$$\Delta\Lambda = 0.$$

If we impose that Λ vanishes at spatial infinity, it vanishes everywhere, due to an elementary property of the Laplace equation, and g reduces everywhere to the identity. Maxwell theory in Coulomb gauge is free of Gribov copies.

In the non-Abelian case, the gauge transformation of the gauge potential is given by $\mathbf{A}^g = g\mathbf{A}g^{-1} - \frac{i}{g_0}(\nabla g)g^{-1}$, with $g = e^{ig_0\alpha^a T^a}$. To first order in the α parameter, it reads $\mathbf{A}^g = \mathbf{A} + \mathbf{D}\alpha$ and (6.42) takes the form $\nabla \cdot \mathbf{D}\alpha^a = 0$. This expression can be regarded as a Schrödinger-type equation for the Faddeev-Popov operator:

$$-\Delta\alpha^a - g_0 f^{abc} \mathbf{A}^b \cdot \nabla\alpha^c = \epsilon[\mathbf{A}]\alpha^a, \quad (6.43)$$

with zero eigenvalue, i.e. $\epsilon[\mathbf{A}] = 0$. For sufficiently small potentials, this equation can be solved for positive ϵ only, i.e. the only solution of (6.42) is the trivial $\alpha = 0$. The domain of small gauge field fluctuations is thus free of gauge copies. For a certain magnitude of \mathbf{A} , the lowest eigenvalue of the Faddeev-Popov operator will vanish, i.e. the Faddeev-Popov operator will develop a zero-mass state, which corresponds to a non-trivial solution of (6.42) of fast decrease at infinity. As the magnitude of \mathbf{A} increases, this becomes a bound state with negative ϵ solution. For another value of the potential, another $\epsilon = 0$ solution appears which in turn becomes a second bound state and so on. The functional space of gauge field configurations can then be divided into regions C_n with respect to the number n of negative eigenvalues of the Faddeev-Popov operator, as depicted in Fig. 6.1.

Gribov considered in a second step gauge configurations lying in the neighbourhood of the boundary of C_0 . We write such a field under the form

$$\mathbf{A} = \mathbf{C} + \mathbf{a},$$

where \mathbf{C} lies on the boundary and \mathbf{a} is small compared to \mathbf{C} . Gribov obtained the transformed field $\mathbf{A}^g = \mathbf{C} + \mathbf{a}^g$, with

$$\mathbf{a}^g = \mathbf{a} + \mathbf{D}[\mathbf{C}]\phi_0,$$

ϕ_0 being a zero-mode of the Faddeev-Popov operator, and proved that if one of the fields $(\mathbf{A}, \mathbf{A}^g)$ lies in C_0 then the other one lies *de facto* in C_1 . He indeed found

$$\epsilon[\mathbf{A}] = -\epsilon[\mathbf{A}^g],$$

i.e. there exists a bound state for one of the fields and none for the other. The hope of Gribov was that this statement would hold for general, non-infinitesimal gauge transformations: for any field in the region C_1 there would be an equivalent field in the region C_0 . By induction, this could be extended to the other regions C_2, C_3 and so on, giving rise to the final statement that all fields outside of C_0 would be gauge transformations of the fields in C_0 . Gribov's proposal to get rid of the gauge ambiguities was to restrict functional integrations performed in the space of gauge configurations to the region C_0 , called *Gribov region*. These functional integrals are cut off at the first boundary, where the lowest non-trivial eigenvalue of the Faddeev-Popov operator vanishes, known as the *first Gribov horizon*.

However, this program has to be reviewed, since we nowadays know that the Gribov region *does*, in general, contain copies.

6.4.2 Minimal Coulomb gauge and fundamental modular region

Despite the fact that the Gribov region is spoiled by gauge copies, Gribov's proposal to restrict the functional integral to this region was not abandoned but refined.

Let us leave this discussion aside for a moment and describe how a configuration lying in the Gribov region can be reached along the gauge orbit of a given configuration \mathbf{A} . We consider the following functional:

$$F_A[g] = \int dx \operatorname{tr} [\mathbf{A}(x) \cdot \mathbf{A}^g(x)], \quad g = e^{ig_0 \alpha^a T^a}, \quad (6.44)$$

which is the L^2 norm of the potential along the gauge orbit. To second order in the parameter α , this expression reads

$$F_A[g] = F_A[1] + 2 \int dx \operatorname{tr} [\partial_i A_i(\mathbf{x}) \alpha(\mathbf{x})] + \int dx \operatorname{tr} [\alpha^\dagger(\mathbf{x}) (-\partial_i D_i) \alpha(\mathbf{x})] + \mathcal{O}(\alpha^3).$$

Following a gauge fixing procedure introduced by Zwanziger [Zwa82], we choose g such that the functional (6.44) attains a minimum along the gauge orbit. In this case, we have transversality of the potential $\partial_i A_i^g = 0$ and positivity of the Faddeev-Popov operator $-\nabla \cdot \mathbf{D}[A^g] \geq 0$, since the Hessian matrix is positive at a minimum. The set of these minima is by definition the Gribov region C_0 , which we denote in the following by Ω .

Let us now return to the problem of copies inside the Gribov region. The gauge-fixing prescription as a minimization procedure of (6.44) shows clearly that Ω is not free of gauge copies, since $F_A[g]$ may have many local minima along the gauge orbit. In place of the Gribov region, one considers the set of all absolute minima obtained by minimization of (6.44) along all gauge orbits. This restricted set is called *fundamental modular region* or *F.M.R.* and

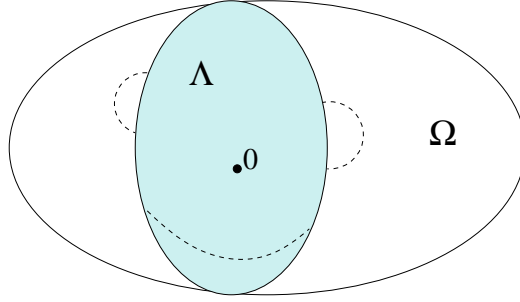


Figure 6.2: Sketch of the Gribov region Ω and the fundamental modular region Λ . The point $\mathbf{A} = 0$ lies in Λ and points on the boundary of Λ have to be identified.

is denoted by Λ . The Zwanziger prescription combined with the restriction of functional integrations to Λ is called *minimal Coulomb gauge*. The F.M.R. contains the point $\mathbf{A} = 0$, is bounded in Ω , convex and points lying on the boundary have to be identified, for considerations of continuity [SvBZ03]. This is sketched in Fig. 6.2. At the practical level, the restriction to the F.M.R. is implemented in an effective Hamiltonian by the addition of a *horizon function* to the Coulomb gauge Hamiltonian. The role of this function is to cut off the functional integration at the boundary of the F.M.R. $\partial\Lambda$, while the integration is performed over the unrestricted configuration space. The horizon function has been analytically implemented in the case of a lattice Coulomb Hamiltonian in the thermodynamical limit [Zwa97]. We discuss in the next chapter how the problem of Gribov copies is handled in the numerical framework of lattice gauge theory.

6.4.3 Coulomb potential vs. Wilson potential

Our task in this section is to disentangle the Coulomb potential, a quantity derived as a byproduct of the Coulomb gauge quantization scheme, from the Wilson potential, derived in a complete gauge invariant way from the expectation value of the Wilson loop.

Coulomb potential. It is derived from the partition function (6.38) by addressing the $A_0 A_0$ correlator (cf. remark 4 in Sec. 6.2.1):

$$g_0^2 \langle A_0^a(x) A_0^b(y) \rangle = \frac{-1}{Z} \frac{\delta^2 Z}{\delta J_0^a(x) \delta J_0^b(y)},$$

following elementary rules of functional derivation. Differentiating the expression (6.39), equivalent to (6.38), with respect to J_0 acts on the Coulomb term part H_{Coul} of the Hamiltonian (6.40) and yields after a straightforward calculation [CZ02b]

$$\frac{-1}{Z} \frac{\delta^2 Z}{\delta J_0^a(x) \delta J_0^b(y)} = g_0^2 \langle \mathcal{V}_{\text{Coul}}^{ab}(\mathbf{x}, \mathbf{y}) \rangle \delta(x_0 - y_0) - g_0^2 \langle (\mathcal{V}_{\text{Coul}} \rho_{\text{gl}})^a(x) (\mathcal{V}_{\text{Coul}} \rho_{\text{gl}})^b(y) \rangle. \quad (6.45)$$

The instantaneous part of the correlator defines the *Coulomb potential*:

$$\boxed{V_{\text{Coul}}(\mathbf{x} - \mathbf{y}) \delta^{ab} = \mathcal{N} g_0^2 \langle \mathcal{V}_{\text{Coul}}^{ab}(\mathbf{x}, \mathbf{y}) \rangle}, \quad (6.46)$$

i.e. the *vacuum expectation value* of the $\mathcal{V}_{\text{Coul}}$ operator, up to some constant factor \mathcal{N} . For a pair of static quark and antiquark, we find below $\mathcal{N} = -C_N$, where C_N is the quadratic Casimir of the fundamental representation N of $SU(N)$. The second term is denoted by

$$P_0^{ab}(x-y) = -g_0^2 \langle (\mathcal{V}_{\text{Coul}} \rho_{\text{gl}})^a(x) (\mathcal{V}_{\text{Coul}} \rho_{\text{gl}})^b(y) \rangle,$$

whose physical interpretation will be given later on.

Wilson potential. We sketch briefly how the potential of a static quark-antiquark pair can be extracted from the vacuum expectation value of the Wilson loop³.

We consider the evolution in time of a pair of quark and anti-quark of mass m_q placed at \mathbf{x} and \mathbf{y} at time $t = 0$:

$$|\Phi_{qq}(\mathbf{x}, \mathbf{y}, 0)\rangle = \bar{\Psi}^q(\mathbf{x}, 0) U(\mathbf{x}, 0; \mathbf{y}, 0) \Psi^q(\mathbf{y}, 0) |0\rangle. \quad (6.47)$$

where, for arbitrary time t , $U(\mathbf{x}, t; \mathbf{y}, t) = P e^{i \int_{\mathbf{x}}^{\mathbf{y}} \mathbf{A}(\mathbf{z}, t) \cdot d\mathbf{z}}$, with the path-ordering prescription P due to the fact that the gauge potentials are non-commuting matrices. This phase ensures the gauge invariance of the state. The propagation in time is described by the correlator (we drop for clarity the spinor and colour indices)

$$G(\mathbf{x}', \mathbf{y}', \mathbf{x}, \mathbf{y}, t) = \langle 0 | T(\bar{\Psi}^q(\mathbf{y}', t) U(\mathbf{y}', t; \mathbf{x}', t) \Psi^q(\mathbf{x}', t) \bar{\Psi}^q(\mathbf{x}, 0) U(\mathbf{x}, 0; \mathbf{y}, 0) \Psi^q(\mathbf{y}, 0) |0\rangle.$$

This quantity possesses the following path integral representation

$$G(\mathbf{x}', \mathbf{y}', \mathbf{x}, \mathbf{y}, t) = \frac{1}{Z} \int \mathcal{D}A \mathcal{D}\psi \mathcal{D}\bar{\psi} \mathcal{D}\Psi^q \mathcal{D}\bar{\Psi}^q \bar{\Phi}_{qq}(\mathbf{x}', \mathbf{y}', t) \Phi_{qq}(\mathbf{x}, \mathbf{y}, 0) e^{iS}, \quad (6.48)$$

with $Z = \int \mathcal{D}A \mathcal{D}\psi \mathcal{D}\bar{\psi} \mathcal{D}\Psi^q \mathcal{D}\bar{\Psi}^q e^{iS}$. The action S can be decomposed in three parts: $S = S_{YM}[A] + S_F[\psi, \bar{\psi}, A] + S_q[\Psi^q, \bar{\Psi}^q, A]$, where we distinguish the pair of quark and anti-quark Ψ^q and $\bar{\Psi}^q$ from the dynamical quarks $\psi, \bar{\psi}$.

If the limit for heavy fermions $m_q \rightarrow \infty$ is taken, as well as the limit for large Euclidean times ($T := it, T \rightarrow \infty$), we expect that the correlation function will show the following behaviour⁴:

$$G(\mathbf{x}', \mathbf{y}', \mathbf{x}, \mathbf{y}, t) \xrightarrow{m_q \rightarrow \infty, T \rightarrow \infty} \delta^{(3)}(\mathbf{x} - \mathbf{x}') \delta^{(3)}(\mathbf{y} - \mathbf{y}') C(\mathbf{x}, \mathbf{y}) e^{-E(R)T}, \quad (6.49)$$

where $E(R)$ is the ground state energy in the presence of the static pair separated by the distance $R = |\mathbf{x} - \mathbf{y}|$ and $C(R)$ is a function accounting for the overlap of (6.47) with the ground state.

³A more detailed derivation can be found in the references [Rot97, BV].

⁴In analogy with the following example in quantum mechanics. In a one-dimensional theory whose Hamiltonian is given by H , the evolution in time of a given state $|\Phi(0)\rangle = |\psi\rangle$ is governed by the time evolution operator $e^{-it\hat{H}}$: $\langle \Phi(t) | \Phi(0) \rangle = \langle \psi | e^{-it\hat{H}} | \psi \rangle$. Expanding the matrix element with respect to the eigenstates $|n\rangle$ of \hat{H} , we find

$$\langle \Phi(t) | \Phi(0) \rangle = \sum_n \langle \psi | n \rangle \langle n | \psi \rangle e^{-iE_n t},$$

where E_n labels the eigenvalues of H . We can extract the contribution of the state of lowest energy by studying the propagation amplitude for large Euclidean ($t \rightarrow -iT$) times:

$$\langle \Phi(t) | \Phi(0) \rangle \xrightarrow{T \rightarrow \infty} |\langle \psi | 0 \rangle|^2 e^{-E_0 T}.$$

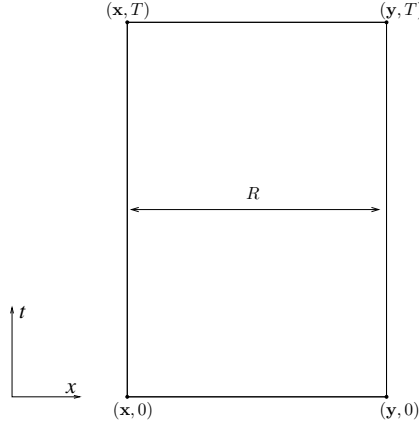


Figure 6.3: The contour Γ for which the expectation value of the Wilson loop (6.50) is evaluated.

The large mass limit is taken by integrating out the quark degrees of freedom $\Psi^q, \bar{\Psi}^q$ in (6.48) (the action S_q is quadratic in these fields). The resulting fermion determinant drops out in the limit $m_q \rightarrow \infty$ since it approaches the same constant value in numerator and denominator. We skip here the details of the calculation, which are irrelevant for our purposes. In the large mass limit, the correlator reads

$$G(\mathbf{x}', \mathbf{y}', \mathbf{x}, \mathbf{y}, t) \xrightarrow{m_q \rightarrow \infty} \delta^{(3)}(\mathbf{x} - \mathbf{x}') \delta^{(3)}(\mathbf{y} - \mathbf{y}') P_+ P_- e^{-2im_q t} \left\langle \text{Tr} \left[P e^{-i \oint_{\Gamma} A_{\mu}(z) dz^{\mu}} \right] \right\rangle.$$

The line integral is performed over a closed rectangular path Γ with spatial and temporal extension $R = |\mathbf{x} - \mathbf{y}|$ and t respectively, whose corners are located at the points $(\mathbf{x}, 0)$, $(\mathbf{y}, 0)$, (\mathbf{x}, t) and (\mathbf{y}, t) . The P_{\pm} matrices are the projectors $P_{\pm} = \frac{1}{2}(1 \pm \gamma^0)$. The expectation value is the average of the *Wilson loop* $\text{Tr} \left[P e^{-i \oint_{\Gamma} A_{\mu}(z) dz^{\mu}} \right]$ over all gluonic and fermionic fluctuations:

$$\langle \text{Tr} P e^{i \oint_{\Gamma} A_{\mu}(z) dz^{\mu}} \rangle = \frac{\int \mathcal{D}A \mathcal{D}\psi \mathcal{D}\bar{\psi} \text{Tr} \left[P e^{-i \oint_{\Gamma} A_{\mu}(z) dz^{\mu}} \right] e^{iS_{YM+F}}}{\int \mathcal{D}A \mathcal{D}\psi \mathcal{D}\bar{\psi} e^{iS_{YM+F}}}. \quad (6.50)$$

We continue the exponential to imaginary times ($t \rightarrow -iT$) and find

$$G(\mathbf{x}', \mathbf{y}', \mathbf{x}, \mathbf{y}, T) \xrightarrow{m_q \rightarrow \infty} \delta^{(3)}(\mathbf{x} - \mathbf{x}') \delta^{(3)}(\mathbf{y} - \mathbf{y}') P_+ P_- e^{-2m_q T} \langle W_{\Gamma}[A] \rangle_{\text{Eucl.}},$$

where we denote the Wilson loop by $W_{\Gamma}[A] = \text{Tr} \left[P e^{i \oint_{\Gamma} A_{\mu}(z) dz^{\mu}} \right]$. The contour is now the rectangle of Fig. 6.3 in Euclidean space-time and the expectation value $\langle \dots \rangle_{\text{Eucl.}}$ is taken with respect to the Euclidean action. Taking the limit $T \rightarrow \infty$ and comparing to (6.49), we have

$$\langle W_{\Gamma}[A] \rangle_{\text{Eucl.}} \xrightarrow{T \rightarrow \infty} F(R) e^{-E(R)T}, \quad (6.51)$$

where $F(R)$ reflects again the overlap of our trial state with the ground state of the system. Finally, the interaction energy of the static quark-antiquark pair separated by a distance R is given by

$$E(R) = - \lim_{T \rightarrow \infty} \frac{1}{T} \ln \langle W_{\Gamma}[A] \rangle_{\text{Eucl.}}$$

For clarity and to avoid any confusion, we will denote this energy by $E_{min}(R)$ in the following. It defines the *Wilson potential*

$$E_{min}(R) = E_{se} + V_W(R)$$

as its R -dependent part, the constant part E_{se} representing the quark self-energies.

Let us at this stage emphasize that the whole procedure is performed in a complete gauge invariant way. The final result indeed involves only the Wilson loop, which is a gauge invariant object.

Coulomb vs. Wilson. Let us now consider the energy of the static $q\bar{q}$ state in Coulomb gauge. It reads

$$E_{qq} = \langle \Phi_{qq} | H | \Phi_{qq} \rangle - \langle 0 | H | 0 \rangle, \quad (6.52)$$

where the explicit form of H is given by the Coulomb gauge Hamiltonian (6.40). We will handle this problem by means of group theory considerations, following the derivation performed in Ref. [Zwa03].

The quark and antiquark of the $q\bar{q}$ pair live in the fundamental representation N and \bar{N} of the gauge group $SU(N)$, respectively. Expressed in terms of wave functionals, our trial state reads

$$\Phi_{qq}[A] = \Psi_{qq}^s \Psi_0[A],$$

where the state Ψ_{qq}^s belongs to the singlet (i.e. colourless) part of the decomposition $N \times \bar{N} = 1 + (N^2 - 1)$ and $\Psi_0[A]$ is the wave functional of the vacuum state in the absence of external quarks. In the following, we will use the compact notation $|\Phi_{qq}\rangle = |s\rangle|0\rangle_A$, for the trial state, and $\langle \dots \rangle_A = \int \mathcal{D}A \dots$, for the expectation value. The Coulomb term H_{Coul} of the Hamiltonian (6.40) depends on the external quark fields through the colour-charge density J_0 in (6.41). For the infinitely massive quark and antiquark, which are considered as point-like particles sitting at \mathbf{x} and \mathbf{y} respectively, the colour charge density reads

$$J_0^a(\mathbf{z}) = \lambda_q^a \delta(\mathbf{z} - \mathbf{x}) + \lambda_{\bar{q}}^a \delta(\mathbf{z} - \mathbf{y}),$$

in terms of the Hermitian generators⁵ of the gauge group $SU(N)$ in the fundamental representation N . Due to the decomposition of the total colour charge density $\rho = \rho_{\text{gl}} + J_0$ in (6.41), we can write the Coulomb term H_{Coul} as follows:

$$H_{\text{Coul}} = H_{\text{gl}} + H_{\text{gl qu}} + H_{\text{qu qu}},$$

where H_{gl} is the Hamiltonian in the absence of external quarks, $H_{\text{gl qu}}$ is linear in J_0 and

$$H_{\text{qu qu}} = g_0^2 \frac{1}{2} \sum_{a,b} \int d\mathbf{z}_1 d\mathbf{z}_2 J_0^a(\mathbf{z}_1) \mathcal{V}_{\text{Coul}}^{ab}(\mathbf{z}_1, \mathbf{z}_2) J_0^b(\mathbf{z}_2).$$

The first contribution will return the vacuum energy in the absence of external quarks:

$$\langle \Phi_{qq} | H_{\text{gl}} | \Phi_{qq} \rangle = \langle s | s \rangle \langle 0 | H_{\text{gl}} | 0 \rangle_A = E_0.$$

⁵These matrices act on the first and second indices of the wave functional Φ_{qq} according to $(\lambda_q^a \Phi_{qq})_{\alpha\beta} = (\lambda_N^a)_{\alpha\gamma} \Phi_{qq, \gamma\beta}$ and $(\lambda_{\bar{q}}^a \Phi_{qq})_{\alpha\beta} = -\Phi_{qq, \alpha\gamma} (\lambda_N^a)_{\gamma\beta}$, where λ_N^a are the $N^2 - 1$ Hermitian generators of the gauge group $SU(N)$.

The second term vanishes due to $\langle s | \lambda_{q,\bar{q}}^a | s \rangle = 0$ since $|s\rangle$ is a colour-singlet state. The most interesting part arises from the third term, which gives the contribution

$$\langle \Phi_{qq} | H_{\text{qu qu}} | \Phi_{qq} \rangle = \sum_{i,j \in \{q,\bar{q}\}} \sum_{a,b} \langle s | \lambda_i^a \lambda_j^b | s \rangle \langle 0 | \mathcal{V}_{\text{Coul}}^{ab}(\mathbf{x}, \mathbf{y}) | 0 \rangle_A.$$

From group theory, we know that $\langle s | \lambda^a \lambda^b | s \rangle = -\frac{1}{N^2-1} \delta^{ab} C_N$, where C_N denotes the Casimir of the representation N . Taking all contributions into account, we find

$$E_{qq} = E'_{se} - \underbrace{C_N g_0^2 \langle 0 | \mathcal{V}_{\text{Coul}}^{aa}(\mathbf{x}, \mathbf{y}) | 0 \rangle_A}_{V_{\text{Coul}}(R)}.$$

The first term, independent of R , contains the contribution $i = j = q$ and $i = j = \bar{q}$, i.e. the quark self-energies. The second term, the R -dependent part of the energy E_{qq} , is precisely the Coulomb potential (6.46) of the massive quark-antiquark pair. We find $\mathcal{N} = -C_N$ in the present case.

We can now put all pieces together and compare the two potentials $V_W(R)$ and $V_{\text{Coul}}(R)$. On the one hand, we computed the *ground state energy* $E_{\text{min}}(R)$ of the static $q\bar{q}$ pair, which can be extracted from the expectation value of the Wilson loop. On the other hand, we computed the *total energy* E_{qq} of the system by taking the expectation value (6.52) of the Coulomb gauge Hamiltonian. We have therefore the inequality

$$E_{\text{min}}(R) \leq E_{qq}(R).$$

If the potentials $V_W(R)$ and $V_{\text{Coul}}(R)$ are confining, then we assume that the static quark self-energies E_{se} and E'_{se} are negligible compared to the potentials for sufficiently large R . From this we have, asymptotically,

$$\boxed{V_W(R) \leq V_{\text{Coul}}(R)}. \quad (6.53)$$

The inequality (6.53) was in the recent past investigated by means of lattice simulations. The approach of Cucchieri-Zwanziger [CZ03] is to evaluate the expectation value $\langle M^{-1}(-\Delta)M^{-1} \rangle$ in (6.46). They found a saturation of the inequality, i.e. $V_{\text{Coul}} \simeq V_W$. The approach of Greensite-Olejnik [GO03] is based on the study of the $\langle A_0 A_0 \rangle$ correlator. A great advantage of the method is that Coulomb potential and Wilson potential are the $T \rightarrow 0$ and $T \rightarrow \infty$ limit of the same lattice observable, respectively. This allows a direct comparison. They checked the validity of the inequality (6.53) but found no saturation. Their result is $2V_W < V_{\text{Coul}} < 3V_W$. In the next chapter, we perform the calculation of the Coulomb potential in a similar way to the Cucchieri-Zwanziger approach, which we restrict to a study at fixed time.

Coulomb potential vs. polarization. The Wilson potential is obtained by averaging the Wilson loop operator over all gluonic *and* fermionic fluctuations. If we perform in (6.50) the integration over $\psi, \bar{\psi}$, we obtain formally

$$\langle W_\Gamma[A] \rangle_{\text{Eucl.}} = \frac{\int \mathcal{D}A W_\Gamma[A] \text{Det}[K[A]] e^{-S_{YM}^{\text{Eucl.}}[A]}}{\int \mathcal{D}A \text{Det}[K[A]] e^{-S_{YM}^{\text{Eucl.}}[A]}} ,$$

where $K[A]$ is the matrix $K_{x\alpha,y\beta}[A] = [\gamma_\mu(\partial_\mu + iA_\mu) + m]_{\alpha\beta} \delta^{(4)}(x - y)$. The effects due to the dynamical fermions can be switched off by setting $\text{Det}[K] = 1$, which corresponds to the so-called *quenched approximation*.

Lattice simulations showed in this approximation that the potential $V_W(R)$ rises linearly at large R , i.e. $V_W(R) = \sigma R$, where σ is the so-called *string tension*, signalling the confinement of the two static quarks. Phenomenologically, the linear rising energy corresponds to the concentration of the colour electric flux lines in a string developing between the quarks. If no dynamical quarks are present in the theory, the energy needed to separate the quarks hides in the string developing between the two sources. If dynamical quarks are present, i.e. $\text{Det}[K] \neq 1$, the extraction of a pair of dynamical quarks out of the vacuum appears energetically more favorable than the development of a string binding the two static sources. A pair of mesons is formed at separation R , each meson being formed of one external quark and one dynamical quark. In this case, the potential $V_W(R)$ represents no more the interaction of two external quarks in the vacuum but the potential of two mesons at separation R and should in this respect be regarded as an analogue of a Van der Waals interaction potential. The Wilson potential is no more confining, which does not mean that the theory does not confine colour charges any more. A more fundamental quantity should be found, which does not lose its confining property, even in the presence of dynamical quarks.

Let us return to the Coulomb potential, in particular to the decomposition (6.45) of the correlator $\langle A_0 A_0 \rangle$ in the instantaneous part V_{Coul} and the P_0 term, on the physical meaning of which we comment briefly. The P_0 term represents the *vacuum polarization* induced by the dynamical quarks, the minus sign appearing in front of P_0 signalling that it corresponds to screening. By virtue of the inequality (6.53), the first term in (6.45) is confining in the absence of dynamical quarks, since the Wilson potential is confining, and dominates the polarization term. When the quark determinant is switched on, the Wilson potential loses its confining property, signalling that the screening term P_0 dominates the Coulomb potential. This latter, however, is perhaps still linearly confining even when the Wilson potential is not: the long range of V_{Coul} could precisely be what renders the production of dynamical quark from the vacuum energetically favorable [CZ02b]. In this respect, the Coulomb potential provides, under this assumption, a good candidate for an order-parameter of the confinement of the colour charge even when dynamical quarks are present. This statement has however to be refined in view of recent calculations of the Coulomb potential at finite temperature, as explained below. Lattice investigations of the Coulomb potential with dynamical quarks have, to our knowledge, not yet been performed.

Potentials at finite temperature. Wilson and Coulomb potential can be, by means of lattice techniques, studied as a function of the temperature. In the quenched approximation, i.e. in the absence of polarization effects, it is well known that the string tension $\sigma(T)$ drops to zero above a critical temperature T_C signalling the transition from a confining phase ($\sigma \neq 0$) to a deconfined phase ($\sigma = 0$). A recent lattice study of the Coulomb potential at finite temperature [GOZ04] has shown that the Coulomb string tension σ_{Coul} does not vanish above the critical temperature T_C . This quite surprising result can, however, be explained by an analogy with the calculation of 'spatial' Wilson loops. If we would indeed compute the Wilson loop (6.50) for a spatial contour, along, let us say, the x and y directions, we would find that the spatial Wilson 'potential' would not lose its confining property above T_C . Now, since the Coulomb potential operator $\mathcal{V}_{\text{Coul}}$ is defined, at fixed time, in a three

dimensional 'spatial' time slice, it is argued that the same mechanism possibly applies to the case of the Coulomb potential. In the lattice language to be defined in the next chapter, the Coulomb potential does not reflect deconfinement for $T > T_C$ since the spatial links in a time slice, which enter the definition of the potential, do not lose their confining property above the critical temperature.

6.4.4 Coulomb potential and renormalization

The Coulomb potential is a renormalization group invariant quantity [Zwa98, CZ02b]. This is due to the remarkable fact that the quantity $g_0 A_0$ is in Coulomb gauge invariant under renormalization. More exactly, we have [the indices B and R stand for *bare* and *renormalized*, resp.]

$$g_0 A_0^B(x) = g_R A_0^R(x), \quad (6.54)$$

i.e. the renormalization of the coupling and the wave function renormalization of the gauge potential produce an invariant quantity. The calculations were performed in the so-called *interpolating gauge* characterized by the condition $\partial_i A_i + \lambda \partial_0 A_0 = 0$, where λ is a real positive parameter [BZ99]. This gauge is renormalizable and has the advantage that it can be treated at finite λ using standard BRST methods, i.e. inherits the computational tools developed in the covariant quantization of gauge theories. The calculations are performed at finite λ and the Coulomb gauge results are obtained by taking the limit $\lambda \rightarrow 0$. As a consequence of (6.54), the Coulomb potential possesses the property

$$V_{\text{Coul}}^B(k, g_0, \Lambda) = V_{\text{Coul}}^R(k, g_R, \mu),$$

where Λ is an ultraviolet cutoff and μ the renormalization mass. In particular, the Coulomb potential provides a convenient definition of the running coupling constant,

$$\alpha_s(|\mathbf{k}|/\Lambda_{\text{Coul}}) = C \mathbf{k}^2 V_{\text{Coul}}(|\mathbf{k}|) \quad (6.55)$$

with some group theoretic prefactors C and Λ_{Coul} a finite QCD mass scale.

6.4.5 Confinement scenario

We defined in (6.41) the Faddeev-Popov operator $M = -\nabla \cdot \mathbf{D}$. It is clear that this quantity plays a crucial role in the problem of colour confinement, since it is the only operator entering the Coulomb potential, up to the trivial Laplace operator. The vacuum expectation value of the Faddeev-Popov operator, i.e.

$$D^{ab}(\mathbf{x} - \mathbf{y}) := \langle M^{-1}[A]_{(\mathbf{x}, \mathbf{y})}^{ab} \rangle. \quad (6.56)$$

is the *ghost propagator*⁶. The Fourier transform $V_{\text{Coul}}(\mathbf{k})$ of the Coulomb potential can be parameterized in the following way [Zwa98]:

$$V_{\text{Coul}}(|\mathbf{k}|) = -C_N \mathbf{k}^2 D^2(\mathbf{k}) f(\mathbf{k}). \quad (6.57)$$

The dimensionless function $f(\mathbf{k})$ measures the deviation of the Coulomb potential from the factorization

$$\langle M^{-1}[A](-\Delta) M^{-1}[A] \rangle \rightarrow \langle M^{-1}[A] \rangle (-\Delta) \langle M^{-1}[A] \rangle, \quad (6.58)$$

⁶This quantity is indeed equivalent to the correlation function $\langle \bar{c}^a(\mathbf{x}) c^b(\mathbf{y}) \rangle$ of the *ghost fields* $c^a(\mathbf{x})$, which arise from a functional representation of the determinant in (6.38) in terms of Grassman fields.

in which case we have $f(\mathbf{k}) \equiv 1$.

When Gribov pointed out the problem of gauge copies and discussed the possible restriction of the gauge field integration to the first Gribov region Ω , he already stressed the possible relation between this restriction to Ω and the confinement problem by discussing the infrared behaviour of the ghost propagator. The confinement scenario is nowadays stated as follows. The Coulomb potential $V_{\text{Coul}} \propto \langle M^{-1}[A](-\Delta)M^{-1}[A] \rangle$ is long range (i.e. enhanced in the regime of small momenta) because $M^{-1}[A]$ is long range. This results from entropy considerations: since the dimension of configuration space is very large, it is reasonable to think that most of the configurations are located close to the Gribov horizon (just as the volume measure $r^{d-1}dr$ of a sphere in d dimensions is enhanced near the radius). This suggests that the near-zero eigenvalues of the Faddeev-Popov operator dominate at large quark separations.

Our investigations in the framework of lattice gauge theory reported in the next chapter will concern the study of the ghost propagator (6.56) and the Coulomb potential. Since these quantities can be determined independently, we can also address the function $f(\mathbf{k})$ and therefore study the deviation of the Coulomb potential from the factorization (6.58).

It was recently pointed out [GOZ04] that the confinement scenarios based on the dominance on some subsets of gauge field configurations, i.e. the center vortices or magnetic monopoles mentioned in the introduction, are compatible with Gribov's scenario of confinement. When such configurations are gauge transformed to minimal Coulomb gauge (Sec. 6.4.2), they lie on the boundary $\partial\Lambda$ of the fundamental modular region Λ .

6.5 Summary

In this chapter, we discussed the quantization of Maxwell and Yang-Mills theory in the light of the Dirac quantization scheme for constrained systems. We focused in particular on the Coulomb gauge fixing procedure for which transversality of the gauge potential is imposed: $\partial_i A_i = 0$. Coulomb gauge is a physical gauge, in the sense that all constraints can be eliminated at the level of the Hamiltonian and the Hilbert space contains only the physical transverse degrees of freedom. In particular, Gauss's law is automatically satisfied in the quantized theory and must not be imposed afterwards on the physical states. Transversality has however its price: the formulation in Coulomb gauge lacks the Lorentz covariance of the original Lagrangian, which is restored at the level of the S -matrix, due to gauge invariance. A particular advantage of the elimination of the longitudinal degrees of freedom in the Hamiltonian is the Coulomb term in which the Coulomb interaction operator can be read off directly: $\mathcal{V}_{\text{Coul}} = M^{-1}[A](-\Delta)M^{-1}[A]$, with the Faddeev-Popov operator $M[A] = -\nabla \cdot \mathbf{D}[A]$.

The Coulomb gauge quantization scheme is spoiled by the presence of Gribov copies, i.e. gauge-equivalent transverse configurations. This problem is bypassed by restricting the configuration space to the fundamental modular region Λ which is the ensemble of the global minima of the functional (6.44) on each gauge orbit. This region is included in the Gribov region Ω defined by the condition $M[A] \geq 0$, which Gribov originally (and erroneously) believed to be free of gauge copies.

The Coulomb potential $V_{\text{Coul}} = -C_N g_0^2 \langle \mathcal{V}_{\text{Coul}} \rangle$ is not the Wilson potential V_W of a static quark anti-quark pair extracted from the gauge invariant Wilson loop. The latter

represents the ground state energy of the pair, whereas the former represents the total energy. This fact gives rise to the inequality $V_W \leq V_{\text{Coul}}$. From this, we know that the Coulomb potential is confining when the Wilson potential is confining, i.e. for instance in the absence of polarization effects induced by dynamical quarks. Since the Coulomb potential is an upper bound of the Wilson potential, it could possibly remain confining even when the Wilson potential is not, for instance due to polarization effects. In view of a recent study of the Coulomb potential at finite temperature, V_{Coul} can however not serve as an order parameter for the confinement of colour charges, since it does not lose its confining property in the deconfined phase, i.e. above the critical temperature T_C . From entropy considerations, it is believed that most of the gauge field configurations are located close to the border of the Gribov region Ω , leading to an enhancement of the Coulomb potential at large scales, i.e. in the regime of small momenta. This is the modern formulation of Gribov's confinement scenario, in which the mechanisms based on the dominance of center vortices or magnetic monopoles do fit, since it is proved that these special configurations lie precisely on the border of the fundamental modular region, when they are transformed to minimal Coulomb gauge.

Chapter 7

Coulomb gauge on the lattice

This chapter is devoted to the investigation of Yang-Mills theory in the Coulomb gauge formulation by means of lattice simulations. We study in particular the ghost propagator and the Coulomb potential for the gauge group $SU(2)$. Gluonic correlations are also addressed via the study of the equal-time transverse gluon propagator. We compare our results with the most recent analytical study performed in the Hamilton formalism [FRa]. We review in the first section some basic concepts of the lattice approach to gauge theories, which can be skipped by the reader who is mainly interested in the results. In the intermediate sections (7.2 to 7.4), we give a precise description of our numerical procedure: gauge fixing, measurements and definitions of the lattice observables. Finally, the results for gluon and ghost propagators as well as for the Coulomb potential are presented for the cases $D = 2 + 1$, $D = 3 + 1$ and critically discussed.

Conventions. We use throughout this chapter the “lattice conventions”, see Sec. C.1, and limit ourselves to the gauge group $SU(2)$.

7.1 Basic facts about lattice gauge theories

7.1.1 Basic definitions

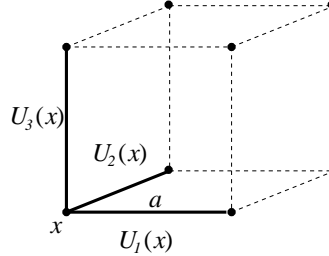
The space-time is discretized and considered as a D -dimensional lattice with *lattice spacing* denoted by a . The lattice extension is fixed by a D -plet of integer parameters $\{N_1, \dots, N_D\}$ and the *lattice volume* is the dimensionless number $V = N_1 \times \dots \times N_D$.

In the framework of a gauge theory formulated in the continuum, the *gauge potential* A_μ is the *connection* in the space-time equipped with the *gauge group*, which we denote by G . Expressed in simple words, its role is to compare the phase φ of a field $\psi(x) = R(x)e^{i\varphi(x)}$ at two different points x_1 and x_2 in space-time. Expressed in mathematical terms, we have for the points $x_1 = x$ and $x_2 = x + dx$:

$$\psi(x + dx) = U(x)\psi(x), \quad \text{with } U(x) = e^{iA_\mu(x)dx^\mu}.$$

The matrix $U(x)$, element of the gauge group G , specifies the rotation of the basis frame in the gauge symmetry space upon transport between the neighbouring space-time points x and $x + dx$. The matrix $A_\mu(x)$ belongs to the Lie algebra associated to G .

On the lattice, the 'transporters' $U(x)$ are considered as fundamental degrees of freedom, in place of the potentials $A_\mu(x)$. At each lattice site x , D matrices $U_1(x), \dots, U_D(x) \in G$ are given, one for each link connecting x with its D neighbours in the directions given by the unit vectors, i.e. $x + a\mathbf{e}_1, \dots, x + a\mathbf{e}_D$.



The link connecting $x + a\mathbf{e}_\mu$ to x is given by the inverse element $U_\mu^{-1}(x)$. The links are the fundamental dynamical degrees of freedom and a state of the system is specified by the ensemble $\{U_\mu(x)\}$. The action of a lattice *gauge transformation* at the site x is defined by

$$U_\mu^g(x) = g(x)U_\mu(x)g^\dagger(x + a\mathbf{e}_\mu), \quad (7.1)$$

with $g(x), g^\dagger(x + a\mathbf{e}_\mu) \in G$. For the case $G = SU(2)$, a link U can be represented in terms of the Pauli matrices σ :

$$U = a_0 + \mathbf{a} \cdot \boldsymbol{\sigma} \quad \text{or} \quad U = \cos \theta + i\boldsymbol{\sigma} \cdot \mathbf{n} \sin \theta, \quad (7.2)$$

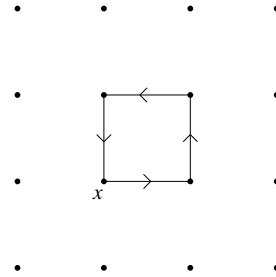
where the point (a_0, \mathbf{a}) lives on the unit sphere $S^3 \equiv a_0^2 + \mathbf{a}^2 = 1$ and \mathbf{n} is a unit vector.

In the continuum, the field strength $F_{\mu\nu}(x)$ analyses the change in phase of a field along an infinitesimal closed path of base-point x . In mathematical terms, the matrix

$$U_{P_{\mu\nu}}(x) = \exp(iF_{\mu\nu}(x)dx^\mu dx^\nu) \quad (7.3)$$

specifies the rotation of the basis frame in the gauge symmetry space upon transport along an infinitesimal rectangular closed path of sides dx_μ and dx_ν [there is no summation on repeated indices]. On the lattice, these paths are taken along the sides of the elementary squares, which are called *plaquettes*, and $U_{P_{\mu\nu}}(x)$ is given by the product of the links spanning the plaquette:

$$U_{P_{\mu\nu}}(x) = U_\mu(x)U_\nu(x+a\mathbf{e}_\mu)U_\mu^{-1}(x+a\mathbf{e}_\nu)U_\nu^{-1}(x).$$



The matrix $U_{P_{\mu\nu}}(x)$ transforms according to $U_{P_{\mu\nu}}^g(x) = g(x)U_{P_{\mu\nu}}(x)g^{-1}(x)$ under a gauge transformation. Taking the trace $\text{tr}[U_{P_{\mu\nu}}]$ builds the most fundamental gauge invariant object on the lattice.

7.1.2 Wilson's action - Partition function - Observable

The *Wilson* representation of the action in $SU(N)$ Yang-Mills theory is given by

$$S_W[\beta, U] = \beta \sum_{P_{\mu\nu}} \left(1 - \frac{1}{N} \text{Re tr}[U_{P_{\mu\nu}}] \right), \quad \beta = \frac{2N}{g_0^2} a^{D-4}, \quad (7.4)$$

where g_0 denotes the bare coupling. Note the gauge invariance of S_W since it essentially resums all lattice plaquettes. Recalling (7.3) and using the representation (7.2) of $U_{P_{\mu\nu}}$, we have, for $SU(2)$,

$$S_W[\beta, U] = \frac{4a^{D-4}}{g_0^2} \sum_{P_{\mu\nu}} (1 - \cos \theta_{P_{\mu\nu}}) \xrightarrow{a \rightarrow 0} \sum_x \sum_{\mu\nu} \sum_a \frac{a^D}{4g_0^2} F_{\mu\nu}^a F_a^{\mu\nu} \simeq \int d^D x \frac{1}{4g_0^2} F_{\mu\nu}^a F_a^{\mu\nu},$$

i.e. the Wilson action corresponds to the Yang-Mills action in the naive $a \rightarrow 0$ limit.

The lattice gauge theory is defined by the *partition function*

$$\boxed{Z(\beta) = \int \mathcal{D}U e^{-S_W[\beta, U]}} \quad (7.5)$$

in Euclidean space-time. The quantum Yang-Mills theory is mapped onto a problem of statistical physics, with respect to the link ensemble $\{U_\mu(x)\}$. The measure $\mathcal{D}U$ is the so-called *Haar measure* and has the property of gauge invariance: $\mathcal{D}U^g = \mathcal{D}U$.

The quantum expectation value of an *observable* $\mathcal{O}[U]$ is obtained by averaging over all field configurations

$$\boxed{\langle \mathcal{O} \rangle(\beta) = \frac{1}{Z(\beta)} \int \mathcal{D}U \mathcal{O}[U] e^{-S_W[\beta, U]}. } \quad (7.6)$$

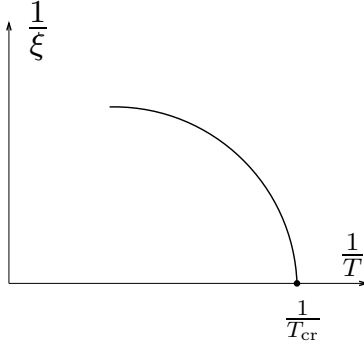
7.1.3 Continuum limit

A simple and naive rescaling of a to zero is not sufficient to define a continuum quantum theory from the partition function (7.5). Let us examine how the limit $a \rightarrow 0$ can be performed.

Before discussing this point, we make a digression and consider a simpler statistical problem, namely a spin system describing the thermodynamical properties of ferromagnetic matter. We consider the *correlation length* ξ measuring the typical extension of clusters composed of equally oriented spins. Mathematically, it is obtained by studying the decrease of the spin-spin correlator as a function of the distance:

$$\langle s(\mathbf{x})s(\mathbf{y}) \rangle(T) \propto \exp\left(-\frac{|\mathbf{x} - \mathbf{y}|}{\xi(T)}\right).$$

As a function of the temperature, the correlation length shows the following behaviour:



For a critical value of the temperature T_{cr} , a divergence in the spin correlation length occurs. The correlation function becomes independent of the position, which in reality signals the appearance of large clusters of correlated spins and the transition to the phase of spontaneous magnetization.

Let us now return to lattice gauge theory. Suppose that we want to extract the mass spectrum of the corresponding field theory. This is done by studying the appropriate correlation functions for large Euclidean times. The existence of a continuum limit of the lattice field theory implies that

$$\frac{\hat{m}(g_0)}{a} \xrightarrow{a \rightarrow 0} m_{\text{phys}}, \quad (7.7)$$

with \hat{m} the mass measured in lattice units for a given value of the coupling g_0 . If the corresponding physical mass, m_{phys} , is finite, then \hat{m} has to vanish in the continuum limit. Thinking of \hat{m} in terms of an inverse correlation length, the continuum field theory can only be realized at a *critical point* of the statistical system described by the partition function (7.5). This point corresponds to a critical value of the bare coupling g_0^{cr} , in analogy with the critical temperature of the spin system. The condition (7.7) implies also that there must exist a relation $g_0(a)$ between the coupling constant and the lattice spacing, which guarantees that physical quantities have a finite limit at vanishing lattice spacing. For a well-defined renormalizable theory, this relation should moreover yield unique finite limits for all observables, i.e. the function $g_0(a)$ should not depend on the observable.

The evolution $g_0(a)$ is obtained in the following way. Let us consider the static $q\bar{q}$ potential discussed in the previous chapter. The potential is in physical units given by

$$V_W(R, g_0, a) = \frac{1}{a} \hat{V}_W \left(\frac{R}{a}, g_0 \right),$$

where R is the physical separation of the quark-antiquark pair. The coupling g_0 must be tuned in such a way as to ensure that the physical potential $V_W(R, g_0(a), a)$ is independent of the lattice spacing, i.e. $\frac{d}{da} V_W(R, g_0(a), a) = 0$. This is expressed mathematically by the so-called renormalization group (RG) equation:

$$\left[a \frac{\partial}{\partial a} - \beta(g_0) \frac{\partial}{\partial g_0} \right] V_W(R, g_0, a) = 0, \quad \beta(g_0) = -a \frac{\partial g_0}{\partial a}. \quad (7.8)$$

The function $\beta(g_0)$, which precisely describes the dependence of the coupling on the lattice spacing, plays a central role in the theory of renormalization. In particular, the critical values g_0^{cr} for which a continuum limit can be achieved correspond to the zeros of the β -function, the so-called *fixed points*. The β function is obtained perturbatively, i.e. as an expansion in

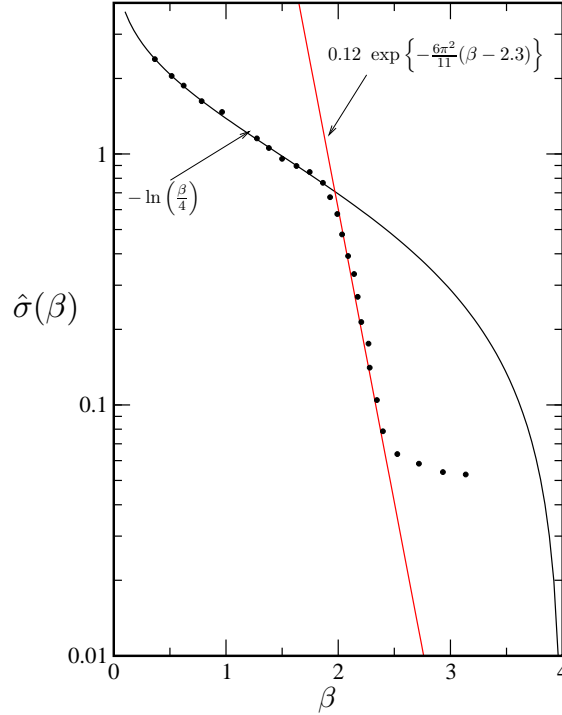


Figure 7.1: The string tension $\hat{\sigma}$ as a function of β for $SU(2)$ in $D = 3 + 1$. The scaling window corresponds to the interval $[2.1, 2.6]$. For $\beta < 2.1$, the measurements follow the strong coupling curve $-\ln\left(\frac{\beta}{4}\right)$, while the deviation from the scaling function for $\beta > 2.6$ is due to finite size effects.

powers of g_0 , by inserting the perturbative expansion of the potential into the RG equation (7.8). This yields $\beta(g_0) = -\beta_0 g_0^3 - \beta_1 g_0^5 + \mathcal{O}(g_0^7)$. We see that $g_0 = 0$ is a critical value of the coupling constant: when the lattice spacing is decreased, g_0 is driven towards the fixed point $g_0^{\text{cr}} = 0$, i.e. the continuum limit will be realized at vanishing bare coupling. Solving for a , we find

$$a(g_0) = \frac{1}{\Lambda_L} f(g_0), \quad f(g_0) = (\beta_0 g_0^2)^{-\frac{\beta_1}{2\beta_0^2}} \exp\left(-\frac{1}{2\beta_0 g_0^2}\right) \quad (7.9)$$

where a dimensional integration constant Λ_L has been introduced.

How to be sure that we are extracting continuum physics when performing calculations with a finite (even small !) lattice spacing¹ ?

Let us recall the condition of finiteness for an observable \mathcal{O} , reformulated in terms of g_0 :

$$\left(\frac{1}{a(g_0)}\right)^{d_{\mathcal{O}}} \hat{\mathcal{O}}(g_0) \xrightarrow{g_0 \rightarrow g_0^{\text{cr}}} \mathcal{O}_{\text{phys}},$$

where $d_{\mathcal{O}}$ is the energy dimension of the observable and $\hat{\mathcal{O}}$ is measured in lattice units. Inserting (7.9) into this relation, we obtain

$$\hat{\mathcal{O}}(g_0) \xrightarrow{g_0 \rightarrow g_0^{\text{cr}}} \hat{C}_{\mathcal{O}} [f(g_0)]^{d_{\mathcal{O}}}, \quad (7.10)$$

¹The critical value $g_0^{\text{cr}} = 0$ corresponding to $a = 0$ cannot be reached when performing the calculations on a computer. Even small, the lattice spacing remains of course finite !

where $\hat{C}_{\mathcal{O}}$ is the dimensionless constant $\mathcal{O}_{\text{phys}}/\Lambda_L^{d_{\mathcal{O}}}$. Quantities behaving like $\hat{\mathcal{O}}$ show *asymptotic scaling*, a behaviour signaling that we are extracting continuum physics from the numerical investigation of the observable $\hat{\mathcal{O}}$ on the lattice. At a practical level, there exists in general only a narrow region in the coupling constant space, called *scaling window*, where $\hat{\mathcal{O}}(g_0)$ scales according to (7.10). Physics will indeed no longer fit on the lattice if g_0 becomes too small (finite size effects), while increasing the bare coupling may render the lattice too coarse to account for fluctuations taking place on a small scale (strong coupling limit).

The constant Λ_L has introduced a scale, in terms of which the physical observable is measured:

$$\mathcal{O}_{\text{phys}} = \hat{C}_{\mathcal{O}} \Lambda_L^{d_{\mathcal{O}}}. \quad (7.11)$$

The appearance of a dimensional quantity like Λ_L in a theory which is *a priori* free of any scale is well known from perturbation theory in the continuum, where the regularization of divergent integrals requires the introduction of a scale. This is called *dimensional transmutation*. In this work, the scale in $D = 3 + 1$ is set by adjusting the string tension extracted from the study of the Wilson $q\bar{q}$ potential to the experimental value σ_{exp} . For $D = 3 + 1$ and $SU(2)$, the relation (7.10) reads:

$$\hat{\sigma}(g_0) = \sigma_{\text{exp}} a^2(g_0) = 0.12 \exp \left\{ -\frac{6\pi^2}{11}(\beta - 2.3) \right\}, \quad \sigma_{\text{exp}} = (440 \text{ MeV})^2. \quad (7.12)$$

The scaling behaviour of $\hat{\sigma}(g_0)$ is illustrated in Fig. 7.1, extracted from Ref. [CJR83], where we can clearly identify the scaling window $2.1 \leq \beta \leq 2.6$. In $D = 2 + 1$, we express all dimensional quantities in units of the bare coupling squared g_0^2 , which has the dimension of a mass, see (7.4). The scaling window is given by $3.5 \leq \beta \leq 7$.

7.2 Fixing the Coulomb gauge

The lattice formulation does not only provide a gauge theory with a momentum cut-off. The finiteness of the system ensures that the integration over redundant configurations of the gauge field, i.e. Gribov copies, has harmless consequences. The fixing of a gauge is thus in principle not required in the lattice formulation of a gauge theory. This is actually true as long as we deal with gauge invariant observables: the investigation of gauge-dependent quantities, like propagators, of course requires the fixing of a gauge.

7.2.1 General framework

Our starting point is the lattice pendant of the partition function (6.38) obtained in Coulomb gauge:

$$Z(\beta) = \int \mathcal{D}U \Delta_f(U) \delta(f(U)) \exp(-S_W[\beta, U]),$$

where $\Delta_f(U)$ is the lattice Faddeev-Popov determinant and $f(U)$ is the gauge condition expressed in terms of the link variables. The expectation value of an observable \mathcal{O} reads in this case

$$\langle \mathcal{O}_f \rangle(\beta) = \frac{1}{Z(\beta)} \int \mathcal{D}U \mathcal{O}(U) \Delta_f(U) \delta(f(U)) \exp(-S_W[\beta, U]),$$

where the suffix f indicates that the expectation value depends on the gauge. A straightforward implementation is however rendered difficult by the calculation of the Faddeev-Popov

determinant. Instead of this, we derive an equivalent expression. Integrating numerator and denominator over gauge transformations g , we have

$$\begin{aligned} \langle \mathcal{O}_f \rangle(\beta) &= \frac{1}{Z(\beta)} \int \mathcal{D}g \int \mathcal{D}U \mathcal{O}(U) \Delta_f(U) \delta(f(U)) \exp(-S_W[\beta, U]) \\ &= \frac{1}{Z(\beta)} \int \mathcal{D}g \int \mathcal{D}U \mathcal{O}(U^g) \Delta_f(U^g) \delta(f(U^g)) \exp(-S_W[\beta, U]) \\ &= \frac{1}{Z(\beta)} \int \mathcal{D}U \mathcal{O}(U^g(U)) \exp(-S_W[\beta, U]), \end{aligned} \quad (7.13)$$

where we have renamed the integration variable $U \rightarrow U^g$ in the second step and used the gauge invariance of the Haar measure and the Wilson action. The integration over g has eliminated the delta function and the Faddeev-Popov determinant in the third step. The function $g(U)$ denotes the ensemble of gauge transformations $g(x)$ gauging the given configuration U in such a way that

$$f(U^g(U)) = 0. \quad (7.14)$$

The expression (7.13) suggests the following procedure: before a measurement is performed, the lattice is frozen and the gauge transformation $g(U)$ solution of (7.14) is computed. The lattice is then transformed to the gauged configuration, for which the observable is evaluated.

7.2.2 Gauge fixing as a minimization problem

The implementation of the gauge fixing condition² $f(U) = \hat{\nabla} \cdot \hat{\mathbf{A}} = 0$ works as follows. The task to be performed is to find, for a frozen configuration U , the gauge transformation $g_{min}(U)$ which minimizes the following functional

$$F_U[g] = \sum_t \sum_{\mathbf{x}, i} \text{Re Tr}(1 - U_i^g(\mathbf{x}, t)). \quad (7.15)$$

Let us show how the minimization procedure of $F_U[g]$ leads to the Coulomb gauge condition. As the gauge fixing procedure involves only spatial links, each time slice t decouples from its neighbours $t + 1$ and $t - 1$. The gauge fixing of the spatial links $U_i(\mathbf{x}, t)$ indeed has no influence on the links $U_i(\mathbf{x}, t + 1)$ and $U_i(\mathbf{x}, t - 1)$. We consider the gauge fixing procedure in a given time slice t , i.e. the minimization of the functional

$$F_U^t[g] = \sum_{\mathbf{x}, i} \text{Re Tr}(1 - U_i^g(\mathbf{x}, t)) \quad (7.16)$$

at fixed t . For convenience, we drop the t dependence of the links and the gauge functions. Let us parameterize the gauge function g by $g(\tau, \mathbf{x}) := \exp(i\tau\omega(\mathbf{x}))$, where τ is a real parameter and $\omega(\mathbf{x})$ an element of the Lie algebra, for all \mathbf{x} . In terms of the τ parameter, the gauge condition in each time slice is reformulated:

$$\left. \frac{d}{d\tau} F_{U_{min}}^t[\omega, \tau] \right|_{\tau=0} = 0, \quad \left. \frac{d^2}{d\tau^2} F_{U_{min}}^t[\omega, \tau] \right|_{\tau=0} \geq 0, \quad \text{for all } \omega, \quad (7.17)$$

²We use the 'lattice notation' defined in Appendix C.

where $U_{min} = U^{g_{min}(U)}$. The differentiation of the gauge functional is performed in Sec. C.7 and reads

$$\frac{d}{d\tau} F_U^t[\tau, \omega] = \langle \omega, \hat{\nabla}^{(-)} \cdot \hat{\mathbf{A}}^\tau \rangle.$$

The first condition in (7.17) yields the transversality of the lattice potential at the minimum configuration $A_{min}^{\tau=0}$, since $\langle \omega, \hat{\nabla}^{(-)} \cdot \hat{\mathbf{A}}_{min}^{\tau=0} \rangle = 0$ must hold for all ω . The derivative of the gauge potential with respect to the parameter τ is, up to the minus sign, the lattice covariant derivative of ω (see Sec. C.5):

$$\frac{d^2}{d\tau^2} F_U^t[\tau, \omega] = \langle \omega, -\hat{\nabla}^{(-)} \cdot \hat{\mathbf{D}}[U]\omega \rangle.$$

This yields the condition $\langle \omega, -\hat{\nabla}^{(-)} \cdot \hat{\mathbf{D}}[U_{min}]\omega \rangle \geq 0$ which implies the positivity of the lattice Faddeev-Popov operator at the minimum of F_U^t . Recalling the discussion of Sec. 6.4.2 of the previous chapter, we find that the minimization procedure of F_U is similar to the minimization procedure of (6.44). The set of all configurations U_{min} for which the functional (7.15) is a minimum on each gauge orbit at $g = 1$ represents the lattice Gribov region Ω . *Minimal* Coulomb gauge would be furthermore numerically achieved if the minimization procedure is implemented in a such a way as to provide the absolute minimum of (7.15). In this case, the obtained configuration would lie in the fundamental modular region Λ . The global minimum along the gauge orbit can unfortunately not be found in a systematical way by means of standard minimization procedures, e.g. iterated overrelaxation. Improvement is however possible, for instance by implementing the simulated annealing method, which reduces the attraction of the nearest local minima. This is discussed in the next section.

7.2.3 Complete gauge fixing

In the Coulomb gauge formulation, there are essentially two ways of fixing the gauge completely over the whole lattice.

Gauging each time slice. The most obvious solution is to fix the gauge in each time slice separately using the method of minimization of the previous section. After this procedure has been performed, the lattice gluon field is 3-dimensionally transverse in each time slice. But the gauge fixing is at yet incomplete because it leaves a t -dependent but \mathbf{x} -independent gauge transformation $g(t)$ arbitrary. There is indeed still the freedom to perform the following gauge transformations:

$$U_i(\mathbf{x}, t) \rightarrow g(t)U_i(\mathbf{x}, t)g^\dagger(t), \quad (7.18)$$

$$U_0(\mathbf{x}, t) \rightarrow g(t)U_0(\mathbf{x}, t)g^\dagger(t+1). \quad (7.19)$$

The standard procedure is to involve the gauge field $A_0^g(x)$ for residual gauge fixing. An example is the Cucchieri-Zwanziger condition [CZ02a], which makes the temporal links as close to unity as possible by minimizing the “vertical” functional

$$F_{\text{ver,U}}[g] = \sum_{\mathbf{x}, t} \text{ReTr}(1 - U_0^g(\mathbf{x}, t)) \xrightarrow{g(t)} \min.$$

Remark: A completion of the gauge fixing which does not involve temporal links should however be more satisfactory, since we know from the previous chapter that A_0^g is in Coulomb

gauge not fixed by a supplementary gauge condition but integrated out from the path integral, giving rise to Gauss's law. A natural choice would be to define a matrix $G^{ab}(t_0)$ in terms of the spatial links in each time slice t_0 and to implement a gauge condition with respect to the transformation property of G under the remaining gauge degree of freedom.

Quasi-temporal gauge. A complete lattice gauge fixing can be achieved in the framework of the quasi-temporal gauge. In this scheme, the two following conditions are enforced:

$$\begin{aligned} A_0(\mathbf{x}, t) &= 0, \\ \partial_i A_i(\mathbf{x}, t_0) &= 0, \end{aligned} \tag{7.20}$$

for all t and fixed t_0 , i.e. combines the temporal gauge condition $A_0 = 0$ with the Coulomb condition in a fixed time slice. The quasi-temporal gauge fixing is implemented as follows [CPPV96]. First, the Coulomb condition (7.20) is implemented by minimizing the functional $F_U^{t_0}[g]$ in (7.16). Second, we perform gauge transformations on all temporal links $U_0(\mathbf{x}, t)$ in such a way that

$$U_0^g(\mathbf{x}, t) = \sqrt[N_t]{P(\mathbf{x})} \tag{7.21}$$

for all t 's and fixed \mathbf{x} , where $P(\mathbf{x}) = \prod_l^{N_t} U_0(\mathbf{x}, t_l)$ is the Polyakov loop at the spatial point \mathbf{x} and N_t labels the number of lattice points in the time direction. This procedure differs slightly from the original method used by Conti and collaborators [CPPV96]. The temporal gauge condition is not exactly implemented on the lattice: it is only realized in the limit $N_t \rightarrow \infty$. One can easily show (see Sec. C.7) that the gauge transformation $g(\mathbf{x}, t_s)$ to be performed in order to achieve (7.21) is given by

$$g(\mathbf{x}, t_s) = \prod_l^{s-1} [\sqrt[N_t]{P(\mathbf{x})}]^\dagger g(\mathbf{x}, 1) \prod_l^{s-1} U_0(\mathbf{x}, t_l), \tag{7.22}$$

i.e. all gauge transformations are obtained recursively from $g(\mathbf{x}, 1)$, which has to be set to unity $g(\mathbf{x}, 1) = 1$ in order to ensure the invariance of the Polyakov loop.

A clear advantage of the quasi-temporal gauge is that we only need to fix the Coulomb gauge in one time slice. It is obvious that the method is only suitable for investigations of observables at equal-time. Due to the fact that $g(\mathbf{x}, 1) = 1$, we can furthermore spare the gauge fixing of the temporal links $U_0(\mathbf{x})$ if we restrict ourselves to the time slice $t = 1$, provided that the observables of interest depend only on spatial links $U_i(\mathbf{x})$.

In the present work, we investigate *equal-time propagators*, i.e. two-point correlation functions of the type

$$C_{\mathcal{O}}(\mathbf{x} - \mathbf{y}) = \langle \hat{\mathcal{O}}(t_0, \mathbf{x}) \hat{\mathcal{O}}(t_0, \mathbf{y}) \rangle,$$

at fixed time t_0 , which are also the quantities of interest studied in the Hamiltonian formalism. The computations in this analytical approach are indeed performed in the Schrödinger picture, i.e. the dynamical evolution of the system is contained in the wave functional solution of the Schrödinger equation, while the quantum operators are time-independent. In view of this restriction to equal-time quantities, we choose the quasi-temporal gauge for the present simulations. Since the observables of interest do not depend on the temporal links, we do not need the fixation of the temporal gauge (7.21) but only transversality of the gauge field in the first time slice $t = 1$.

7.2.4 Numerical implementation

We describe briefly the numerical minimization procedure of the functional (7.16). For the interested reader, a more detailed description of the algorithms is given in Appendix D.

As stated in the previous section, we perform gauge fixing in one time slice, in view of the fact that we investigate equal-time observables. We choose the time slice $t = 1$ and drop in the following the time dependence of links and gauge transformations. Our gauge fixing procedure works in two steps. First, we compute the field of gauge transformations $\{g_{min}(\mathbf{x})\}$ using a method based on the simulated annealing algorithm. We proceed in a second step with the iterated overrelaxation procedure.

Simulated annealing. The aim of the *simulated annealing* method [PFTV] is to force the system to escape the attraction of the nearest local minimum and to lead it towards the absolute minimum³ on the current gauge orbit. The idea is to consider the gauge functional $F_U[g]$ as the action of a fictitious field theory with respect to the set of the gauge transformations $g(\mathbf{x})$. The partition function is given by

$$Z_U(\beta_{SA}) = \int Dg \exp(-\beta_{SA} F_U[g]).$$

Note that the lattice configuration U is frozen during all the simulated annealing process. By increasing step by step the free parameter β_{SA} (which plays the role of the inverse temperature), we try by cooling to retrieve the ground state of the fictitious field theory. The thermalization steps are performed using the standard Creutz update algorithm (see D.1). Once the field $g_{min}(\mathbf{x})$ has been found, the whole lattice is gauge transformed to $U^{g_{min}}$.

Iterated overrelaxation. The *iterated overrelaxation* method consists in local updates of the lattice configuration. At each site \mathbf{x} the optimal gauge transformation $g(\mathbf{x})$ is computed and immediately performed. The best choice for $g(\mathbf{x})$ is given by

$$g(\mathbf{x}) = cV(\mathbf{x}), \quad \text{with } V(\mathbf{x}) = \left\{ \sum_i \left[U_i(\mathbf{x}) + U_i^\dagger(\mathbf{x} - \mathbf{e}_i) \right] \right\}^\dagger,$$

and the normalization constant $c = \left(\sqrt{\text{Det}(V)} \right)^{-1}$. This procedure has to be performed site by site and repeated until the gauge functional relaxes to a minimum. We do not fix the number of lattice sweeps but stop the gauge-fixing procedure by means of an abort condition. The gauge-fixing process is monitored by the following quantity

$$\theta = \frac{1}{2N} \sum_{\mathbf{x}} \text{Tr} \left[\Delta(\mathbf{x}) \Delta^\dagger(\mathbf{x}) \right],$$

with

$$\Delta(\mathbf{x}) = \sum_i \left[U_i(\mathbf{x} - \mathbf{e}_i) - U_i(\mathbf{x}) - U_i^\dagger(\mathbf{x} - \mathbf{e}_i) + U_i^\dagger(\mathbf{x}) \right],$$

³Let us emphasize that this method is an improvement of standard minimization procedures, like the iterated overrelaxation algorithm discussed below, and by no means furnishes the global minimum in a systematical way.

which gives rise to

$$\theta \simeq \int d^d x \text{Tr} [(\partial_i A_i)^2]$$

in the continuum limit. The monitoring parameter θ decreases during the gauge-fixing process and should be strictly zero when a minimum of the functional F has been reached. At the practical level, the process should be stopped if θ drops below a certain small parameter θ_s fixed in advance. In order to avoid the problem of critical slowing down, the minimum is overshot by performing the local gauge transformations with the modified matrices

$$g_\omega(\mathbf{x}) = [cV(\mathbf{x})]^\omega,$$

where the parameter ω is chosen such as to optimize the speed of convergence towards the minimum of F .

7.3 Lattice measurements

At the practical level, the final goal of a lattice calculation is to compute the expectation value of an observable in a certain gauge $f(U) = 0$ by performing the integration (7.13). Theoretically, all link configurations have to be taken into account when computing the average. Although the number of configurations is finite, this is of course practically not possible. The same problem is encountered in statistical physics, where the numerical value of a thermodynamical quantity results from an average over a huge amount of microstates. In this context, the problem has been solved in the following way. Instead of integrating over all microstates of the physical system, among which only a fraction significantly contributes to the average, a stochastic sequence of configurations $\{C_1, C_2, \dots\}$ is generated, each C_i occurring with a probability proportional the Boltzmann factor $\exp(-\frac{1}{T}E[C_i])$. This is the basic idea of a *Monte-Carlo* simulation procedure. In the context of lattice gauge theories, a set of link configurations U_i is sampled stochastically with respect to the weight factor $\exp(-S_W[\beta, U_i])$ and the expectation value is approximated by the mean value of the observable over this sequence of N_{MC} configurations

$$\langle \mathcal{O} \rangle \simeq \frac{1}{N_{MC}} \sum_{i=1}^{N_{MC}} \mathcal{O}(U_i). \quad (7.23)$$

7.3.1 Numerical procedure

The numerical procedure works as follows:

- (a) initialize by assigning randomly a link configuration,
- (b) thermalize the lattice according to the Wilson action by performing N_{TH} updates of the whole lattice,
- (c) freeze a link configuration, gauge transform it if necessary and evaluate the observable(s),
- (d) perform N_{UP} updates of the whole lattice,
- (e) repeat the two latter steps N_{MC} times,
- (f) perform the average (7.23).

In the present work, since we limit ourselves to the study of equal-time observables, step (c) consists in fixing the Coulomb gauge in the quasi-temporal gauge scheme and perform the measurements in a single time slice. In steps (b) and (d), we perform lattice updates using Creutz's heatbath algorithm (see Sec. D.1 for technical details).

7.3.2 Renormalization

The evaluation of the average (7.23) is only a step towards the numerical estimate of an observable. Let us indeed recall that the expectation value (7.13), of which (7.23) is an approximation, is performed at various β , i.e. for various values of the coupling g_0 in the scaling window, or, expressed in a more familiar language, for various values of the UV-cutoff. After the simulations have been performed, we obtain a set of unrenormalized, or *bare*, estimates $\mathcal{O}_B(p, \beta)$, here as a function of the momentum p . Multiplicative renormalizability of the theory implies that a rescaling of the data for each β value is sufficient to let the results fall on top of a single curve describing the momentum dependence of the corresponding renormalized quantity. In practice, the renormalized quantity \mathcal{O}_R is obtained by determining suitable “matching factors” $Z(\beta, \mu)$ which “collapse” data obtained at different β on a single curve:

$$\mathcal{O}_R(p, \mu) = Z(\beta, \mu)\mathcal{O}_B(p, \beta).$$

The residual dependence on the *renormalization point* μ , which corresponds in practice to the freedom of rescaling the results by an arbitrary global factor, is fixed by imposing a renormalization condition:

$$\mathcal{O}_R(\mu, \mu) = C.$$

In the present studies of propagators, we adjust the normalization factors $Z(\beta, \mu)$ in such a way that our numerical estimates correspond to the free propagators in the UV regime. This can be done in $D = 2 + 1$ but the task is complicated by the presence of anomalous dimension factors in $D = 3 + 1$. This will be discussed later on.

7.3.3 Simulation parameters

For the interested reader, we summarize the parameters used in our numerical simulations.

D=2+1. The simulations are performed for the lattice volume $V = 68^3$ and the couplings $\beta = 3.5, 4.0, 4.5, 5.0, 6.0, 7.0$ in the scaling window. After initialization, the lattice is thermalized by means of $N_{TH} = 500$ update steps and each measurement is followed by $N_{UP} = 30$ lattice sweeps. The scale is fixed by the bare coupling constant g_0^2 .

D=3+1. The simulations are performed for the lattice volumes $V = 24^4$, $V = 26^4$ and $V = 32^4$. For each value of the coupling, we give the value of the dimensionless string tension (7.12), the UV cutoff $\Lambda = \pi/a$, the lattice spacing and the lattice extension L in fm for the 24^4 and 32^4 lattices. We use the conversion: $1\text{m} \simeq 5.1 \times 10^6 \text{ eV}^{-1}$.

β	$\hat{\sigma}(\beta)$	Λ (GeV)	a (fm)	L (fm)
2.1	0.35	2.3	0.26	6.3 - 8.4
2.2	0.21	3.0	0.20	5.0 - 6.5
2.3	0.12	4.0	0.15	3.7 - 4.9
2.4	0.07	5.2	0.12	2.8 - 3.7
2.5	0.04	6.8	0.09	2.1 - 2.8
2.6	0.02	9.8	0.06	1.5 - 2.0

Gauge fixing.

- *Simulated annealing*: the lattice is cooled from $\beta_{SA} = 0.2$ to $\beta_{SA} = 50$ with the step $\Delta\beta_{SA} = 0.2$ and $N_{UP} = 10$ sweeps at each coupling.
- *Iterated overrelaxation*: the process is stopped if the monitoring parameter θ drops below the value $\theta_s = 10^{-12}$ and overshoot with the parameter $\omega = 1.7$.

The choices we made concerning the numerical implementation of the gauge fixing procedures and the values of the parameters were guided by the careful analysis of several minimization algorithms performed by Cucchieri and Mendes [CM96].

7.4 Lattice observables

Our numerical simulations are, in relation to Gribov's confinement scenario, devoted to the study of the ghost propagator and the Coulomb potential. We address also the equal-time gluon propagator, whose inverse is compared with the so-called gap function studied in the Hamiltonian formalism. We recall the definitions of each observable in the continuum, in coordinate and momentum space, and define the corresponding quantities on the lattice.

7.4.1 Ghost propagator

The ghost propagator is defined as the expectation value of the inverse Faddeev-Popov operator $M = -\nabla \cdot \mathbf{D}$:

$$D^{ab}(\mathbf{x} - \mathbf{y}) = \left\langle M^{-1}[A] \Big|_{(\mathbf{x}, \mathbf{y})}^{ab} \right\rangle.$$

We address the ghost propagator in momentum space. Due to translation invariance, we can write, using (C.4),

$$\tilde{D}^{ab}(\mathbf{p}, \mathbf{k}) = \delta^{(d)}(\mathbf{p} + \mathbf{k}) D^{ab}(\mathbf{p}), \quad \text{with} \quad D^{ab}(\mathbf{p}) = \int d^d x D^{ab}(\mathbf{x}) e^{i\mathbf{p} \cdot \mathbf{x}}.$$

Since D^{ab} is diagonal in colour space, we have

$$D^{ab}(\mathbf{p}) = \delta^{ab} D(\mathbf{p})$$

with

$$\begin{aligned} D(\mathbf{p}) &= \frac{1}{3} \sum_{a=1}^3 D^{aa}(\mathbf{p}) \\ &= \frac{1}{3V} \sum_{a=1}^3 \int d^d x d^d y \left\langle M^{-1}[A] \Big|_{(\mathbf{x}, \mathbf{y})}^{aa} \right\rangle \cos(\mathbf{p} \cdot (\mathbf{x} - \mathbf{y})), \end{aligned}$$

where $V = \int d^d x$ is the volume of the time slice. The quantity $\langle M^{-1}[A]|_{(\mathbf{x}, \mathbf{y})} \rangle$ has energy dimension $d - 2$. This is easily verified since it reduces to the inverse Laplace operator in the Abelian case. The ghost propagator thus has energy dimension -2 in momentum space and we may define the *ghost form factor* $d(\mathbf{p})$

$$D(\mathbf{p}) = \frac{d(\mathbf{p})}{|\mathbf{p}|^2},$$

a dimensionless quantity which measures the deviation from the free ghost propagator $D_0(\mathbf{p}) = \frac{1}{|\mathbf{p}|^2}$. On the lattice, we compute the dimensionless quantity:

$$\hat{D}(\hat{\mathbf{p}}) = \frac{1}{3\mathbf{N}_d} \sum_{a=1}^3 \sum_{\bar{\mathbf{x}}, \bar{\mathbf{y}}}^{\mathbf{N}_d} \langle \hat{M}^{-1}[U]|_{(\bar{\mathbf{x}}, \bar{\mathbf{y}})}^{aa} \rangle \cos\left(\frac{2\pi}{\mathbf{N}_d} \bar{\mathbf{p}} \cdot (\bar{\mathbf{x}} - \bar{\mathbf{y}})\right), \quad (7.24)$$

with $\hat{D}(\hat{\mathbf{p}}) = a^{-2}D(\mathbf{p})$. The arguments $\bar{\mathbf{p}}, \bar{\mathbf{x}}, \bar{\mathbf{y}} = 1, 2, \dots, \mathbf{N}_d$ in the cosine function are now integers labelling the sites in one d -dimensional slice of the direct and reciprocal lattice, as defined in (C.2). For technical details, see also Sec. C.6 and C.8. The ghost form factor is given by

$$d(\hat{\mathbf{p}}) = |\hat{\mathbf{p}}|^2 \hat{D}(\hat{\mathbf{p}}).$$

The inversion of M is performed using the conjugate gradient method, see Sec. C.8 and D.2 for technical details. In order to get rid of the possible zero modes of the Faddeev-Popov matrix, the conjugate gradient method is applied to the linear system

$$MMx = Mb$$

rather than the system $Mx = b$. See the method proposed in [SS96].

Remark. In the Hamiltonian formalism [FRa], the definition of the ghost form factor includes the bare coupling constant:

$$\langle M^{-1} \rangle = \frac{1}{-\nabla^2} \frac{d}{g_0}. \quad (7.25)$$

The different definitions do not prevent a direct comparison of the lattice and Hamiltonian approaches since they only differ in the proportionality factor $g_0(\Lambda)$. On the lattice, this supplementary dependence on the cut-off is indeed eliminated when determining the matching factors $Z(\Lambda)$ as described in Sec. 7.3.2. This is of course correct as long as the bare coupling in the Hamiltonian picture does not depend on the momentum.

7.4.2 Coulomb potential and form factor $f(p)$

The Coulomb potential is given by the expression (6.46), which reads explicitly

$$V_{\text{Coul}}(\mathbf{x} - \mathbf{y}) \delta^{ab} = -C_N g_0^2 \left\langle [M^{-1}[A](-\Delta)M^{-1}[A]]_{(\mathbf{x}, \mathbf{y})}^{ab} \right\rangle, \quad C_2 = \frac{3}{4}. \quad (7.26)$$

We address the Coulomb potential in momentum space:

$$V_{\text{Coul}}(\mathbf{p}) = \frac{-1}{4V} \sum_{a=1}^3 \int d^d x d^d y \left\langle [M^{-1}[A](-\Delta)M^{-1}[A]]_{(\mathbf{x}, \mathbf{y})}^{aa} \right\rangle \cos(\mathbf{p} \cdot (\mathbf{x} - \mathbf{y})).$$

Since the expectation value in (7.26) has energy dimension $d - 2$, and g_0^2 energy dimension $4 - D$, we verify that $V_{\text{Coul}}(\mathbf{x} - \mathbf{y})$ has always the dimension of an energy whereas $V_{\text{Coul}}(\mathbf{p})$ has energy dimension $2 - D$ in momentum space. We then make the following ansatz

$$V_{\text{Coul}}(\mathbf{p}) = -\frac{3}{4}g_0^2 \frac{d^2(\mathbf{p})f(\mathbf{p})}{|\mathbf{p}|^2}, \quad (7.27)$$

where $d(\mathbf{p})$ is the ghost form factor and the dimensionless function $f(\mathbf{p})$ measures the deviation from the potential as a factorization of the three operators in (7.26):

$V_{\text{Coul}}(\mathbf{p}) = -\frac{3}{4}g_0^2 \frac{d^2(\mathbf{p})}{|\mathbf{p}|^2}$. On the lattice, we address the dimensionless quantity:

$$\hat{V}_{\text{Coul}}(\hat{\mathbf{p}}) = \frac{-1}{4\mathbf{N}_d} g_0^{2d-4} \sum_{a=1}^3 \sum_{\bar{\mathbf{x}}, \bar{\mathbf{y}}}^{\mathbf{N}_d} \left\langle [M^{-1}[U](-\Delta)M^{-1}[U]]_{(\bar{\mathbf{x}}, \bar{\mathbf{y}})}^{aa} \right\rangle \cos \left(\frac{2\pi}{\mathbf{N}_d} \hat{\mathbf{p}} \cdot (\bar{\mathbf{x}} - \bar{\mathbf{y}}) \right). \quad (7.28)$$

Remark. In view of the definition (7.25) of the ghost form factor, the dependence on the bare coupling constant g_0 in the Coulomb potential drops out in the Hamiltonian formalism.

7.4.3 Equal-time transverse gluon propagator

The equal-time gluon propagator is defined by

$$G_{ij}^{ab}(\mathbf{x} - \mathbf{y}) = \langle A_i^a(\mathbf{x}, t_0) A_j^b(\mathbf{y}, t_0) \rangle, \quad (7.29)$$

at fixed time $t = t_0$. We directly address the propagator in momentum space. The gluon propagator is diagonal in colour space and, in Coulomb gauge, transverse in momentum space. We may then write:

$$G_{ij}^{ab}(\mathbf{p}) = \delta^{ab} \left(\delta_{ij} - \frac{p_i p_j}{\mathbf{p}^2} \right) G(\mathbf{p})$$

with

$$\begin{aligned} G(\mathbf{p}) &= \frac{1}{3(d-1)} \sum_{a=1}^3 \sum_{i=1}^d G_{ii}^{aa}(\mathbf{p}) \\ &= \frac{1}{3(d-1)V} \sum_{a=1}^3 \sum_{i=1}^d \int d^d x d^d y \langle A_i^a(\mathbf{x}) A_i^a(\mathbf{y}) \rangle \cos(\mathbf{p} \cdot (\mathbf{x} - \mathbf{y})). \end{aligned} \quad (7.30)$$

In the ‘‘continuum’’ conventions of Appendix B, the gauge potential has energy dimension $[A(\mathbf{x})] = D/2 - 1$. Let us now translate (7.30) into our lattice unit conventions (Sec. C.1):

$$G(\mathbf{p}) = \frac{1}{3(d-1)Vg_0^2} \sum_{a=1}^3 \sum_{i=1}^d \int d^d x d^d y \langle A_i^a(\mathbf{x}) A_i^a(\mathbf{y}) \rangle \cos(\mathbf{p} \cdot (\mathbf{x} - \mathbf{y})).$$

[Recall that the potential has in these conventions always the dimension of an energy, i.e. $[A(\mathbf{x})] = 1$.] Since the coupling constant g_0^2 has dimension $[g_0^2] = 4 - D$, we verify that the dimension of $G(\mathbf{p})$ is unchanged. We define the lattice gluon propagator as the dimensionless quantity

$$\hat{G}(\hat{\mathbf{p}}) = \frac{1}{3(d-1)\mathbf{N}_d} \sum_{a=1}^3 \sum_{i=1}^d \sum_{\bar{\mathbf{x}}, \bar{\mathbf{y}}}^{\mathbf{N}_d} \langle \hat{A}_i^a(\bar{\mathbf{x}}) \hat{A}_i^a(\bar{\mathbf{y}}) \rangle \cos \left(\frac{2\pi}{\mathbf{N}_d} \hat{\mathbf{p}} \cdot (\bar{\mathbf{x}} - \bar{\mathbf{y}}) \right).$$

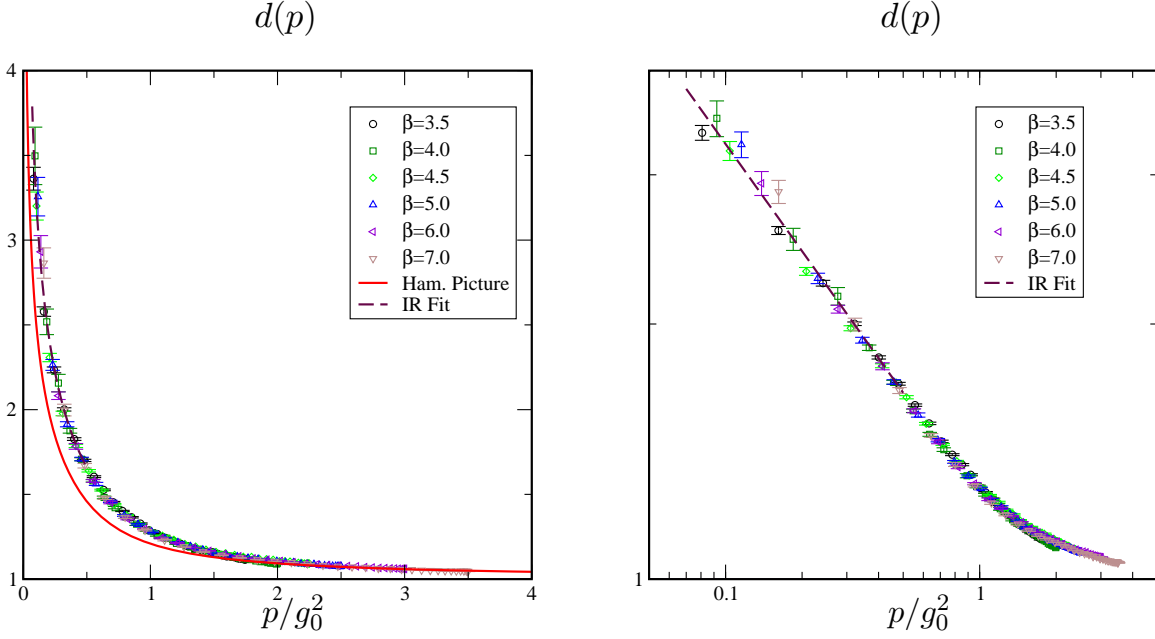


Figure 7.2: Ghost form factor in $D = 2 + 1$ as a function of the dimensionless momentum p/g_0^2 for the lattice volume $V = 68^3$. The lattice data are compared to the results provided by the Hamiltonian approach [FRb].

In particular $\hat{G}(\hat{\mathbf{p}}) = G(\mathbf{p})g_0^2$ for $D = 2 + 1$ and $\hat{G}(\hat{\mathbf{p}}) = G(\mathbf{p})\frac{g_a^2}{a}$ for $D = 3 + 1$. Using the addition formula to transform the factor $\cos\left(\frac{2\pi}{\mathbf{N}_d}\bar{\mathbf{p}} \cdot (\bar{\mathbf{x}} - \bar{\mathbf{y}})\right)$, we finally find, after a straightforward calculation,

$$\hat{G}(\hat{\mathbf{p}}) = \frac{1}{3(d-1)\mathbf{N}_d} \times \sum_{a=1}^3 \sum_{i=1}^d \left\langle \left[\sum_{\bar{\mathbf{x}}}^{\mathbf{N}_d} \hat{A}_i^a(\bar{\mathbf{x}}) \cos\left(\frac{2\pi}{\mathbf{N}_d}\bar{\mathbf{p}} \cdot \bar{\mathbf{x}}\right) \right]^2 + \left[\sum_{\bar{\mathbf{x}}}^{\mathbf{N}_d} \hat{A}_i^a(\bar{\mathbf{x}}) \sin\left(\frac{2\pi}{\mathbf{N}_d}\bar{\mathbf{p}} \cdot \bar{\mathbf{x}}\right) \right]^2 \right\rangle.$$

7.5 Numerical results

7.5.1 D=2+1

In our simulations in $D = 2 + 1$, we consider, without loss of generality, 2-momenta aligned along the x axis in the first time slice:

$$\mathbf{p} = (p, 0).$$

Ghost propagator. Our numerical results for the ghost form factor $d(p)$ are shown in Fig. 7.2 and were obtained by generating $100 < N_{MC} < 200$ configurations for the lattice $V = 68^3$. We adjusted the numerical results by using multiplicative renormalizability such that the UV behaviour is that of the free ghost form factor, i.e. $d(p) \rightarrow 1$. The lattice data are compared to the analytical results provided by the Hamiltonian approach [FRb].

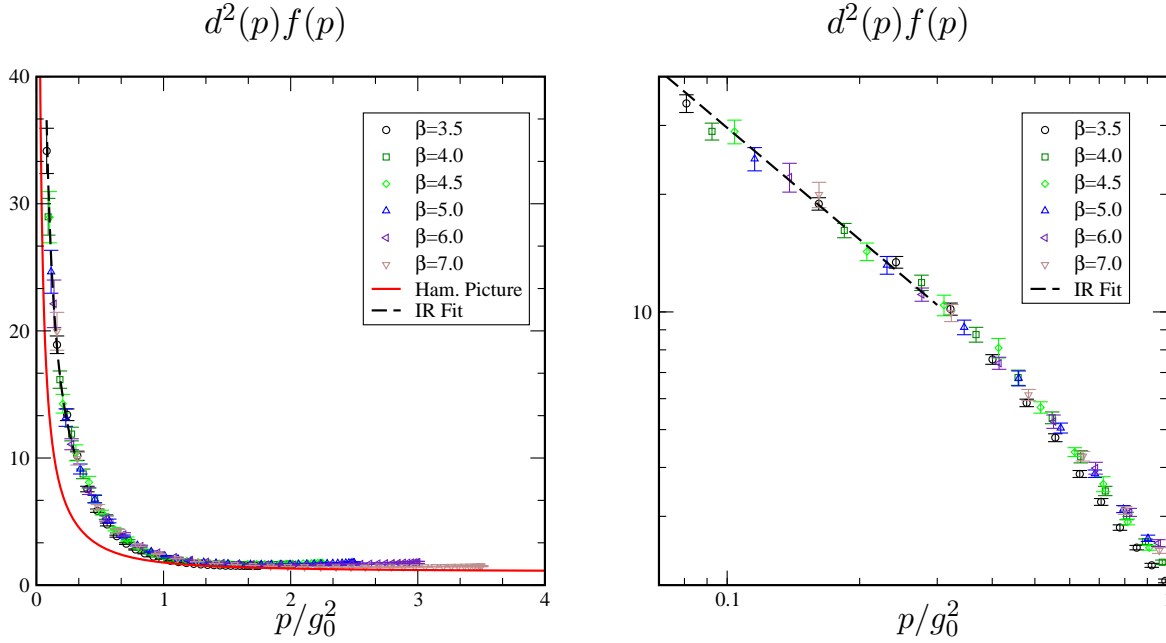


Figure 7.3: The dimensionless quantity $d^2(p)f(p) \propto p^2 V_{\text{Coul}}(p)$ in $D = 2 + 1$ as a function of the dimensionless momentum p/g_0^2 for the lattice volume $V = 68^3$.

The agreement is satisfactory at the qualitative and quantitative level, except for a small discrepancy in the intermediate region. The ghost propagator is divergent for both approaches in the IR regime, reflecting the enhancement of the numbers of gauge field configurations sitting in the neighbourhood of the Gribov horizon at large distances $|\mathbf{x} - \mathbf{y}|$. We fit the lattice data in the IR regime by the simple scaling ansatz

$$d(p) = \frac{a}{(p/g_0^2)^b}, \quad p/g_0^2 < 0.5.$$

The fitting curve shown in Fig. 7.2 corresponds to

$$a = 1.24(1), \quad b = 0.42(1). \quad (7.31)$$

Coulomb potential. The results concerning the evaluation of the Coulomb potential are reported in Fig. 7.3. Ghost propagator and Coulomb potential are computed during the same run and the simulation parameters are therefore identical. Again, renormalization of the lattice results is performed in such a way that the Coulomb potential shows the perturbative behaviour, i.e. $d^2(p)f(p) \rightarrow 1$, in the UV regime.

We plot the dimensionless quantity $d^2(p)f(p)$. The agreement with the Hamiltonian picture is satisfactory at the qualitative level, whereas a quantitative discrepancy characterizes again the intermediate regime, as for the ghost propagator. We make again a simple scaling ansatz

$$d^2(p)f(p) = \frac{a}{(p/g_0^2)^b}, \quad p/g_0^2 < 0.5$$

in the IR regime. The fit is shown in Fig. 7.3 and corresponds to

$$a = 3.3(1), \quad b = 0.95(1). \quad (7.32)$$

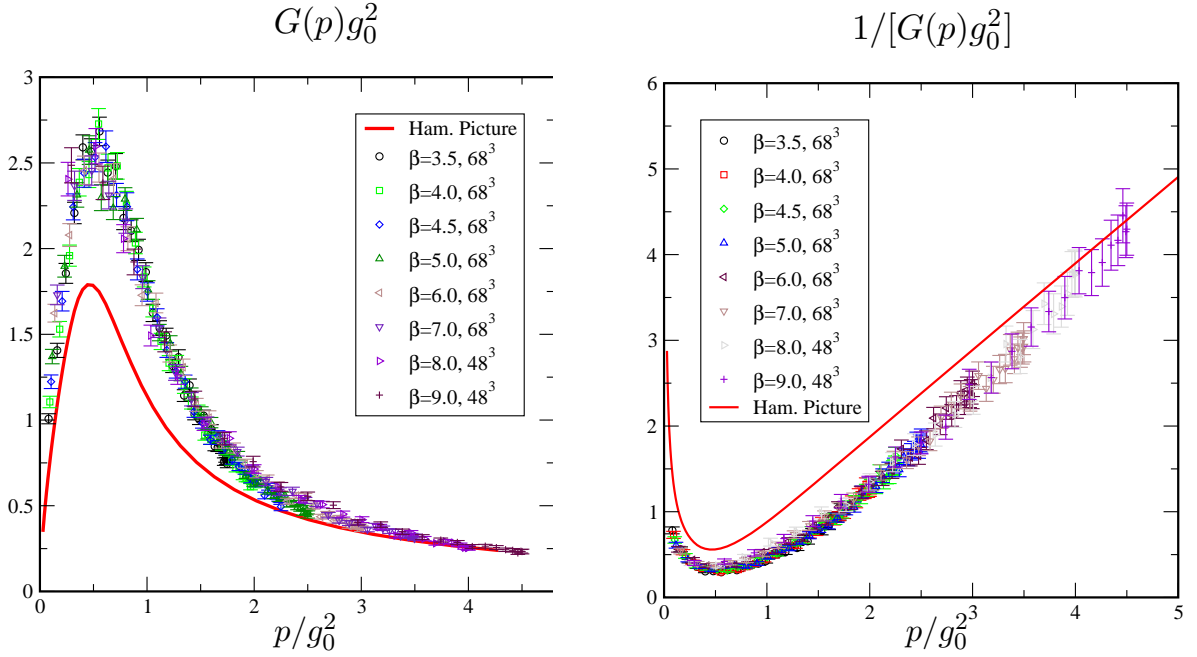


Figure 7.4: Transverse gluon propagator (left panel) and inverse gluon propagator (right panel) in $D = 2 + 1$ as a function of the dimensionless momentum p/g_0^2 for the lattice volumes $V = 68^3$ and $V = 48^3$. The lattice estimates are compared with the gap function $\omega(p)$ obtained in the Hamiltonian formalism [FRb].

The lattice data are therefore compatible with linear confinement, which corresponds to $b = 1$ (see Sec. E.3).

Form factor $f(p)$. An advantage of our method is the determination of the form factor $f(p)$ as a by-product of the computations of ghost propagator and Coulomb potential. From the IR behaviour of those quantities, we get the low momentum regime of $f(p)$ in (7.27). Combining (7.31) with (7.32), we obtain

$$f(p) \propto \frac{1}{(p/g_0^2)^{0.11(1)}},$$

i.e. the factorization factor weakly depends on the momentum transfer.

Equal-time transverse gluon propagator. The simulations were performed with the lattice volumes $V = 48^3$, $V = 68^3$ and the estimates were obtained by averaging over $N_{MC} = 300$ configurations. Our lattice results are compared to the calculations performed in the Hamiltonian picture [FRb] and plotted in Fig. 7.4.

The renormalization condition is fixed by

$$G_{\text{lattice}}(\mu) = G_{\text{Hamilton}}(\mu), \quad \mu = 4.5g_0^2. \quad (7.33)$$

In Fig. 7.4, we plot $G(p)$ and $G^{-1}(p)$ expressed in units of the bare coupling constant. The inverse equal-time gluon propagator is generally interpreted as the energy *dispersion relation* for the gluons. In the Hamiltonian formalism, this quantity corresponds to the so-called *gap*

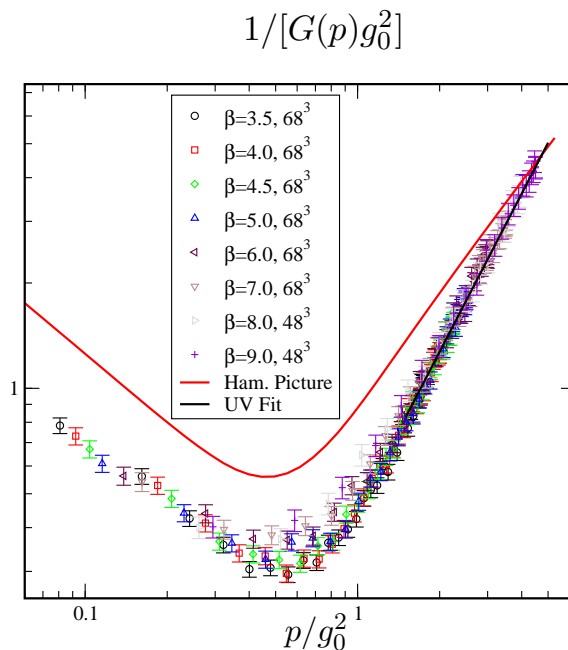


Figure 7.5: Inverse gluon propagator in $D = 2 + 1$ as a function of the dimensionless momentum p/g_0^2 for the lattice volumes $V = 48^3$ and $V = 68^3$.

function⁴ $\omega(p)$. Due to asymptotic freedom, the gluons can be treated as free particles in the UV regime, where the gap function tends to $\omega(p) = p$. If the inverse of our equal-time gluon propagator corresponds to ω , it should also show this asymptotic behaviour.

We see that the lattice results converge very slowly towards the perturbative behaviour, which seems to be attained within the error bars for $p/g_0^2 > 3.5$ and the chosen renormalization condition (7.33). However, a more careful examination of our numerical estimates actually reveals a striking feature of the lattice results. This is shown in the logarithmic plot in Fig. 7.5. We find out that the perturbative regime is characterized by the powerlaw

$$(g_0^2 G(p))^{-1} = a \left(\frac{p}{g_0^2} \right)^b, \quad p/g_0^2 > 2, \quad (7.34)$$

with

$$a = 0.45(1), \quad b = 1.50(1),$$

as fitted from the lattice results. This anomalous scaling $G(p) \propto 1/p^{1+\eta}$, with $\eta \simeq 0.5$, will also be found in $D = 3 + 1$. The reason for which the transverse gluon propagator, computed as a naive expectation value of gluonic correlations in a given time slice, fails to reproduce the perturbative behaviour of the gap function is until now unclear and still under ongoing debate. Since this anomaly occurs both in $D = 2 + 1$ and $D = 3 + 1$, an explanation based on renormalization effects is to be excluded. This delicate point is further discussed below.

⁴This denomination recalls that calculations in the Hamiltonian formalism are based on a variational approach.

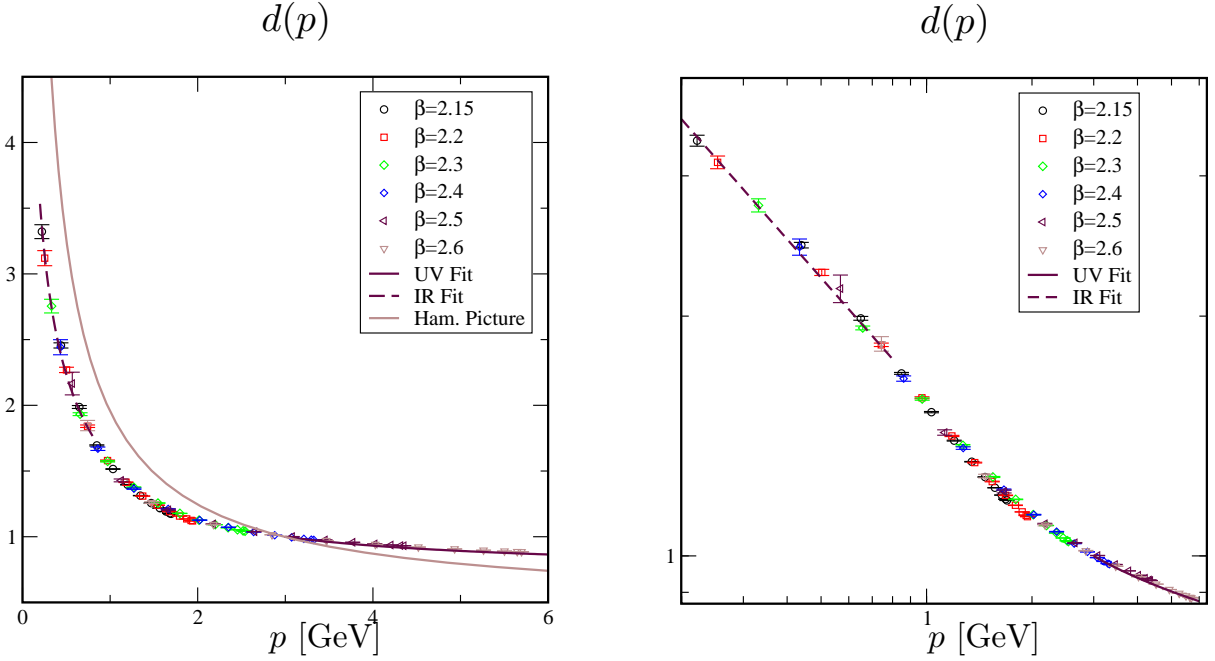


Figure 7.6: Ghost form factor in $D = 3 + 1$ as a function of the momentum p for the lattice volume $V = 24^4$, compared to the Hamiltonian approach [FRa].

7.5.2 $D=3+1$

We choose the 3-momenta aligned along the x -axis in the first time slice:

$$\mathbf{p} = (p, 0, 0).$$

Ghost propagator. We report the results for the ghost form factor $d(p)$ in Fig.7.6. The simulations were performed for the lattice volume $V = 24^4$ and $100 < N_{MC} < 200$ configurations were generated. We renormalized the results by enforcing the condition $d(p = 3 \text{ GeV}) = 1$.

We fit the high momentum dependence by means of the logarithmic ansatz

$$d(p) = \frac{a_{uv}}{\ln(p/\Lambda_{QCD})^{\gamma_{gh}}}, \quad p > 1 \text{ GeV}.$$

We find the values

$$a_{uv} = 1.0(1), \quad \gamma_{gh} = 0.24(1).$$

Since the fitting parameters are strongly correlated, it is difficult to extract a reliable value for Λ_{QCD} . Taking also into account the high momentum behaviour of the Coulomb potential (see below), we find that

$$\Lambda_{QCD} = 1.1(5) \text{ GeV}$$

reproduces the data in a satisfactory way. For the IR analysis, we adopt a simple scaling law:

$$d(p) = \frac{a_{ir}}{(p^2/\Lambda_{QCD}^2)^\kappa}, \quad p < 1 \text{ GeV}.$$

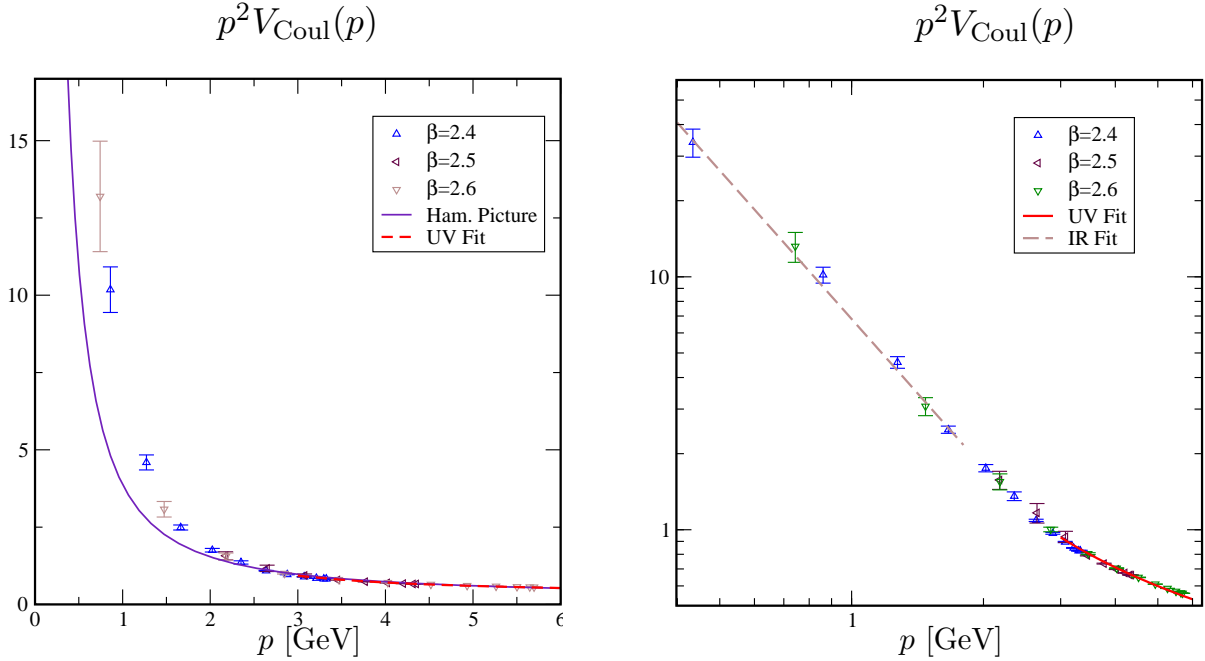


Figure 7.7: The dimensionless quantity $p^2 V_{\text{Coul}}(p)$ in $D = 3 + 1$ as a function of the momentum p for the lattice volume $V = 24^4$, compared to the results obtained in the Hamiltonian picture [FRa].

The IR fit is also shown in Fig. 7.6. We find

$$a_{ir} = 1.58(1), \quad \kappa = 0.25(1).$$

We rescaled the results of Ref. [FRa] obtained in the Hamiltonian picture. They are compared to the lattice data in Fig. 7.6, left panel. The comparison is discussed in a separate section below in the light of the results for the Coulomb potential and the form factor $f(p)$.

When renormalizing the lattice results, we found out that the ghost wave function renormalization has the simple β dependence $Z \propto 1/\beta$. This information therefore suggests that the ghost form factor multiplied by the squared coupling constant, $g_0^2 d(p)$, is independent of the UV cut-off, i.e. is invariant under renormalization group transformations.

Coulomb potential. The results are reported in Fig. 7.7 and were obtained with the same run parameters as for the ghost propagator. Renormalization is performed by demanding that the perturbative result for the running coupling constant [CZ02b, BCLM] in (6.55) is recovered at large momentum:

$$p^2 V_{\text{Coul}}(p) = \frac{6\pi}{11 \ln(p^2/\Lambda_{QCD}^2)}, \quad p \gg \Lambda_{QCD}.$$

The data reproduces the logarithmic correction in a satisfactory way.

A careful analysis of the data reveals that the numerical estimates at the couplings $\beta = 2.15, 2.2$ and 2.3 do not scale with those performed at $\beta = 2.4, 2.5$ and 2.6 in a satisfactory way. They are moreover characterized by an enhanced statistical error in the low

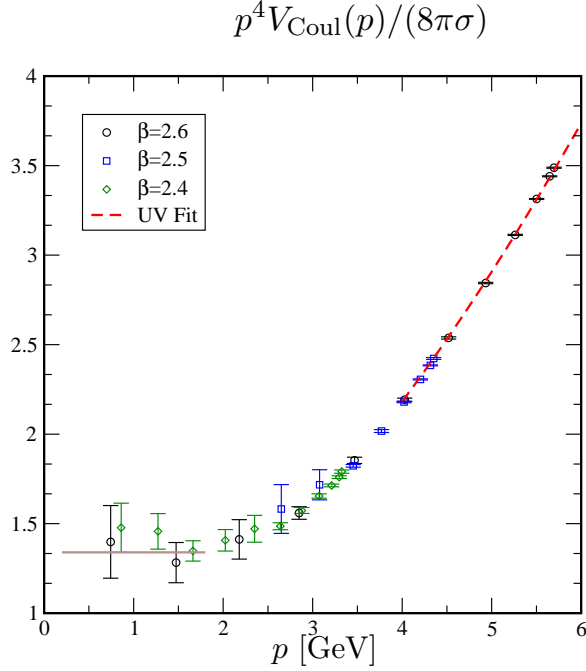


Figure 7.8: The quantity $p^4 V_{\text{Coul}}(p)$ in $D = 3 + 1$ in units of the Wilson string tension σ as a function of the momentum p for the lattice volume $V = 24^4$.

momentum regime. Therefore, we limit ourselves to the sets $\beta \in [2.4, 2.6]$ for the IR analysis. New runs are being performed, which implement an inversion of the Faddeev-Popov operator based on the 'minres' algorithm [PS75]. The results will be presented elsewhere [LMon].

In the low momentum regime, the lattice estimates are parameterized by

$$p^2 V_{\text{Coul}}(p) = \frac{a_{ir}}{(p^2/\Lambda_{QCD}^2)^b}.$$

We perform two IR fits of our data. Letting the fit parameter b free, we obtain

$$a_{ir} = 6.81(1), \quad b = 0.95(5). \quad (7.35)$$

The fit is shown in Fig. 7.7, right panel (dashed line). Constraining the parameter b to the value $b = 1$ exactly corresponding to a linear potential (see Sec. E.3), we obtain the estimate of the Coulomb string tension:

$$p^2 V_{\text{Coul}}(p) = \frac{8\pi\sigma_{\text{Coul}}}{p^2}, \quad \sigma_{\text{Coul}} = 0.258(4) \text{ GeV}^2.$$

This corresponds to the ratio $\sigma_{\text{Coul}}/\sigma = 1.3(2)$, which can be also read off in Fig. 7.8. This value tends to confirm the results obtained in Ref. [CZ03], i.e. a saturation of the inequality (6.53).

As for the ghost propagator, we compare the lattice data with the rescaled results of Ref. [FRa] obtained in the Hamiltonian picture. This is shown in Fig. 7.7, left panel. The comparison is discussed below.

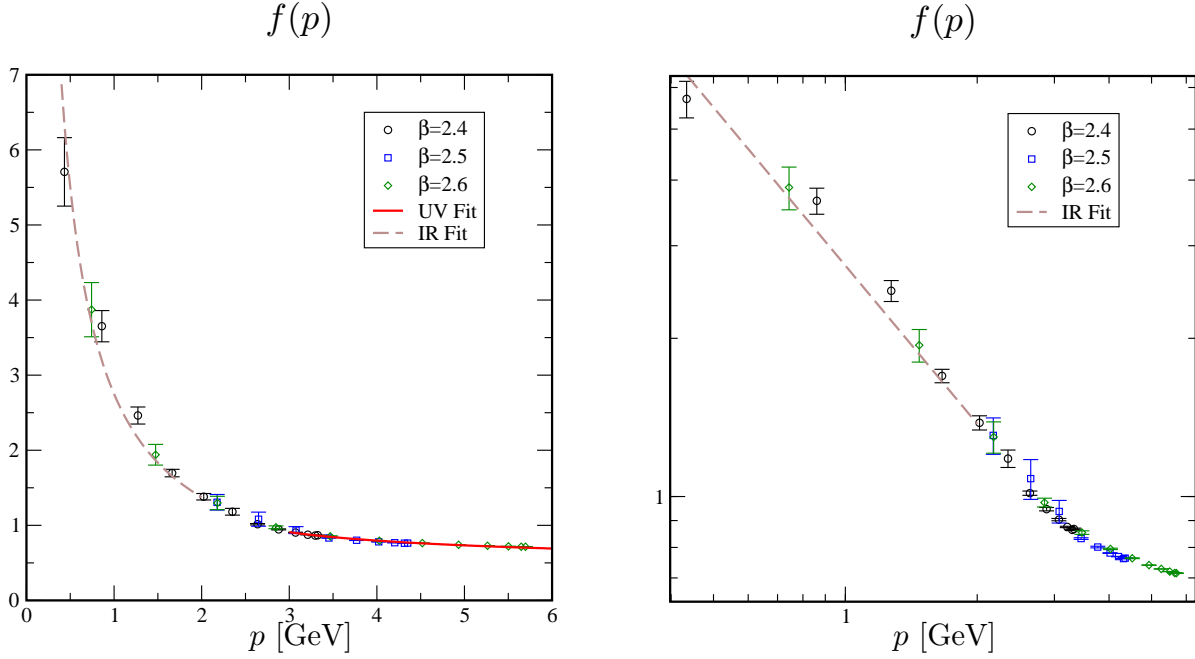


Figure 7.9: The form factor $f(p)$ in $D = 3 + 1$ as a function of the momentum p for the lattice volume $V = 24^4$.

Form factor $f(p)$. From the results for the ghost form factor and the Coulomb potential, it is clear that $f(p)$ cannot weakly depend on p in the low momentum regime. In order to extract $f(p)$ from the lattice data, we divide the bare data for $p^2 V_{\text{Coul}}(p)$ by the bare ghost form factor. The function $f(p)$ is shown in Fig. 7.9. The high energy data are reproduced by the ansatz

$$f(p) = \frac{a_{uv}}{\ln(p/\Lambda_{QCD})^{\gamma_f}}, \quad p > \Lambda_{QCD}.$$

Our UV fit corresponds to

$$a_{uv} = 0.91(1), \quad \gamma_f = 0.52(2).$$

The sum rule dictated by the UV behaviour of the Coulomb potential, i.e. $2\gamma_{gh} + \gamma_f = 1$, is satisfied to good precision, since we find

$$2\gamma_{gh} + \gamma_f = 1.00(2).$$

The low momentum data support the existence of a $1/p$ singularity, i.e.

$$f(p) = \frac{a_{ir}}{(p^2/\Lambda_{QCD}^2)^{\kappa_f}},$$

with

$$a_{ir} = 2.75(2), \quad \kappa_f = 0.5(1).$$

The enhancement of the factorization form factor f at low momentum suggests strong non-Gaussian correlations between the ghost fields, which rule out the factorization assumption in the IR regime.

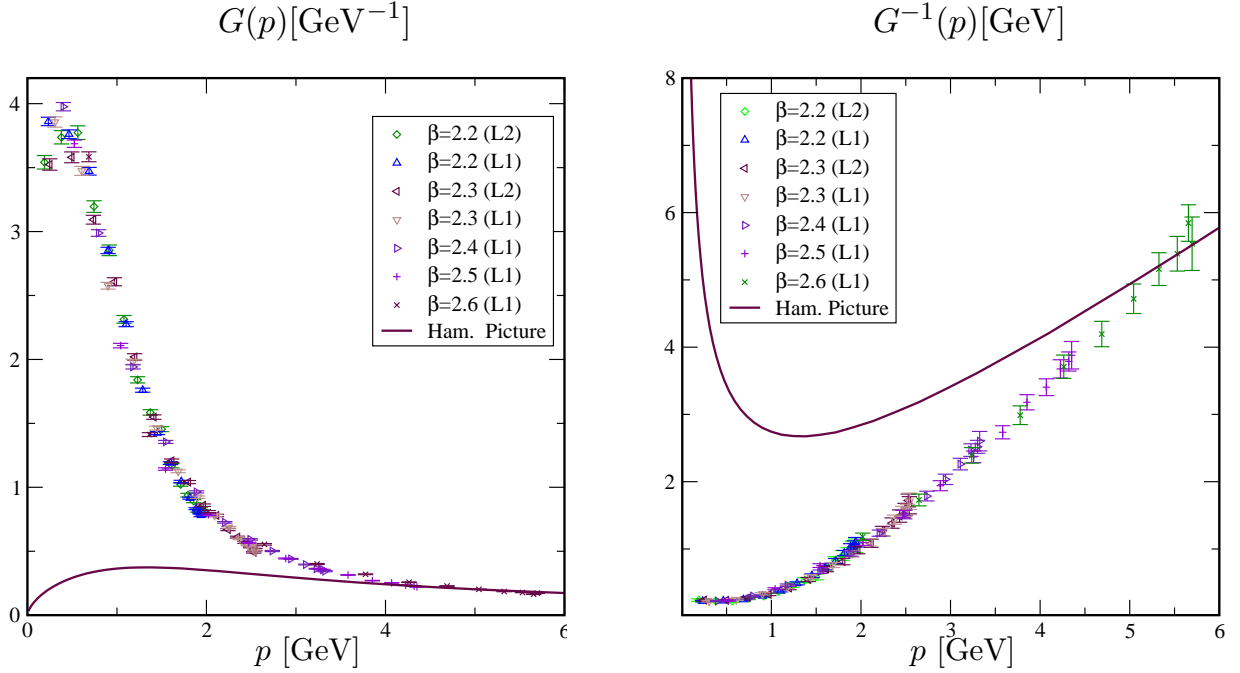


Figure 7.10: Transverse gluon propagator (left panel) and inverse gluon propagator (right panel) in $D = 3 + 1$ as a function of the momentum p for the lattice volumes $V = 26^4$ (L1) and $V = 32^4$ (L2), compared with the results obtained in the Hamiltonian picture [FRa].

Lattice vs. Hamilton picture. Let us begin with the Coulomb potential. Both approaches support a linear confining potential: we find the exponent $b = 0.95(5)$ in (7.35) and the value $b = 0.85$ is obtained in Ref. [FRa]. Linear confinement corresponds to $b = 1$. In the Hamiltonian approach, the value of the Coulomb string tension σ_{Coul} is not deduced from the IR limit of the potential but chosen in advance as a condition setting the renormalization scale. In Ref. [FRa], the authors choose the value $\sigma_{\text{Coul}} = 3\sigma$ found in Ref. [GO03]. This does not correspond to our choice of a renormalization scale and explains why we have to rescale the Hamiltonian results. In Fig. 7.7, left panel, let us remark that the lattice and Hamiltonian data are in good agreement in the UV regime ($p > 3$ GeV).

In Ref. [FRa], the IR behaviour of the Coulomb potential is dictated by the ghost form factor only, i.e. $d(p) \propto 1/p$ and $\lim_{p \rightarrow 0} f(p) = 1$. On the contrary, we found $d(p) \propto 1/\sqrt{p}$ and $f(p) \propto 1/p$ in the IR regime, i.e. the form factor $f(p)$ plays a significant role in the confining property of the potential. The IR behaviour of the ghost form factor in Hamiltonian and lattice approaches can be directly compared in Fig. 7.6, left panel. We remark also a significant discrepancy in the UV regime.

Equal-time transverse gluon propagator. We report our results for the gluon propagator and the would-be gap function in Fig. 7.10 and Fig. 7.11. The numerical estimates were obtained for the lattice volumes $V = 26^4$ (L1) and $V = 32^4$ (L2) by averaging the observables over $N_{MC} = 400$ (L1) and $N_{MC} = 200$ (L2) lattice configurations, and are compared with the gap function $\omega(p)$ provided by the Hamiltonian approach [FRa].

As in $D = 2 + 1$, we normalized the lattice data such that the last measured point

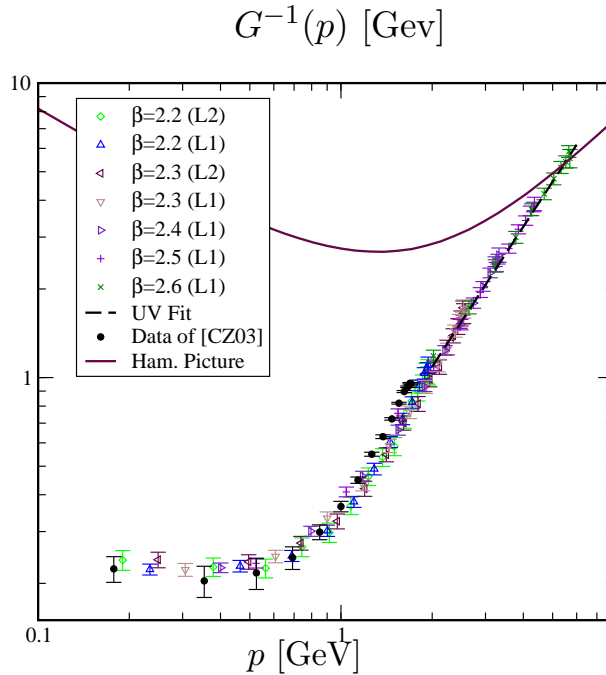


Figure 7.11: Inverse transverse gluon propagator in $D = 3 + 1$ as a function of the momentum p for the lattice volumes $V = 26^4$ (L1) and $V = 32^4$ (L2) and compared with the results obtained in [CZ02a] ($V = 30^4$).

coincides with the value obtained in the Hamiltonian picture. We remark immediately a dramatic qualitative discrepancy between analytical and numerical estimates. The plot of the would-be gap function in logarithmic scale in Fig. 7.11, reveals the two main features of our numerical results. First, and in contrast to the case $D = 2+1$, the gap function approaches a finite value at vanishing momentum. Second, the UV behaviour is well approximated by

$$G(p) \propto \frac{1}{p} \left(\frac{\Lambda_{QCD}}{p} \right)^\eta, \quad \eta = 0.54(1). \quad (7.36)$$

As in the case $D = 2 + 1$, we find an anomalous behaviour of the inverse gluon propagator in the high momentum regime, which tends to invalidate its interpretation as energy dispersion relation. As shown in Fig. 7.11, our results are compatible with the previous study of the gluon propagator in Coulomb gauge [CZ02a]. A remaining task for the next future is to find out whether this discrepancy is due to the numerical implementation of the equal-time gluon propagator or to more profound reasons which invalidate the relation $G^{-1}(p) \equiv \omega(p)$, i.e. the equivalence between the gap function as an energy dispersion relation and the inverse gluon propagator measured at fixed time.

7.6 Summary and outlook

This chapter was devoted to the lattice investigation of the ghost propagator and the Coulomb potential in pure $SU(2)$ Yang-Mills theory in the Coulomb gauge formulation. We addressed also the equal-time transverse gluon propagator. After a brief review of elementary concepts in lattice gauge theory, we described in details our numerical procedure. In particular, we fix

the gauge and perform the measurements in a given time slice on the lattice. Numerical gauge fixing is achieved via a combination of the simulated annealing and iterated overrelaxation algorithms.

We performed simulations in $D = 2 + 1$ and $D = 3 + 1$. Concerning ghost propagator and Coulomb potential, it turned out that lattice and Hamiltonian approaches are in good qualitative agreement in the three dimensional case. In four dimensions, a direct comparison is rendered difficult by different implementations of the renormalization program. The lattice calculation of the ghost propagator in $D = 3 + 1$ reveals that the combination $g_0^2 d(p)$ is cutoff independent, i.e. suggests that it is invariant under renormalization group transformations. Our results are in three and four dimensions compatible with a linear confining potential. In $D = 3 + 1$, we obtain $\sigma_{\text{Coul}} = 1.3(2)\sigma$ for the string tension. Combining the results for the ghost propagator and the Coulomb potential, we can study the deviation $f(p)$ of the Coulomb potential from the factorization $V_{\text{Coul}}(p) \propto d^2(p)/p^2$. An enhancement of $f(p)$ at small momenta signals non-Gaussian correlations between the ghost fields, which rule out the factorization assumption.

Our numerical study of gluonic correlations has revealed a striking feature of the equal-time gluon propagator. This one shows an anomalous scaling $(1/p)^{1+\eta}$, with $\eta = 0.50(1)$ in $D = 2 + 1$ and $\eta = 0.54(1)$ in $D = 3 + 1$, in the perturbative regime, which can invalidate the interpretation of the inverse propagator as energy dispersion relation for the gluons. In $D = 3 + 1$, we moreover find that the gluon propagator becomes in the IR regime independent of the momentum transfer, whereas it diverges in the Hamiltonian approach. We point out that our results are in agreement with a previous lattice study of the gluon propagator [CZ02a].

In view of our results for the transverse gluon propagator, it appears crucial to reserve future work for further investigations of gluonic correlations in the Coulomb gauge formulation of Yang-Mills theory. The possible origins of the strong anomalous scaling are still under ongoing debate. As further investigations, we propose to study full gluonic correlations, i.e. correlations of the type $\langle A_i^a(\mathbf{x}, t_0) A_j^b(\mathbf{y}, t_1) \rangle$ between different time slices t_0 and t_1 . This requires a complete gauge fixing of the lattice. This investigation will provide information on the p_0 -dependence of the *generalized* gluon propagator, from which the equal-time propagator is obtained by momentum projection:

$$G(\mathbf{p}) = \int \frac{dp_0}{2\pi} G^{\text{gen.}}(p) = \int \frac{dp_0}{2\pi} \frac{g(p_0, \mathbf{p})}{p_0^2 + \mathbf{p}^2}.$$

In case the numerical study of this quantity would provide the expected perturbative behaviour in the UV regime, we could state that the description of the energy dispersion relation in terms of gluonic correlations in one fixed time slice is not complete and has to be extended to the projection of generalized correlations. If the scaling of the gluon propagator would remain anomal, the question could be asked whether the interpretation of the inverse propagator as a dispersion relation is valid. In such a case, the anomalous scaling of the equal-time propagator could be possibly explained by its dependence on non-perturbative features included in the p_0 -dependence of the generalized form factor $g(p_0, \mathbf{p})$.

Appendix A

Conventions and notations

A.1 Units, metric and notations

We work in the units $c = \hbar = 1$. The metric is given by $g_{\mu\nu} = \text{diag}(+, -, -, -)$ in Minkowsky space and $g_{\mu\nu} = \delta_{\mu\nu}$ in Euclidean space.

We adopt the following notation conventions.

- The space-time dimension is denoted by D , the dimension of the spatial hyper-space by d , i.e. $D = d + 1$. For any vector V in space-time, the temporal component is denoted by V_0 and the spatial part by \mathbf{V} .
- Greek symbols: $\mu, \nu, \rho, \dots \in [1, D]$ are space-time indices while α, β, \dots denote spinor indices.
- Latin symbols: $i, j, k, \dots \in [1, d]$ are spatial indices, while colour indices in $SU(N)$ Yang-Mills theory are denoted by $a, b, c, \dots \in [1, N^2 - 1]$.

A.2 $SU(N)$ algebra

Any group element $g \in SU(N)$ can be written

$$g(\Lambda) = e^{i\Lambda^a T^a}, \quad (\text{A.1})$$

in terms of the $N^2 - 1$ *traceless hermitian generators* T^a . They span the $SU(2)$ *Lie algebra* and satisfy the following commutation relations

$$[T^a, T^b] = i f^{abc} T^c, \quad (\text{A.2})$$

where the numbers f^{abc} are the *structure constants*. They obey the *Jacobi identity*

$$f^{ade} f^{bcd} + f^{bde} f^{cad} + f^{cde} f^{abd} = 0. \quad (\text{A.3})$$

The matrices t^a of the *fundamental representation* satisfy the following orthogonality relation:

$$\text{tr}[t^a, t^b] = \frac{1}{2} \delta^{ab}. \quad (\text{A.4})$$

From this relation, it can be shown that the structure constants f^{abc} are totally antisymmetric. A further representation of the algebra, the *adjoint representation* is defined by means of the structure constants:

$$[T_A^a]^{bc} = -if^{abc}. \quad (\text{A.5})$$

The orthogonality relation reads in this representation:

$$\text{tr}[T_A^a, T_A^b] = N\delta^{ab}.$$

The *Casimir operator* is defined by $C = T^a T^a$ and reads

$$t^a t^a = \frac{N^2 - 1}{2N}, \quad T_A^a T_A^a = N$$

in the fundamental and adjoint representation, respectively.

Let us particularize to the gauge group $SU(2)$. The fundamental representation is given in terms of the Pauli matrices by

$$t^a = \frac{\tau^a}{2},$$

with

$$\tau^1 = \begin{pmatrix} 0 & 1 \\ 1 & 0 \end{pmatrix}, \quad \tau^2 = \begin{pmatrix} 0 & -i \\ i & 0 \end{pmatrix}, \quad \tau^3 = \begin{pmatrix} 1 & 0 \\ 0 & -1 \end{pmatrix}.$$

The structure constants read in this case:

$$f^{abc} = \varepsilon^{abc}.$$

The Casimir operator is given by

$$t^a t^a = \frac{3}{4}, \quad T_A^a T_A^a = 2$$

in the fundamental and adjoint representation, respectively.

Appendix B

Non-Abelian gauge theory in the continuum

We fix in this appendix the conventions used in chapter 6 concerning gauge transformation, covariant derivative, field strength and Lagrangian.

B.1 Covariant derivative - Gauge potential

The *gauge transformation* of a field $\phi(x)$ is defined by

$$\phi(x) \rightarrow g(x)\phi(x) \quad \text{with } g(x) = e^{ig_0\alpha^a(x)T^a}, \quad (\text{B.1})$$

where g_0 is the bare coupling constant and the generators have the dimension of the representation to which the field belongs. The *covariant derivative* operator is defined by

$$D_\mu = \partial_\mu - ig_0A_\mu,$$

where the connection, or *gauge potential*, $A_\mu = A_\mu^a T^a$ has to transform according to

$$A_\mu \rightarrow gA_\mu g^{-1} - \frac{i}{g_0}(\partial_\mu g)g^{-1} \quad (\text{B.2})$$

in order to ensure that $D_\mu \rightarrow gD_\mu$. Expanding the exponential in (B.1) to first order in α , we have

$$A_\mu^a \rightarrow A_\mu^a + \partial_\mu\alpha^a + g_0 f^{abc} A_\mu^b \alpha^c. \quad (\text{B.3})$$

For constant gauge transformations and using (A.5), the latter expression simplifies to

$$A_\mu^a \rightarrow A_\mu^a + ig_0[\alpha^c T_A^c]^{ab} A_\mu^b,$$

which shows that the gauge potential transforms according to the adjoint representation. When acting on a field operator $\phi = \phi^a T^a$, the covariant derivative reads

$$[D_\mu\phi]^a = \partial_\mu\phi^a + g_0 f^{abc} A_\mu^b \phi^c, \quad \text{or } D_\mu\phi = \partial_\mu\phi - ig_0[A_\mu, \phi].$$

The gauge transformation (B.3) can then be expressed as

$$A_\mu^a \rightarrow A_\mu^a + [D_\mu\alpha]^a. \quad (\text{B.4})$$

The covariant derivative can also be derived by considering gauge transformations belonging to a one-parameter subgroup of the gauge group G :

$$g(\tau, x) = \exp(i g_0 \tau \omega(x)),$$

where $\omega(x)$ is an element of the Lie algebra associated to G and τ a real parameter. Inserting this expression into the potential transformation (B.2), we obtain

$$A_\mu^g(x, \tau) = e^{i g_0 \tau \omega(x)} A_\mu(x) e^{-i g_0 \tau \omega(x)} + \tau \partial_\mu \omega(x).$$

Differentiating with respect to τ and taking the value at $\tau = 0$, one has

$$\left[\frac{d}{d\tau} A_\mu^g(x, \tau) \right]_{\tau=0} = \partial_\mu \omega(x) - i g_0 [A_\mu(x), \omega(x)], \quad (\text{B.5})$$

which is the covariant derivative applied to ω .

B.2 Field strength - E and B fields

The *field strength* tensor is obtained by considering the commutator of two covariant derivatives acting on a field ϕ :

$$\frac{1}{g_0} [[D_\mu, D_\nu] \phi]_a = f^{abc} F_{\mu\nu}^b \phi^c,$$

where

$$F_{\mu\nu}^b = \partial_\mu A_\nu^b - \partial_\nu A_\mu^b + g_0 f^{bde} A_\mu^d A_\nu^e, \quad (\text{B.6})$$

This relation is obtained by calculating straightforwardly the commutator and by using the antisymmetry property of the structure constants and the Jacobi identity (A.3). An alternative formulation is given in terms of the commutator of the gauge potentials:

$$F_{\mu\nu} = \partial_\mu A_\nu - \partial_\nu A_\mu - i g_0 [A_\mu, A_\nu].$$

The components of the field strength tensor define the colour electric and magnetic fields, that are given by

$$E_k^a = F_{0k}, \quad B_k^a = -\frac{1}{2} \varepsilon_{ijk} F_{ij}^a.$$

They read explicitly in terms of the gauge potential

$$E_k^a = -\partial_k A_0^a + \partial_0 A_k^a + g_0 f^{abc} A_0^b A_k^c, \quad B_k^a = -\varepsilon_{ijk} \left[\partial_i A_j^a + g_0 \frac{1}{2} f^{abc} A_i^b A_j^c \right] \quad (\text{B.7})$$

and have the following vectorial form

$$\mathbf{E}^a = -\nabla A_0^a - \partial_0 \mathbf{A}^a - g_0 f^{abc} A_0^b \mathbf{A}^c, \quad \mathbf{B}^a = \nabla \times \mathbf{A}^a - g_0 \frac{1}{2} f^{abc} \mathbf{A}^b \times \mathbf{A}^c. \quad (\text{B.8})$$

B.3 Lagrangian - classical field equations

The Lagrangian of the $SU(N)$ Yang-Mills theory reads

$$\mathcal{L}_{SU(2)} = -\frac{1}{4}F_{\mu\nu}^a F_a^{\mu\nu}.$$

The coupling to matter fields is taken into account via the additional term $g_0 A_\mu J^\mu$:

$$\mathcal{L}_{SU(2)+\text{matter}} = -\frac{1}{4}F_{\mu\nu}^a F_a^{\mu\nu} + g_0 A_\mu J^\mu. \quad (\text{B.9})$$

Since $[g_0] = 2 - D/2$, $[A] = D/2 - 1$, we have $[J] = d$, i.e. the current J has the dimension of a density. Deriving the Euler-Lagrange equations corresponding to the Lagrangian (B.9) gives the classical equations of motion, the non-Abelian pendant of the Maxwell equations:

$$D^\mu F_{\mu\nu}^a = g_0 J_\nu^a.$$

Appendix C

Lattice technicalities

C.1 Conventions

We work in Euclidean space, i.e. with the metric $g_{\mu\nu} = \delta_{\mu\nu}$. Contrary to continuum field theory, a gauge transformation is defined in the lattice conventions by

$$g(x) = e^{i\alpha^a(x)T^a},$$

i.e. the bare coupling constant is absorbed in the gauge parameters α^a . As a consequence, the coupling drops out of the covariant derivative, which reads

$$D_\mu = \partial_\mu - iA_\mu.$$

We have therefore the correspondence $A_{\text{lat}} = g_0 A_{\text{cont}}$. Applying this rule, we obtain for the Yang-Mills Lagrangian:

$$\mathcal{L} = -\frac{1}{4g_0^2} F_{\mu\nu}^a F_{\mu\nu}^a.$$

C.2 Basic concepts

Direct and reciprocal lattice. The space-time is discretized and considered as a D -dimensional lattice with lattice spacing a . The lattice extension is given by the D -plet $\{N_1, \dots, N_D\}$. A lattice site is labeled by a D -plet of integer parameters (n_1, n_2, \dots, n_D) with $n_\mu \in [1, N_\mu]$ and $\mu \in [1, D]$, corresponding to the physical point $x = (x_1, x_2, \dots, x_D) = (an_1, an_2, \dots, an_D)$. The coordinate x_D in our conventions is the time coordinate and denoted by $t := x_D$. We denote the coordinates in a d -dimensional time slice by $\mathbf{x} = (x_1, \dots, x_d)$.

We impose periodic boundary conditions: for any function $f(x)$, we have

$$f(x + aN_\mu \mathbf{e}_\mu) = f(x), \quad \mu \in [1, D] \tag{C.1}$$

[no summation on μ], where \mathbf{e}_μ denotes the unit vector in the direction μ . As a consequence, any function f can be expanded in the following way (we consider a one-dimensional lattice of N points for simplicity):

$$f(x) = \frac{1}{\sqrt{N}} \sum_{n_p=1}^N \tilde{f}(n_p) e^{-i\frac{2\pi}{N}n_x n_p}.$$

For simplicity, we use the notation $n_x \equiv \bar{x}$ and $n_p \equiv \bar{p}$. With this convention, the expansion of f becomes

$$f(x) = \frac{1}{\sqrt{N}} \sum_{\bar{p}=1}^N \tilde{f}(\bar{p}) e^{-i\frac{2\pi}{N}\bar{x}\bar{p}}. \quad (\text{C.2})$$

Using Dirac's formalism, we rewrite this expression under the form

$$\langle f|x \rangle = \sum_{p=1}^N \langle f|p \rangle \langle p|x \rangle.$$

The ket $|p\rangle$ is expressed in the coordinate representation by

$$\langle p|x \rangle = \frac{1}{\sqrt{N}} e^{-i\frac{2\pi}{N}\bar{x}\bar{p}}, \quad \langle x|p \rangle = \langle p|x \rangle^*, \quad (\text{C.3})$$

and the set $\{|p\rangle\}$ satisfies

$$\sum_{p=1}^N |p\rangle \langle p| = 1.$$

Applying $\langle x|$ and $|y\rangle$ respectively to the left and right hand side of this relation, we find the representation of the Kronecker-delta in the base $\{|p\rangle\}$:

$$\langle x|y \rangle = \frac{1}{N} \sum_{\bar{p}=1}^N e^{-i\frac{2\pi}{N}(\bar{x}-\bar{y})\bar{p}} = \delta_{xy}$$

by resumming the geometric series. In momentum space, the analog expression reads

$$\langle p|q \rangle = \delta_{pq}.$$

The expansion (C.2) in D dimensions reads

$$f(\mathbf{x}) = \frac{1}{\sqrt{N_1 \dots N_D}} \sum_{\bar{p}_1=1}^{N_1} \dots \sum_{\bar{p}_D=1}^{N_D} \tilde{f}(\bar{\mathbf{p}}) e^{-i\frac{2\pi}{N_1}\bar{x}_1\bar{p}_1} \dots e^{-i\frac{2\pi}{N_D}\bar{x}_D\bar{p}_D}.$$

We simplify this expression by using the short hand notation:

$$f(\mathbf{x}) = \frac{1}{\sqrt{\mathbf{N}}} \sum_{\bar{\mathbf{p}}} \tilde{f}(\bar{\mathbf{p}}) e^{-i\frac{2\pi}{\mathbf{N}}\bar{\mathbf{x}}\cdot\bar{\mathbf{p}}}.$$

Representation in momentum space. For any observable G , we define $\tilde{G}(p, q) := \langle p|G|q \rangle$. Introducing two complete sets of states in coordinate space, we obtain, using (C.3),

$$\tilde{G}(p, q) = \frac{1}{N} \sum_{\bar{x}=1}^N \sum_{\bar{y}=1}^N e^{i\frac{2\pi}{N}\bar{p}\bar{x}} G(\bar{x}, \bar{y}) e^{-i\frac{2\pi}{N}\bar{q}\bar{y}}.$$

If the observable G moreover possesses the property of translation invariance, it is diagonal in momentum space:

$$\tilde{G}(p, q) = \delta_{pq} \underbrace{\sum_{\bar{x}'=1}^N G(\bar{x}') \cos\left(\frac{2\pi}{N}\bar{p}\bar{x}'\right)}_{:=G(p)},$$

where the diagonal element $G(p) = \langle p|G|p\rangle$ can also be expressed as

$$G(p) = \frac{1}{N} \sum_{\bar{x}=1}^N \sum_{\bar{y}=1}^N G(\bar{x}, \bar{y}) \cos\left(\frac{2\pi}{N}\bar{p}(\bar{x} - \bar{y})\right). \quad (\text{C.4})$$

Differential operators. We define

$$\begin{aligned} \hat{\nabla}_{\mu}^{(-)} f(x) &= f(x) - f(x - a\mathbf{e}_{\mu}), & \nabla_{\mu}^{(-)} &= \frac{1}{a} \hat{\nabla}_{\mu}^{(-)}, \\ \hat{\nabla}_{\mu}^{(+)} f(x) &= f(x + a\mathbf{e}_{\mu}) - f(x), & \nabla_{\mu}^{(+)} &= \frac{1}{a} \hat{\nabla}_{\mu}^{(+)}. \end{aligned}$$

The second derivative in the direction μ is defined by

$$\hat{\nabla}_{\mu}^2 f(x) = f(x + a\mathbf{e}_{\mu}) - 2f(x) + f(x - a\mathbf{e}_{\mu}), \quad \nabla_{\mu}^2 = \frac{1}{a^2} \hat{\nabla}_{\mu}^2.$$

Applying this operator to the momentum representation (C.2) of a function f , we find (for a one-dimensional lattice)

$$\hat{\nabla}^2 f(x) = \sum_{\bar{p}=1}^N (-4) \sin^2\left(\frac{\pi}{N}\bar{p}\right) \tilde{f}(\bar{p}) e^{-i\frac{2\pi}{N}\bar{x}\bar{p}}. \quad (\text{C.5})$$

In D dimensions, the Laplace operator is given by $\hat{\nabla}^2 = \sum_{\mu=1}^D \hat{\nabla}_{\mu}^2$.

Lattice momentum. The expression (C.5) suggests the definition of a *lattice momentum*

$$\hat{p}_{\mu} = 2 \sin\left(\frac{\pi}{N}\bar{p}_{\mu}\right).$$

From a practical point of view, this short hand notation is a convenient way to express the lattice representation of propagators in momentum space by their analogous expressions in the continuum.

C.3 Links and lattice gauge potential

The basic object in lattice gauge theory is the link, which describes the parallel transport along the segment connecting two adjacent lattice points. The quantity $U_{\mu}(x)$ is an element of the gauge group G attached to the segment $[x, x + a\mathbf{e}_{\mu}]$. The lattice gauge potential is defined by

$$U_{\mu}(x) = \exp(i\hat{A}_{\mu}(x)),$$

and therefore dimensionless and hermitian. In terms of the link, it is expressed as

$$U_\mu(x) - U_\mu^\dagger(x) = 2i\hat{A}_\mu(x) + \mathcal{O}(a^2). \quad (\text{C.6})$$

In particular, we have, for $SU(2)$,

$$\hat{A}_\mu^a(x) = 2 \text{Imtr}[t^a U_\mu(x)] \quad (\text{C.7})$$

in the fundamental representation. Moreover, a $SU(2)$ link can be represented in terms of the Pauli matrices

$$U_\mu(x) = a_\mu^0(x) + i\mathbf{a}_\mu(x) \cdot \boldsymbol{\tau}, \quad (\text{C.8})$$

where the vector $(a_\mu^0, \mathbf{a}_\mu)$ lives on the unit sphere S^3 :

$$a_\mu^0(x)^2 + \mathbf{a}_\mu(x)^2 = 1.$$

The lattice gauge potential is given by

$$\hat{A}_\mu^a(x) = 2a_\mu^a(x).$$

C.4 Gauge transformation

A local gauge transformation on the link $U_\mu(x)$ at the point x is defined by

$$U_\mu^g(x) = g(x)U_\mu(x)g^{-1}(x + a\mathbf{e}_\mu), \quad (\text{C.9})$$

where $g(x)$ and $g^{-1}(x + a\mathbf{e}_\mu)$ are both elements of the gauge group. Expanding $U_\mu^g(x)$ to first order in a , we find

$$U_\mu^g(x) = 1 + ia[g(x)A_\mu(x)g^{-1}(x) - ig(x)\nabla_\mu^{(+)}g^{-1}(x)] + \mathcal{O}(a^2),$$

which permits to express the gauge transformation of the lattice gauge potential

$$\hat{A}_\mu^g(x) = g(x)\hat{A}_\mu(x)g^{-1}(x) - ig(x)\hat{\nabla}_\mu^{(+)}g^{-1}(x).$$

Let us point out that, due to the definition of the gauge transformation (C.9), the transformation of the lattice gauge potential in the lattice conventions differs from the corresponding transformation in the continuum (B.2).

C.5 Covariant derivative

We derive the lattice expression of the covariant derivative by considering gauge transformations belonging to a one-parameter subgroup of G :

$$g(\tau, x) = \exp(i\tau\omega(x)),$$

where $\omega(x)$ is an element of the Lie algebra and τ a real parameter. In analogy with the relation (B.5), we compute the derivative of the lattice gauge potential with respect to the τ parameter [we use the short hand notations $\hat{A}^g(x, \tau) = \hat{A}^\tau(x)$ and $U^g(x, \tau) = U^\tau(x)$]:

$$\frac{d}{d\tau}\hat{A}_\mu^{\tau, a}(x) = 2 \text{Imtr} \left[t^a \frac{d}{d\tau} U_\mu^\tau(x) \right]. \quad (\text{C.10})$$

The derivative of $U_\mu^\tau(x)$ is given by

$$\frac{d}{d\tau}U_\mu^\tau(x) = i\omega(x)U_\mu^\tau(x) - iU_\mu^\tau(x)\omega(x + a\mathbf{e}_\mu).$$

Inserting into (C.10), we obtain

$$\frac{d}{d\tau}\hat{A}_\mu^{\tau,a}(x) = -\text{tr}\left[t^a\left(-\omega(x)U_\mu^\tau(x) + U_\mu^\tau(x)\omega(x + \hat{\mu}) - U_\mu^{\tau,\dagger}(x)\omega(x) + \omega(x + \hat{\mu})U_\mu^{\tau,\dagger}(x)\right)\right], \quad (\text{C.11})$$

where we replaced $a\mathbf{e}_\mu$ by $\hat{\mu}$ to simplify the notation. The covariant derivative contains the gauge potential, which is on the lattice given in terms of the links by (C.6). We therefore let appear an expression which is proportional to the difference $U_\mu(x) - U_\mu^\dagger(x)$. We make the ansatz $\text{tr}[F^a(x)(U_\mu(x) - U_\mu^\dagger(x))]$, where F^a contains the matrices t^a , $\omega(x)$ and $\omega(x + \hat{\mu})$. If we take for F^a the commutator $[\omega(x) + \omega(x + \hat{\mu}), t^a]$, the familiar structure of the commutator term of the covariant derivative can indeed be derived:

$$\begin{aligned} \text{tr}[[\omega(x) + \omega(x + \hat{\mu}), t^a](U_\mu^\tau(x) - U_\mu^{\tau,\dagger}(x))] & \quad (\text{C.12}) \\ &= -\text{tr}\left[[t^a, t^b]\left(\omega^b(x) + \omega^b(x + \hat{\mu})\right)\left(U_\mu^\tau(x) - U_\mu^{\tau,\dagger}(x)\right)\right] \\ &= f^{abc}\left(\omega^b(x) + \omega^b(x + \hat{\mu})\right)2\text{Imtr}\left[t^c U_\mu^\tau(x)\right] \\ &= f^{abc}\hat{A}_\mu^{\tau,c}(x)\left(\omega^b(x) + \omega^b(x + \hat{\mu})\right). \end{aligned}$$

A little bit of algebra permits to show that

$$2 \times (\text{C.11}) + (\text{C.12}) = \text{tr}[\{\omega(x) - \omega(x + \hat{\mu}), t^a\}(U_\mu^\tau(x) + U_\mu^{\tau,\dagger}(x))],$$

which gives

$$\begin{aligned} \frac{d}{d\tau}\hat{A}_\mu^{\tau,a}(x) &= -\frac{1}{2}\text{tr}[[\omega(x + \hat{\mu}) + \omega(x), t^a](U_\mu^\tau(x) - U_\mu^{\tau,\dagger}(x)) \\ &\quad + \{\omega(x + \hat{\mu}) - \omega(x), t^a\}(U_\mu^\tau(x) + U_\mu^{\tau,\dagger}(x))]. \end{aligned}$$

The anticommutator term can be rewritten as $-G_\mu^{ab}(x)\hat{\nabla}_\mu^{(+)}\omega^b(x)$, with

$$G_\mu^{ab}(x) = \frac{1}{2}\text{tr}\left[\{t^a, t^b\}\left(U_\mu^\tau(x) + U_\mu^{\tau,\dagger}(x)\right)\right]. \quad \text{The lattice covariant derivative finally reads, setting } \tau = 0,$$

$$[\hat{D}_\mu[U]\omega]^a(x) = -G_\mu^{ab}(x)\hat{\nabla}_\mu^{(+)}\omega^b(x) + \frac{1}{2}f^{abc}\hat{A}_\mu^b(x)(\omega^c(x) + \omega^c(x + a\mathbf{e}_\mu)). \quad (\text{C.13})$$

For $SU(2)$, the expression $G_\mu^{ab}(x)$ can be simplified. Using the representation (C.8), we have

$$G_\mu^{ab}(x) = a_\mu^0(x)\text{tr}\left[\{t^a, t^b\}\right] = a_\mu^0(x)\delta^{ab}.$$

C.6 Faddeev-Popov operator

The lattice Faddeev-Popov operator is defined by

$$[\hat{M}[U]\omega]^a(x) = -\hat{\nabla}_\mu^{(-)} \cdot (\hat{D}[U]\omega)^a(x)$$

and acts on the field $\omega(x)$ in the following way

$$[\hat{M}[U]\omega]^a(x) = \sum_{\mu} \{G_{\mu}^{ab}(x)\hat{\nabla}_{\mu}^{(+)}\omega^b(x) - [x \rightarrow x - a\mathbf{e}_{\mu}] - \frac{1}{2}f^{abc} [\hat{A}_{\mu}^b(x)\omega^c(x + a\mathbf{e}_{\mu}) - \hat{A}_{\mu}^b(x - a\mathbf{e}_{\mu})\omega^c(x - a\mathbf{e}_{\mu})]\}, \quad (\text{C.14})$$

using the expression (C.13) for the lattice covariant derivative and the transversality condition of the gauge potential in Coulomb gauge.

C.7 Lattice gauge fixing

1. We compute the derivative with respect to the parameter τ of the gauge functional $F_U^t[g]$ in Sec. 7.2.2. In the τ parametrization, a gauge-transformed link is given by

$$U_i^{\tau}(\mathbf{x}) = g(\tau, \mathbf{x})U_i(\mathbf{x})g^{\dagger}(\tau, \mathbf{x} + a\mathbf{e}_i).$$

Differentiating with respect to τ , we obtain

$$\frac{d}{d\tau}U_i^{\tau}(\mathbf{x}) = i\omega(\mathbf{x})U_i^{\tau}(\mathbf{x}) - iU_i^{\tau}(\mathbf{x})\omega(\mathbf{x} + a\mathbf{e}_i).$$

The derivative of F_U^t then reads

$$\begin{aligned} \frac{d}{d\tau}F_U^t[\omega, \tau] &= - \sum_{t, i, \mathbf{x}} \text{ReTr}[(i\omega(\mathbf{x}) - i\omega(\mathbf{x} + a\mathbf{e}_i))U_i^{\tau}(\mathbf{x})] \\ &= \sum_{t, i, \mathbf{x}} \text{ImTr}[\omega(\mathbf{x})(U_i^{\tau}(\mathbf{x}) - U_i^{\tau}(\mathbf{x} - a\mathbf{e}_i))]. \end{aligned}$$

Expanding the imaginary part explicitly, we obtain

$$\begin{aligned} \frac{d}{d\tau}F_U^t[\omega, \tau] &= -\frac{i}{2} \sum_{t, \mathbf{x}} \text{Tr}[\omega(\mathbf{x})[\sum_i (U_i^{\tau}(\mathbf{x}) - U_i^{\tau, \dagger}(\mathbf{x})) - \sum_i (U_i^{\tau}(\mathbf{x} - a\mathbf{e}_i) - U_i^{\tau, \dagger}(\mathbf{x} - a\mathbf{e}_i))]] \\ &= \sum_{\mathbf{x}} \text{Tr}[\omega(\mathbf{x}) \sum_i (\hat{A}_i^{\tau}(\mathbf{x}) - \hat{A}_i^{\tau}(\mathbf{x} - a\mathbf{e}_i))], \end{aligned}$$

recalling (C.6). In a more compact notation, this can be rewritten as

$$\frac{d}{d\tau}F_U^t[\omega, \tau] = \langle \omega, \hat{\nabla}^{(-)} \cdot \hat{\mathbf{A}}^{\tau} \rangle.$$

2. We prove the relation (7.22) permitting to gauge transform the lattice to the temporal gauge $A_0(x) = 0$. Let us recall that we want to achieve, at fixed \mathbf{x} ,

$$U^g(\mathbf{x}, 1) = U^g(\mathbf{x}, 2) = \dots = U^g(\mathbf{x}, N_t) = U^g = \sqrt[N_t]{P(\mathbf{x})}.$$

We dropped for clarity the index 0 indicating that we work on temporal links. Using the simplified notation $U_i = U(\mathbf{x}, i)$, $g_i = g(\mathbf{x}, i)$, $i = 1, \dots, N_t$, we have

$$\begin{aligned} U^g &= g_1 U_1 g_2^{\dagger} \longrightarrow g_2 = U^{g, \dagger} g_1 U_1 \\ U^g &= g_2 U_2 g_3^{\dagger} \longrightarrow g_3 = U^{g, \dagger} U^{g, \dagger} g_1 U_1 U_2 \\ &\dots \\ U^g &= g_{N_t} U_{N_t} g_1^{\dagger} \longrightarrow g_1 = \underbrace{U^{g, \dagger} U^{g, \dagger} \dots U^{g, \dagger}}_{N_t \text{ factors}} g_1 U_1 U_2 \dots U_{N_t}. \end{aligned}$$

The Polyakov line $P(\mathbf{x}) = U_1 U_2 \dots U_{N_t}$ has to remain invariant under the transformations g_i . This is achieved if, for instance,

$$U^g = \sqrt[N_t]{P(\mathbf{x})}, \quad g_1 = P^\dagger(\mathbf{x})g_1P(\mathbf{x}),$$

which is verified if we set $g_1 = 1$. The choice of Conti and collaborators [CPPV96] is

$$U_1^g = U_2^g = \dots = U_{N_t-1}^g = 1, \quad U_{N_t}^g = P(\mathbf{x}).$$

C.8 Inverse Faddeev-Popov operator

We complete the discussion of Sec. 7.4.1 and Sec. 7.4.2.

Ghost propagator. The ghost propagator is obtained by averaging diagonal elements of the inverse Faddeev-Popov operator. Applying the addition formula to the cosine factor in (7.24), we obtain

$$\begin{aligned} \hat{D}(\hat{\mathbf{p}}) &= \frac{1}{3\mathbf{N}_d} \left\langle \sum_{a,b=1}^3 \sum_{\bar{\mathbf{x}}}^{\mathbf{N}_d} \left[\cos \left(\frac{2\pi}{N_1} \bar{x}_1 \bar{p} \right) \delta^{ab} \underbrace{\sum_{c=1}^3 \sum_{\bar{\mathbf{y}}}^{\mathbf{N}_d} \hat{M}^{-1}[U]_{(\bar{\mathbf{x}}, \bar{\mathbf{y}})}^{bc} \cos \left(\frac{2\pi}{N_1} \bar{y}_1 \bar{p} \right) \delta^{ca}}_{\text{Conj. Grad.}} \right. \right. \\ &+ \left. \left. \sin \left(\frac{2\pi}{N_1} \bar{x}_1 \bar{p} \right) \delta^{ab} \underbrace{\sum_{c=1}^3 \sum_{\bar{\mathbf{y}}}^{\mathbf{N}_d} \hat{M}^{-1}[U]_{(\bar{\mathbf{x}}, \bar{\mathbf{y}})}^{bc} \sin \left(\frac{2\pi}{N_1} \bar{y}_1 \bar{p} \right) \delta^{ca}}_{\text{Conj. Grad.}} \right] \right\rangle. \end{aligned}$$

The calculation of the underbraced sums is performed using the conjugate gradient algorithm (see Sec. D.2).

Coulomb potential. Applying the addition formula to the cosine factor in (7.28), we obtain

$$\begin{aligned} \hat{V}_{\text{Coul}}(\hat{\mathbf{p}}) &= \frac{-1}{4\mathbf{N}_d} g_0^{2d-4} \left\langle \sum_{a,b,c=1}^3 \sum_{\bar{\mathbf{x}}}^{\mathbf{N}_d} \left[\cos \left(\frac{2\pi}{N_1} \bar{x}_1 \bar{p} \right) \delta^{ab} \sum_{\bar{\mathbf{y}}}^{\mathbf{N}_d} \mathcal{V}_{\text{Coul}}^{bc}(\bar{\mathbf{x}}, \bar{\mathbf{y}}) \cos \left(\frac{2\pi}{N_1} \bar{y}_1 \bar{p} \right) \delta^{ca} \right. \right. \\ &+ \left. \left. \sin \left(\frac{2\pi}{N_1} \bar{x}_1 \bar{p} \right) \delta^{ab} \sum_{\bar{\mathbf{y}}}^{\mathbf{N}_d} \mathcal{V}_{\text{Coul}}^{bc}(\bar{\mathbf{x}}, \bar{\mathbf{y}}) \sin \left(\frac{2\pi}{N_1} \bar{y}_1 \bar{p} \right) \delta^{ca} \right] \right\rangle. \end{aligned}$$

Inserting two complete sets in coordinate space:

$$\mathcal{V}_{\text{Coul}}^{bc}(\mathbf{x}, \mathbf{y}) = \sum_{f=1}^3 \sum_{\bar{\mathbf{z}}, \bar{\mathbf{t}}}^{\mathbf{N}_d} M^{-1}[U]_{(\bar{\mathbf{x}}, \bar{\mathbf{z}})}^{bf} \langle \mathbf{z} | (-\Delta) | \mathbf{t} \rangle M^{-1}[U]_{(\bar{\mathbf{t}}, \bar{\mathbf{y}})}^{fc}$$

and using the fact that the Laplace operator is diagonal, we obtain for the cosine part, up to the prefactor $-1/4\mathbf{N}_d g_0^{2d-4}$,

$$\left\langle \underbrace{\sum_{a,f=1}^3 \sum_{\bar{\mathbf{z}}=1}^{\mathbf{N}_d} \sum_{b=1}^3 \sum_{\bar{\mathbf{x}}}^{\mathbf{N}_d} \hat{M}^{-1}[U]_{(\bar{\mathbf{x}}, \bar{\mathbf{z}})}^{bf} \cos \left(\frac{2\pi}{N_1} \bar{x}_1 \bar{p} \right) \delta^{ab} (-\Delta_{\bar{\mathbf{z}}})}_{\text{Conj. Grad.}} \underbrace{\sum_{c=1}^3 \sum_{\bar{\mathbf{y}}}^{\mathbf{N}_d} \hat{M}^{-1}[U]_{(\bar{\mathbf{z}}, \bar{\mathbf{y}})}^{fc} \cos \left(\frac{2\pi}{N_1} \bar{y}_1 \bar{p} \right) \delta^{ca}}_{\text{Conj. Grad.}} \right\rangle$$

and similarly for the sine part.

Appendix D

Lattice algorithms

The aim of the following sections is to give a short and practical summary of the numerical procedures used in this work. The reader interested in the theoretical concepts from which these algorithms are derived is invited to consult the references given in each section.

D.1 Heatbath algorithm

In this work, two numerical procedures are based on the heatbath algorithm of Creutz and collaborators [CJR83]:

- lattice thermalisation,
- simulated annealing procedure.

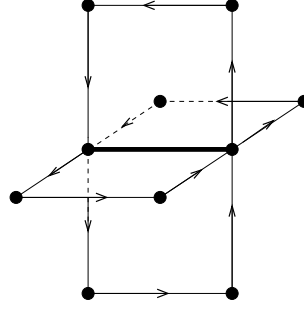
The heatbath algorithm is a *local* algorithm: it is performed at all lattice points, which are visited successively. At each point, a $SU(2)$ matrix, denoted here generically by $g(x)$, is updated, inducing a change in the action $S[g]$. This variation of S can, in both procedures concerned here, be written under the form

$$\delta S = -\beta \operatorname{tr}(V(x)\delta g(x)),$$

with some matrix $V(x)$, which we particularize to each problem below. The aim of the update procedure is to lead a statistical system towards thermal equilibrium at temperature $T = 1/\beta$. In this case, a configuration g occurs with a probability proportional to the Boltzmann factor $e^{-S[g]}$:

$$dP(g) \propto dg e^{\frac{1}{2}\beta \operatorname{tr}(gV)}.$$

Lattice thermalization. In this case, the elements to be updated are the links $U_\mu(x)$. This is done with respect to the Wilson action (7.4). At a given lattice point x and for a given link $U_\mu(x)$, the matrix $V(x)$ is found by collecting all terms in the action (7.4) containing the link $U_\mu(x)$. As illustrated in the figure below, $V(x)$ is given by the sum of the “open plaquettes” around $U_\mu(x)$, i.e. all plaquettes involving the link $U_\mu(x)$ (the bold link in the figure) from which $U_\mu(x)$ has been removed.



Simulated annealing. The basis idea of the simulated annealing procedure has been discussed in Sec. 7.2.4. The elements to be updated are the local gauge transformations $g(\mathbf{x})$. This is done with respect to the gauge functional $F_U[g]$, which is interpreted as the action of a fictitious field theory. Identifying all the terms in $F_U[g]$ containing the transformation $g(\mathbf{x})$, we find

$$V(\mathbf{x}) = \sum_{i=1}^d \left(U_i^\dagger(\mathbf{x} - a\mathbf{e}_i) g^\dagger(\mathbf{x} - a\mathbf{e}_i) + U_i(\mathbf{x}) g^\dagger(\mathbf{x} + a\mathbf{e}_i) \right).$$

The simulated annealing procedure is characterized by the following parameters:

- β_{SA} : coupling or inverse temperature of the fictitious field theory,
- $\Delta\beta_{SA}$: coupling increment,
- N_{UP}^{SA} : number of lattice updates (“thermalization”) at fixed coupling.

The matrix $V(x)$ is in each case given by the sum of $SU(2)$ matrices and is therefore proportional to another $SU(2)$ element \bar{g} :

$$V = k\bar{g}, \quad k = \sqrt{\det(V)}.$$

The invariance of the group measure can be used to absorb \bar{g} in the probability distribution. Setting $g = \tilde{g}\bar{g}^{-1}$, we have

$$dg e^{\frac{1}{2}k\beta\text{tr}(g\bar{g})} = d\tilde{g} e^{\frac{1}{2}k\beta\text{tr}(\tilde{g})}.$$

Using the representation (C.8) for \tilde{g} gives

$$dP(a_0, \mathbf{a}) \propto d^4a \delta(a^2 - 1) e^{\beta ka_0}.$$

By eliminating $|\mathbf{a}|$ using the delta function, we obtain the appropriate weighting on the hypersphere $a_0^2 + |\mathbf{a}|^2 = 1$:

$$dP(a_0, \theta_{\mathbf{a}}, \varphi_{\mathbf{a}}) \propto da_0 d\Omega_{\mathbf{a}} \sqrt{1 - a_0^2} e^{\beta ka_0},$$

where $d\Omega_{\mathbf{a}} = \sin(\theta_{\mathbf{a}})d\theta_{\mathbf{a}}d\varphi_{\mathbf{a}}$ is the differential solid angle of \mathbf{a} . Changing the variable a_0 to $z = e^{\beta ka_0 - \beta k}$ gives

$$dP(z, \theta_{\mathbf{a}}, \varphi_{\mathbf{a}}) \propto dz d\Omega_{\mathbf{a}} \sqrt{1 - a_0^2(z)}, \quad e^{-2\beta k} \leq z \leq 1.$$

The variable z is generated randomly in the allowed interval and rejected with probability $\sqrt{1 - a_0^2(z)}$. This is done practically by generating a random number $z_0 \in [0, 1]$ until the condition $z_0 < \sqrt{1 - a_0^2(z)}$ is satisfied. The direction of \mathbf{a} is then determined by generating the angles $\theta_{\mathbf{a}}$ and $\phi_{\mathbf{a}}$ randomly. The generated group element $g(x)$ can be reconstructed. Finally, the original group element is replaced by $g'(x)$ given by

$$g'(x) = \tilde{g}(x)\bar{g}^{-1}(x).$$

The whole procedure is repeated until all the elements $g(x)$ have been updated.

D.2 Conjugate gradient

The conjugate gradient algorithm permits to solve a system of linear equations of the type

$$M\vec{x} = \vec{b},$$

where \vec{b} is a known vector and M is a known, square, symmetric, positive-definite matrix. We present the algorithm without proof, under the form of a recipe. The interested reader can find details in the Numerical Recipes manual [PFTV] or in the nice lecture script by J.R. Shewchuk [She]. The system is solved by finding a vector \vec{x} that minimizes the function

$$f(\vec{x}) = \frac{1}{2}\vec{x}^T M\vec{x} - \vec{b}^T \cdot \vec{x} + c.$$

In the following, $\vec{d}_{(i)}$ denotes the direction of descent and $\vec{r}_{(i)}$ is the residual $\vec{r}_{(i)} = \vec{b} - M\vec{x}_{(i)}$ at the iteration i .

The first value $\vec{d}_{(0)}$ and $\vec{r}_{(0)}$ are given by

$$\vec{d}_{(0)} = \vec{r}_{(0)} = \vec{b} - M\vec{x}_{(0)},$$

with the initial guess $\vec{x}_{(0)}$. The recursion works as follows:

1. compute

$$\alpha_{(i)} = \frac{\vec{r}_{(i)}^T \cdot \vec{r}_{(i)}}{\vec{d}_{(i)}^T M \vec{d}_{(i)}},$$

2. update the residual \vec{r} and the vector \vec{x}

$$\begin{aligned} \vec{r}_{(i+1)} &= \vec{r}_{(i)} - \alpha_{(i)} M \vec{d}_{(i)}, \\ \vec{x}_{(i+1)} &= \vec{x}_{(i)} + \alpha_{(i)} \vec{d}_{(i)}, \end{aligned}$$

3. compute

$$\beta_{(i)} = \frac{\vec{r}_{(i+1)}^T \cdot \vec{r}_{(i+1)}}{\vec{r}_{(i)}^T \cdot \vec{r}_{(i)}},$$

4. update the direction of descent

$$\vec{d}_{(i+1)} = \vec{r}_{(i+1)} + \beta_{(i)} \vec{d}_{(i)}.$$

The iteration is halted when the norm of the residual drops below a given small constant ε :

$$\vec{r}_{(i)}^T \cdot \vec{r}_{(i)} < \varepsilon.$$

The vector \vec{x} is the numerical estimate of $M^{-1}\vec{b}$.

Appendix E

Elementary calculations

E.1 Plane center vortices

Let us start from general considerations in $SU(N)$ Yang-Mills theory in D dimensions. In the continuum, a $SU(N)$ center vortex is defined by the following gauge potential:

$$\mathcal{A}_\mu^{\text{CV}}[\Sigma, x, k] = -E(k) \int_\Sigma d^{D-2} \tilde{\sigma}_{\mu\kappa} \partial_\kappa D(x - \bar{x}(\sigma)). \quad (\text{E.1})$$

In this expression, Σ describes the $D - 2$ dimensional vortex sheet, for which $\bar{x}_\mu(\sigma) = \bar{x}_\mu(\sigma_1, \dots, \sigma_{D-2})$ denotes a parametrization and $D(x)$ is the Green function of the D -dimensional Laplacian. Furthermore,

$$d^{D-2} \tilde{\sigma}_{\mu\kappa} = \frac{1}{(D-2)!} \epsilon_{\mu\kappa\alpha_1 \dots \alpha_{D-2}} d^{D-2} \sigma_{\alpha_1 \dots \alpha_{D-2}} \quad (\text{E.2})$$

is the dual of the $(D - 2)$ -dimensional volume element

$$d^{D-2} \sigma_{\alpha_1 \dots \alpha_{D-2}} = \epsilon_{k_1 \dots k_{D-2}} \frac{\partial \bar{x}_{\alpha_1}}{\partial \sigma_{k_1}} \dots \frac{\partial \bar{x}_{\alpha_{D-2}}}{\partial \sigma_{k_{D-2}}} d\sigma_1 \dots d\sigma_{D-2}.$$

The color structure is taken into account by $E(k) = E^a(k) T_c^a$ which satisfies

$$e^{iE(k)} = Z(k), \quad k = 1, \dots, N-1, \quad (\text{E.3})$$

where T_c are the generators of the Cartan subalgebra and $Z(k)$ denotes the $N - 1$ non-trivial center elements of the $SU(N)$ group. Let us particularize to the gauge group $SU(2)$. In this case, the Cartan subalgebra is Abelian (i.e. is based on only one generator) and there exists only one non-trivial center element $Z = -1$. The color structure of the center vortex is simply given by

$$E = E_3 T_c^3 \quad \text{with } E_3 = 2\pi, \quad T_c^3 = \frac{\tau^3}{2}.$$

The property (E.3) is trivially satisfied since we have $e^{i\pi\tau^3} = -1$. Returning to the center vortex (E.1), let us consider a loop C in space-time and the associated Wilson loop:

$$W_{\mathcal{A}^{\text{CV}}[\Sigma, k]}[C] = e^{i \oint_C dx_\mu \mathcal{A}_\mu^{\text{CV}}[\Sigma, x, k]}.$$

It can be shown that [ER00]

$$\oint_C dx_\mu \mathcal{A}_\mu^{\text{CV}}[\Sigma, x, k] = E(k)L(C, \Sigma),$$

where $L(C, \Sigma)$ is the linking number between C and Σ . As a consequence, the center vortex contributes a non-trivial element of the gauge group to any Wilson loop it pierces. For the group $SU(2)$, this reads

$$W_{\mathcal{A}^{\text{CV}}[\Sigma]}[C] = (-1)^{L(C, \Sigma)}.$$

This simple identity is crucial for the center vortex confinement scenario, since it leads to the area-law behaviour of the average Wilson loop in presence of center vortices [ER00].

In this work, we concentrate on *plane* vortex surfaces. In mathematical terms, we make the following choice for the vortex surface Σ :

$$\Sigma = \begin{cases} \bar{x}_1 = 0 \\ \bar{x}_2 = 0 \end{cases}.$$

Using the parametrization $\bar{x}(\sigma) = (0, 0, \sigma_1, \dots, \sigma_{D-2})$, $\sigma_1, \dots, \sigma_{D-2} \in]-\infty, \infty[$, from which the volume element (E.2) can be easily computed, and the expression of the Green function $D(x)$, we obtain the following expression describing plane center vortices:

$$\mathcal{A}_\mu^{\text{CV}}(x, k) = \frac{E(k)}{2\pi} \frac{1}{x_1^2 + x_2^2} (x_2, -x_1, 0, \dots, 0)_\mu.$$

E.2 Numerical computation of the Wilson loop

Due to the loop discretization, the Wilson integral reduces to the sum of integrals over line segments:

$$\oint A(x) \cdot dx = \sum_{i=1}^{N_{\text{Ppl}}} \int_{x^{(i)}}^{x^{(i+1)}} A(x) \cdot dx.$$

Each of the segments $[x^{(i)}, x^{(i+1)}]$ can be parametrized as

$$x(t) = x^{(i)} + t(x^{(i+1)} - x^{(i)}), \quad t \in [0, 1],$$

and the line integrals become

$$\int_{x^{(i)}}^{x^{(i+1)}} A(x) \cdot dx = \int_0^1 dt A(x(t)) \cdot (x^{(i+1)} - x^{(i)}).$$

E.2.1 Constant magnetic field

For the potential $A(x) = \frac{B}{2}(-x_2, x_1, 0, \dots, 0)$, the t integral is performed trivially and we find

$$\int_{x^{(i)}}^{x^{(i+1)}} A(x) \cdot dx = \frac{B}{2} \left(x_1^{(i)} x_2^{(i+1)} - x_2^{(i)} x_1^{(i+1)} \right).$$

E.2.2 Vortex field

For the potential $A(x) = \frac{1}{2} \frac{1}{(x_1 - x_1^V)^2 + (x_2 - x_2^V)^2 + d^2}$ ($x_2 - x_2^V, -(x_1 - x_1^V), 0, \dots, 0$) describing a vortex centered upon $(x_1^V, x_2^V, 0, \dots, 0)$, the line integral reduces to

$$\int_{x^{(i)}}^{x^{(i+1)}} A(x) \cdot dx = \left[x_1^{(i)} x_2^{(i+1)} - x_2^{(i)} x_1^{(i+1)} + x_1^V (x_2^{(i)} - x_2^{(i+1)}) - x_2^V (x_1^{(i)} - x_1^{(i+1)}) \right] \\ \times \int_0^1 dt \frac{1}{A + 2Bt + Ct^2},$$

with

$$\begin{aligned} A &= (x_1^{(i)} - x_1^V)^2 + (x_2^{(i)} - x_2^V)^2 + d^2, \\ B &= (x_1^{(i)} - x_1^V) (x_1^{(i+1)} - x_1^{(i)}) + (x_2^{(i)} - x_2^V) (x_2^{(i+1)} - x_2^{(i)}), \\ C &= (x_1^{(i+1)} - x_1^{(i)})^2 + (x_2^{(i+1)} - x_2^{(i)})^2. \end{aligned}$$

The indefinite integral is given by

$$\int \frac{dt}{A + 2Bt + Ct^2} = \begin{cases} \frac{1}{\sqrt{AC - B^2}} \arctan \left(\frac{Ct + B}{\sqrt{AC - B^2}} \right), & \text{if } AC > B^2, \\ \frac{1}{2\sqrt{B^2 - AC}} \ln \left| \frac{Ct + B - \sqrt{B^2 - AC}}{Ct + B + \sqrt{B^2 - AC}} \right|, & \text{if } AC < B^2. \end{cases}$$

E.3 Linear potential in Fourier space

In our lattice study of Yang-Mills theory in Coulomb gauge, we address the Coulomb potential in momentum space. Let us briefly discuss the representation in Fourier space of a linearly rising potential.

The non-relativistic potential $V(r)$ is obtained from the measured $V(k)$ in momentum space by Fourier transformation [we work in $D = 3 + 1$]:

$$\begin{aligned} V(r) &= \int \frac{d^3 k}{(2\pi)^3} V(k) e^{i\mathbf{k} \cdot \mathbf{r}} \\ &= \frac{1}{2\pi^2} \int_0^\infty dk k^2 V(k) \frac{\sin(kr)}{kr}. \end{aligned} \quad (\text{E.4})$$

For the electrostatic Coulomb potential $V(k) = 1/k^2$, we have simply

$$V(r) = \frac{1}{4\pi r}$$

since $\int_0^\infty dx \sin(x)/x = \pi/2$ (Fresnel's integral). In Yang-Mills theory, we have $k^2 V(k) = d^2(k)f(k)$. The resulting potential is linearly confining if

$$d^2(k)f(k) = -\frac{A}{k^2}. \quad (\text{E.5})$$

Inserting this expression in (E.4), regularizing the integral by means of an IR cut-off Λ and changing the variable $kr \equiv K$, we obtain

$$V(r) = -\frac{A}{2\pi^2} \int_{\Lambda r}^\infty dK \frac{\sin(K)}{K^3} r.$$

The remaining integral over K possesses a r -independent part:

$$\int_{\Lambda r}^{\infty} dK \frac{\sin(K)}{K^3} = -\frac{\pi}{4} + f(\Lambda r)$$

which furnishes the linearly rising part of the potential

$$V_{\text{lin}}(r) = \frac{A}{8\pi} r$$

and the Coulomb string tension $\sigma_{\text{Coul}} = A/8\pi$.

This result can be obtained in a more straightforward but less rigorous way by differentiating the expression (E.4) with respect to r . This yields

$$\frac{dV}{dr} = \frac{1}{2\pi^2} \int_0^{\infty} dk k^2 V(k) \left[\frac{\cos(kr)}{r} - \frac{\sin(kr)}{kr^2} \right].$$

Inserting (E.5), we obtain

$$\frac{dV}{dr} = -\frac{A}{2\pi^2} \underbrace{\int_0^{\infty} \frac{dK}{K} \left[\frac{\cos(K)}{K} - \frac{\sin(K)}{K^2} \right]}_{=-\pi/4},$$

which provides directly the Coulomb string tension.

Bibliography

- [AFvS03] Reinhard Alkofer, Christian S. Fischer, and Lorenz von Smekal. Infrared exponents and the running coupling of Landau gauge QCD and their relation to confinement. *Eur. Phys. J.*, A17:773, 2003.
- [AvS01] Reinhard Alkofer and Lorenz von Smekal. The infrared behavior of QCD Green's functions: Confinement, dynamical symmetry breaking, and hadrons as relativistic bound states. *Phys. Rept.*, 353:281, 2001.
- [BCLM] Jacques C. R. Bloch, Attilio Cucchieri, Kurt Langfeld, and Tereza Mendes. Propagators and running coupling from SU(2) lattice gauge theory. hep-lat/0312036.
- [Bur82] A. Burnel. Choice of a gauge in the light of Dirac quantization. *Phys. Rev.*, D26:442–454, 1982.
- [BV] Nora Brambilla and Antonio Vairo. Quark confinement and the hadron spectrum. hep-ph/9904330.
- [BZ99] Laurent Baulieu and Daniel Zwanziger. Renormalizable non-covariant gauges and Coulomb gauge limit. *Nucl. Phys.*, B548:527–562, 1999.
- [CJR83] M. Creutz, L. Jacobs, and C. Rebbi. Monte Carlo Computations in lattice gauge theories. *Phys.Reports*, 95:201, 1983.
- [CL80] N. H. Christ and T. D. Lee. Operator ordering and feynman rules in gauge theories. *Phys. Rev.*, D22:939, 1980.
- [CM96] Attilio Cucchieri and Tereza Mendes. Critical Slowing-Down in SU(2) Landau Gauge-Fixing Algorithms. *Nucl. Phys.*, B471:263–292, 1996.
- [CPPV96] Livio Conti, Claudio Parrinello, Silvano Petrarca, and Anastassios Vladikas. Testing the Quasi-temporal Gauge on the Lattice. *Phys. Lett.*, B373:164–170, 1996.
- [CZ02a] Attilio Cucchieri and Daniel Zwanziger. Numerical study of gluon propagator and confinement scenario in minimal Coulomb gauge. *Phys. Rev.*, D65:014001, 2002.
- [CZ02b] Attilio Cucchieri and Daniel Zwanziger. Renormalization group calculation of color Coulomb potential. *Phys. Rev.*, D65:014002, 2002.

- [CZ03] Attilio Cucchieri and Daniel Zwanziger. Gluon propagator and confinement scenario in Coulomb gauge. *Nucl. Phys. Proc. Suppl.*, 119:727–729, 2003.
- [DDFGO] L. Del Debbio, M. Faber, J. Greensite, and S. Olejnik. Center dominance, center vortices, and confinement. hep-lat/9708023.
- [DGLMP00] A. Di Giacomo, B. Lucini, L. Montesi, and G. Paffuti. Colour confinement and dual superconductivity of the vacuum. II. *Phys. Rev.*, D61:034504, 2000.
- [Dir64] P.A.M. Dirac. *Lectures on Quantum Mechanics*. Yeshiva University, 1964.
- [ER00] M. Engelhardt and H. Reinhardt. Center projection vortices in continuum Yang-Mills theory. *Nucl. Phys.*, B567:249, 2000.
- [ESW96] R.K. Ellis, W.J. Sterling, and B.R. Webber. *QCD and Collider Physics*. Cambridge Univ. Press, Cambridge, 1996.
- [FRa] C. Feuchter and H. Reinhardt. Quark and gluon confinement in Coulomb gauge. hep-th/0402106.
- [FRb] Claus Feuchter and Hugo Reinhardt. *Private communication*.
- [GO03] Jeff Greensite and Stefan Olejnik. Coulomb energy, vortices, and confinement. *Phys. Rev.*, D67:094503, 2003.
- [GOZ04] Jeff Greensite, Stefan Olejnik, and Daniel Zwanziger. Coulomb energy, remnant symmetry, and the phases of non-Abelian gauge theories. 2004.
- [Gre03] J. Greensite. The confinement problem in lattice gauge theory. *Prog. Part. Nucl. Phys.*, 51:1, 2003.
- [Gri78] V. N. Gribov. Quantization of non-Abelian gauge theories. *Nucl. Phys.*, B139:1, 1978.
- [GT90] D.M. Gitman and I.V. Tyutin. *Quantization of Fields*. Springer-Verlag, 1990.
- [Kug97] T. Kugo. *Eichtheorie*. Springer, 1997.
- [LMon] K. Langfeld and L. Moyaerts. Propagators in Coulomb Gauge from SU(2) lattice gauge theory. in preparation.
- [LRG02] K. Langfeld, H. Reinhardt, and J. Gattnar. Gluon propagators and quark confinement. *Nucl. Phys.*, B621:131–156, 2002.
- [MR03] Pieter Maris and Craig D. Roberts. Dyson-Schwinger equations: A tool for hadron physics. *Int. J. Mod. Phys.*, E12:297–365, 2003.
- [PFTV] W.H. Press, B.P. Flannery, S.A. Teukolsky, and W.T. Vetterlink. *Numerical Recipes*.
- [PS75] C.C. Paige and M.A. Saunders. *SIAM J. Numerical Analysis*, 12:617–629, 1975.
- [Rot97] H. J. Rothe. Lattice gauge theories: An Introduction. *World Sci. Lect. Notes Phys.*, 59, 1997.

- [RW94] Craig D. Roberts and Anthony G. Williams. Dyson-Schwinger equations and their application to hadronic physics. *Prog. Part. Nucl. Phys.*, 33:477–575, 1994.
- [She] Jonathan Richard Shewchuk. *An Introduction to the Conjugate Gradient Method Without the Agonizing Pain*. Lecture notes, <http://www.cs.cmu.edu/quake-papers/painless-conjugate-gradient.ps>.
- [SS96] H. Suman and K. Schilling. First Lattice Study of Ghost Propagators in SU(2) and SU(3) Gauge Theories. *Phys. Lett.*, B373:314–318, 1996.
- [SS02] Adam P. Szczepaniak and Eric S. Swanson. Coulomb gauge QCD, confinement, and the constituent representation. *Phys. Rev.*, D65:025012, 2002.
- [SvBZ03] L. Stodolsky, Pierre van Baal, and V. I. Zakharov. Defining $\langle A^2 \rangle$ in the finite volume Hamiltonian formalism. *Phys. Lett.*, B552:214–222, 2003.
- [Zwa82] Daniel Zwanziger. Nonperturbative modification of the Fadeev-Popov formula and banishment of the naive vacuum. *Nucl. Phys.*, B209:336, 1982.
- [Zwa94] Daniel Zwanziger. Fundamental modular region, Boltzmann factor and area law in lattice gauge theory. *Nucl. Phys.*, B412:657–730, 1994.
- [Zwa97] Daniel Zwanziger. Lattice Coulomb Hamiltonian and Static Color-Coulomb Field. *Nucl.Phys.*, B485:185, 1997.
- [Zwa98] Daniel Zwanziger. Renormalization in the Coulomb gauge and order parameter for confinement in QCD. *Nucl.Phys.*, B518:237, 1998.
- [Zwa03] Daniel Zwanziger. No confinement without Coulomb confinement. *Phys. Rev. Lett.*, 90:102001, 2003.

Danksagung - Remerciements

Mein erster und besonderer Dank gilt meinem Betreuer Herrn PD Dr. Kurt Langfeld. Sein ständiges Interesse, seine unermüdliche Bereitschaft zu Diskussionen und seine Unterstützung haben ganz wesentlich zum Gelingen dieser Arbeit beigetragen. Besonders hilfreich war sein unerschöpflicher Enthusiasmus, der jede Etappe meiner Promotion begleitete und das Überwinden unvermeidlicher Hindernisse immer erleichtert hat.

Danken möchte ich auch Herrn Prof. Dr. Hugo Reinhardt für die freundliche Aufnahme in seine Arbeitsgruppe und hilfreiche Diskussionen.

Einen ganz herzlichen Dank möchte ich Herrn Dr. Holger Gies für seine Unterstützung, seine ausführlichen und erleuchtenden Korrespondenzen und das Korrekturlesen dieser Arbeit aussprechen. An seinem tiefen Verständnis der theoretischen Physik teilhaben zu können war für mich besonders bereichernd.

Unter allen Faktoren, die zum Erfolg einer Doktorarbeit beitragen, ist ein freundliches Arbeitsklima von besonderer Bedeutung. Bei allen (Ex-)Mitgliedern der Arbeitsgruppe und des Graduiertenkollegs möchte ich mich von Herzen für die hervorragende Atmosphäre in- und außerhalb des Institutes bedanken. Ein besonderer Dank gilt Herrn PD Dr. Reinhard Alkofer für seine Unterstützung, sowie Christian Fischer, Jochen Gattnar, Oliver Schröder und Torsten Tok, die durch ihre Freundlichkeit meine Integration ins Leben der Arbeitsgruppe erleichtert haben. Gerne erinnere ich mich an spannende Diskussionen über Musik und Subtilitäten der deutschen und französischen Sprachen mit meinem ehemaligen Bürokollegen Steven Ahlig. Ich danke ebenso Markus Kloker für die fröhliche Atmosphäre im Büro, Claus Feuchter, Burghard Grüter, Jan Kuckei und Sebastian Weiss für zahlreiche Diskussionen und angenehm verbrachte Momente in Tübingen. Schließlich möchte ich Dominik Epple für seine hilfreichen Hinweise zum Thema Computerverwaltung danken.

Besonders dankbar bin ich den beiden Sprechern des Europäischen Graduiertenkollegs *Hadronen im Vakuum, in Kernen und Sternen*, Herrn Prof. Dr. Dr. h. c. mult. Amand Fäßler und Herrn Prof. Dr. Dr. h. c. Ingo Sick, für ihr Engagement. Ich bedanke mich für die finanzielle Unterstützung, ohne die diese Arbeit nicht möglich gewesen wäre, und die Übernahme der Reisekosten nach Norman, Oklahoma, die meine Teilnahme am QFEXT03 Workshop ermöglicht hat.

Schließlich möchte ich allen Personen bedanken, die ich in meinen nicht-physikalischen Tätigkeiten kennengelernt habe und die ganz wesentlich meinen Aufenthalt in Tübingen bereichert haben.

Diese Arbeit wurde unterstützt von der DFG unter GRK683.

Je voudrais enfin remercier toutes les personnes qui, de l'autre côté du Rhin, ont contribué à la réussite de ce travail.

J'adresse un merci tout particulier à mes parents, qui, malgré l'éloignement et mes trop rares visites en Belgique, me soutiennent et m'accordent leur confiance comme ils l'ont fait tout au long de mes études.

Au moment de clôturer ce travail, j'aimerais remercier chaleureusement Mr. Roland Grégoire, qui, me communiquant son enthousiasme, m'a permis tout au long de mes études musicales d'entretenir et de renforcer mon intérêt pour les sciences physiques.

Enfin, ces dernières lignes seront pour tous mes amis, musiciens ou anciens condisciples de l'Université de Liège qui, de près ou de loin, m'ont soutenu durant mon séjour à Tübingen.

J'aimerais particulièrement remercier Thierry et Elisabeth de Marneffe pour d'inoubliables périples en Scandinavie et d'innombrables excursions spontanées, Jean-Philippe Lansberg et Christophe Becco, pour les soirées culinaires de Chênee, les légendaires excursions touristiques en France et leurs régulières visites en Souabe, Stéphane Sante, à qui je dois l'essentiel de mes découvertes musicales, Noé Lecocq, Hervé Caps, pour de mémorables soirées de Nouvel An et enfin Benoît Roland à qui je dois, entre autres, une inoubliable visite de l'accélérateur HERA à DESY.

Lebenslauf

Persönliche Daten

Name: Laurent Moyaerts
geboren: 18.11.1974, Verviers, Belgien
Familienstand: ledig, keine Kinder
Staatsangehörigkeit: belgisch
Adresse: Stauffenbergstraße 31/1, 72074 Tübingen

Ausbildung

1980-1986 Grundschule in Verviers, Belgien
1986-1992 Gymnasium Thil Lorrain in Verviers, Abitur
1992-1995 Musikstudium an den Musikhochschulen Lüttich und Brüssel, Belgien
1995-2000 Studium der Physik mit Abschluss “Licence en Sciences Physiques”, Universität Lüttich;
Diplomarbeit: **Geometrie und Topologie in Eichtheorien**
09/2000–06/2004 Promotion in theoretischer Physik, Institut für Theoretische Physik, Universität Tübingen;
Anfertigung der Dissertation
A Numerical Study of Quantum Forces: Casimir Effect, Vortices and Coulomb Gauge Yang-Mills Theory
unter Anleitung von PD Dr. Kurt Langfeld

Stipendien und Beschäftigungen

09/2000–06/2001 geprüfte wissenschaftliche Hilfskraft am Institut für Theoretische Physik, Univ. Tübingen
07/2001–06/2004 Stipendium des europäischen Graduiertenkollegs “Hadronen im Vakuum, in Kernen und Sternen”, Institut für Theoretische Physik, Univ. Tübingen

Akademische Lehrer

Bastin, Burnel, Cudell, Cugnon, Dauby, Delmelle, Demaret, De Rop, Dumont, Evrard, Garnir, Gaspard, Grandjean, Heinrich, Kartheuser, Lejeune, Lion, Lorquet, Magain, Noels, Roubens, Rulmont, Schmeits, Schmets, Simon

December 4, 2004